Combustion Characterization of Bio-derived Fuels and Additives

Hashemi, Hamid

Publication date:
2015

Document Version
Publisher's PDF, also known as Version of record

Combustion Characterization of Bio-derived Fuels and Additives

A thesis presented for the degree of
Doctor of Philosophy

Written by

Hamid Hashemi

Supervisors:

Peter Glarborg

Jakob Munkholt Christensen

CHEC Research Centre
Department of Chemical and Biochemical Engineering
Technical University of Denmark (DTU)

January 2015

Summary

Climate change has become a serious concern nowadays. The main reason is believed to be the high emission of greenhouse gases, namely CO_2 which is mainly produced from the combustion of fossil fuels. At the same time, energy demand has increased exponentially while the energy supply mainly depends on fossil fuels, especially for transportation. The practical strategy to address such problems in medium term is to increase the efficiency of combustion-propelled energy-production systems, as well as to reduce the net release of CO_2 and other harmful pollutants, likely by using non-conventional fuels.

Modern internal combustion engines such as Homogeneous Charge Compression Ignition (HCCI) engines are more efficient and fuel-flexible compared to the conventional engines, making opportunities to reduce the release of greenhouse and other polluting gases to the environment. Combustion temperature in modern engines, gas turbines, and industrial burners has been reduced to prevent nitrogen oxides (NO_x) formation. Besides that, the pressure has commonly been elevated to promote the efficiency of the systems. Under such conditions, ignition and pollutant formation are determined by reaction kinetic.

Alternative fuels may be produced from different sources. If biomass feedstock is used in their production, they have the potential to reduce the net CO_2 release to the environment. However, the oxidation chemistry of alternative fuels is less known compared to the conventional fuels. In design/optimization of modern combustion-propelled systems reliable chemical kinetic models are vital while such models are rare for alternative fuels. This knowledge gap has been a challenging factor in utilizing alternative fuels in large scale.

This thesis is dedicated to provide characteristic data for fuel oxidation at high pressure and intermediate temperature. Such data provide a detailed insight into the oxidation chemistry and are vital tools in developing chemical kinetic models. Selected

fuels for this study, hydrogen, methane, ethane, ethanol, and dimethyl ether (DME), all can be produced from bio-sources. Their reaction kinetics are essential in modeling more complicated bio-derived fuels. Moreover, hydrogen, ethanol, and DME have been considered as additives to improve combustion properties of other fuels. In this work, experiments were carried out in a laminar flow reactor at the temperatures of 450–900 K and pressures of 20–100 bar. The results provided information about the onset temperature of reaction and the gas composition upon reaction initiation. A wide range of stoichiometry was tested, from very fuel-lean to strong fuel-rich mixtures. For ethanol and DME, further pyrolysis experiments were carried out. The results indicated that the onset temperature of reaction varied considerably among the fuels. DME highly diluted in nitrogen ignited at 525 K, independent of the stoichiometry and much lower compared to the other fuels. Ethane, ethanol, methane, and hydrogen ignited at higher temperatures, subsequently. The effect of doping methane by DME was also investigated and it was found that even small amount of DME can promote the methane oxidation considerably.

The flow reactor data have been interpreted in terms of a detailed chemical kinetic model, drawn mostly from earlier work from the same laboratory. The modeling predictions have been in good agreement with the measurements in the flow reactor. The model was further evaluated against high-pressure ignition delays as well as flame speed measurements in literature, and it successfully predicted most of the data. The reaction pathway of different fuels have been discussed, and sensitive reactions have been identified. A few reactions with high sensitivity but with poorly determined rate constants have been identified for further studies. The model was also used to analyze the complex behavior of the ignition of selected fuels against temperature and pressure. This mechanism can be utilized for further studies involving oxidation at high pressures and intermediate temperatures.

Dansk Resumé (Summary in Danish)

Klimaforandringer tages nu meget alvorligt, og hovedårsagen til disse forandringer menes at være udledningen af drivhusgasser, særligt CO_2, fra afbrændingen af fossile brændsler. Samtidigt stiger det globale energiforbrug eksponentielt, og denne energi stammer hovedsageligt fra fossile brændsler-specielt i transportsektoren. I den nære tidshorisont forsøger man i praksis at mindske problemerne ved at øge effektiviteten af forbrændings-drevne, energiproducerende systemer og ved at nedbringe netto-udledningen af CO_2 og andre skadelige komponenter - f.eks. ved at benytte ikke-konventionelle brændsler.

Moderne forbrændingsmotorer såsom Homogeneous Charge Compression Ignition (HCCI) motorer er mere effektive og fleksible mht. brændslet ift. konventionelle forbrændingsmotorer, hvilket skaber muligheder for at reducere udledningen af drivhusgasser og andre forurenende gasser til miljøet.

I moderne motorer, gasturbiner og industrielle brændere er forbrændingstemperaturen blevet nedbragt for at sænke dannelsen af nitrogenoxider (NO_x). Derudover er trykket blevet øget for at øge effektiviteten af disse forbrændingsbaserede systemer. Under sådanne forhold med forholdsvis lave temperaturer og forholdsvis høje tryk bestemmes dannelsen af forurenende komponenter af reaktionskinetikken - hastigheden af de reaktioner der foregår.

Alternative brændsler kan produceres fra forskellige ressourcer, og hvis disse brændsler produceres ud fra biomasse har de potentialet til at mindske CO_2-udledningen fra forbrændingssystemerne. Oxidationskemien for alternative brændsler er imidlertid ikke lige så velbeskrevet som den tilsvarende kemi for konventionelle brændsler. Til design og optimering af moderne forbrændingssystemer er det af vital betydning at have detaljerede kinetiske modeller for brændslet (modeller for de kemiske elementarreaktioner, der styrer oxidationskemien), men for de alternative brændsler er sådanne detaljerede og troværdige modeller stadig relativt sjældne.

Denne mangel i den eksisterende viden har været en udfordring for udnyttelsen af alternative brændsler i stor skala.

Denne afhandling fokuserer på gennem nye målinger at bidrage til forståelsen af oxidationen af brændsler ved højt tryk og moderat temperatur. Sådanne data giver en detaljeret indsigt i oxidationskemien og er af afgørende betydning for udviklingen af troværdige, detaljerede modeller for reaktionskinetikken. De brændsler, der er udvalgt i dette studium, er brint, methan, ethan, ethanol og dimethyl ether (DME). Disse brændsler kan alle kan fremstilles fra vedvarende ressourcer. Desuden er en forståelse for reaktionskinetikken for disse brændsler af essentiel betydning i beskrivelsen af mere komplicerede vedvarende brændsler. Desuden overvejes brugen af brint, ethanol og DME som additiver til andre brændsler for at forbedre forbrændingsegenskaberne. I dette studium blev der udført forsøg i en laminar flow-reaktor i temperaturområdet 450–900 K og trykområdet 20–100 bar. Resultaterne har givet informationer om antændingstemperaturer og om sammensætningen af produktgassen. Der er blevet udført forsøg i et vidt span af støkiometrier fra ilt-rige til ilt-fattige fødeblandinger. For ethanol og DME blev der desuden udført pyrolyseeksperimenter under ilt-frie forhold. Resultaterne indikerer, at reaktionens antændingstemperatur varier kraftigt for de forskellige brændsler. For DME stærkt fortyndet i nitrogen sker antændingen ved 525 K uafhængigt af støkiometrien – en temperatur der er meget lavere end for de øvrige undersøgte brændsler. Antændingstemperaturen for de øvrige brændsler stiger i følgende rækkefølge: ethan, ethanol, methan og brint. Effekten af at tilsætte små mængder DME til methan blev også undersøgt, og undersøgelserne viser, at selv småmængder af DME kan fremme oxidationen af methan betragteligt.

Flow-reaktor resultaterne er blevet fortolket med en detaljeret kinetisk model. Modellen er baseret på tidligere arbejde fra denne forskningsgruppe og er blevet udvidet for at give en forbedret beskrivelse og forståelse af oxidationen af de undersøgte brændsler. Forudsigelseren fra modellen er generelt i god overensstemmelse med de eksperimentelle resultater fra målingerne i flow-reaktoren. Den kinetiske model blev desuden evalueret mod højtryks tændingsforsinkelses- og flammehastighedsmålinger i den videnskabelige litteratur, og modellen viser sig i stand til at forudsige hovedparten af de eksperimentelt bestemte resultater. Reaktionsvejene i oxidationen af de forskellige brændsler er blevet diskuteret, og de elementarreaktioner, som har den største effekt påden overordnede reaktionshastighed, er blevet identificeret. Dette arbejde har udpeget enkelte elementarreaktioner, som ikke har velbeskrevne reaktion-

shastigheder, men som har stor betydning for oxidationsreaktionerne. Bestemmelsen af de præcise hastigheder for disse reaktioner vil være en oplagt videreførelse af dette arbejde. Den udviklede kinetiske model blev også anvendt til at analysere den komplicerede sammenhæng mellem antændingen af udvalgte brændsler og faktorer som temperatur og tryk. Den i projektet udviklede og verificerede kinetiske model vil kunne anvendes i fremtidige studer af oxidationsreaktioner ved højt tryk og moderate temperaturer.

Preface & Acknowledgment

This thesis is an outcome of my study as a PhD student over 2011–2014 at DTU Chemical Engineering, Combustion and Harmful Emission Control (CHEC) group. Professor Peter Glarborg has been the main supervisor throughout the project with assistant professor Jakob M. Christensen as a co-supervisor. I would like to express my sincere thanks to Peter Glarborg for giving me the opportunity to pursue this project.

In conducting experiments of hydrogen, methane, ethanol, and dimethyl ether, I have benefited from great helps of Jakob M. Christensen. The experiments of ethane were carried out by Jon G. Jacobsen and Christian L. Rasmussen, both were students at DTU chemical engineering when conducting the experiments. I have analyzed the data and developed the model under supervision of Peter Glarborg and Jakob M. Christensen. Chapter 5, which presents the results of hydrogen oxidation experiments, has been adopted from our publication in the *Proceeding of Combustion Institute (Vol. 35 (2015) 553–560).* I thank Sander Gersen (DNV GL-Oil & Gas) for modeling and discussing RCM results included in this article.

I would like to thank Peter Glarborg and Jakob M. Christensen, for their patience, understanding, and great support over this project. I acknowledge the financial support of this project by DTU (European Graduate School) and MAN Diesel & Turbo. I have enjoyed working with fellow PhD students, technicians, and administrative staffs at CHEC; thank you all for the nice atmosphere you made here. Finally, and most of all, I would like to thank my family for their love and support during this project.

Hamid Hashemi
Kgs. Lyngby, Denmark
January 2015

Contents

Outline

A short description of the contents of each chapter is given below.

- Chapter 1 briefly introduces the energy supply challenges to the reader. Properties and common production methods of the investigated fuels are also discussed shortly.

- Chapter 2 describes the experimental facility, the high-pressure laminar-flow reactor.

- Chapter 3 gives the equations describing the plug-flow model used for simulations. The calculations of reaction rate and thermochemical properties are discussed concisely.

- Chapter 4 introduces different methods of characterizing combustion and discuses their applications in evaluating chemical kinetic models.

- Chapter 5 presents the hydrogen oxidation results. This chapter is a slightly modified reprint of a paper published in *Proc. Combust. Inst. 35 (2015) 553–560* [1].

- Chapter 6 presents the results of methane oxidation which includes the flow reactor measurements at 600–900 K and 100 bar as well as a developed detailed chemical kinetic model.

- Chapter 7 describes the outcome of ethane oxidation experiments and simulations which includes flow-reactor measurements at 600–900 K and 20–100 bar.

- Chapter 8 presents the results of ethanol oxidation measured at 600–900 K and 50 bar as well as the developed chemical kinetic model.

– Chapter 9 provides the results of the dimethyl ether (DME) oxidation. Furthermore, the effect of adding DME to methane on the oxidation properties of their mixture is investigated.

– Chapter 10 summarizes all the species profiles measured in the flow reactor and compares the chemical reactivity across investigated fuels with the help of the validated model.

Chapter 1

Introduction

Climate change has become a serious concern nowadays. The main reason of the devastating changes in the climate is believed to be the high emission of greenhouse gases mainly from human activities. The energy demand has increased exponentially (fig 1.1) and even though the fuel efficiency improved globally, the CO_2 emission has increased considerably (fig 1.2). The steady increase in the global energy demand as well as the release of carbon dioxide and other harmful pollutants from the combustion of most fossil fuels are the major motivations to seek alternative sources of energy. CO_2–neutral sources of energy which do not involve combustion have a long way ahead to mature and the combustion of fossil fuels will thus remain the major source of energy for decades [2, 3]. Consequently, the focus should be on how to reduce the pollutants from combustion. In medium term, fossil-derived fuels which produce less pollutants and have a higher energy efficiency may relieve the environmental problems to some extent.

Natural gas is expected to have the highest growth rate among the fuels. For an equivalent amount of heat, burning of natural gas produces less carbon dioxide and other harmful pollutants than burning petroleum or coal (see table 1.1). In addition to its environmental benefit, natural gas will be cheaper and widely accessible [4]. As a result, natural gas is expected to partly replace coal and liquid petroleum fuels in power generation for electricity and industrial processes [3]. However, the consumption of liquid petroleum fuels will grow. These fuels remain as the major source of the energy for decades although their share in the worldwide energy supply will decrease [2, 3]. The growth in the consumption of liquid fuels will be mainly in the transportation and industrial sectors. Despite initially promising, the environmental aspects of liquid biofuels limit their widespread production. Other alternative fuels, in the gaseous phase

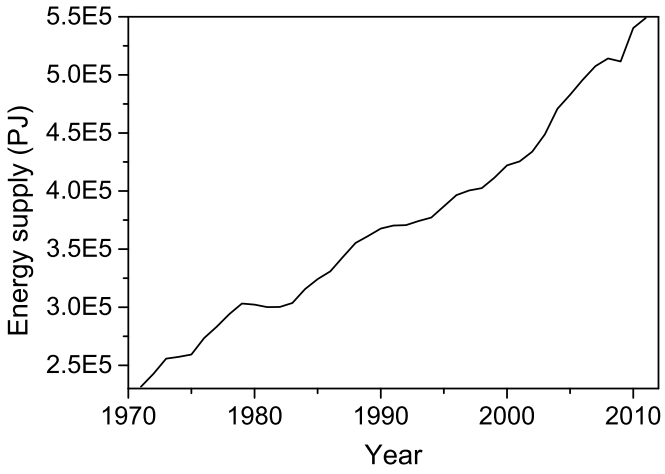

Figure 1.1: Worldwide total primary energy supply [8].

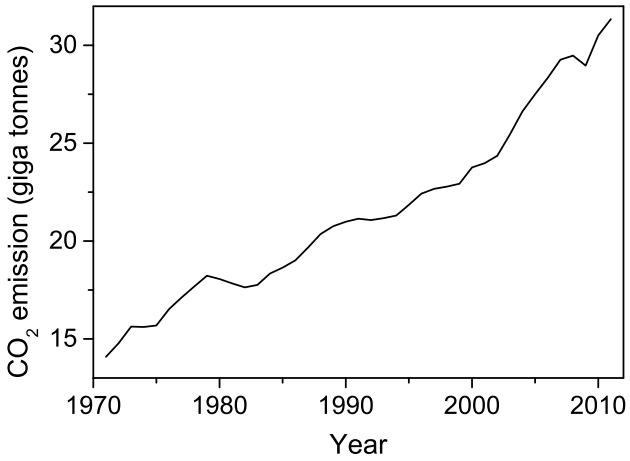

Figure 1.2: Worldwide total CO_2 emissions from fossil fuel combustion [8].

at ambient conditions, have not been widely adopted by the transport industry. Engines using liquid fuels and being highly developed over years provide higher power to weight and/or power to volume ratios compared to the competitor engines using gaseous fuels. The alternative fuels may also have strikingly different ignition properties. Moreover, some alternative fuels require modifications in combustion devices or maintenance methods. The lack of supply infrastructure has also been a prohibitive factor in adopting alternative fuels.

In compression-ignition (CI) engines, also known as diesel engines, the air is first

Table 1.1: Higher heating values (HHV) and carbon release of selected fuels (from ref [9], unless stated). The carbon release does not include the production processes.

	HHV [a] [MJ / Kg]	[MJ / Kmol]	C release [g / MJ]
Hydrogen	141.8	286	0
Methane	55.5	891	13.5
Natural gas	54	-	13.9
Ethane	51.9	1561	15.4
Dimethyl ether (DME)	31.7	1460	16.5 [b]
Heptane	48.1	4817	17.5
Ethanol	29.7	1367	17.6
Octane	47.9	5470	17.6
Gasoline	46.5	-	17.6
Decane	47.6	6778	17.7 [b]
Hexadecane	47.3	10699	18.0 [b]
Kerosene	46.4	-	18.5
Coal, high bituminous	36.3	-	23.5
Coal, low bituminous	28.9	-	26.3
Coal, anthracite	34.6	-	27.3

[a] higher heating value (liquid water in products)
[b] calculated here

compressed by the piston movement and then fuel is injected to the cylinder at a suitable time. Due to high pressure and temperature of the gases at the moment of injection , the mixture ignites without help of any external flame or spark. The cetane number is used to characterize diesel fuels and is an inverse function of ignition delay time (see section 4.2.2 for definition), so the higher cetane number means faster ignition of the fuel. If the fuel ignites faster in CI engines, there will be more time to complete the oxidation so the emission of unburned hydrocarbons will decrease and the efficiency will improve. Conventional diesel fuels usually have a cetane number of 40–50 [5] while fuels with higher cetane numbers are always preferred.

The octane number is used for the fuels of spark-ignited (SI) engines. In SI engines, fuel and air are premixed and then compressed by piston movement. At a suitable time, the spark ignites the mixture so a flame is formed and progresses inside the cylinder. Contrary to the CI engines, autoignition is not desired in SI engines. If the mixture ignites before the advent of the flame front, it leads to what is known as ”knock” in engines which deteriorates efficiency and stability of engines. The octane number

shows the resistance of the fuel to autoignition, so it is an inverse function of cetane number. In SI engines, fuels with high octane numbers are preferred. E85 gasoline, a common fuel for SI engines, consists of 15% ethanol mixed with gasoline and its octane number is around 102–105.

While most vehicles use either SI or CI engines, there are emerging technologies to improve the engines, e.g. the concept of homogeneous charge compression ignition (HCCI) engines. HCCI is a promising technology for internal combustion engines in which the fuel and air are premixed and then the mixture enters the cylinder, similar to SI engines, but the oxidation starts with the autoignition of the mixture, instead of a spark used in SI engines. A fuel-rich zone found in CI engines is avoided here as the mixture is homogeneously premixed, so the formation of soot and particulate matter (PM) is inhibited. The mixture is also highly diluted by air so the maximum temperature of the cycle decreases considerably. Lower temperatures inhibit the thermal formation of NO_x while the thermal efficiency of the engines is preserved close to that of CI engines [6]. The major challenge in the design and operation of HCCI engines is controlling the moment of autoignition, which is largely governed by chemical kinetics [7]. Therefore reliable detailed chemical kinetic models are vital in the design of such engines.

Low-temperature combustion is not limited to HCCI engines and can be found in many modern devices, in order to inhibit the thermal formation of NO_x. At low temperatures, the effect of chemical kinetic on the overall process is enhanced. Modern combustion devices are expected to have some degree of fuel flexibility while keeping high efficiency. As ignition properties of fuels may differ noticeably, predictive tools are vital in design and even operation of combustion devices.

In this work, combustion and reaction kinetic of hydrogen, methane, ethane, ethanol, and dimethyl ether were investigated at conditions relevant for engines and industrial applications. Tables 1.1 and 1.2 give some combustion properties of these fuels. An overview of the experiments conducted in this project can be found in table 1.3. In addition to stoichiometric conditions which are relevant in many applications, some experiments were conducted at very reducing and oxidizing conditions. In this way, models are evaluated at extreme cases.

In the following sections, the properties of individual fuels and the methods commonly used for their production will be discussed briefly.

Table 1.2: Combustion and physical properties of selected fuels (from ref [9], unless stated).

Fuel	Formula	Boil. T [a] [K]	Flam. limits [b] %	Ignit. T [c] [K]	S_L [d] [cm / s]
Hydrogen	H_2	20	4.0–74.0	–	210 [10]
Methane	CH_4	112	5.0–15.0	810	36 [11]
Ethane	C_2H_6	185	3.0–12.5	745	40 [12]
Ethanol	CH_3CH_2OH	351	3.3–19.0	636	40 [10]
DME	CH_3OCH_3	248	3.4–27.0	623	42 [13]
Heptane [e]	C_7H_{16}	372	1.05–6.7	477	37 [14]
Decane [f]	$C_{10}H_{22}$	447	0.8–5.4	483	
Octane [e]	C_8H_{18}	399	1.0–6.5	479	33 [14]
Hexadecane [f]	$C_{16}H_{34}$	560	–	475	

[a] boiling temperature at atmospheric pressure
[b] flammability limits in volume percentage in air (at ambient temperature and pressure)
[c] autoignition temperature
[d] laminar flame speed measured at ambient initial conditions for stoichiometric fuel/air mixtures.
[e] surrogates for gasoline
[f] surrogates for diesel fuel

Table 1.3: Overview of experiments conducted in the flow reactor.

Fuel	Φ [a]	P [bar]	T [K]	N_2 [molar %]
H_2	12	50	700–900	99.01
	1.03	50	700–900	99.54
	0.05	50	700–900	98.24
	0.0009	50	700–900	5.92 [b]
CH_4	19.7	100	700–900	98.03
	1	100	700–900	99.53
	0.06	100	700–900	95.93
C_2H_6	37.2	20	650–900	98.79
	39.7	50	600–900	98.79
	46.6	100	600–900	98.81
	0.82	20	675–900	99.73
	0.81	50	600–900	99.71
	0.91	100	600–900	99.72
	0.035	20	675–900	94.54
	0.034	50	650–900	94.47
	0.038	100	600–900	94.71
Ethanol	∞ [c]	50	600–900	99.31
	43	50	600–900	99.44
	1	50	600–900	98.65
	0.1	50	600–900	89.86
DME	∞ [c]	50	450–900	99.89
	20.2	50	450–900	99.91
	1	50	450–900	99.90
	0.04	50	450–900	98.91
DME + CH_4 [d]	20.2	100	450–900	98.03
	1	100	450–900	99.52
	0.04	100	450–900	96.21

[a] fuel-air equivalence ratio
[b] diluted in oxygen instead of nitrogen
[c] pyrolysis experiments
[d] with the DME to CH_4 ratios of 1.8–3.2%

1.1 Hydrogen

Contrary to fossil fuels, hydrogen cannot be found naturally, so it is considered more as an energy carrier. In industrial scale, hydrogen is produced from steam reforming of methane which is an endothermic reaction,

$$CH_4 + H_2O = CO + 3\,H_2 \tag{R 1.1}$$

and is followed by the water-gas shift reaction

$$CO + H_2O = CO_2 + H_2 \tag{R 1.2}$$

On the whole, this process gives four moles of hydrogen per each consumed mole of methane. Alternatively, hydrogen can be produced from the partial oxidation of methane or other hydrocarbons:

$$2\,CH_4 + O_2 = 4\,H_2 + 2\,CO \tag{R 1.3}$$

The gasification of coal can also be another source of hydrogen. To produce CO_2–neutral hydrogen, energy and chemical feedstock should be provided from sources other than the fossil fuels. It has been a controversial issue whether CO_2 release is decreased by producing hydrogen and burning it in engines or not. A study by McCarthy and Yang [15] showed that if hydrogen was produced by the electrolysis of water and was used in car engines, the overall CO_2 efficiency might even be worse than the conventional petroleum fuels. An alternative source of hydrogen production is syngas (H_2 + CO) from biomass and waste gasification which can potentially cut down CO_2 release.

Regardless of its production method, using hydrogen fuel introduces some challenges. A wider flammability range raises safety concerns (see table 1.1). The flame speed of hydrogen is much faster than other fuels, so modifying the combustion systems may be vital. Moreover, hydrogen even in the liquefied form offers an energy to volume ratio considerably smaller than petroleum fuels.

Strong motivations exist to study the hydrogen oxidation. The ignition properties of syngas are determined by hydrogen chemistry [16]. Hydrogen, as an energy carrier, may be produced commercially from renewable sources such as sun light and wind. The interesting sensitivity of hydrogen flammability limits to pressure and temper-

ature has been the topic of many studies (e.g.[17]). The hydrogen chemistry highly influences the oxidation of other fuels. Due to the significant contribution of H_2/O_2 reactions to the radical pool, these steps are among the most important reactions in ignition under many conditions. Chemical kinetic models for the combustion of hydrocarbon fuels all need an accurate hydrogen sub-mechanism [18].

Many practical combustion systems are designed to work at high pressure to increase efficiency. The gas temperature in modern devices has been also reduced compared to the earlier systems to minimize the thermal formation of nitrogen oxides. Yet combustion at high pressure and intermediate temperatures has been rarely studied, somewhat due to difficulties in conducting experiments at these conditions. As shown in figure 1.3, data from this study cover conditions which have not been studied before.

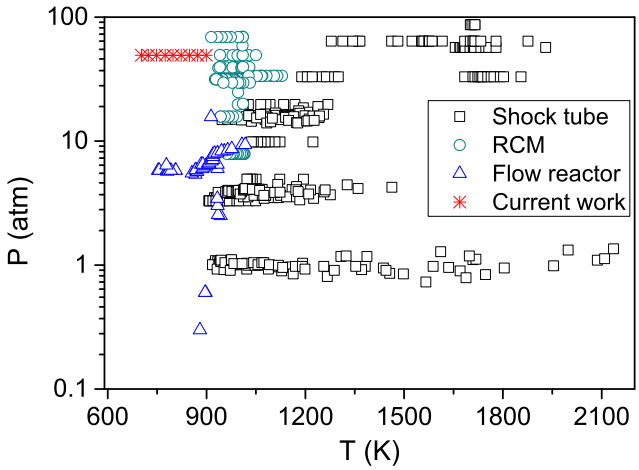

Figure 1.3: Temperature- and pressure-coverage of earlier experiments of hydrogen and the present ones.

1.2 Methane

Natural gas (NG) will have the fastest growth among all fuels in following decades and replace partly coal and liquid fuels in power generation for electricity and industrial processes [3]. A larger availability and less emission of pollutants from combustion are among the major reasons to replace other fossil fuels with natural gas. Due to recent successes in excavation of shale gas, natural gas will be cheaper, at least locally [4]. For an equivalent amount of heat, burning of natural gas produces around 20 and 45 percent less carbon dioxide than burning of gasoline and coal, respectively (see table

1.1). In addition to fossil reservoirs, natural gas can be produced from the anaerobic decay of biomass, e.g., agricultural waste and sewage sludge. More restrictive regulation of the release of greenhouse gases can increase the share of natural gas in the energy market even more.

Natural gas consists mainly of methane and to a lesser extent ethane and propane. Table 1.4 shows the typical composition of wellhead natural gas in north America. If commercially attractive, heaver hydrocarbons are separated from natural gas in refinery. Other major components as N_2, CO_2, and H_2S are usually removed by refinery processes before transportation to avoid their adverse effects on combustion or because of corrosion problems. Table 1.5 shows the average composition of liquefied natural gas (LNG) from selected LNG plants. As can be seen, the composition of natural gas varies noticeably due to the reservoir composition or different refinery process. Studies showed that variations in gas composition can affect the ignition properties considerably [19–21].

Table 1.4: Wellhead compositions of north American natural gases [23].

Component mol %	Rio Arriba N. Mex.	Terrell Tex.	Stanton Kans.	San Juan N. Mex.	Olds Field Alberta, Canada
CH_4	96.91	45.64	67.56	77.28	52.34
C_2H_6	1.33	0.21	6.23	11.18	0.41
C_3H_8	0.19		3.18	5.83	0.14
C_4H_{10}	0.05		1.42	2.34	0.16
Heavier HC	0.02		0.04	1.18	0.41
CO_2	0.82	53.93	0.07	0.8	8.22
H_2S		0.01			35.79
N_2	0.68	0.21	21.14	1.39	2.53

The biggest challenge in using natural gas has been its transportation. Due to its low energy to volume ratio, bulk quantities of natural gas should be transported. The economical way thus is to use pipeline. However, constructing pipeline requires a huge capital investment and may not be feasible or economical due to natural earth terrain or political reasons. An alternative solution is to liquefy natural gas and transport it as liquefied natural gas (LNG). To produce LNG, the temperature of the gas is decreased below the boiling temperature of pure methane, 111 K, so most components of natural gas become liquid. Other components of natural gas which become frozen around 111 K should be removed by refinery process beforehand. LNG can be transferred

Table 1.5: The average composition (molar percentage) of LNG from selected plants [24].

Origin	Methane	Ethane	Propane	Other components
Australia - NWS	87.33	8.33	3.33	1.01
Australia - Darwin	87.64	9.97	1.96	0.43
Algeria - Skikda	91.40	7.35	0.57	0.68
Algeria - Bethioua	89.55	8.20	1.30	0.95
Algeria - Arzew	88.93	8.42	1.59	1.06
Brunei	90.12	5.34	3.02	1.52
Egypt - Idku	95.31	3.58	0.74	0.37
Eqypt - Damietta	97.25	2.49	0.12	0.14
Equatorial Guinea	93.41	6.52	0.07	0.00
Indonesia - Arun	91.86	5.66	1.60	0.88
Indonesia - Badak	90.14	5.46	2.98	1.42
Indonesia - Tangguh	96.91	2.37	0.44	0.28
Libya	82.57	12.62	3.56	1.25
Malaysia	91.69	4.64	2.60	1.07
Nigeria	91.70	5.52	2.17	0.61
Norway	92.03	5.75	1.31	0.91
Oman	90.68	5.75	2.12	1.45
Peru	89.07	10.26	0.10	0.57
Qatar	90.91	6.43	1.66	1.00
Russia - Sakhalin	92.53	4.47	1.97	1.03
Trinidad	96.78	2.78	0.37	0.07
USA - Alaska	99.71	0.09	0.03	0.17
Yemen	93.17	5.93	0.77	0.13

with refrigerated tanker ships to destinations and unloaded in regasification terminals. After expansion to gas phase, it can be transported via pipeline to final customers.

Another solution to overcome transportation problem of natural gas is to produce liquid fuels from it. In Fischer-Tropsch process, methane is first converted to syngas by steam reforming,

$$CH_4 + H_2O = CO + 3\,H_2 \qquad \text{(R 1.4)}$$

then the gases are converted to synthetic liquid fuels using the Fischer-Tropsch catalysis. This process has been commercialized but needs capital investment [22]. Alternatively, methane can be partially oxidized which gives methanol in the absence of any catalyst. This process necessitates improved understanding of methane oxidation in design and operation. This process has been investigated (e.g. [22]) but has not been

commercialized yet.

Natural gas has been used as a fuel for internal combustion engines to a limited extent around the world. The lack of necessary infrastructure has been a prohibitive factor in using NG extensively. Conventional engines should be modified to allow efficient consumption of NG. In vehicles, natural gas is generally stored as CNG (Compressed Natural Gas) or LNG, both require bulky and heavy on board storage facilities. Short fueling intervals compared to the conventional gasoline/diesel engines are problematic in cars running with natural gas.

Figure 1.4 shows the pressure- and temperature-coverage of earlier studies. To study combustion of methane at high pressures and intermediate temperatures, relatively long residence time is required which is accessible in flow reactors and rapid compression machines.

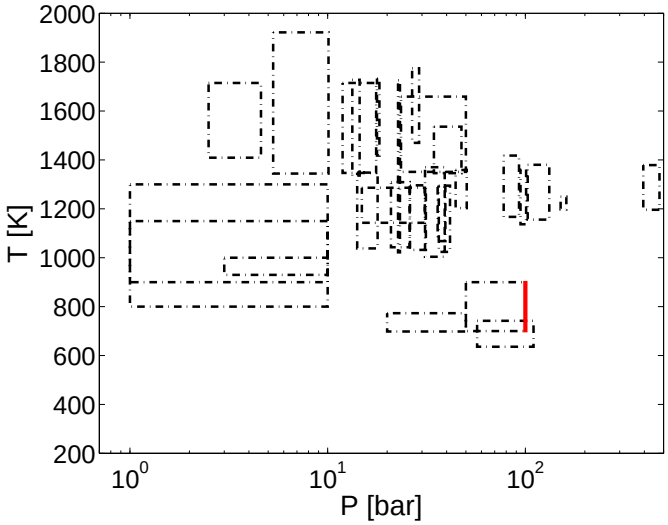

Figure 1.4: Temperature- and pressure-coverage of earlier experiments of methane and the present ones. Dashed lines correspond to earlier experiments in [21, 25–35] and solid red lines mark the present experiments.

1.3 Ethane

Ethane is mainly produced from refining natural gas. Due to its higher value as a chemical feedstock, ethane is separated from natural gas via distillation if its concentration is high enough to make the process commercially attractive. However, natural gas delivered to customers may consist of considerable amounts of ethane, e.g. up to 12% as shown in table 1.5. Compared to methane, neat ethane ignites at a lower temperature

and has a slightly faster flame speed (table 1.1). Disparity in the ethane ratio in NG may change the ignition properties of the fuel considerably [36]. The oxidation mechanism of ethane plays an important role in the hierarchical structure of the chemical mechanisms of hydrocarbons. Moreover, the chemical interaction between ethane and potential additives for natural gas is necessary in chemical kinetic modeling of ignition and pollutant formation.

Figure 1.5 represents available data focused on high-pressure combustion of ethane. As shown, the experiments in this project provide data at a range which has not been investigated to date.

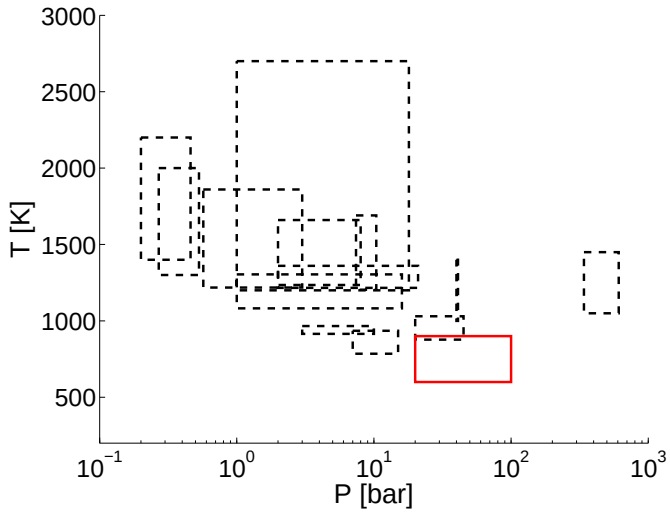

Figure 1.5: Temperature- and pressure-coverage of earlier experiments of ethane and the present ones. Dashed lines: the previous measurements in ref [37–46], red solid lines: the present measurement of species profile in the flow reactor.

1.4 Ethanol

Ethanol is produced at industrial scale from the catalyzed hydration of ethene.

$$C_2H_4 + H_2O = CH_3CH_2OH \qquad \text{(R 1.5)}$$

Alternatively, ethanol can be produced from biomass through the fermentation process. In the fermentation process, different sugars are converted biologically to ethanol. Both methods give a mixture of ethanol and water which is separated by distillation. It has been demonstrated that ethanol-water mixtures can be used directly in HCCI engines, removing the energy deficiency of water removal step and thus promoting the

overall energy efficiency [47, 48]. Ethanol biofuel can potentially reduce the carbon footprint. Nevertheless, studies showed that not all methods of biofuel production are environmentally acceptable and the carbon efficiency of biofuels can be even worse compared to fossil fuels [49]. Among the liquid fuels, biofuels will have the fastest growth in consumption, but they will maintain a minor share of the liquid fuels supply for decades [3].

Ethanol fuel, either neat or in a blend, is used mainly in internal combustion engines. Ethanol addition to gasoline promotes the overall octane number of the fuel while it potentially reduces the emission of particulate matter [50] and CO [51]. Gasoline doped by ethanol is widely used in SI engines [49] in many places, e.g. Brazil and the United States. The addition of ethanol to diesel fuel has also been studied [52, 53] and it was found that adding ethanol can reduce the fuel consumption [52]. The relatively high energy density of ethanol makes it interesting to be used as a neat fuel too. However, widespread usage of ethanol fuel may give rise in the emission of aldehydes [49, 51, 54] which can cause serious health risks.

The combustion of hydrocarbon fuels has been studied over decades. In contrast, the oxidation chemistry of oxygenated fuels is recent and still many links in intermediate steps may be missing. The combustion mechanism of ethanol is a crucial part in models for heavier alcohols often found in complicated biofuels [49].

Figure 1.6 shows a selection of available data for the oxidation and pyrolysis of ethanol. The experiments in this project enrich the earlier data by providing species profile of the most stable components.

1.5 DME

Dimethyl ether (DME) is an isomer of ethanol but with different structure and distinct thermodynamic and ignition properties [49]. In general, DME can be produced from different feedstocks, e.g. oil, natural gas, coal, waste products, and biomass. The current commercial production method is the dehydration of methanol:

$$CH_3OH + CH_3OH = CH_3OCH_3 + H_2O \qquad \text{(R 1.6)}$$

DME from biomass-derived methanol can potentially reduce the CO_2 release to the environment.

Higher cetane number and lower boiling temperature of DME make it an attractive alternative to conventional diesel fuels for use in CI or HCCI engines. Historically,

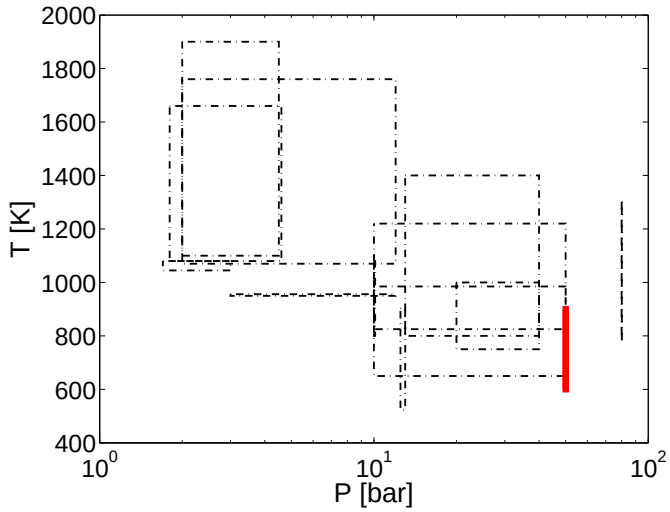

Figure 1.6: Temperature- and pressure-coverage of earlier experiments of ethanol and the present ones. Dashed lines correspond to earlier experiments in [34, 55–65], and solid red lines mark the present experiments.

DME application as an engine fuel has been demonstrated by the Haldor Topsøe company and DTU at the beginning of 1990's. Replacing diesel fuel by DME reduces the emission of particulate matter (PM) and nitrogen oxides (NOx) from slightly modified CI engines [66–71]. The absence of a C–C bond in the molecular structure of DME as well as its high oxygen content are believed to suppress soot formation [69]. DME can also be used for household purposes as well as power generation in gas turbines [72]. Nevertheless, around 40% lower energy density (per unit volume) of liquefied DME and potentially higher emission of aldehydes and CO, compared to diesel fuel, may challenge widespread usage of DME [69]. Poor lubricity and incompatibility with common sealing materials in injection systems are further challenges ahead of DME applications in engines [69].

DME has also been considered as an additive to control the ignition of different fuels. DME addition to natural gas accelerated ignition [73–76] by forming CH_3 and HO_2 radicals [74]. DME addition also accelerated the propagation of methane flame [74, 77] and its addition to LPG reduced NO_x emissions [78]. DME was also an effective additive in ethanol-fueled CI and SI engines [79, 80]. DME was considered as an additive to methanol for use in CI engines in early studies [81–83]. Whereas DME addition accelerates methane ignition, its effect on ethane oxidation was more complicated [84]. Therefore it is vital to understand interactions between DME and the components of natural gas, especially since local variations in the composition of natural gas can be

noticeable. Figure 1.7 shows selected available data for the oxidation and pyrolysis of DME at high pressure. The experiments conducted in this work provide data at higher pressures which are more relevant for industrial and engine applications, compared to earlier studies.

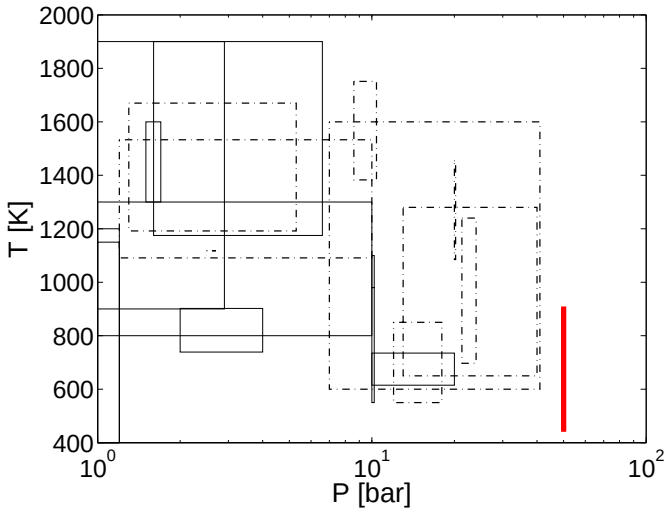

Figure 1.7: Temperature- and pressure-coverage of earlier experiments of DME oxidation and pyrolysis and the present ones. Dashed lines correspond to earlier experiments in [75, 76, 85–101] and solid red lines mark the present experiments.

Chapter 2

Experimental Methodology

2.1 Laminar flow reactor

Figure 2.1 shows a schematic diagram of the laboratory-scale high-pressure laminar-flow reactor used in this project. The reactor was designed to approximate plug flow. The setup was described in detail elsewhere [22, 102] and only a brief description is provided here. The reactions took place in a tubular quartz reactor (inner diameter of 8 mm) to minimize the effects of surface reactions. The quartz reactor was enclosed in a stainless steel tube (i.d. 22 mm, o.d. 38 mm) that acted as a pressure shell. The system was pressurized from the feed gas cylinders and the reactor pressure was monitored upstream of the reactor by a differential pressure transducer and controlled by a pneumatically operated pressure-control valve positioned after the reactor. A pressure control system consisting of two thermal mass flow/ pressure controllers (MFPC) automatically delivered nitrogen to the shell-side of the reactor. The pressure in the shell-side of the reactor was retained close to that inside the reactor in order to inhibit devastating pressure gradients across the fragile quartz glass. The pressure fluctuations of the reactor were as low as ±0.2%.

The steel tube was placed in a tube oven with three individually controlled electrical heating elements that produced an isothermal reaction zone (±6 K) of ~35–48 cm in the middle of the reactor. A moving thermocouple was used to measure the temperature profile inside the pressure shell at the external surface of the quartz tube after stabilizing the system.

The flow rates were regulated by high-pressure digital mass-flow controllers (MFC). The gases were mixed at ambient temperature well before entering the reactor so a complete mixing was expected before the high temperature zone of the reactor.

The liquid feeding system was described in detail in [103]. The liquid was pres-

surized by an HPLC pump. The pressure in the feeding section was controlled by a back-pressure valve that directed part of the liquid flow back into the feed reservoir. The liquid flow to the reactor was controlled by a liquid mass-flow controller. The liquid then evaporated in a custom-made evaporator at a temperature around 520 K and mixed with the incoming gaseous feed before entering the reactor. To avoid condensation of the fed liquid, the connecting tubes were wrapped in heat-tracing tapes. The stability of the liquid feed to the system was the major restriction in feeding low quantities of liquids. A long stabilization period before each test was employed to limit the fluctuations of the liquid feeding system to maximally ±5%.

Downstream of the reactor, the system pressure was reduced to atmospheric level prior to product analysis, which was conducted by an on-line *6890N Agilent Gas Chromatograph* (GC-TCD/FID from Agilent Technologies). All connecting tubes downstream of the reactor and before GC were wrapped in heat tracing tapes to avoid condensation of products.

For each set of experiment, the concentration of reactants as well as the pressure of the system were constrained while temperature of the isothermal zone was gradually increased in small steps around 25 K. By increasing the temperature, the gas velocity increased so the residence time of the gas in the hot zone of the reactor decreased accordingly. After increasing the temperature, around 45 minutes was dedicated for system stabilization and then the GC measurements started.

All GC sampling and measurements were repeated at least two times to improve the accuracy of measurements. The total flow rate was also measured by a bubble flow meter downstream of the reactor. Using a quartz tube and conducting experiments at high pressures were expected to minimize the contribution from heterogeneous reactions at the reactor wall.

Figure 2.2 shows an example of fuel conversion in the flow reactor. In some reactor designs, it is possible to conduct the measurements by using a moving probe inside the reactor and obtain data versus distance (time), e.g. see [91]. However the probe might intrude in the flow field and increase the uncertainty due to the risk of heterogeneous reactions on probe surface. Using a probe could also be operationally difficult at high pressures of this study. To avoid such difficulties, measurements were conducted at the exhaust of the reactor in this work.

In this project, the system was used to study oxidation of hydrogen, methane, ethane, ethanol, DME and DME/methane mixtures at pressures between 20 and 100 bar

and temperatures between 450 and 900 K. The flow rate was varied between 3 and 4.8 Nliter/min (STP: 1 atm and 273.15 K).

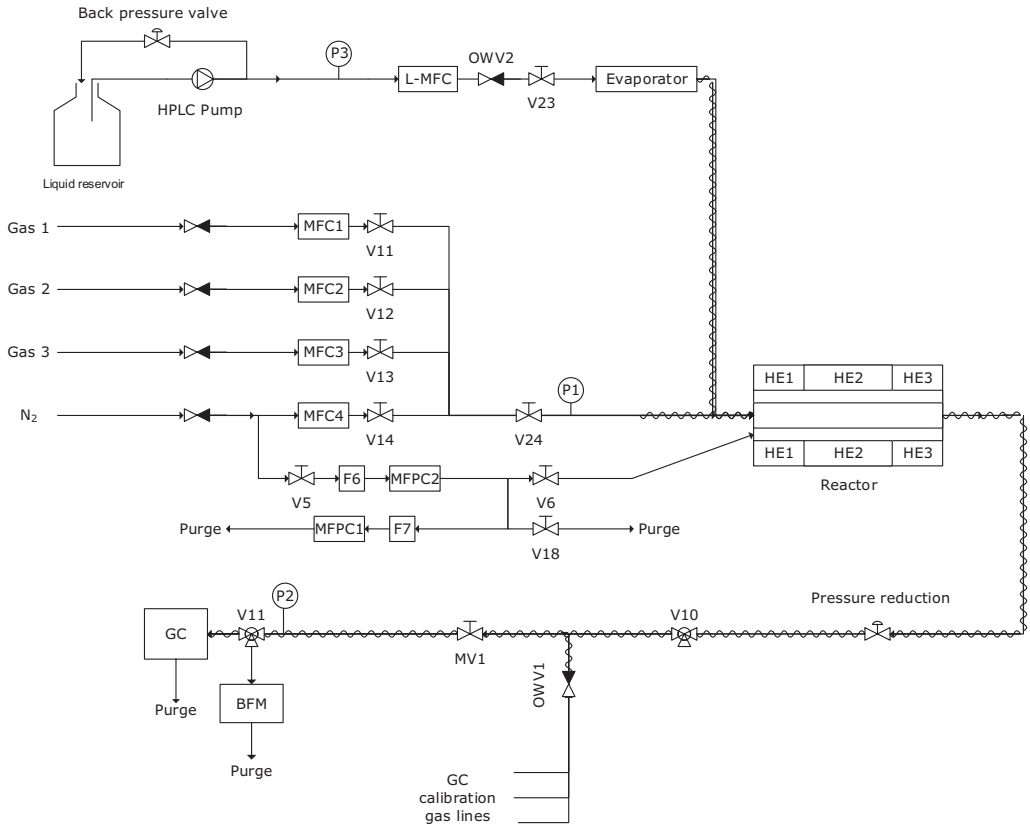

Figure 2.1: Schematic diagram of the experimental setup. BFM, bubble flow meter; GC, gas chromatograph; L-MFC, mass flow controller for liquids; MF(P)C, mass flow (pressure) controller; OWV, one-way valve; P, manometer. Heat tracing tubing is indicated by sinusoidal curves. The diagram is a modified version of that in [103].

2.1.1 Temperature profile

Figure 2.3 shows an example of temperature measurements conducted at 100 bar. The objective was to establish a temperature profile resembling a step function, as much as possible, by adjusting the nominal temperatures of heating elements. The temperature profiles were measured at a few isotherms and then the nominal temperatures of the heating elements (input to the heating system) and temperature profiles were interpolated for intermediate temperatures. The interpretation and simulation of the results would be facilitated if the heating and cooling zones were short enough to be

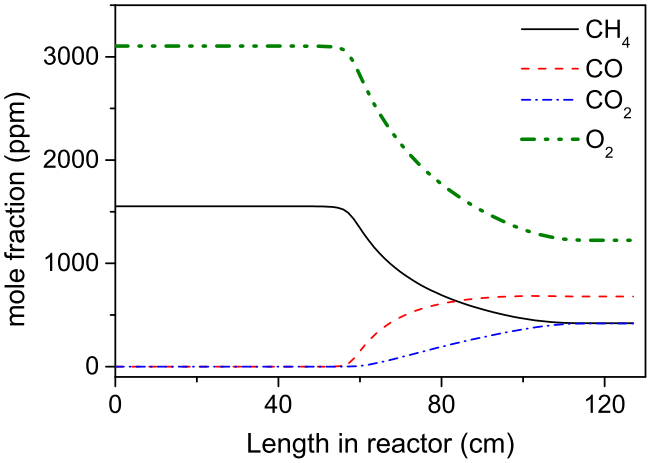

Figure 2.2: Simulated oxidation of stoichiometric methane/oxygen mixture in the laminar flow reactor. Isothermal temperature was 850 K covering x=59–98 cm and pressure was 100 bar. The gas mixture was 3104/1553 ppm of O_2/CH_4 in N_2.

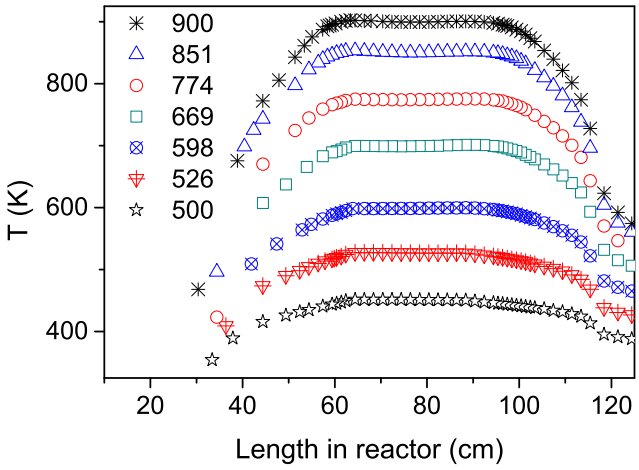

Figure 2.3: Temperature profile measured at the external surface of the quartz reactor at different isotherms. The flow was pure nitrogen at 3.23 NL/min (STP: 1 atm and 273 K) and at pressure of 100 bar.

negligible against the isothermal length. However, even for short cooling and heating zones, the residence time of the gases at heating and cooling zones were considerable due to lower gas velocity. For DME, a very reactive fuel at low temperatures, it was found necessary in the calculations of this project to include the full temperature profile and not only the isothermal part. In ethane experiments, we noticed that the heating zone at high pressures was longer than what was expected. As a result, the gases experienced a considerable time at temperatures high enough to react but below the isothermal temperature. Therefore the full temperature profile should be utilized in the simulation there. In general, including the temperature profiles could promote the accuracy of simulations, so the profiles were implemented in most of the simulations in this project despite being computationally more demanding.

In earlier studies in the same reactor [22, 32], it was presumed that the temperature profile was changed only by input to the heating system and the total flow rate. Over the present experiments, it was found that the temperature profile was sensitive to pressure too. Figure 2.4 shows temperature profiles at three different pressures while the other controlling parameters of the system were fixed. The isothermal zone of the reactor (±6 K) shrunk considerably at higher pressures, from 42 cm to 28 cm and then 24 cm when pressure increased from 30 bar to 50 and then 100 bar.

The causes of the heating zone extension with increasing pressure was not totally clear. It could be due to a larger flow at higher pressures. The flow rate of the reacting mixture was accurately controlled by the mass flow controllers and checked by the bubble flow measurements, but a larger flow of nitrogen in the pressure-shell could occur. The MFPC (mass flow/ pressure controllers) controlled the pressure and flow in the void between the quartz tube and the shell. If outside the quartz tube pressure was larger than the inside, the inlet MFPC allowed high pressure nitrogen to enter the void to compensate for it. On the other hand, if pressure outside the quartz tube was too high, the outlet MFPC evacuated nitrogen to the purge system. Consequently, a zigzag pattern was usually seen in the pressure of gases in the shell. It seemed that the fluctuating pattern was intensified at higher pressures, so larger amounts of nitrogen might enter and leave the shell. A higher flow of nitrogen required more energy for heating up, so the temperature dropped. Regardless of the involved factors, for all experiments except the ethane tests, the isothermal zone was extended by increasing the nominal temperature of the upstream heating element.

A potential source of uncertainty in the interpretation of data from the flow re-

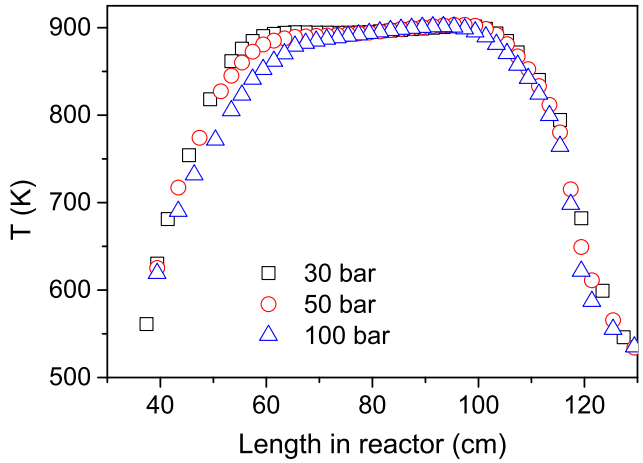

Figure 2.4: Effect of pressure on temperature profile. The flow was pure nitrogen at 3.1 NL/min (STP: 1 atm and 273 K) and inputs of the heating system were fixed.

actor was the temperature rise due to exothermic reactions. Presently, the reactants were strongly diluted in inert gases to limit the undesired temperature rise. When the mixture has the highest exothermicity, measuring the temperature profile indicated a marginal difference compared to the flow of pure nitrogen. The narrow quartz tube used here also accelerated the thermal equilibrium between the reactive gas inside the reactor and the heating bath gas surrounding it. Consequently, the temperature rise due to exothermicity was estimated to be a limited effect under most conditions.

2.2 Gas chromatograph (GC)

The products of reactions were analyzed using a *6890N Agilent Gas Chromatograph* (GC-TCD/FID from Agilent Technologies). The GC had three operational columns (DB1, Porapak N, and Molesieve 13x). To detect H_2, argon was used as carrier gas in the GC. To detect other components as O_2, N_2, CH_4, CO, CO_2, C_2H_4, C_2H_6, C_3H_8, CH_2O, dimethyl ether (CH_3OCH_3), methanol (CH_3OH), ethanol (CH_3CH_2OH), and acetaldehyde (CH_3CHO), helium was used as carrier gas.

For gaseous compounds the integral of GC peaks were related to molar fractions by calibration against certified gas mixtures (± 2 % from AGA A/S). For liquid compounds, the calibration was typically based on gas mixtures prepared by injecting a known quantity of the liquid component into a known volume of nitrogen in a Tedlar bag and allowing the liquid to evaporate. The calibration points obtained by this

method had larger uncertainties. To avoid difficulties in handling formaldehyde, its calibration was produced by correlating TCD response factors for other components to calculated thermal conductivities estimated from the Chapman-Enskog kinetic theory [104]. The TCD response factor for formaldehyde was then determined by using a calculated thermal conductivity with this correlation. In the calculation of the thermal conductivity of formaldehyde, the employed Lennard-Jones force constants (σ = 3.65 $\mathring{A}$, ε/K = 313.9 K) were in turn estimated from the critical properties (Lide [105]) using the method of Satterfield [106].

In general, the uncertainty of the GC measurements was estimated to be around 6%. Nevertheless, the signal to noise ratio of formaldehyde in the TCD detector was relatively small, so a larger uncertainty in the reported formaldehyde was estimated especially at ppm levels. Moreover, distinguishing methanol from acetaldehyde was not possible due to signal overlapping under the GC configuration used. The signal areas corresponding to the sum of these components were measured and quantified by using the response factor of methanol, but the reported quantity were less accurate especially when a considerable yield of acetaldehyde was expected.

Chapter 3

Modeling

The results from experiments in the flow reactor should be translated into a chemical kinetic model for extrapolation to other conditions. To avoid difficult interpretation of data from complex flows, the reactor was designed to approximate a plug flow pattern. In this chapter, the equations governing flow and chemistry in plug flows are discussed and derived.

3.1 Plug flow reactor

The interpretation and simulation of the results are easier if the flow in the reactor can be approximated by a steady-state plug flow. In plug flows, the fluid is perfectly mixed in the radial direction and each ”plug” or lateral slice of the fluid in the reactor has uniform fluid properties, e.g., temperature, pressure, velocity, and composition. If all the fluid elements of a plug move only in the direction of the reactor main axis, then a flat velocity profile is formed, and all fluid elements have the same residence time in the reactor. In plug flows it is required that the fluid has a negligible diffusive transport in the direction of the bulk flow, so plugs are not mixed together. To evaluate the flow pattern in our reactor, we need to characterize its flow regime first, whether it is laminar or turbulent. The dimensionless quantity of Reynolds number, Re, is used to characterize laminar and turbulent flows. Re shows the ratio of inertial forces to viscous forces and is defined for the flow in circular tubes as:

$$Re = \frac{\rho u D}{\mu} \tag{3.1}$$

where ρ is the gas density, u is the gas velocity, D is the diameter of the tubular reactor, and μ is the gas dynamic viscosity. Re should be smaller than ~2100 for laminar flows in tubes [107]. For the flows investigated in this project, the calculated Reynolds

number was ~700 at maximum, far below the upper limit of the laminar flows.

In principle, the laminar flows in tubes have a parabolic velocity profile. On the other hand, if the tube is long enough, the molecular diffusion in lateral direction have enough time to smooth the lateral gradients of fluid properties [108] which makes the flow pattern resembling the plug flow. A useful concept to describe diffusion in flows is "dispersion". Dispersion characterizes the spreading of fluid elements as a result of different local flow velocities and molecular diffusion [22, 102] and is shown by dispersion coefficient, D_{disp} $\left[m^2/s\right]$. The dimensionless number of "intensity of dispersion" is defined as:

$$\frac{D_{disp}}{uL} = \frac{\text{spreading by dispersion}}{\text{spreading by bulk flow}} \tag{3.2}$$

where L shows the length of the reactor. A small value of $\frac{D_{disp}}{uL}$ indicates that the fluid elements are spread in the reactor by the main flow and plugs are not mixed together, so plug flow is a good approximation.

Another dimensionless number to characterize the laminar flow is the Bodenstein number, Bo, defined as the product of Reynolds and Schmidt numbers:

$$Bo = Re \times Sc = \frac{\rho u D}{\mu} \times \frac{\mu}{\rho u D_{AB}} = \frac{\text{mass transfer by convection}}{\text{mass transfer by diffusion}} \tag{3.3}$$

where D_{AB} is the molecular diffusion coefficient. For the flow reactor used here, Rasmussen [22] calculated Bo number and $\frac{D_{disp}}{uL}$ for representative mixtures of gases (N_2 /O_2 / CH_4) at 600–900 K, 10–100 bar, and flow rates from 1 to 5 NL/min. According to his calculations, the deviation of the flow pattern from the plug flow is relatively small at flow rates below 3 NL/min but it grows slightly at higher flow rates.

3.1.1 Mass and energy conservation

The plug flow reactor is modeled as a closed system without any mass transfer across the boundaries. All plugs entering the reactor experience a similar residence time and react isolated from the preceding and following ones. Moreover, there is no variation in any direction except the flow direction, here x, and the axial diffusion of any quantity is assumed to be negligible compared to the corresponding convective term [109]. The

mass balance equation then can be written as:

$$\rho\, u\, A = \text{constant} \Rightarrow$$
$$\rho\, u\, \frac{dA}{dx} + \rho\, A\, \frac{du}{dx} + A\, u\, \frac{d\rho}{dx} = 0 \tag{3.4}$$

where ρ, u, and A are mass density, gas velocity, and cross sectional area of the reactor, respectively. For a reactor with constant A, it becomes:

$$\rho\, A\, \frac{du}{dx} + A\, u\, \frac{d\rho}{dx} = 0 \tag{3.5}$$

Although the total mass of every plug is constant, the mass fraction of individual species can change due to the reactions. The mass balance for the i^{th} species:

$$\rho\, u\, A\, \frac{dY_i}{dx} = MW_i\, \dot{\omega}_i\, A \tag{3.6}$$

where Y_i and MW_i are the the mass fraction and the molecular weight of the i^{th} species, respectively. $\dot{\omega}_i(x)$ is the chemical production rate of the i^{th} species due to gas-phase reactions which will be shown in section 3.2.1 to be a function of mixture composition, temperature, and pressure. Consequently:

$$\frac{dY_i}{dx} = \frac{MW_i\, \dot{\omega}_i}{\rho\, u} = f(T,\, P,\, u,\, Y_1, \ldots Y_i) \tag{3.7}$$

There is no need to solve the energy equation for systems with constrained temperature. For an adiabatic reactor, the energy equation can be written as:

$$\rho u A \left(\bar{c_P}\, \frac{dT}{dx} + u\, \frac{du}{dx} + \sum_{i=1}^{N_{sp}} \frac{dY_i}{dx}\, h_i \right) = 0 \tag{3.8}$$

where h_i is the specific enthalpy of the i^{th} species and $\bar{c_P}$ is the mean heat capacity at constant pressure per unit mass of gas. Adding a gas equation of state, the system of equations can be solved now. The residence time of the gas in the reactor, τ, can be calculated by integrating

$$\frac{d\tau}{dx} = \frac{1}{u} \tag{3.9}$$

3.2 Detailed kinetic modeling

To solve the presented system of equations, it is necessary to calculate the production/consumption rate as well as thermodynamic properties for both stable and non-stable species. In following sections we briefly describe the formulation used to calculate reaction rates and thermodynamic properties.

3.2.1 Chemical reaction rates

As an example of a chemical reaction, a simple bimolecular elementary reaction in which species C and D react to form E and F is considered:

$$\mathrm{C} + \mathrm{D} \rightarrow \mathrm{E} + \mathrm{F} \tag{R 3.1}$$

The rate of the depletion of the reactant C is given by:

$$\frac{d[C]}{dt} = -k(T) \times [C] \times [D] \tag{3.10}$$

$[C]$ shows the concentration of the component C in mole per unit volume and $k(T)$ is called the reaction rate constant although it depends on temperature. The reaction rate can be defined as:

$$R.R. = k(T) \times [C] \times [D] \tag{3.11}$$

The temperature-dependent rate constant for a reaction proceeding in forward direction is commonly simulated by a modified Arrhenius form equation:

$$k = A \times T^n \times \exp(\frac{-E}{R_u T}) \tag{3.12}$$

A is pre-exponential factor, n is temperature exponent, E is activation energy, and R_u is universal gas constant. It is common in combustion communities to use the units of s, cal, cm^3, K, and mol to describe parameters in equation (3.12). The units of rate constant (k) in equation (3.12) depend on the reaction order and are s^{-1}, $cm^3\, mol^{-1}\, s^{-1}$, and $cm^6\ mol^{-2}\ s^{-1}$ for the first, second, and third order reactions, respectively. The units for A are thus determined by the temperature exponent, n, and the units of k. The term $\left(\frac{-E}{R_u T}\right)$ is dimensionless, so the activation energy of E is in $cal\ mol^{-1}$ if R_u and T are given in $cal\ mol^{-1}\ K^{-1}$ and K, respectively.

For reversible reactions, two sets of rate constants are used to represent the reactions in both forward and reverse directions. The total rate of formation/ depletion of component C in the reversible version of reaction R 3.1 is then given by:

$$\frac{d[C]}{dt} = -k_f(T)\,[C]\,[D] + k_r(T)\,[E]\,[F] \tag{3.13}$$

k_f and k_r are the rate constants for the forward and the reverse reactions, respectively.

When a reversible reaction reaches to equilibrium, the total rate of formation/ depletion of each component should be zero, so,

$$\begin{gathered}\frac{d[C]}{dt} = 0 \Rightarrow \\ \frac{k_f(T)}{k_r(T)} = \frac{[E][F]}{[C][D]}\end{gathered} \tag{3.14}$$

which by definition is equal to thermodynamic equilibrium constant based on concentrations, K_C,

$$K_C = \frac{[E]\,[F]}{[C]\,[D]} = \frac{k_f(T)}{k_r(T)} \tag{3.15}$$

We can calculate the equilibrium constant based on partial pressures by using the changes of standard state Gibb's function $\left(-\Delta G_T^0\right)$ in the reaction:

$$K_P = \exp(\frac{-\Delta G_T^0}{R_u T}) \tag{3.16}$$

Gibb's function is defined as:

$$G = H - TS \tag{3.17}$$

where H and S are enthalpy and entropy, respectively. Substituting equation (3.17) in (3.16):

$$K_P = \exp\left(\frac{\Delta S^0}{R} - \frac{\Delta H^0}{R_u T}\right) \tag{3.18}$$

where ΔS^0 and ΔH^0 refer to the changes of entropy and enthalpy while passing completely from reactants to the products. The standard state thermodynamic properties

can be assumed to be functions of only temperature, so

$$K_P = f(T) \tag{3.19}$$

Using the ideal gas law, K_C can be found from K_P and the total pressure of the system. Therefore the reaction rate constants for the forward and the reverse directions are related via the thermodynamic state of components involved in the reaction:

$$K_C = f(T, P) = \frac{k_f(T)}{k_r(T)} \tag{3.20}$$

In reality, for many reactions the rate constants cannot be accurately reproduced by a simple Arrhenius equation. To overcome this problem, a combination of Arrhenius equations is used where the rate constant at each temperature is given by the sum of all Arrhenius equations. Moreover, the rate constant in some reactions is a function of both temperature and pressure. The methods to treat pressure-dependent reactions will be discussed later.

For a mixture with N_{sp} number of species (reactants), the j^{th} reaction can be represented in the general form as [109]:

$$\sum_{i=1}^{N_{sp}} \nu'_{ij} \chi_i = \sum_{i=1}^{N_{sp}} \nu''_{ij} \chi_i \tag{3.21}$$

where ν_{ij} are the stoichiometric coefficients and χ_i is the chemical symbol for the i^{th} species. The superscripts $'$ and $''$ indicate forward and reverse stoichiometric coefficients, respectively. The net rate of j^{th} reaction, q_j, is calculated as:

$$q_j = k_{fj} \prod_{i=1}^{N_{sp}} [\chi_i]^{\nu'_{ij}} - k_{rj} \prod_{i=1}^{N_{sp}} [\chi_i]^{\nu''_{ij}} \tag{3.22}$$

where $[\chi_i]$ is the molar concentration of the i^{th} species and k_{fj} and k_{rj} are the forward and reverse rate constants of the j^{th} reaction. The production rate of the i^{th} species can be given as [109]:

$$\dot{\omega}_i = \frac{d[\chi_i]}{dt} = \sum_{j=1}^{J} \nu_{ij} q_i \tag{3.23}$$

where J is the total number of reactions and v_{ij} is defined as:

$$v_{ij} = v''_{ij} - v'_{ij} \tag{3.24}$$

In other words:

$$\dot{\omega}_i = f\left(P,\, T,\, Y_1,\, \ldots, Y_{N_{sp}}\right) \tag{3.25}$$

3.2.2 Pressure dependent reaction rate constant

A classical example of pressure-dependent reaction is the recombination of methyl radicals:

$$\mathrm{CH_3 + CH_3 = C_2H_6} \tag{R 3.2}$$

This reaction proceeds as written in (R 3.2) at its high-pressure limit, but it needs a collision partner (M) to receive energy to proceed at its low-pressure limit:

$$\mathrm{CH_3 + CH_3 + M = C_2H_6 + M} \tag{R 3.3}$$

This reaction in general is shown by

$$\mathrm{CH_3 + CH_3(+ M) = C_2H_6(+ M)} \tag{R 3.4}$$

At the pressures between the low- and high-pressure limits, called ”fall-off” region, the reaction has a more complicated dependency. To describe the rate constant at the fall-off region, two sets of Arrhenius rate parameters are needed for low and high pressure limits:

$$k_0 = A_0\, T^{n_0}\, \exp\left(\frac{-E_0}{R\,T}\right) \tag{3.26}$$

$$k_\infty = A_\infty\, T^{n_\infty}\, \exp\left(\frac{-E_\infty}{R\,T}\right) \tag{3.27}$$

where 0 and ∞ subscripts show parameters corresponding to the low- and high-pressure limits, respectively. The rate constant at any given pressure is then calculated by

$$k = \frac{k_0\, k_\infty\, [M]}{k_\infty\, +\, k_0\, [M]}\, F \tag{3.28}$$

where $[M]$ is the total concentration of the mixture, in mole per unit volume. If F is assumed to be unity, the equation (3.28) gives the Lindermann [110] expression. A better accuracy of k in the fall-off region is given by the more complicated Troe [111] format for F, in which F is a function of k_0, k_∞, $[M]$, and T. The formula for the calculation of F in Troe format can be found in [111] or [109].

Recently, another method to describe pressure-dependent rate constants by using logarithmic interpolation has widely been used. For a given reaction in this method, the rate constants are provided at different pressures, e.g. at pressure of P_i:

$$k_i = A_i \times T^{n_i} \times \exp(\frac{-E_i}{R_u T}) \tag{3.29}$$

Then for every desired pressure at which the parameters are not provided directly, a logarithmic interpolation is used to estimate the rate constant from those at lower and upper pressures, e.g. for pressure of P between P_i and P_{i+1} the rate constant is given by [109]:

$$\ln(k) \;=\; \ln\, k_i + (\ln\, k_{i+l} - \ln\, k_i)\, \frac{\ln\, P - \ln\, P_i}{\ln\, P_{i+1} - \ln\, P_i} \tag{3.30}$$

This method provides a simple way to model complicated sensitivities of rate constants to pressure and temperature, but the rate parameters should be provided at a sufficient number of pressures to obtain a good accuracy in the interpolation.

3.2.3 Thermodynamic data

An equation of state to establish the relations between density, temperature, pressure, and species mass fractions is needed to close the system of equations. At high pressure and low temperature, interaction between gas molecules is relatively high, so ideal gas law should be used with caution. To evaluate ideal gas law at specific conditions, the compressibility factor of gases (Z) is used as an measure of the extent of nonideality [112]:

$$Z \;=\; \frac{P\,V}{N\,R_u\,T} \tag{3.31}$$

For ideal gases, Z is unity. Rasmussen [22] calculated the compressibility factor (Z) for representative gas mixtures at the operational conditions of the current reactor and found it to be close to unity, within ±4%, so the ideal gas law can be used safely in

the conditions of the flow reactor.

The reference state thermodynamic properties are assumed to be only a function of temperature [109]. For a perfect gas mixture, the standard-state specific heats and enthalpies are also the actual values [109], i.e. $H_i = H_i^0$ and $C_{Pi} = C_{Pi}^0$.

To solve the energy equation (3.8), the values of $\bar{c_p}$ and h_i should be known for every temperature. The mean specific heat capacity at constant pressure for a mixture of ideal gases can be calculated as:

$$\bar{c_P} = \sum_{i=1}^{N_{sp}} Y_i \, c_{P,i} \tag{3.32}$$

Y_i and $c_{P,i}$ show mass fraction and specific heat capacity (per unit mass) of the i^{th} species. The specific heat per unit mass can be converted to the corresponding molar value via:

$$\bar{c_P} = \frac{\overline{C_P}}{\overline{MW}} \tag{3.33}$$

where $\overline{C_P}$ and $\overline{MW}$ are the mean specific heat per mole and mean molecular weight of the mixture, respectively. The specific enthalpy of the i^{th} species (in energy per unit mass), h_i, can be calculated from the molar enthalpy of the i^{th} species, H_i:

$$h_i = \frac{H_i}{MW_i} \tag{3.34}$$

The molar enthalpy of the i^{th} species at standard state can be calculated if C_{Pi} and $H_i(0)$ are known:

$$H_i = \int_0^T C_{Pi} \, dT + H_i(0) \tag{3.35}$$

where $H_i(0)$ is the molar enthalpy at zero Kelvin. The molar entropy at standard state is also calculated by knowing C_{Pi} and $S_i(0)$:

$$S_i = \int_0^T \frac{C_{Pi}}{T} \, dT + S_i(0) \tag{3.36}$$

The sensitivity of C_P to temperature is non-linear and can be determined by using theoretical or experimental methods for every component. For computation, it is convenient to fit polynomial equations to C_P of each species over the entire temperature range of interest. For easier handling of the fitted equation, the non-dimensional value of $\frac{C_P}{R_u}$ is approximated by a polynomial equation:

$$\frac{C_{Pi}}{R_u} = \sum_{m=1}^{M} a_{mi} T^{m-1} \tag{3.37}$$

where a_{mi} are the coefficients of the polynomial fit and M is the total number of coefficients of the polynomial. Consequently, the enthalpy can be found from equation (3.35) as:

$$\frac{H_i}{R_u T} = \sum_{m=1}^{M} \frac{a_{mi} T^{m-1}}{m} + \frac{a_{M+1,i}}{T} \tag{3.38}$$

where $a_{M+1,i}$ is the standard heat of formation at zero K divided by the universal gas constant , $\frac{H_i(0)}{R_u}$. From equation (3.36) and by defining $a_{M+2,i}$ equal to $\frac{S_i(0)}{R_u}$,

$$\frac{S_i}{R_u} = a_{1i} \ln T + \sum_{m=2}^{M} \frac{a_{mi} T^{m-1}}{m-1} + a_{M+2,i} \tag{3.39}$$

Now, to calculate enthalpy, entropy, and specific heat at desired temperatures, $M+2$ number of a_i coefficients is needed. Such fitting coefficients are available through extensive thermodynamic database as [113, 114].

3.3 Solver (Chemkin)

The ODE system described in equations of (3.5), (3.7) and (3.8) is generally stiff, as there is a large difference between time scales of evolution of different species [109]. To solve the equations, Chemkin software package [109] is used which is able to calculate the rate constants of reactions and their thermodynamic properties as well. The Arrhenius parameters as well as polynomial coefficients for thermodynamic fitting are inputted to the program as text files. Chemkin [109] utilizes a modified version of software package Daspk [115, 116] using backward-differencing methods for time integration to solve the stiff equations as well as the first order sensitivity coefficients. The first order sensitivity coefficients are calculated for species mole fractions and temperature

respect to the changes in pre-exponential factors (A's) in rate constants. The coefficient then are normalized according to the methods described in [109].

Chapter 4

Combustion characteristics and reaction mechanisms

Detailed chemical kinetic models are vital to predict ignition, extinction, heat release, and pollutants formation in combustion. Historically, it is believed that Semenov's theory of chain mechanisms and thermal explosions [117] was the starting point for the modern science of detailed combustion reactions [118]. To develop chemical kinetic models, a systematic method advocated by Westbrook and Dryer [18] has widely been used over years. In this approach, the hierarchical structure of combustion system was emphasized in which every subset of the mechanism relies on the subsets of simpler molecules, as shown in figure 4.1. To develop a mechanism systematically, it is necessary to adopt subsets of the simpler molecules or develop them first and then step by step adding species and reactions relevant for more complex molecules. After addition of each subset, the mechanism should be validated by comparison of the mechanism predictions with measured combustion characteristics. It should be noted that addition of a subset for a more complex molecule may change the prediction of the model for simpler molecules too. Especially adding steps acting as a sink of radicals can introduce new reaction paths affecting simpler molecules models considerably. To avoid such problems, the developing mechanism should be reevaluated frequently against combustion characteristics of simpler molecules.

4.1 Reaction mechanism at low temperatures

Over years, some guidelines have been developed to predict the combustion mechanisms of different class of fuels, e.g. alkanes, alcohols, etc. As will be demonstrated later for ethane, these general mechanisms are not always indisputable but they are a

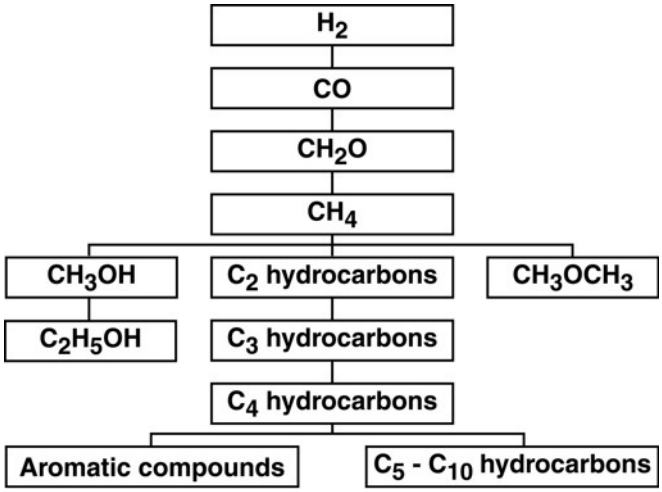

Figure 4.1: Hierarchical structure of oxidation mechanisms for simple hydrocarbon fuels and selected oxygenated fuels [112].

good starting point in developing chemical kinetic models.

Figure 4.2 shows a suggested mechanism for oxidation of alkanes [118, 119] at low-intermediate temperatures. The oxidation of an alkane (called 'RH' here) is usually initiated with hydrogen abstraction by O_2 [118, 119]:

$$RH + O_2 = R + HO_2 \quad \text{(R 4.1)}$$

Later, the conversion is mainly governed by H-abstraction by OH

$$RH + OH = R + H_2O \quad \text{(R 4.2)}$$

The R resembles an alkyl radical here. At low temperatures, the alkyl radical adds to O_2 to give alkylperoxyl radicals, ROO.

$$R + O_2 = ROO \quad \text{(R 4.3)}$$

The ROO radical may undergo an internal isomerization to form the hydroperoxyalkyl radical, QOOH.

$$ROO = QOOH \quad \text{(R 4.4)}$$

Alternatively, the ROO radical may dissociate to an alkene (Q) and a hydroperoxyl radical.

$$ROO = Q + HO_2 \quad \text{(R 4.5)}$$

At temperatures low enough, the QOOH radical can add to another molecular oxygen giving OOQOOH. The formed OOQOOH then isomerizes to HOOUOOH which finally dissociates to give two hydroxyl radicals per consumed fuel molecule [118, 119], as shown in figure 4.2.

As temperature increases, the ROO radical becomes unstable, i.e. the reaction of R 4.3 reaches to equilibrium [118, 119]. The reaction path then changes and the dissociation of the alkylperoxyl radical is more favored:

$$\mathrm{ROO} = \mathrm{Q} + \mathrm{HO_2} \tag{R 4.6}$$

Hydroperoxyl radicals usually combine to form hydrogen peroxide at intermediate temperatures,

$$\mathrm{HO_2} + \mathrm{HO_2} = \mathrm{H_2O_2} + \mathrm{O_2} \tag{R 4.7}$$

or abstract a hydrogen atom from the fuel molecule,

$$\mathrm{RH} + \mathrm{HO_2} = \mathrm{R} + \mathrm{H_2O_2} \tag{R 4.8}$$

As the dissociation of hydrogen peroxide to hydroxyl radicals is only favored at relatively high temperatures, the branch to $\mathrm{Q} + \mathrm{HO_2}$ is almost a chain-terminating path at low temperatures. These changes in the reaction pathways, namely preference of (R 4.6) over (R 4.4), is the main reason for negative temperature coefficient (NTC) behavior, which is observed for many alkanes. At NTC temperatures, the fuel oxidation is inhibited by increasing temperature, in contrast to the trend common at other temperatures. In general, if the chemical kinetic model is developed for low-intermediate temperatures (below 1000 K) applications, the reactions following oxygen addition to alkyl radicals (R 4.3) should be included in the model. For high temperatures application, removing this pathway results in marginal errors [118].

4.2 Combustion characteristics

To evaluate chemical kinetic models, it is necessary to compare their predictions of combustion parameters with experimental measurements. The evaluating parameters, combustion characteristics, should be independent from device and configurations, as much as possible. To better reveal the chemical details, it is desirable to avoid turbulent combustion and to simplify the flow field as possible [49]. Here, we briefly discuss three combustion characteristics widely used in this project to evaluate models: species pro-

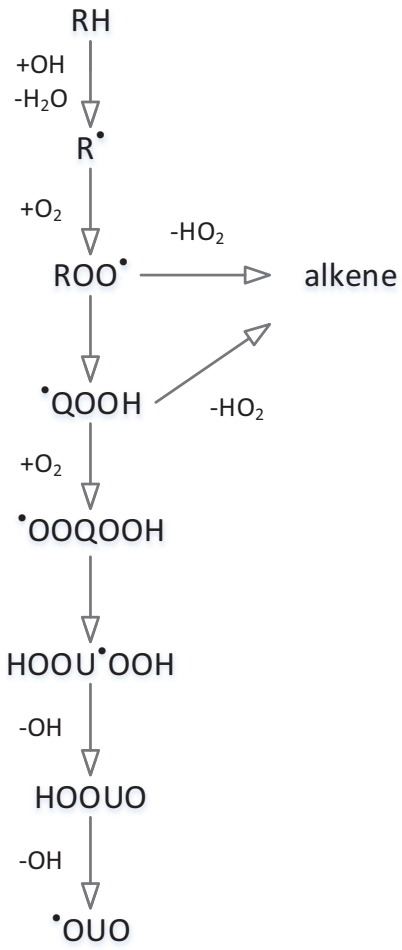

Figure 4.2: The general reaction pathway for low temperature oxidation of alkanes.

file, ignition delay time, and laminar burning velocity. Samples of such characteristics can be found in Chapter 10.

4.2.1 Species profile

The species conversion profiles from combustion are very useful tools in studying oxidation and pollutant formation processes. If the thermodynamic state of a mixture is well known, and in the absence of heterogeneous reactions, variations in the composition can be solely related to gas phase reactions. A few devices have been designed to obtain the species conversion profiles, e.g. flow reactors, shock tubes, jet-stirred

reactors, and different burners. In this project, a laminar flow reactor is used to obtain the conversion profiles of different species. Gas residence time in flow reactors may reach a few seconds, so flow reactors are convenient to study combustion chemistry at low–intermediate temperatures, where the reactions are relatively slow and reaction kinetic plays a crucial role in many process. A drawback of flow reactors is the large ratio of wall surface area to gas volume, which makes measurements conducted in them sensitive to heterogeneous reactions. In the device used in this work, this problem has mainly been solved as discussed in details in Chapter 2. In this work measurements are conducted at the end of the reactor as explained in section 2.1. By increasing temperature in small intervals and repeating measurements, conversion profiles against temperature are generated.

Shock tubes can also be used to measure the species profiles under controlled conditions. In shock tubes, the tube is divided by a diaphragm into two sections of the ”deriving gas” which is filled by a gas at high pressure and the ”test section” which contains the test mixture at lower pressure. After bursting the diagram, a shock wave (incident shock) is formed and travels through the tube, and increases the temperature and pressure of the mixture almost instantaneously. In a usual design, the shock wave is reflected from the end-wall, again increasing the temperature and pressure, whereas in the design of single-pulse shock tubes the reflected wave is avoided by adding a ”dump tank” (see Yasunaga and Tranter [120] for details). The main restriction in shock tubes is the limited residence time available, usually around few milliseconds at maximum. Due to the reflection of the expansion fan from the other side of the tube (the deriving section), pressure and temperature drop soon. Furthermore, measuring species profiles in shock tubes may be challenging as intrusive methods disturb the flow field while non-intrusive methods can provide relatively limited data. Over long residence times and before the advent of the expansion fan, pressure and temperature increase gradually behind the shock wave. Such pressure/temperature variations have been observed even in non-reactive mixtures and are believed to be results of fluid dynamic nonidealities which are generally device-dependent [121]. The methods to treat this problem will be discussed in the next section (4.2.2).

4.2.2 Ignition delay time

Ignition is usually accompanied by a rapid increase in temperature (and pressure for constant volume systems) and in the concentration of intermediate radicals. If the temperature of a combustible mixture is increased sufficiently, the mixture ”auto-ignites”,

which means ignition without any external source of flame or high energy. Even after an instantaneous increment in temperature, there is a time interval before autoignition. This time interval is called the "ignition delay time" and is a fundamental characteristic of a given combustible mixture at specific temperature and pressure.

To identify ignition experimentally, it is common to use one of these criteria: the maximum of pressure or its gradient ($\frac{dP}{dt}$), or the maximum of CH_3 or OH concentrations or their gradients ($\frac{d[CH_3]}{dt}$ and $\frac{d[OH]}{dt}$). Figure 4.3 shows the profiles of pressure and the OH radical for a stoichiometric hydrogen-air mixture in which ignition delay was around 2.3 millisecond. During the ignition delay period, the radical-pool population increases exponentially and some important chain-branching reactions take place at this time whereas the amounts of consumed fuel and released heat are negligible and temperature remains almost constant [122]. The ignition starts when a huge consumption of fuel is possible due to the expansion of the radical pool. The ignition delay time is highly sensitive to temperature as the reaction rates are. Moreover, mixture composition and pressure also affect the ignition delay time. In practice, when the ignition delay is needed over a limited range of conditions, a simple equation in the Arrhenius form is fitted to the available data,

$$\tau = A \ \exp(B/T) \tag{4.1}$$

where A and B can be a function of mixture composition, pressure, and temperature.

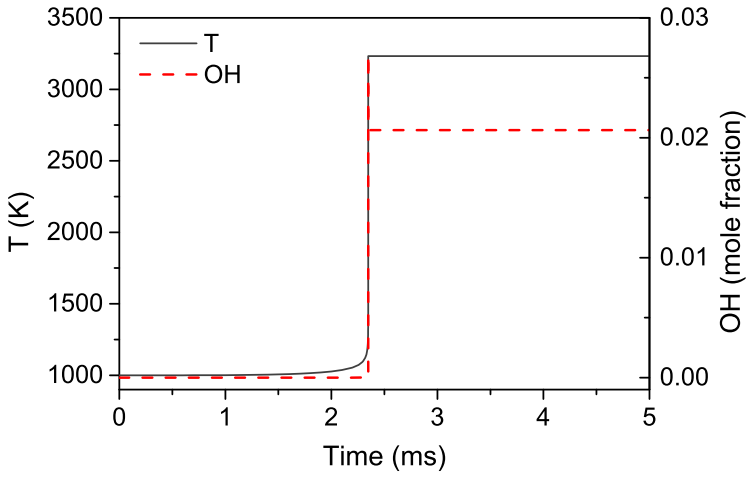

Figure 4.3: The ignition of stoichiometric hydrogen-air mixture at 50 bar and 1000 K. The simulations were conducted using a model with constant internal energy (u) and volume (V).

There are a few methods to measure the ignition delay time of gases. Due to almost instantaneous increase of temperature and pressure in shock tubes, they are convenient devices to study ignition delay time. Despite that, as discussed earlier (section 4.2.1), their major limitation is in their relatively short residence time, hardly enough for the ignition delays of most fuels at intermediate temperatures which are in order of milliseconds. The discussed gradual increase of temperature and pressure behind the shock wave can influence the interpretation of measured values considerably. To simulate ignition delay times from shock tubes, commonly a model with constant volume and internal energy (adiabatic) is used. For long ignition delays when the gradual pressure rise behind the shock wave becomes important, the model should be modified to include such variations. Chaos and Dryer [121] suggested a method to compensate for the pressure variations in which pressure history is recorded for a non-reactive mixture and then the specific volume of the mixture, which is kept constant usually, is varied according to the isentropic equation:

$$v(t) = \frac{1}{\rho_0}\left[\frac{P(t)}{P_0}\right]^{-1/\gamma} \tag{4.2}$$

where v is the specific volume, P the measured pressure, γ the specific heat ratios, and P_0 and ρ_0 are the pressure and density just after the shock wave. Whenever feasible in this work, the modified model is used for the simulations, despite its computational cost.

Another device to measure ignition delay time is the rapid compression machine (RCM). RCM's are designed based on the concept of internal combustion engines in which a piston is used to compress the gas mixture inside the cylinder. Due to the compression, temperature and pressure increase rapidly and the gas mixture may ignite. RCM's typically can deliver pressures of 1–80 bar and temperatures of 600–1200 K. The compression time is usually around 10–70 ms and the test time is between 2 and 500 ms [123]. A key criteria in the design of RCM's is to make the compression stroke as short as possible. Another limiting factor is the heat transferred from the hot gases to the cylinder wall and surroundings. In reality, the heat transfer from the gases is not negligible. This causes a gradual temperature drop which is reflected in a pressure drop after the compression stroke. To include the heat transfer and other complicated aspects of fluid dynamics in simulations, it is a common practice to repeat the experiments with non-reactive mixtures and input the measured pressure-profile in simulating ignition

delay time, similar to what is conducted for long residence time in shock tubes.

4.2.3 Laminar burning velocity

The adiabatic laminar burning velocity, also known as the laminar flame speed, is another fundamental character of combustible mixtures. The laminar burning velocity is defined as the velocity of a steady one-dimensional adiabatic free flame propagating in the doubly infinite domain [124]. Figure 4.4 shows simulated profiles of temperature and axial velocity of a freely propagating flame. The flame can be identified by a large gradient of temperature over a narrow zone. The flame speed is corresponding to the axial velocity of gases upstream of the flame (at $x = -\infty$), which is around 35 cm/s here. The flame speed is affected by temperature, pressure, and gas composition and can be measured in different configurations: Bunsen (and other similar burners) flames, spherically expanding flames, and counterflow flames. The advantages and drawbacks of different configurations will not be discussed here (for details see texts, e.g. [124]). As shown in figure 4.4, the gas temperature behind the flame can exceed 2000 K and the flame speed is more affected by high temperature chemistry. It will been shown later in this work that the calculation of flame speed is highly sensitive to the combustion chemistry of hydrogen. Particularly, hydrogen atoms play an important role as they can diffuse from the hottest parts of the flame to the cooler parts and initiate the reactions there [6].

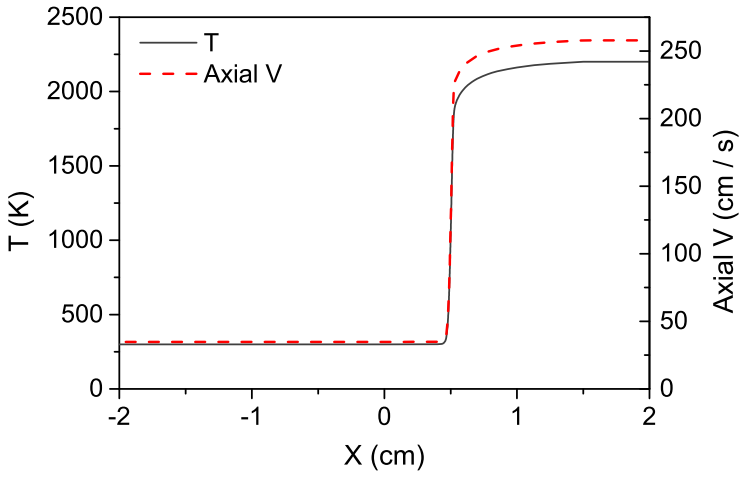

Figure 4.4: The axial velocity and temperature of a freely propagating premixed flame of a stoichiometric methane/air mixture. The initial conditions were 300 K and 1 atm.

Chapter 5

Hydrogen

Abstract

Hydrogen oxidation at 50 bar and temperatures of 700–900 K was investigated in a high pressure laminar flow reactor under highly diluted conditions. The experiments provided information about H_2 oxidation at pressures above the third explosion limit. The fuel–air equivalence ratio of the reactants was varied from very oxidizing to strongly reducing conditions. The results supplement high-pressure data from RCM (900-1100 K) and shock tubes (900-2200 K). At the reducing conditions (Φ = 12), oxidation started at 748–775 K while it was shifted to 798–823 K for stoichiometric and oxidizing conditions (Φ = 1.03 and 0.05). At very oxidizing conditions (O_2 atmosphere, Φ = 0.0009), the temperature for onset of reaction was reduced to 775–798 K. The data were interpreted in terms of a detailed chemical kinetic model, drawn mostly from work of Burke and coworkers. In the present study, the rate constants for the reactions HO_2 + OH, OH + OH, and HO_2 + HO_2 were updated based on recent determinations. The modeling predictions were in good agreement with the measurements in the flow reactor. The predicted H_2 oxidation rate was sensitive to the rate of the HO_2 + OH reaction, particularly at lean conditions, and the present data support recent values for the rate constant. In addition to the current experiments, the mechanism was evaluated against ignition delay time measurements from rapid compression machines and shock tubes. The model was used to analyze the complex dependence of the ignition delay for H_2 on temperature and pressure.

5.1 Introduction

Chemical kinetic models for combustion of hydrocarbon fuels all rely on an accurate hydrogen sub-mechanism [18]. Due to the significant contribution of H_2/O_2 reactions to the radical pool, these steps are among the most important in many ignition problems. Additionally, syngas (H_2+CO) produced from bio-sources attracts attention as an alternative way of using biofuels in conventional energy plants while hydrogen itself has been considered as an energy carrier to be used in conventional engines. Consequently the H_2/O_2 reaction mechanism has been studied extensively. In recent years, several comprehensive studies of hydrogen oxidation have been published [125–128] and rate constants for several key reactions have been refined [129–135]. In particular for reactions of HO_2 and H_2O_2, the novel findings in some cases deviate considerably from previously accepted recommendations [136]. Since this has implications for our understanding of the high-pressure chemistry, a continuous re-examination of the H_2/O_2 chemistry is required.

With the current tendency in designing practical combustion systems to work at high pressure to increase efficiency, reliable benchmark data for validation of the models in this regime become vital. Data for ignition at intermediate to high temperature and high pressure can be achieved in shock tubes and rapid compression machines (RCM). Hydrogen ignition has been investigated in shock tubes more than in any other device, and reported data cover a wide range of temperature and pressure. Recent data include those of Davidson and Hanson [33] at 1190–1930 K and 33–87 atm, Herzler and Naumann [137] at 920–1700 K and 0.9–19.3 bar, Pang et al. [138] at 908–1118 K and 3.0–3.7 atm, Zhang et al. [139] at 1010–1270 K and 5–20 bar, Zhang et al. [35] at 900–1750 K and 18 bar, and Keromnes et al. [128] at 935–2130 K and 1–34 bar. Investigations of hydrogen oxidation at high pressures in RCM, conducted at temperatures of 900–1100 K, include the work of Lee and Hochgreb [140] at 6–40 bar, Mittal et al. [16] at 15–50 bar, Das et al. [141] at 10-70 bar, and Gersen et al. [142] at 20–80 bar. To extend the high-pressure range to even lower temperatures, it is required to use flow reactors since this type of reactor allows for longer reaction times. However, studies of hydrogen oxidation at increased pressure in flow reactors are scarce. The reported work, i.e., Mueller et al. [143] (0.3–15.7 atm, 850–1040 K) and Beerer and McDonell [144] (5.0–6.4 atm, 700–950 K), were conducted at pressures below those of high pressure industrial applications.

The present work aims to extend the experimental characterization of H_2 oxidation

to conditions above the third explosion limit. Experiments are conducted in a laminar flow reactor, with a pressure of 50 bar and temperatures of 700–900 K. The present data, as well as selected data from the literature, are interpreted in terms of a detailed reaction mechanism, based on the comprehensive work of Burke et al. [127] but modified according to recent data on specific reactions. Finally, the complex dependency of ignition times for H_2 on pressure and temperature is discussed.

5.2 Experimental

The experimental setup was a laboratory-scale high-pressure laminar flow reactor designed to approximate plug flow. The plug flow assumption was shown by Rasmussen et al. [102] to be a good approximation for the present operating conditions. The setup is described in detail elsewhere [102] and only a brief description is provided here. The system was used here for investigation of hydrogen oxidation at 50 bar pressure and temperatures up to 900 K. The reactant gases were premixed before entering the reactor. The reactions took place in a tubular quartz reactor with an inner diameter of 8 mm and a total length of 154.5 cm. By using a quartz tube and conducting the experiments at high pressure, we expect the contribution from heterogeneous reactions at the reactor wall to be minimal, and we did not see any indications of surface reactions. The temperature profile in the flow reactor was measured inside the outer wall of the quartz tube. An isothermal reaction zone (±5 K under inert conditions) of 42–43.5 cm was achieved in the reactor. The residence time in the isothermal zone was 8.0–6.3 s (τ [s]=5661/T[K]) with the current flow rate of 3.1 liter/min (STP) and temperatures in the range of 700–900 K. The adiabatic temperature rise due to heat of reaction was calculated to be 22 K. However, due to heat transfer from the hot gas to the surroundings, the actual temperature rise is presuamble much less; measurements for reactive mixtures showed a negligible change (~ 1–2 K). All gases used in the present experiments were high purity gases or mixtures with certified concentrations (±2% uncertainty). The product analysis was conducted by an on-line *6890N Agilent Gas Chromatograph* (GC-TCD/FID from Agilent Technologies). For most species, the relative measuring uncertainty of the GC was in the range of ±6%. However, a higher uncertainty was estimated for measurement of oxygen at the lowest concentrations employed.

5.3 Chemical kinetic model

In a previous study from the current laboratory, measurements and kinetic modeling have been conducted for a mixture of H_2/CO/NO_x at high pressure [102]. The model was evaluated against data for syngas oxidation, but pure hydrogen combustion were not investigated. Considering the recent advances in hydrogen chemistry, a thorough update of the model seemed necessary. The mechanism presented here was based on the recent comprehensive study on high-pressure hydrogen oxidation by Burke et al. [127], but selected reactions were modified according to the discussion below. The full mechanism is available in tabular form, as well as in Chemkin format, as supplemental material, and the reaction numbering below refers to this listing.

5.3.1 R4) OH + OH=O + H_2O

The hydroxyl radical plays an important role both in the atmosphere and in combustion, and self reactions of OH, forming O+H_2O (R4) or H_2O_2 (R15b), are important both in the forward and reverse directions. Because of interference between the two reactions, measuring their rates can be challenging. We have adopted the rate constant for (R13) from Sangwan and Krasnoperov [133] who used a novel approach to distinguish between the two channels and minimize probable effects of surface reactions. They performed measurements in a temperature range of 295–414 K and pressures of 3 and 10 bar. By combining their own results with published data [132, 145, 146], they obtained a rate constant for this reaction for the temperature range of 223–2380 K. Their value is slightly lower than the recommendation of Baulch et al. [136] which was used by Burke et al. [127]. However, it should be noted that recent experimental [147, 148] and theoretical [135, 149] results indicate that the rate constant for (R13) may be faster than recommended by Sangwan and Krasnoperov [133] and more work on this step is desirable.

5.3.2 R13) HO_2 + OH=H_2O + O_2

The rate constant for this reaction, which is one of the termination paths for the OH radical, has been in discussion. Low-temperature results are in good agreement [150], but shock tube data [151] indicated a very unusual temperature dependence with a narrow minimum in the rate constant in the 1000–1200 K range. While these data, together with early high-temperature measurements [152–154], were impressively fitted to Arrhenius format by Rasmussen et al. [102], later studies indicate that the unusual

behavior was most likely an artifact of the experimental interpretation. The shock tube work at intermediate and high temperatures by Hong et al. [129, 131] did not support the early work, indicating that the rate constant was a more smooth function of temperature. This was confirmed recently by Burke et al. [135], who re-interpreted the published experimental data for the rate of R13, considering carefully uncertainties. Their recommended rate constant, obtained from a combination of ab initio calculations and analysis of the experimental data, was adopted in the present work. It is in average 50% lower in the 700-900 K range than the value suggested by Keyser [150] and used in the reference model [127].

5.3.3 R14) $HO_2 + HO_2 = H_2O_2 + O_2$

Recombination of HO_2 plays a critical role in the ignition process. Burke et al. [127] discussed the rate of this reaction, noting that available data at combustion temperatures [151, 155] exhibited significant differences. Recently, Zhou et al. [134] calculated rate coefficients for reaction R14 using statistical rate theory in conjunction with high level ab initio calculations. Their value shows a good agreement with experimental results at temperatures below 500 K [156] and also above 1000 K [151], but in general it is higher (around 50 % at 700 K) than that from Hippler et al. [155], which was used in the reference model [127]. Considering the large discrepancy in the reported measurements, we consider the theoretical value more reliable and use it in the present work.

5.4 Results and Discussion

5.4.1 Oxidation in the laminar flow reactor

The experimental results, obtained at a pressure of 50 bar, temperatures in the range of 700-900 K, and stoichiometries ranging from very fuel-rich to very fuel-lean, were interpreted in terms of a plug-flow model with constant P and T, corresponding to the isothermal part of the reactor. The simulations were conducted with Chemkin [109]. Comparison to results calculated using the full measured temperature profiles confirmed that the heating and cooling regions of the reactor did not contribute significantly to the reaction.

Figure 5.1 compares experimental and calculated concentrations of hydrogen and oxygen for reducing conditions (Φ = 11.9). Hydrogen oxidation is initiated at 748–775 K and reaction is completed at a temperature of 825 K. Simulations are shown for

both the present mechanism and the reference scheme by Burke et al. [127]. For both models, predictions agree well with the measurements. The experimental data indicate that a few ppm of oxygen remains at high temperatures, but this is attributed to the uncertainty in measuring oxygen at low concentrations in the current configuration of the GC with argon as the carrier gas.

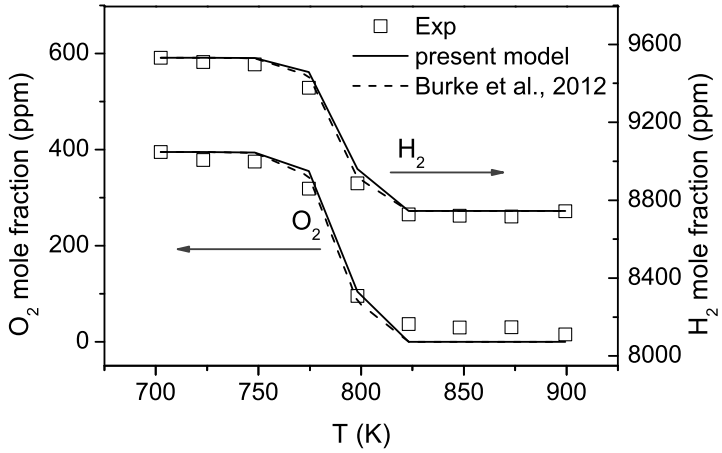

Figure 5.1: Results of experiments under reducing conditions (0.95% H_2 and 0.04% O_2 in N_2, Φ=11.9) at 50 bar pressure. The isothermal zone residence time is given by τ [s]=5661/T[K]. Symbols mark experimental results and lines denote predictions of the present model and the model by Burke et al. [127].

Figure 5.2 shows results for stoichiometric conditions (Φ = 1.03). Here, the onset of reaction is shifted to slightly higher temperatures, 798–823 K. The present mechanism predicts a slightly faster consumption rate for H_2 than the model of Burke et al., but both sets of predictions are in agreement with the experimental results within the uncertainty.

Results for oxidizing conditions can be found in Fig. 5.3. Two sets of experiments are shown, with equivalence ratios of Φ = 0.05 and Φ = 0.0009 (oxygen atmosphere), respectively. Similar to the stoichiometric experiment, reaction is initiated at 798–823 K at Φ = 0.05, but at ϕ = 0.0009 onset of reaction is shifted to slightly lower temperatures (775–798 K). Furthermore, the oxygen atmosphere leads to a more complete conversion of hydrogen at the maximum temperature. Under the conditions of Fig. 5.3, the differences in predictions between the two mechanisms are more pronounced. For both sets of data the modifications in the mechanism made in the present work result in an improved prediction of the hydrogen concentration, especially at the high temperatures. However, both models tend to underpredict the H_2 consumption at temperatures above

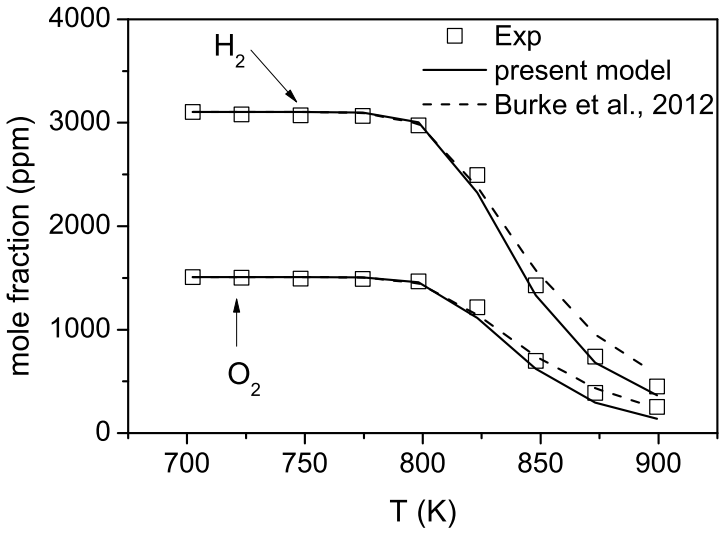

Figure 5.2: Results of experiments under stoichiometric conditions (0.31% H_2 and 0.15% O_2 in N_2, Φ=1.03) at 50 bar pressure. The isothermal zone residence time is given by τ [s]=5661/T[K]. Symbols mark experimental results and lines denote predictions of the present model and the model by Burke et al. [127].

800 K.

Based on a rate of production analysis, the reaction pathways for consumption of hydrogen are determined. Independent of stoichiometry, the consumption paths are generally similar. Hydrogen is mainly consumed via reaction R3 (H_2 + OH = H_2O + H). The atomic hydrogen formed mostly recombines with O_2, H + O_2 (+M) = HO_2 (+M) (R9). Self-reaction of HO_2, HO_2 + HO_2 = H_2O_2 + O_2 (R14), then yields hydrogen peroxide, which subsequently dissociates thermally to form the OH radicals required for chain branching, H_2O_2 (+M) = OH + OH (+M) (R15). Reaction R17b (H_2 + HO_2 = H_2O_2 + H) is important for initiation at all stoichiometries, but only under reducing conditions does it consume a considerable fraction of H_2.

It is known that competition between reactions R1 (H + O_2 = O + OH) and R9 (H + O_2 (+M) = HO_2 (+M)) largely determines the generation of chain carriers in combustion of hydrogen as well as most hydrocarbons [139]. R1 is a chain branching reaction while R9 yields HO_2, a less active radical. For this reason, dominance of R1 over R9 leads to a fast ignition and a higher fuel consumption rate. However, under the conditions of the present study with a high pressure and comparatively low temperatures R1 is not competitive, and the dominance of R9 leads to long ignition delays and a low conversion rate of H_2.

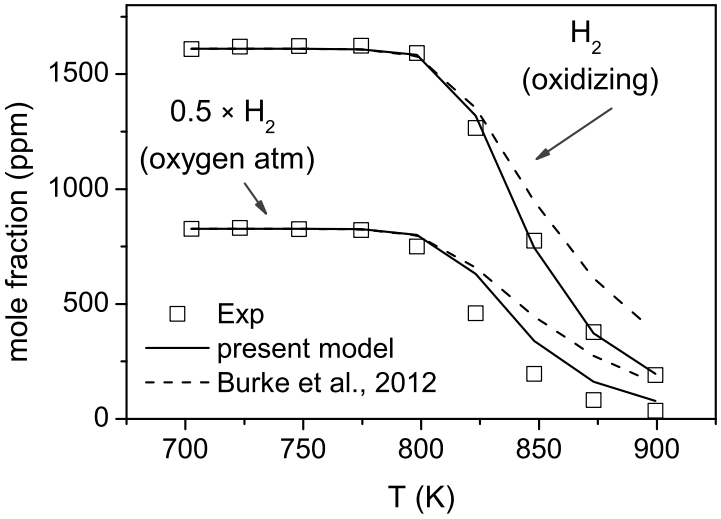

Figure 5.3: Results of experiments under oxidizing conditions (0.16% H_2 and 1.60% O_2 in N_2, Φ=0.05) and experiments in oxygen atmosphere (0.17 % H_2 and 93.92 % O_2 in N_2, Φ=0.0009) at 50 bar pressure. The isothermal zone residence time is given by τ [s]=5661/T[K]. Symbols mark experimental results and lines denote predictions of the present model and the model by Burke et al. [127].

Figure 5.4 shows the results of a sensitivity analysis. For reducing conditions the rate-controlling reactions for H_2 consumption are R17b, R15, and R14, respectively. Oxidation is promoted by the chain branching sequence $H_2 + HO_2 = H_2O_2 + H$ (R17b), H_2O_2 (+M) = OH + OH (+M) (R15), while it is inhibited by the terminating step $HO_2 + HO_2 = H_2O_2 + O_2$ (R14). Therefore, for reducing conditions the competition between R17b and R14 is quite important for the hydrogen conversion rate. The rate constant for R14 was modified in the present work, but the value is close to that used in the reference mechanism of Burke et al. and modeling predictions are very similar under reducing conditions.

For stoichiometric conditions and at a higher temperature, the most sensitive reactions are R17b, R15, R14, and R3. R17b remains the most sensitive step since it promotes initiation; however, it is no longer important for consumption of hydrogen. Predictions now become sensitive to R3, which is the main hydrogen consumption step. Other reactions exhibit small positive (R13, R16, R19) or negative (R1) sensitivity coefficients.

Under oxidizing conditions, R15 and R17b continue to be important for promoting reaction. However, as the oxygen concentration increases, the sensitivity towards reactions involving O_2 increases. Modeling predictions now become more sensitive to the competition between R1 and R9, but due to the dominance of R9 compared to R1 the

coefficients never attain large values. Notably, the chain terminating step HO_2 + OH = H_2O + O_2 (R13) increases in importance and exhibits the largest sensitivity coefficient at 900 K for the conditions of the oxygen atmosphere experiment (Fig. 5.4). While it is not very important for initiation, it plays a significant role for the H_2 consumption rate once reaction is initiated. The difference in modeling predictions between the present mechanism and that of Burke et al. can largely be attributed to the change in the value of k_{13}. The present data support a value of k_{13} at 800-900 K within the range proposed by Hong et al. [129] and Burke et al. [135].

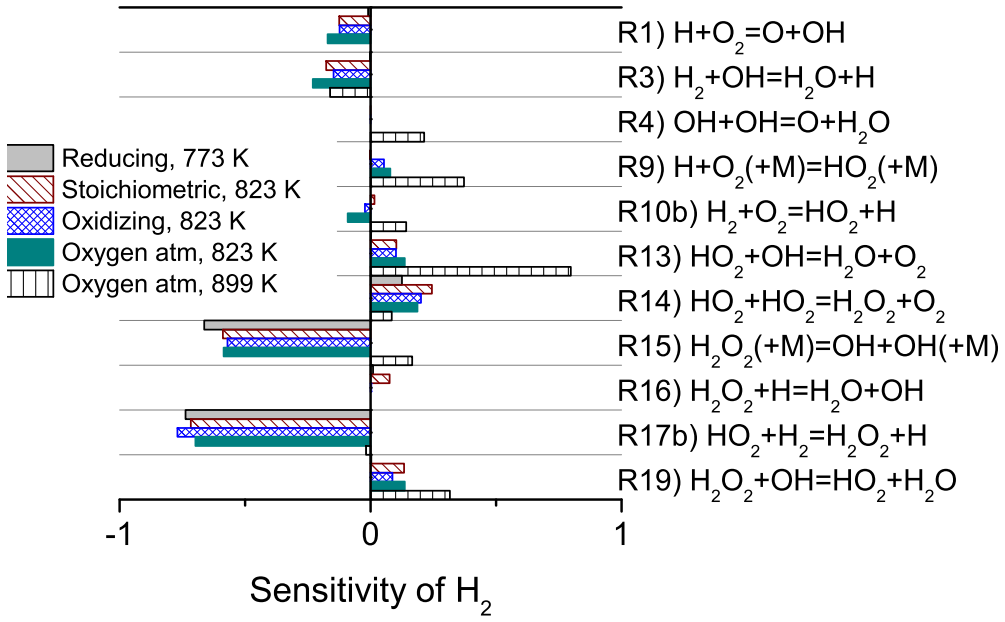

Figure 5.4: Normalized sensitivity coefficients for hydrogen at four investigated stoichiometries in the flow reactor, calculated at the end of the nominal reactor residence time. The sensitivity coefficient is defined as $S_{H_{2,i}} = \frac{(\Delta H_2/H_2)}{(\Delta k_i/k_i)}$. The S_i's are normalized to have $\sum_{i=1}^{N} S_i^2 = 1$ (N is the total number of reactions).

For the present results at pressure of 50 bar and temperatures of 700–900 K, few comparable measurements are available. Pang et al. [138] reported ignition delay times for stoichiometric H_2/O_2 highly diluted in Ar at a pressure of 3.5 atm and temperature above 923 K. Mueller et al. [143] investigated ignition of hydrogen at 880-890 K at 6.5 atm pressure and Φ = 0.3. In the present work ignition has been detected at a lower temperature while the pressure is much higher, above the third explosion limit. On the other hand, Beerer and McDonell [144] reported ignition for H_2/air at pressure,

temperature, and Φ of 5.8 atm, 753 K, and 0.28, respectively. However, every attempt to reproduce their results with the current model and a few other models failed.

For sub-atmospheric pressure and a temperature of 880 K, Mueller et al. [143] found that R1–R3 and R9–R11 were the most sensitive reactions for hydrogen consumption. The controlling reactions under the conditions of the present work are quite different, with H_2O_2 and HO_2 chemistry being dominant. The generation of chain carriers, as well as the oxidation paths once initiation has occurred, is dominated by reactions involving HO_2 and H_2O_2. Reaction of H with O_2 yields HO_2 (R9), and the sequence R15, R17 controls the reaction rate. This is consistent with the finding of Dryer and Chaos [125] that ignition of hydrogen at high pressure is controlled mainly by reactions R15 and R17. Recombination of HO_2 (R14) and reactions OH with HO_2 (R13) and H_2O_2 (R19) are among the important inhibition steps.

5.4.2 Ignition delay times in shock tubes and RCM

The present model is further evaluated by comparing predictions to available data for ignition delay times of hydrogen in shock tubes and RCM reactors. Here comparisons are limited to shock tube data published by Herzler and Naumann [137] and Keromnes et al. [128], respectively, and RCM data from Gersen et al. [142]. Further evaluation of the model by comparison to other published data can be found in the supplemental material.

Figure 5.5 compares modeling predictions with the data from shock tubes and RCM. Overall, the agreement between the current model and the experimental results is good, especially away from the low temperature cases where the uncertainty of the measurements (due to pressure rise prior to ignition) is also increased considerably. Herzler and Naumann [137] reported hydrogen ignition delay time at pressures of 1, 4, and 16 bar and intermediate temperatures. They found that for observation times less than 4.5 ms, pressure changes were negligible so that gas dynamic effects could be neglected and a constant u and v model was suitable for use. The prediction for ignition delay at low temperatures and especially high pressures is overestimated by the constant u, v model. However, as temperature increases, the agreement between the model and the experiments is improved considerably.

In a more recent measurement in the same shock tube device [128], it was found that changing the bath gas from argon to nitrogen increased the ignition delay time considerably. It can be explained partly by considering the difference between argon and nitrogen specific heats; the lower heat capacity of Ar results in a faster temperature

rise from pre-ignition heat release. From the modeling point of view, the rate constant for R9 in argon is lower than that in nitrogen, and as discussed above, promotion of R9 inhibits ignition. Interestingly, changing the bath gas has a larger impact at 4 atm compared to the other pressures.

Gersen et al. [142] measured autoignition delay times for $H_2/O_2/N_2$/Ar mixtures in an RCM reactor at pressures resembling those of the present work. Figure 5.5 includes data obtained as a function of temperature at a constant pressure of $P_c \sim 40$ bar at stoichiometric conditions and $P_c \sim 50$ bar at fuel–lean conditions. The ignition delay time decreased with increase in temperature and a similar sensitivity toward temperature is observed for both stoichiometric mixtures.

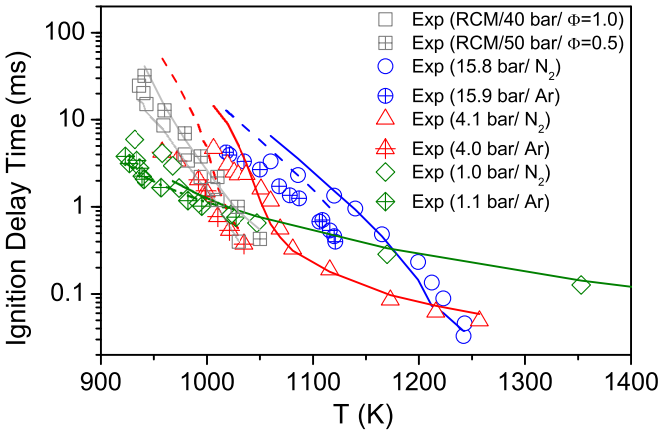

Figure 5.5: Ignition delay time of hydrogen. Symbols mark experimental results obtained by Herzler and Naumann [137] (ϕ=0.5, in 93% Ar) and by Keromnes et al. [128] (ϕ=0.5, in 93% N_2) in shock tubes and by Gersen et al. [142] in a RCM. Lines denote predictions of the present model. The maximum of OH concentration has been used in determination of ignition.

5.4.3 The pressure and temperature dependence of ignition delay times for H_2

The shock tube results of Herzler and Naumann [137] show that the ignition delay for H_2 is a complicated function of pressure and temperature. For fuel–lean mixtures and temperatures below 1060 K, the ignition delay increased as the pressure rose. On the other hand, at temperatures in the range of 1060–1175 K, the ignition delay decreased by pressure rise to 4 bar but increased by a further pressure rise to 16 bar. For temperatures as high as 1250 K, the ignition delay decreased with increasing pressure, as

expected in general for most fuels.

To our knowledge, this complex behavior has not previously been discussed in detail. For this reason we have used the present reaction mechanism to simulate ignition delay times of hydrogen at different temperatures and pressures. The gas composition is selected similar to the experiments by Zhang et al. [139]. As can be seen from Fig. 5.6, three regions and two corresponding inflection points can be recognized for the ignition delay profile versus pressure. When the pressure increases from sub-atmospheric to the first inflection point, the ignition delay decreases gradually. In contrast, between the two inflection points, the ignition delay grows rapidly with an increase in pressure. Finally at pressures above the second inflection point, the ignition delay decreases as pressure rises. The inflection points are very sensitive to temperature; e.g., the first inflection pressure increases from 0.8 atm to 50 atm when the temperature rises from 900 K to 1400 K.

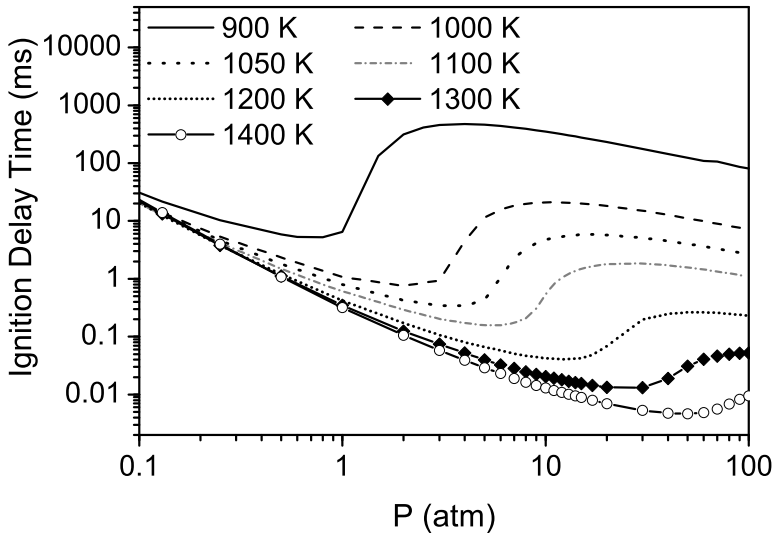

Figure 5.6: Ignition delay times of $H_2/O_2/Ar$ at $\phi = 0.5$. Lines denote model predictions using the constant u, v model. In determination of ignition, the maximum of OH concentration has been used. The investigated gas consists of 3.47% H_2 and 3.47% O_2 in Argon.

The observed variations of ignition delay time with pressure and temperature is in agreement with the existing experimental results. The RCM experiments of Gersen et al. [142] showed that the ignition delay decreases with increase of pressure at temperatures around 1000 K and pressures above 20 atm. Zhang et al. [139] found ignition delay to increase with pressure at temperature and pressure ranges of 1093–1170 K and 5–20 bar, respectively. The results are also consistent with the data in temperature of

1100–1200 K reported by Herzler and Naumann [137]. Moreover, Brower et al. [157] observed the non-monotonic effect of pressure on ignition delay of hydrogen in their simulations.

Based on the rate of production analysis, consumption pathways for hydrogen were determined at pressures of 2, 5, 10, and 40 atm and a typical temperature of 1100 K. Contrary to the situation in the flow reactor, the H + O_2 reaction is not governed solely by R9; R1 plays a significant role and can overcome R9 at low pressures. As a consequence R2 (H_2 + O = H + OH) is able to compete with R3 (H_2 + OH = H_2O + O) as a major consumption step for H_2. While HO_2 conversion to OH was mainly through R14, R15, and R17 at the high-pressure low-temperature conditions, the mechanism becomes more complicated here, and other reactions, such as R11 (HO_2 + H = OH + OH), contribute significantly at some pressures.

It is clear that as the pressure rises, the concentration of the reactants also increases. From a kinetics point of view, it is of interest to separate the effect of the concentration rise from the effect of the pressure increase. To do that, the mole fractions of reactants are reduced as the pressure rises, so the reactant concentrations are kept constant. Furthermore, it is beneficial to test the impact of an increasing concentration while keeping the pressure constant. As displayed in Fig. 5.7, while increasing pressure in general cause a non-monotonic behavior in ignition delay, increasing the pressure but fixing the concentration prolongs the ignition delay. In contrast, concentration growth facilitates ignition at a constant pressure. Therefore, when the pressure of the system increases, the ignition delay time is determined by the balance of these two opposite effects.

In summary it seems that the most important parameters in controlling ignition of hydrogen at the conditions investigated here (900–1400 K and 1–100 atm) are the competition between R1 and R9 for H atom consumption and competition between R2, R3, and R17b for H_2. However, also competition between R10, R11, R12, R14, and R17 in consumption of HO_2 has an impact on the ignition time.

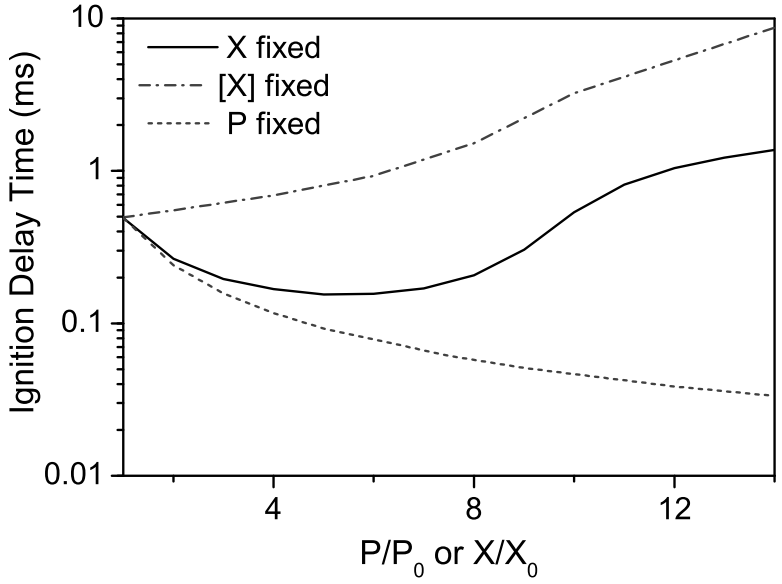

Figure 5.7: Effect of pressure and concentration on ignition delay time of 3.47% H_2 + 3.47% O_2 in Argon at 1100 K. 'X fixed' denotes calculations with constant inlet mole fractions but varying pressure. '[X] fixed' denotes calculations with varying pressure but constant inlet reactant concentrations (mole/m^3), obtained by adjusting inlet mole fractions. 'P fixed' denotes calculations with constant pressure, but varying inlet mole fraction and consequently inlet reactant concentrations. The maximum of temperature gradient is used to detect ignition.

5.5 Conclusion

Hydrogen oxidation was investigated in a laminar flow reactor at 50 bar pressure and temperatures of 700–900 K. Results provided information about the onset temperature for reaction and the H_2 consumption rate upon initiation at conditions above the third explosion limit. Onset of reaction happened at lower temperatures at reducing conditions, compared to stoichiometric and oxidizing conditions. The data were interpreted in terms of a detailed chemical kinetic model. The reaction mechanism was based on recent work of Burke and coworkers, updating the rate constants for OH + OH, HO_2 + OH, and HO_2 + HO_2. Modeling predictions were in good agreement with the measurements in the flow reactor, as well as with selected shock tube and RCM ignition delay data from literature. From the calculations, it was possible to explain H_2 oxidation behavior under conditions dominated by reactions involving HO_2 and H_2O_2 (high pressure, 700-900 K), as well as the complex behavior of hydrogen ignition delays as a function of pressure and temperature in the ranges of 1–100 bar and 900–1400 K.

5.6 Supplementary materials

5.6.1 Reaction mechanism

Table 5.1: Present reaction mechanism for H_2/O_2. $k = AT^n exp(-E/(RT))$, units are mol, cm^3, K, $seconds$, and Cal/mol.

	Reactions	Arrhenius data A	n	E	Reference
R1	$H+O_2 = O+OH$	1.04E+14	0.00	15286	see [127]
R2	$O+H_2 = H+OH$	3.82E+12	0.00	7948	see [127]
	duplicate reaction	8.79E+14	0.00	19170	
R3	$H_2+OH = H_2O+H$	2.16E+08	1.51	3430	see [127]
R4	$OH+OH = O+H_2O$	1.35E+07	1.69	-1166	[133], p.w.
	duplicate reaction	-2.67E+10	0.57	0.0	
R5	$H_2+M = H+H+M$	4.58E+19	-1.40	104380	see [127]
	Enhanced third-body efficiencies: H_2=2.5/ H_2O=12/CO=1.9/ CO_2=3.8/ AR=0.0/ HE=0.0/				
	$H_2+AR = H+H+AR$	5.84E+18	-1.10	104380	
	$H_2+HE = H+H+HE$	5.84E+18	-1.10	104380	
R6	$O+O+M = O_2+M$	6.17E+15	-0.50	0	see [127]
	Enhanced third-body efficiencies: H_2=2.5/ H_2O=12/ CO=1.9/ AR=0.0/ HE=0.0 / CO_2=3.8/				
	$O+O+AR = O_2+AR$	1.89E+13	0.0	-1788	
	$O+O+HE = O_2+HE$	1.89E+13	0.0	-1788	
R7	$O+H+M = OH+M$	4.71E+18	-1.0	0	see [127]
	Enhanced third-body efficiencies: H_2=2.5/ H_2O=12/ CO=1.9/ CO_2=3.8/ AR=0.75/ HE=0.75/				
R8	$H_2O+M = H+OH+M$	6.06E+27	-3.32	120790	see [127]
	Enhanced third-body efficiencies: H_2=3.0/ H_2O=0/CO=1.9/ N_2=2.0/ O_2=1.5/ HE=1.1/ CO_2=3.8/				
	$H_2O+H_2O = H+OH+H_2O$	1.01E+26	-2.44	120180	
R9	$H+O_2(+M) = HO_2(+M)^a$	4.65E+12	0.44	0	see [127]

Continued on next page

Table 5.1 – *continued from previous page*

	Reactions	Arrhenius data A	n	E	Reference
	Low-pressure limit:	6.37E+20	-1.72	525	
	Troe parameters: /0.5 1.00E-30 1.00E+30/				
	Enhanced third-body efficiencies: H_2=2.0/ H_2O=14/ CO=1.9/ Ar=0.67/ O_2=0.78/ HE=0.8/CO_2=3.8/				
	$H+O_2(+M) = HO_2(+M)^b$	4.65E+12	0.44	0	
	Low-pressure limit:	9.04E+19	-1.50	492	
	Troe parameters: /0.5 1.00E-30 1.00E+30/				
	Enhanced third-body efficiencies: H_2=3.0/ H_2O=21/ CO=2.7/ N_2=1.5/ O_2=1.1/ HE=1.2/CO_2=5.4/				
R10	$HO_2+H = H_2+O_2$	2.75E+06	2.09	-1451	see [127]
R11	$HO_2+H = OH+OH$	7.08E+13	0.00	295	see [127]
R12	$HO_2+O = O_2+OH$	2.85E+10	1.00	-723	see [127]
R13	$HO_2+OH = H_2O+O_2$	1.93E+20	-2.49	584	[135]
	duplicate reaction	1.21E+09	1.24	-1310	
R14	$HO_2+HO_2 = H_2O_2+O_2$	1.179E+9	0.77	-1825	[134]
	duplicate reaction	1.251E+12	0.30	7397	
R15	$H_2O_2(+M) = OH+OH(+M)$	2.00E+12	0.90	48749	see [127]
	Low-pressure limit:	2.49E+24	-2.30	48749	
	Troe parameters: /0.43 1E-30 1E+30/				
	Enhanced third-body efficiencies: H_2=3.7/ H_2O=7.5/CO=2.8/ O_2=1.2/ HE=0.65/ CO_2=1.6/ N_2=1.5/ H_2O_2=7.7/				
R16	$H_2O_2 +H = H_2O+OH$	2.41E+13	0.00	3970	see [127]
R17	$H_2O_2 +H = HO_2+H_2$	4.82E+13	0.00	7950	see [127]
R18	$H_2O_2 +O = OH+HO_2$	9.55E+06	2.00	3970	see [127]
R19	$H_2O_2 +OH = HO_2+H_2O$	1.74E+12	0.00	318	see [127]
		7.59E+13	0.00	7270	

[a] For N_2 as the bath gas

[b] For Ar or He as the bath gas

5.6.2 Tabulated data from the flow reactor

Table 5.2: Conditions and results of reducing experiments (0.952% H_2 and 0.039% O_2 in N_2, Φ=12.07) at 50 bar pressure.

Exp-ID	T [K]	τ [s]	H_2 [ppm]	O_2 [ppm]
RD1	702.45	7.964	9532	395
RD2	723.15	7.804	9510	378
RD3	748.15	7.623	9497	375
RD4	774.55	7.445	9377	319
RD5	798.15	7.146	8887	96
RD6	823.15	6.846	8728	37
RD7	847.95	6.566	8721	29
RD8	873.15	6.451	8716	30
RD9	899.35	6.339	8744	15

Table 5.3: Conditions and results of stoichiometric experiments (0.310% H_2 and 0.151% O_2 in N_2, Φ=1.03) at 50 bar pressure.

Exp-ID	T [K]	τ [s]	H_2 [ppm]	O_2 [ppm]
ST1	702.5	7.964	3104	1508
ST2	723.2	7.804	3082	1502
ST3	748.2	7.623	3072	1492
ST4	774.6	7.445	3065	1490
ST5	798.2	7.146	2975	1466
ST6	823.2	6.846	2494	1216
ST7	848.0	6.566	1428	699
ST8	873.2	6.451	738	387
ST9	899.4	6.339	452	253

Table 5.4: Conditions and results of oxidizing experiments (0.1610 % H_2 and 1.6039% O_2 in N_2, Φ=0.05) at 50 bar pressure.

Exp-ID	T [K]	τ [s]	H_2 [ppm]
OX1	702.5	7.964	3104
OX2	723.2	7.804	3079
OX3	748.2	7.623	3062
OX4	774.6	7.445	3067
OX5	798.2	7.146	2991
OX6	823.2	6.846	2497
OX7	848.0	6.566	1433
OX8	873.2	6.451	746
OX9	899.4	6.339	455

Table 5.5: Conditions and results of experiments in oxygen atmosphere (0.1656 % H_2 and 93.9171% O_2 in N_2, Φ=0.0009) at 50 bar pressure.

Exp-ID	T [K]	τ [s]	H_2 [ppm]
VX1	702.5	7.964	1656
VX2	723.2	7.804	1662
VX3	748.2	7.623	1652
VX4	774.6	7.445	1645
VX5	798.2	7.146	1502
VX6	823.2	6.846	920
VX7	848.0	6.566	392
VX8	873.2	6.451	165
VX9	899.4	6.339	71

5.6.3 Comparison of rate constants for selected reactions

Discussion of rate constants for reactions R4, R13, and R14 can be found in the main body of the present paper. Here, rates of these reactions are shown in figures 5.8, 5.9, and 5.10.

The rate suggested by Sangwan and Krasnoperov [133] for reaction R4 has been expressed in a non-Arrhenius form:

$$k = (3.071 \times exp(-T/190K) + 0.181(T/300K)^{1.73}) \times 10^{12} \quad cm^3 mole^{-1} s^{-1}$$

In the present work, we introduced a modified Arrhenius-form equation for the Sang-

wan and Krasnoperov [133] suggestion to be used in CHEMKIN [109]:

$$k = 1.350 \times 10^{7} \times T^{1.689} \times \exp(1166.8/(RT)) - 2.697 \times 10^{10} \times T^{0.567} \quad cm^3 mole^{-1} s^{-1}$$

The Arrhenius-form rate shows at most 4% deviation from the original curve at temperature above 400 K.

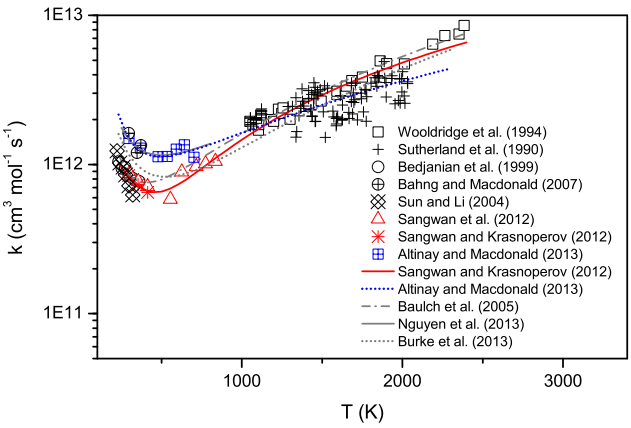

Figure 5.8: Rate constant of reaction R4 (OH+OH=O+H_2O) as a function of temperature. Symbols mark experimental data from Wooldridge et al. [146], Bedjanian et al. [145], Sangwan et al. [132], Sangwan and Krasnoperov [133], Altinay and Macdonald [148], Bahng and Macdonald [147], Sun and Li [158], and Sutherland et al. [159]. Lines denote suggestions by Baulch et al. [136], Burke et al. [135], Sangwan and Krasnoperov [133], Altinay and Macdonald [148], and Nguyen and Stanton [149].

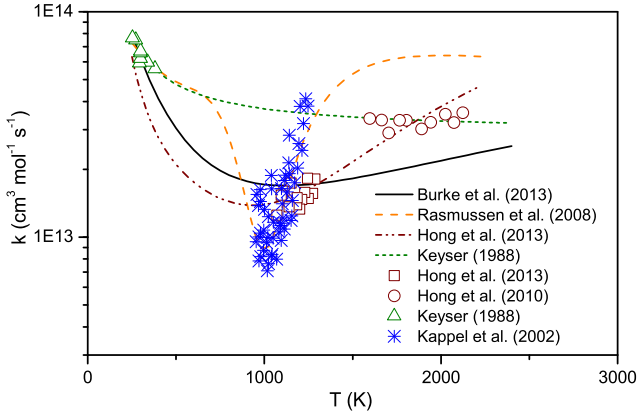

Figure 5.9: Rate constant of reaction R13 (HO_2+OH=H_2O+O_2) as a function of temperature. Symbols mark experimental data from Keyser [150], Kappel et al. [151], and Hong et al. [129, 131]. Lines denote suggested curves from Burke et al. [135], Hong et al. [131], Keyser [150], and Rasmussen et al. [102].

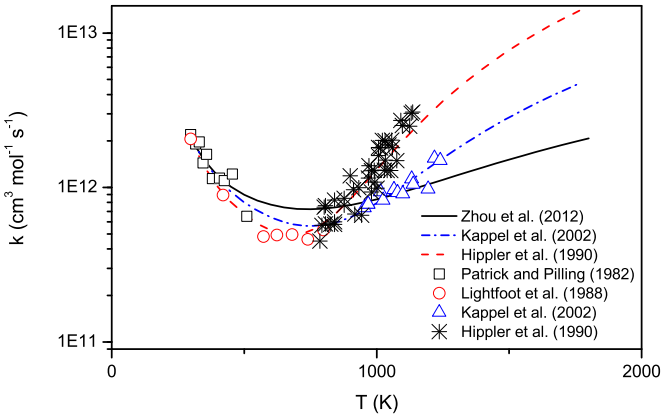

Figure 5.10: Rate constant of reaction R14 (HO_2+HO_2=H_2O_2+O_2) as a function of temperature. Symbols mark experimental data from Patrick and Pilling [156], Kappel et al. [151], Hippler et al. [155], and Lightfoot et al. [160]. Lines denote suggested curves from Kappel et al. [151], Hippler et al. [155], and Zhou et al. [134].

5.6.4 Modeling of the flow reactor

5.6.4.1 Reactor temperature

Temperature profile of the laminar flow reactor measured at the outer wall of the quartz tube is displayed in figure 5.11. Linear interpolation was used to estimate temperature profile for temperatures between the measured ones.

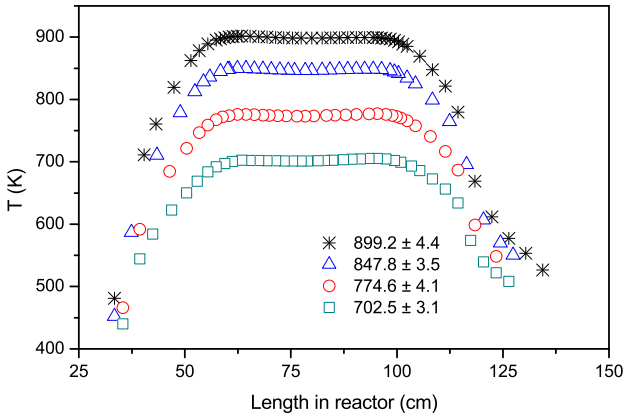

Figure 5.11: Temperature profile measured inside the pressure shell wall of the flow reactor at different isothermal temperatures. The flow was pure nitrogen at 3.06 NL/min at 50 bar pressure.

5.6.4.2 Reaction path analysis

Reaction pathway for consumption of hydrogen under the flow reactor conditions was determined and is shown in figure 5.12. For all stoichiometries and for most of the time, the consumption path is similar. Reaction R17 (the dashed path) became active at the time of ignition but then disappeared from reactions controlling post-ignition consumption of H_2.

$$H_2 + OH = H_2O + H \quad \text{(R3)}$$

$$H + O_2(+M) = HO_2(+M) \quad \text{(R9)}$$

$$HO_2 + HO_2 = H_2O_2 + O_2 \quad \text{(R14)}$$

$$H_2O_2(+M) = OH + OH(+M) \quad \text{(R15)}$$

$$H_2O_2 + H = HO_2 + H_2 \quad \text{(R17)}$$

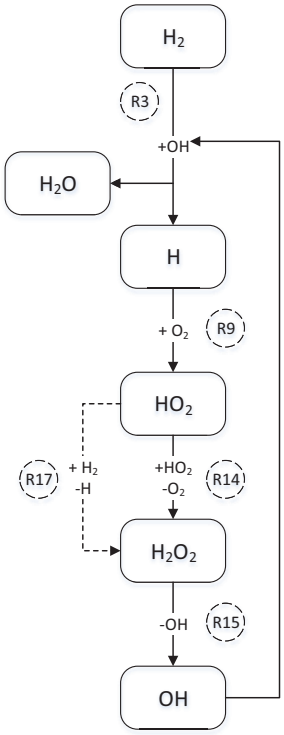

Figure 5.12: Major consumption path of hydrogen for all investigated stoichiometries under the flow reactor conditions. Calculation was done at 773 K for reducing and 823 K for other stoichiometires.

5.6.5 Ignition in the rapid compression machine

To further evaluate the present model at high pressure and moderate temperatures, the mechanism was tested against experimental autoignition delay times of $H_2/O_2/N_2/Ar$ mixtures measured in an RCM (rapid compression machine) by Gersen et al. [142]. The measurements have been done for stoichiometric and fuel–lean mixtures at temperatures and pressures of 940–1050 K and 20–70 bar, respectively. To take into account the effects of heat loss and variable specific volume during the RCM experiments, the specific volume history of the adiabatic core was used as input into the simulations. The specific volume of the adiabatic core was derived from the measured pressure trace up to the point were significant heat release occurs, and extrapolated exponentially thereafter. This method faithfully reproduces the pressure history during compression

and during the post compression stage as shown in ref [161]. Figure 5.13 presents the experimental and calculated pressure trace at fuel–lean conditions. As can be seen, excellent agreement is found between the measured and calculated pressure traces. For calculations, a modified version of the SENKIN code [162] is used. For more details about this simulation procedure, we refer to ref [161].

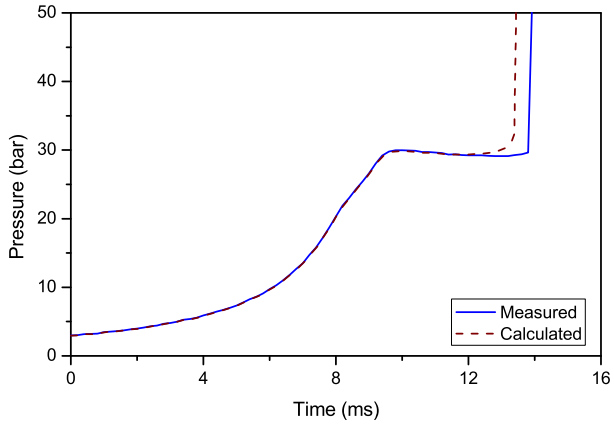

Figure 5.13: Measured (solid line) and computed (dotted line) pressure traces for a fuel lean (ϕ=0.5) $H_2/O_2/N_2$/Ar mixture in the RCM at P_c=30 bar and T_c=1010 K [142].

Figures 5.14 and 5.15 show the comparison between the measured (points) and calculated (lines) autoignition delay times. In figure 5.14 the autoignition delay times are presented as a function of pressure at a constant temperature; T_c ~995 K at stoichiometric conditions and T_c ~1010 K at fuel–lean conditions. For both oxidizing and stoichiometric conditions, ignition delay time decreases as pressure increases in the investigated range. Although ignition delays at both stoichiometries are very close at the lowest pressure, the difference between them increases at higher pressures. The stoichiometric mixture is more sensitive to increase in pressure manifesting itself in a sharper slope in the figure. An excellent agreement between the measurements and computations can be seen for the fuel–lean conditions (see figure 5.14) while for the stoichiometric conditions ignition delay is slightly underestimated.

Figure 5.15 shows the ignition delays versus temperature measured at a constant pressure of P_c ~40 bar at stoichiometric conditions and P_c ~50 bar at fuel–lean conditions. Ignition delay time decreases with increase in temperature and a similar sensitivity toward temperature is observed for both stoichiometric mixtures. From figure 5.15 it can be seen that computations agree very well with the measurements.

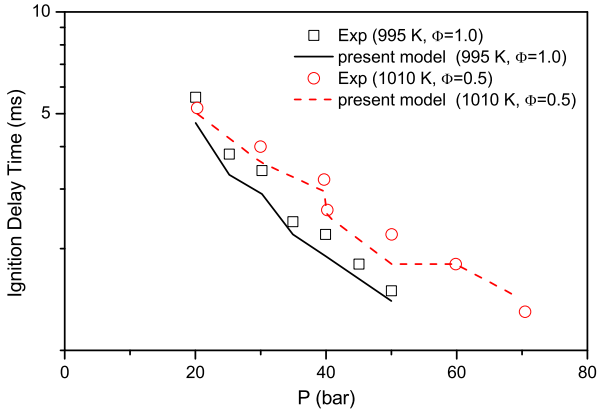

Figure 5.14: Ignition delay time of $H_2/O_2/Ar/N_2$ versus pressure for two different stoichiometries and temperatures. Symbols mark experimental results by Gersen et al. [142] and lines denote the model predictions. $\phi = 0.5$ corresponds to 16.7/16.7/36.7/30.0 of $H_2/O_2/Ar/N_2$ and $\phi = 1.0$ corresponds to 28.6/14.3/27.1/30.0 of $H_2/O_2/Ar/N_2$, respectively.

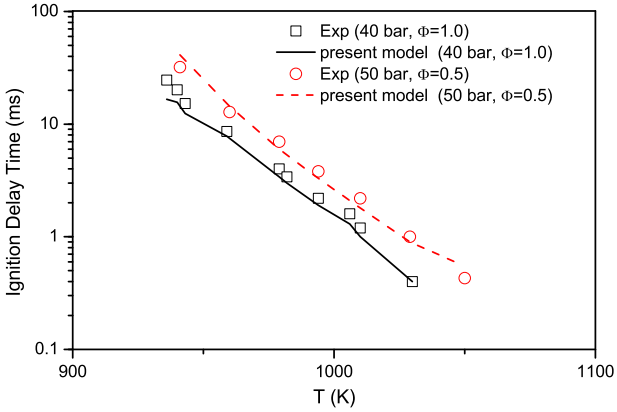

Figure 5.15: Ignition delay time of $H_2/O_2/Ar/N_2$ versus temperature for two different stoichiometries and pressures. Symbols mark experimental results by Gersen et al. [142] and lines denote the model predictions. $\phi = 0.5$ corresponds to 16.7/16.7/36.7/30.0 of $H_2/O_2/Ar/N_2$ and $\phi = 1.0$ corresponds to 28.6/14.3/27.1/30.0 of $H_2/O_2/Ar/N_2$, respectively.

Figure 5.16 represents the sensitivity of H_2 in the RCM modeling. As for ignition in the flow reactor, R17 is the most sensitive reaction. However, R1 and R14 show much stronger influence on ignition delay time compared to the flow reactor conditions. R1 gains more control with increasing temperature. The difference in controlling reactions in the RCM and the flow reactor can be explained by the fact that while the pressure in the RCM is close to the flow reactor, temperature has increased significantly.

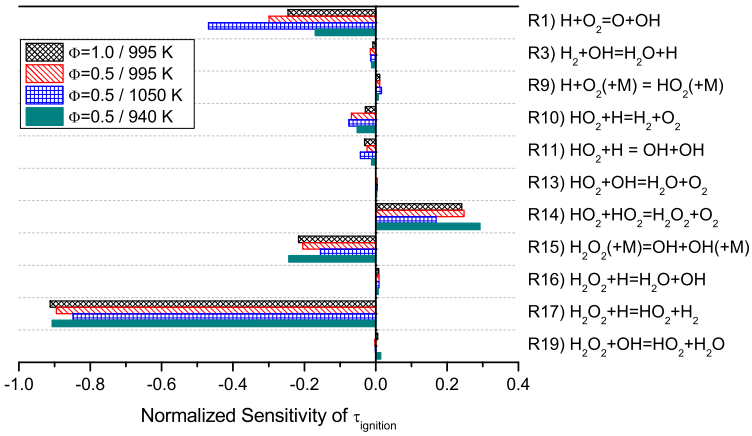

Figure 5.16: Normalized sensitivity of ignition delay time in the RCM at different stoichiometries and temperatures. Pressure was fixed at 40 bar.

5.6.6 Ignition delay time in shock tubes

Ignition delay time of hydrogen at high pressures and intermediate to high temperatures has been measured by Davidson and Hanson [33]. As shown in figure 5.17, at different pressures and gas compositions the ignition delay time decreases as temperature increases, similar to observation for the experiments in the RCM. A temperature range of 1340–1360 K (at 64 bar) was covered by both experimental sets of E and F. Both cases represent similar pressure, temperature, and equivalence ratio but case E is more diluted by nitrogen. As can be seen, ignition delay in case E is higher than case F. Here, increasing the concentrations of reactants while the equivalence ratio is fixed, reduces ignition delay.

Cases B and F overlapped in temperature around 1300 K. From case F to B, combination of an increase in reactant concentration and a drop in pressure shortens the ignition delay considerably. It is in agreement with the discussed non-monotonic sen-

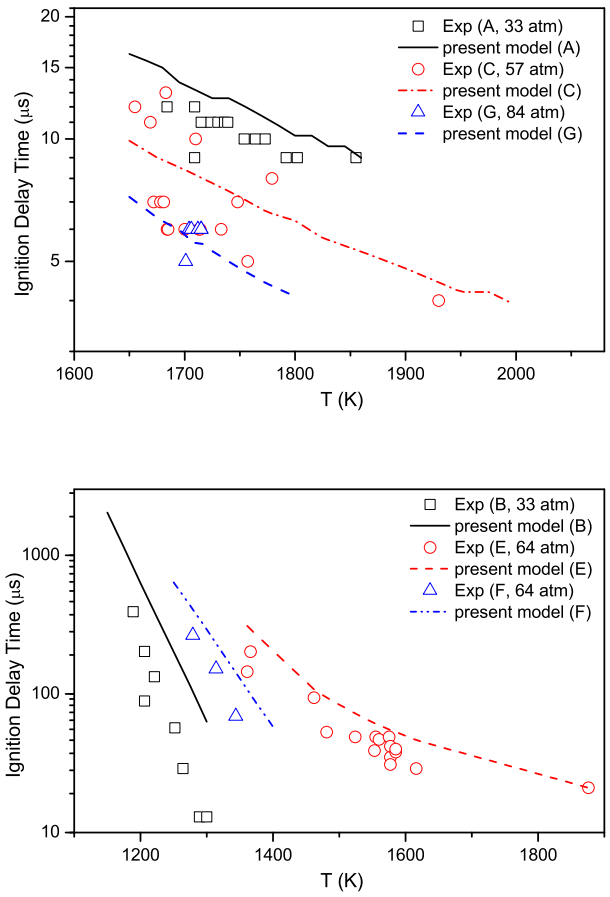

Figure 5.17: Ignition delay time of $H_2/O_2/N_2$ at stoichiometric conditions. Symbols mark experimental results obtained in a shock tube by Davidson and Hanson [33] and lines denote model predictions using the constant u, v model. In determination of ignition, maximum of [OH] gradient has been used. *"A"*, *"C"*, *"F"*, and *"G"* denote experiments on 0.5% H_2 + 0.25% O_2 at 33, 57, 64, and 87 atm pressures, respectively. *"B"* represents results of experiments at 33 atm pressure and 2% H_2 + 1% O_2. *"E"* shows results at 64 atm pressure and 0.1% H_2 + 0.05% O_2.

sitivity of hydrogen ignition delay to pressure.

In general, the present model can follow the ignition delay time variations fairly well, while usually the delay time is over-predicted. However, at higher pressures agreement between the model and the measurements improves; e.g. for case G (87 atm) the model prediction is in the range of uncertainty of the measurements.

In a recent work by Dryer and Chaos [125], the large differences between measurements and chemical kinetic prediction of ignition delay time at low temperatures has been discussed. They have found that in this regime, compressible flow, mixing,

and surface reactions are the main sources of the reported large difference between models prediction and measurements. In a more recent work by Chaos and Dryer [121], they have found that the ignition delay time measurements in shock tubes, especially at the low temperature range of its operation, can be affected significantly by slight pressure (and associated temperature) increases before ignition. Such pre-ignition pressure variations can result in measurement of ignition delay at a higher pressure than what was sought. This pressure/temperature increase has been observed even for non-reactive mixtures, and it is not related to consumption of reactants. Instead, it is believed to be a result of fluid dynamic nonidealities [121].

To compensate for this effect in the simulation, a model suggested in [121] is used. There, instead of the conventional constant u and v model, volume is variable and is changed by pressure according to the isentropic equation,

$$v(t) = \frac{1}{\rho_0}\left[\frac{P(t)}{P_0}\right]^{-1/\gamma}$$

where v is the specific volume, P the measured pressure, γ the specific heat ratios, and P_0 and ρ_0 are the pressure and density just after the shock wave. In this way, the pressure profile for a non-reactive mixture in the shock tube is used for calculation of specific volume according to the isentropic equation of state for ideal gas. The calculated volume profile then is used as an input to Chemkin [109].

Nevertheless, such a correction for the data by Davidson and Hanson [33] is not possible due to lack of the relevant pressure history. Absence of such necessary correction can partly explain the deviation of the model from measured data at low temperatures.

Zhang et al. [139] have investigated hydrogen ignition delay in a shock tube at pressures of 5, 10, and 20 bar. In figure 5.18 their measurements as well as the results of simulations with the present model are shown. All experiments were conducted in a fuel–lean mixture and with the reactants concentration higher than the experiments by Davidson and Hanson [33]. According to their measurements in a non–reactive mixture, pressure was constant until 1.5 ms after the shock and then increased with a slope of 4% per ms. This pressure profile is used as an input to the model as outlined earlier.

As expected, the ignition delay time decreases considerably as the temperature rises at all investigated pressures. However, the stated non–monotonic sensitivity of

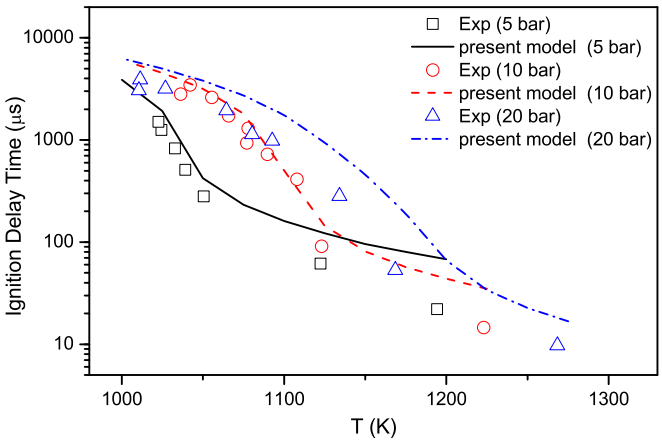

Figure 5.18: Ignition delay time of $H_2/O_2/Ar$ at $\phi = 0.5$. Symbols mark experimental results obtained in shock tube by Zhang et al. [139] and lines denote the current model predictions. In determination of ignition, maximum of OH concentration has been used. Gas composition in all experiments is 3.47% H_2 and 3.47% O_2 in Argon.

ignition delay to pressure is more evident at low temperatures. Although the effect of pressure on ignition delay was negligible for temperatures above 1170 K, ignition delay increased with pressure rise at lower temperatures.

In a recent measurement by Keromnes et al. [128] using the same shock tube as in ref [137], it was found that changing the bath gas from argon to nitrogen affected the ignition delay time of the mixture considerably (see figures 5.19 and 5.20). Shorter ignition delay in argon atmosphere can be explained partly by considering large differences between their specific heats. Lower heat capacity of Ar results in a faster temperature rise because of pre-ignition heat release. Moreover, rate of R9 is lower in argon atmosphere especially at the low pressure limit. The lower rate of R9 means more activation of the chain branching competitor, R1, which leads to a faster ignition. Interestingly, changing the bath gas showed a more dominant effect at 4 atm compared to the other pressures.

Data for fuel–richer and –leaner mixtures were also provided in the same study by Keromnes et al. [128]. As can be seen in figure 5.21, ignition delay for the lean case is longer than for the rich case and it seems that effect of stoichiometry became more evident at lower temperatures.

All in all, agreement between the current model and the experimental results is good especially far from extreme low temperature situations, where the uncertainty

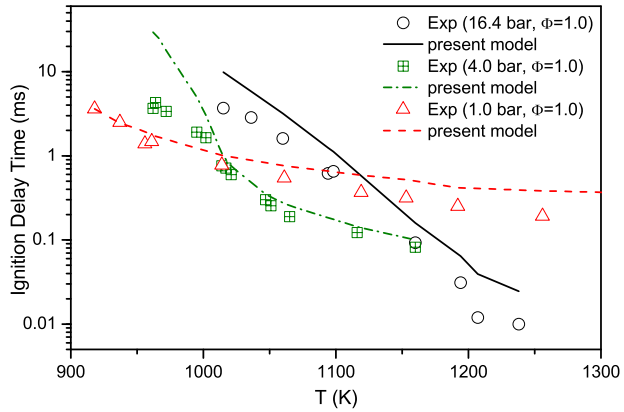

Figure 5.19: Ignition delay time of hydrogen. Symbols mark experimental results at ϕ=1 (in Ar) from Herzler and Naumann [137]. Lines denote model predictions using the constant u, v model. Maximum of OH concentration has been used in determination of ignition.

of the measurements also increases considerably.

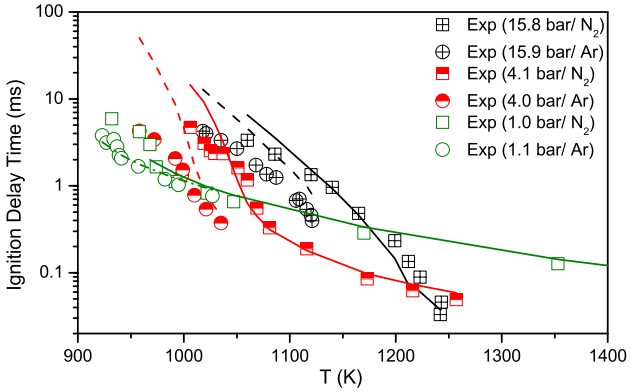

Figure 5.20: Ignition delay time of hydrogen. Symbols mark experimental results at ϕ=0.5 (in N_2) from Keromnes et al. [128] and (in Ar) from Herzler and Naumann [137]. Lines denote model predictions using the constant u, v model. Maximum of OH concentration has been used in determination of ignition.

5.6.6.1 Sensitivity analysis for shock tube

For a better understanding of the ignition chemistry, a temperature of 1100 K was selected as a typical case for sensitivity analysis. Here at higher temperatures comparing to the flow reactor, competition between reactions R1 and R9 largely determines the branching ratio of the combustion system as reported previously in ref [127]. Espe-

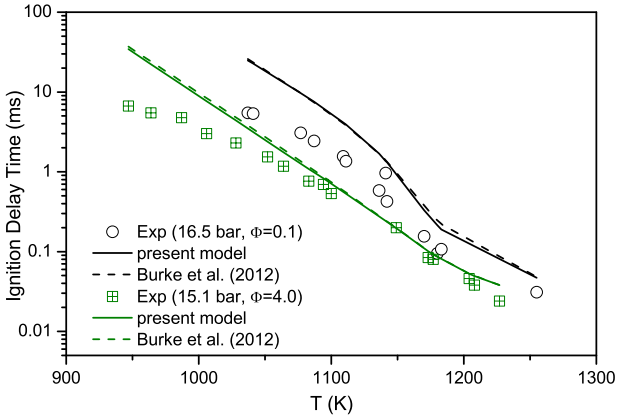

Figure 5.21: Ignition delay time of $H_2/O_2/Ar$ at $\phi = 0.1$ and $\phi = 4.0$. Symbols mark experimental results obtained in shock tube by Keromnes et al. [128] and lines denote model predictions using the current. In determination of ignition, maximum of OH concentration has been used. Composition of the gas mixture for fuel rich and lean conditions are 12.5/1.6/85.9 and 0.8/4.0/95.2 $H_2/O_2/Ar$ respectively. Simulations have been done in the average pressures of 15.1 and 16.5 bar.

cially at 2 atm and 40 atm pressures, competition between R1 and R9 controls the ignition while R9 governs the overall rate at 5 and 10 atm. Additionally, R2 ($O+H_2=H+OH$) was an influential chain–branching reaction at low pressures, while it lost its importance at higher pressures. At pressures as high as 40 atm, reactions R15 and R17 also play important roles in ignition of hydrogen at the investigated temperature of 1100 K.

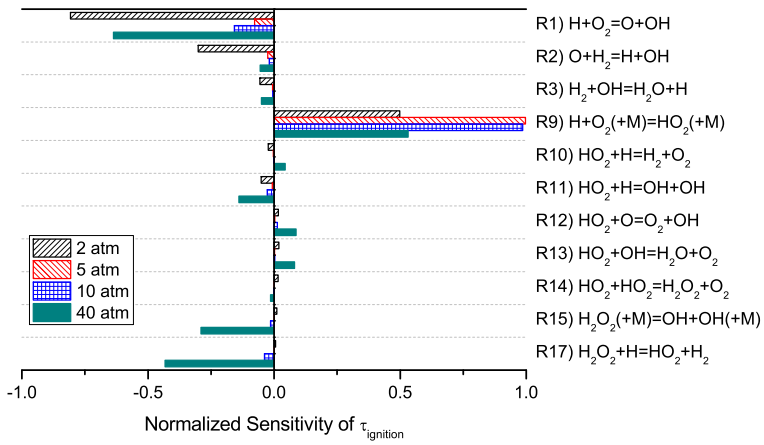

Figure 5.22: Normalized sensitivity of ignition delay time for temperature of 1100 K and gas composition of 3.47% H_2 and 3.47% O_2 in Argon.

5.6.6.2 Reaction path analysis for shock tube

To recognize initial steps in ignition of hydrogen, reaction path analysis was performed at the time of 0.01% consumption of initial hydrogen. The analysis was repeated for pressures of 2, 5, 10, and 40 atm, all for an initial temperature of 1100 K. As can bee seen from figure 5.23, the first step in ignition of hydrogen is similar to consumption of hydrogen of lower temperature in the flow reactor; H_2 + OH = H_2O + H. However, while at the flow reactor conditions reaction R9 was dominant in the consumption of H radical, here R1 is dominant at low pressures but it is overtaken by R9 at higher pressures. The formed hydroperoxyl radical is generally converted via R11 at low pressures while it is required to proceed via R17 and then R15 at higher pressures.

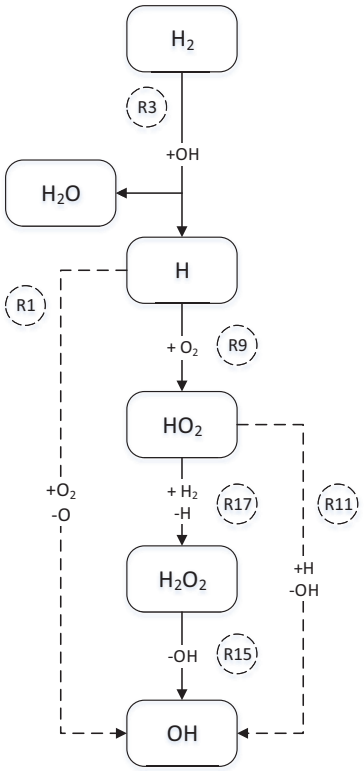

Figure 5.23: Reaction path for hydrogen at time of 0.01% consumption of H_2 for pressures of 2, 5, 10, and 40 atm. Initial temperature was 1100 K. Dashed line were major paths in low pressures. The gas mixture consisted of 3.47% H_2 and 3.47% O_2 in argon.

5.6.6.3 Effect of stoichiometry on ignition delay time

Variation of ignition delay time with fuel equivalence ratio can be interesting. Keromnes et al. [128] have found noticeable differences between ignition delays measured in $\phi = 0.1$ and $\phi = 4.0$. To further investigate effect of stoichiometries, the recent reaction mechanism was used to simulate ignition delay time of hydrogen at different stoichiometries and pressures while temperature was kept constant and equal to 1100 K. The inert gas (argon) concentration was kept constant and equal to 95% to avoid too large concentrations of hydrogen or oxygen. As can be seen in figure 5.24 the effect of stoichiometry is different at various pressures. At 2 and 5 atm, ignition delay time grows with increase in fuel to oxidizer ratio. However, for higher pressures the trend is not linear; the delay time initially decreases and later increases with rise of equivalence ratio for 10 and 40 atm pressures. The minimum of ignition delay time can be found in the fuel–lean side for 10 atm while interestingly it shifts to fuel–rich side for 40 atm pressure.

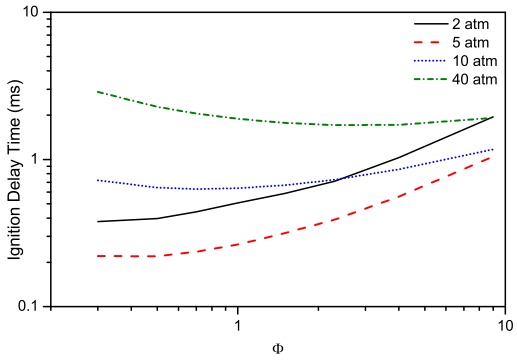

Figure 5.24: Ignition delay time of $H_2/O_2/Ar$ at 1100 K temperature and different stoichiometries. Lines denote model predictions using the constant u, v model. In determination of ignition, maximum of OH concentration has been used. The mixture always consists 95% argon.

5.6.7 Laminar burning velocity

Measuring laminar burning velocity of hydrogen has attracted lots of interest during the years. Most of studies have been dedicated to hydrogen/air mixtures at low initial temperatures and atmospheric pressure [10, 19, 163–170]. To evaluate the models for their predictive ability, the unstretched burning velocity of hydrogen/air mixture was calculated with Chemkin [109]. By adjusting values of Grad and Curv parameters,

a suitable resolution verified by grid independency tests has been achieved. Furthermore, it was found that considering multi-component transport model and thermal diffusion (Soret effect) improved the results considerably. A selection of published measurements of atmospheric flame speed is plotted in figure 5.25. Most of the measurements have reported the maximum of burning velocity at $\phi \simeq 1.8$ while the reported velocity at this point varied from 261 to 298 cm/s, showing discrepancies up to 15%. Generally, divergence of data increased with rise of equivalence ratio.

The present model shows a good agreement under fuel–lean conditions whereas it lies in the uncertainty range of measurements under fuel–rich conditions. As a general trend, the most recent measurements reported higher burning velocity for fuel–rich side which improves the agreement between the model and the experiments. Difference between the present model and the base model by Burke et al. [127] in prediction of flame speed is negligible under tested conditions.

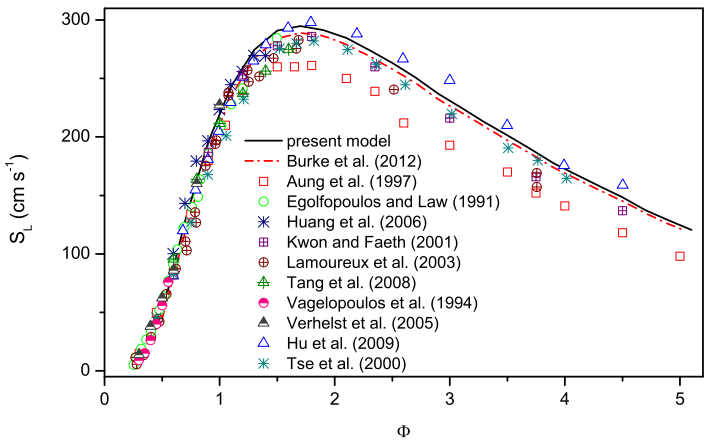

Figure 5.25: Unstretched laminar burning velocity of H_2/Air at initial conditions of 298 K and 1 atm. Lines denote model predictions and symbols mark experimental results from literature; Aung et al. [163], Egolfopoulos and Law [10], Hu et al. [164], Huang et al. [19], Kwon and Faeth [165], Lamoureux et al. [166], Tang et al. [167], Tse et al. [168], Vagelopoulos et al. [169], and Verhelst et al. [170].

Chapter 6

Methane

Abstract

Methane oxidation at the high pressure of 100 bar and intermediate temperatures of 700–900 K was investigated in a laminar flow reactor at fuel-air equivalence ratios (Φ) of 0.06, 1.0, and 19.7. It was found that under the investigated conditions, the conversion of methane started at 723 K under reducing conditions (Φ=19.7) and at 750 K under stoichiometric (Φ=1) and oxidizing (Φ=0.06) conditions. A chemical kinetic model for methane oxidation was developed and evaluated against the present data as well as data from literature. The modeling yielded satisfactory predictions for the onset temperature of the fuel conversion in the flow reactor as well as the mixture composition upon ignition. Furthermore, the model compared well with measured ignition delay times and flame speeds from literature, so its applicability under a wider range of conditions was demonstrated.

6.1 Introduction

The contribution of natural gas to the global energy supply is increasing, at least in the short term [171]. A large availability and a low emission of pollutants in combustion are among the major reasons to replace other fossil fuels by natural gas. For an equivalent amount of heat, burning of natural gas produces around 20 and 45 percent less carbon dioxide than burning gasoline and coal, respectively. This reduction in the emission of green–house gases can reduce the climate change problem significantly. Due to recent successes in excavation of shale gas, natural gas will be cheaper according to some scenarios [4].

While the combustion of natural gas has been studied for years, it remains as a

challenging area [21, 29, 32, 35, 75, 139]. Some of the challenges in using natural gas are higher ignition temperature, longer ignition delay time, and lower burning velocity of natural gas compared to conventional petroleum–based fuels. Depending on the application, these variations can have adverse consequences if appropriate measures are not taken.

Experimental methods to study the effects of changing fuel in practical conditions are not always economic or even feasible. Ignition, as a potentially challenging issue in the combustion of natural gas, is mainly governed by chemical kinetics. Thus a reliable chemical kinetic model for methane as the major component of natural gas is vital in the design and optimization of combustion devices. The oxidation mechanism of methane, as the simplest practical fuel, has been extensively studied (e.g. see [32, 172–175]). However, with the recent advances in determining reaction rates, values in some cases deviate considerably from previously accepted recommendations. Therefore, the re-examination of the oxidation chemistry of methane is required.

Combustion at high pressures and intermediate temperatures plays a key role in many applications, e.g. internal combustion engines. Even at higher temperatures, autoignition depends not only on chemical processes and thermokinetic interactions at the time of ignition, but also on the earlier, lower temperature chemistry creating the necessary conditions [176]. Detailed chemical kinetic models are essentially developed by comparing calculated combustion characteristics with the measured ones, e.g., ignition delay time, flame speed, and species evolution profiles. However, data for natural gas at high pressures and intermediate temperatures are scarce. Figure 6.1 shows the pressure and temperature range covered by earlier studies.

The relatively long resident time which is required to study combustion at high pressures and intermediate temperatures can be realized in flow reactors and rapid compression machines. Rytz and Baiker [26] investigated the partial oxidation of methane to methanol in a flow reactor at 698–773 K and 20–50 bar. Melvin [25] measured the ignition delay time of methane in the pressures of 58–110 atm and temperatures around 623 K inside a steel static reactor. Dagaut et al. [27] conducted experiments in a jet-stirred reactor at 900–1300 K and 1–10 atm. Hunter et al. [28] carried out experiments on CH_4/O_2 mixtures in a flow reactor at 930–1000 K and 3–10 atm and found the reaction pathways of methane independent of pressure and temperature for those conditions. Rasmussen et al. [32] measured methane conversion in a laminar flow reactor at 50–100 bar and 700–900 K. Based on their results, they called for fur-

ther investigation of reactions involving alkylperoxyl radicals (e.g. CH_3OO). Further measurements at different conditions can extend the benchmark data on methane conversion at high pressures and intermediate temperatures.

The major aim of this work was to investigate methane oxidation at high pressures and intermediate temperatures by conducting experiments in a laminar flow reactor at 700–900 K and 100 bar. A detailed chemical kinetic model was developed by updating previous models from the same laboratory [32, 102, 177–179] and was compared with the measured data and other available combustion characteristics at the highest pressures reported.

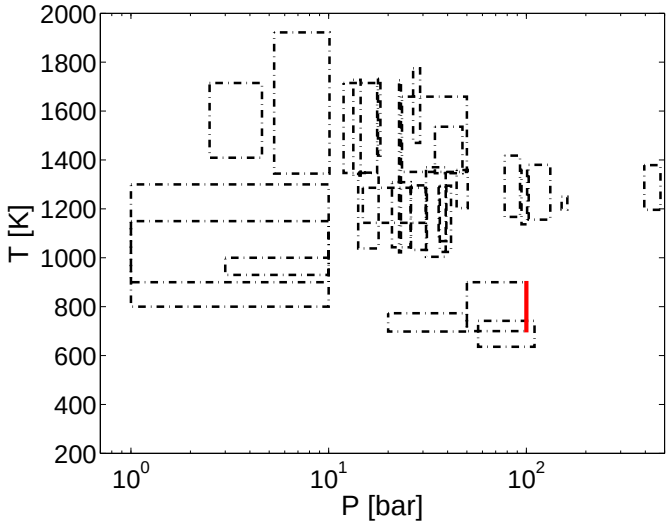

Figure 6.1: Temperature- and pressure-coverage of earlier experiments and the present ones. Dashed lines correspond to earlier experiments in [21, 25–35] and solid lines mark the present experiments.

6.2 Experimental

The experimental setup was a laboratory–scale high–pressure laminar flow reactor designed to approximate plug flow. The setup was described in detail elsewhere [102] and only a brief description is provided here. The system was used here to investigate methane oxidation chemistry at 100 bar pressure, temperatures up to 900 K, and a flow rate of 3.23 Nliter/min (STP; 1 atm and 273.15 K).

The reactions took place in a tubular quartz reactor (inner diameter of 8 mm), enclosed in a stainless steel tube that acted as a pressure shell. Using a quartz tube and conducting experiments at high pressure are expected to minimize the contribution

from heterogeneous reactions at the reactor wall. The steel tube was placed in a tube oven with three individually controlled electrical heating elements that produced an isothermal reaction zone (±6 K) of 37–39 cm. A moving thermocouple was used to measure the temperature profile inside the pressure shell wall after stabilizing the system. The system was pressurized from the feed gas cylinders. The reactor pressure was monitored upstream of the reactor by a differential pressure transducer and controlled by a pneumatic pressure valve positioned after the reactor. The pressure fluctuations were less than 0.2 % during the experiments. The reactant gases were premixed before entering the reactor. All gases used in the present experiments were high purity gases or mixtures with certified concentrations (±2% uncertainty). Downstream of the reactor, the system pressure was reduced to atmospheric level prior to product analysis, which was conducted by an on-line *6890N Agilent Gas Chromatograph* (GC-TCD/FID from Agilent Technologies). All GC sampling and measurements were repeated at least two times to reduce uncertainties of measurements.

For gaseous compounds the GC peak areas were related to concentrations by calibration against certified gas mixtures (± 2 % from AGA A/S). For liquid compounds, usually the calibration was based on gas mixtures prepared by injecting a known quantity of the liquid component into a known volume of nitrogen in a Tedlar bag and allowing the liquid to evaporate. To avoid difficulties in handling formaldehyde, its calibration was provided by correlating TCD response factors for other components to calculated thermal conductivities estimated from the Chapman-Enskog kinetic theory [104]. The TCD response factor for formaldehyde was then determined by using a calculated thermal conductivity with this correlation. In the calculation of the thermal conductivity of formaldehyde, the employed Lennard-Jones force constants (σ = 3.65 $\AA$, ε/K = 313.9 K) were in turn estimated from the critical properties (Lide [105]) using the method of Satterfield [106].

The plug flow assumption was shown by Rasmussen et al. [102] to be a good approximation for the present operating conditions. Figure 6.2 shows the measured temperature profiles for different isotherms with the flow of pure nitrogen. The residence time of gases in the isothermal zone of the reactor can be estimated as τ [s]=9557/T[K]. However, it was found that inputting the temperature profile improves the accuracy of simulation. Therefore, a plug flow reactor with fixed temperature profile and constrained pressure was used for modeling in Chemkin [109]. A source of uncertainty in determining the gas temperature was the effect of heat released from combustion. Due

to the high level of dilution, this effect was limited. Simulations in Chemkin [109] with a constant pressure and enthalpy (adiabatic) model lead to maximum 21 K temperature rise. However, because of the fast heat transfer from the hot gases to the pressure shell, especially in such a narrow reactor, the deviation of the gas temperature from the measured temperature should be even smaller.

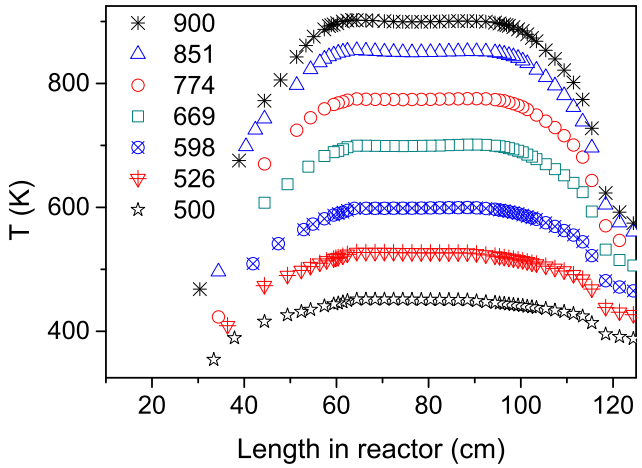

Figure 6.2: Temperature profile measured inside the pressure shell wall of the reactor at different isothermal temperatures. The flow was pure nitrogen at 3.23 NL/min and 100 bar pressure.

6.3 Chemical kinetic model

A chemical kinetic model developed in [32, 102, 178–180] has been the base of the present model. Recently we updated and evaluated the hydrogen subset of the model [1]. The reactions which are important under conditions investigated here and belong to C_1 subset are reviewed in this work and more accurate rate constants are implemented when possible.

The dissociation of the formyl radical (R3) as well as its reaction with molecular oxygen (R4) are the major sources of CO in the combustion of hydrocarbons [181].

$$HCO(+M) = H + CO(+M) \quad \text{(R3)}$$

$$HCO + O_2 = CO + HO_2 \quad \text{(R4)}$$

Namely, the calculation of flame speed is affected by these reactions [181]. Colberg and Friedrichs [182] measured the rate of R4 and fitted a rate constant for the temperatures

of 739–1108 K. As shown in figure 6.3, this reaction showed a slight dependency on temperature. The suggested rate constant by Colberg and Friedrichs [182] deviates considerably from other measurements at low temperatures, outside its fitting range. More recently, data from measurements at higher temperatures became available by Fassheber et al. [183]. In addition to their measurements, Fassheber et al. [183] used earlier experimental results to fit a rate constant covering a wide range of temperatures, so their suggested rate constant is adopted here.

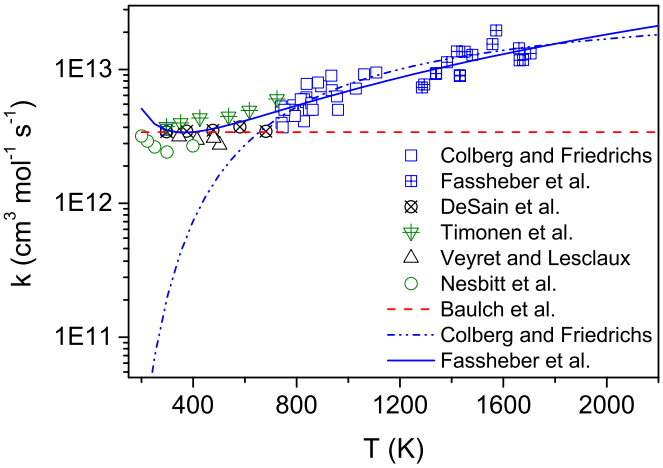

Figure 6.3: Reaction rate constant for (R4) HCO + O_2=CO + HO_2. Symbols mark measurements from Colberg and Friedrichs [182], Fassheber et al. [183], Nesbitt et al. [184], Veyret and Lesclaux [185], and Timonen et al. [186], and DeSain et al. [187]. Lines denote suggested rate constants from Baulch et al. [136] and Colberg and Friedrichs [182], and Fassheber et al. [183].

The dissociation of the formyl radical (R3) has been more controversial. Hippler et al. [188] measured the rate of this reaction at 1–140 bar and 590–800 K and derived a pressure-dependent rate constant with the help of earlier measurements. Simultaneously, Krasnoperov et al. [189] measured the rate of HCO dissociation at 0.8–100 bar and 498–769 K. The measured rate by Krasnoperov et al. [189] was considerably slower than that by Hippler et al. [188] for a wide range of temperatures and pressures related to combustion. More recently, Yang et al. [190] studied theoretically the rate of HCO dissociation over the temperatures of 300–2700 K and the pressures of 0.01–1000 atm. At atmospheric pressure and medium temperatures, their determined rate is within the earlier suggestions by Hippler et al. [188] and Krasnoperov et al. [189]. At high temperatures, where this reaction is sensitive in calculating flame speed, the rate by Yang et al. [190] agrees better with the one by Krasnoperov et al. [189]. Here we adopt

the rate constant from Yang et al. [190] while further study of this reaction is crucial.

The formaldehyde chemistry plays a key role in methane combustion [28]. Under conditions of this work, formaldehyde is mainly converted via either thermal decomposition (R5 and R6) or reactions with OH (R8) or HO_2 (R9). While one channel for dissociation of formaldehyde is a chain-branching reaction:

$$CH_2O(+M) = HCO + H(+M) \tag{R5}$$

the other channel produces stable products:

$$CH_2O(+M) = CO + H_2(+M) \tag{R6}$$

The rate constants of both reactions are taken from a recent theoretical study by Troe [191]. For the reaction between formaldehyde and a hydrogen radical,

$$CH_2O + H = HCO + H_2 \tag{R7}$$

the rate constant is taken from a recent study by Wang et al. [192] who conducted measurements at 1300–2000 K and extended the rate constant to 200–3000 K by using TST calculations. The reaction between formaldehyde and the hydroxyl radical,

$$CH_2O + OH = HCO + H_2O \tag{R8}$$

is taken from a work by Wang et al. [193] who investigated this reaction behind a reflected shock over 950–1400 K. By adding low-temperature data from literature, they fitted a rate constant over 200–1400 K. For the reaction between formaldehyde and HO_2,

$$CH_2O + HO_2 = HCO + H_2O_2 \tag{R9}$$

we adopt the rate constant from Eiteneer et al. [194].

At high temperatures, the recombination of the methyl and hydrogen radicals,

$$CH_3 + H(+M) = CH_4(+M) \tag{R10}$$

is an important terminating reaction [195]. This reaction is especially sensitive in cal-

culating flame speed [77, 196, 197]. The preferred rate constant is from a recent theoretical study by Troe and Ushakov [198] which compares well with earlier measurements.

The autoignition of alkanes is driven by reactions forming the hydroxyl radical [199]. The first step in the reaction pathways of methane oxidation at medium temperatures and high pressures is the H-abstraction by an OH radical, R13 [32].

$$CH_4 + OH = CH_3 + H_2O \tag{R13}$$

The rate of this reaction is taken from a study by Srinivasan et al. [200].

An important chain-terminating reaction in the combustion of hydrocarbons is the reaction between a methyl and a hydroxyl radical. This multi-channel reaction can proceed to different products:

$$\begin{aligned} CH_3 + OH(+M) &= CH_2 + H_2O(+M) && \text{(R15)}\\ &= CH_2(S) + H_2O(+M) && \text{(R16)}\\ &= CH_3OH(+M) && \text{(R17)}\\ &= CH_2OH + H(+M) && \text{(R18)}\\ &= CH_3O + H(+M) && \text{(R19)}\\ &= H_2 + HCOH(+M) && \text{(R20)}\\ &= H_2 + CH_2O(+M) && \text{(R21)} \end{aligned}$$

Jasper et al. [201] investigated theoretically the reaction of CH_3 + OH and derived pressure-dependent rate constants consistent with earlier measurements. The branch to CH_3OH was the major channel at high pressures and intermediate temperatures, but the $CH_2(S)$ and CH_2OH channels were promoted by increasing temperature. At atmospheric pressure and temperatures ~2000 K, which is relevant in flame calculations, the branches to CH_2OH, $CH_2(S)$, and HCOH were dominant. The HCOH radical isomerizes rapidly to formaldehyde [201], so the reactions R20 and R21 can be combined into a single reaction producing formaldehyde and molecular hydrogen.

More recent measurements by Sangwan et al. [202] at 294–714 K and 1–100 bar threw doubt on the pressure dependency of this reaction. At high pressures and 700–1000 K, the total conversion rate of CH_3 + OH measured by Sangwan et al. [202] agreed well with that by Jasper et al. [201]. However, Jasper et al. [201] predicted a stronger pressure dependency; the total rate decreased twofold when the pressure was reduced

from 100 bar to 1 bar (at 700 k) while the results of Sangwan et al. [202] indicated an almost pressure–independent rate constant. The measurements by Sangwan et al. [202] could not give the branching ratios, so the rate constants in Jasper et al. [201] are adopted here while further study of this reaction is warranted.

The combustion chemistry of hydrocarbons is generally more complicated at intermediate temperatures (500–1000 K) compared to that at higher temperatures, partly due to the behavior of peroxyl radicals [176]. The hydroperoxyl (HO_2) and methyl (CH_3) radicals are among the major intermediate species during the oxidation of natural gas at intermediate temperatures and high pressures [203], so their association can be an important reaction [204]. The reaction can proceed as either a chain–branching step,

$$CH_3 + HO_2 = CH_3O + OH \tag{R22}$$

or as a chain–terminating step,

$$CH_3 + HO_2 = CH_4 + O_2 \tag{R23b}$$

The chain-branching reaction (R22) was studied theoretically by Jasper et al. [205]. At 700 K, their results agree well with an earlier theoretical study by Zhu and Lin [206], but deviate at higher temperatures. Jasper et al. [205] predicted a weaker sensitivity to temperature, compared to Zhu and Lin [206]. More recently, the rate of R22 was measured by Hong et al. [203] at 1054–1249 K (3.5 atm) as well as by Sangwan and Krasnoperov [207] at 295 K (1 bar). Both measurements agree well with the results of Jasper et al. [205], so the rate constant in Jasper et al. [205] is adopted here.

The chain-terminating path (R23b) affects considerably the ignition-delay calculations of methane [208]. Srinivasan et al. [208] measured the rate of this reaction at 1655–1822 K and extrapolated the rate constant to the temperatures of 200–2000 K via theoretical calculations. Their suggested rate constant is 20–40% lower (at 700–2000 K) compared to the earlier theoretical study by Zhu and Lin [206]. More recently, Hong et al. [203] measured the rate of this reaction at temperatures of 1000–1200 K. Both the suggested rates by Zhu and Lin [206] and Srinivasan et al. [208] are in the uncertainty range of the experimental data by Hong et al. [203]. Jasper et al. [205] calculated the rate of the chain-branching reaction (R22) by using the the rate constant advocated by Srinivasan et al. [208] for R23b. Therefore, the suggested rate constant in [208] is

adopted here to keep consistency.

The reaction between a methyl radical and molecular oxygen is among the most important propagation reactions in the combustion of methane [209]. This reaction can proceed to different products, depending on conditions:

$$CH_3 + O_2(+M) = CH_3OO(+M) \quad \text{(R24)}$$

$$CH_3 + O_2 = CH_3O + O \quad \text{(R25)}$$

$$= CH_2O + OH \quad \text{(R26)}$$

The branch to CH_3OO (R24) is expected to be the dominant path at low temperatures whereas due to the growth of the reverse reaction, this path reaches to equilibrium at high temperatures [32, 119]. For R24, the pressure-dependent rate constants are taken from a study by Fernandes et al. [210]. The rate constants for two other branches (R25 and R26) are adopted from shock-tube measurements by Srinivasan et al. [211].

For most alkanes, the isomerization of the alkylperoxyl radicals to the hydroperoxide radicals (ROO $\longrightarrow$ QOOH) is expected to be an important step in fuel conversion. For the isomerization of the methylperoxyl radical,

$$CH_3OO(+M) = CH_2OOH(+M)$$

an energy barrier of ~160 kJ/mol [212] should be prevailed. This reaction competes with the dissociation of methylperoxyl radical,

$$CH_3OO(+M) = CH_3 + O_2(+M) \quad \text{(R24b)}$$

The reaction R24 is believed to be a barrierless exothermic reaction [210]. To proceed in the reverse direction (R24b), an energy difference of ~135 kJ/mol [114] should be surmounted. Consequently, the isomerization to hydroperoxide is not expected at low-medium temperatures as CH_3OO dissociation is more favored.

The methylperoxyl (CH_3OO) reactions are quite important for modeling methane oxidation at low temperatures [32], but our understanding of these reactions is far from perfect. Only a few of CH_3OO reactions have been studied experimentally and even the measured reactions have suffered from high uncertainties in measurements or in extrapolation to combustion related temperatures [213]. For the reaction between

methylperoxyl and hydrogen radicals,

$$CH_3OO + H = CH_3O + OH \quad \text{(R27)}$$

we accept the suggested rate in [213]. Data have not been available for the reaction between a methylperoxyl radical and an oxygen atom,

$$CH_3OO + O = CH_3O + O_2 \quad \text{(R28)}$$

so the rate of this reaction is estimated by analogy to HO_2 + O reaction.

For the reaction between methylperoxyl and hydroxyl radicals,

$$CH_3OO + OH = CH_3OH + O_2 \quad \text{(R29)}$$

Tsang and Hampson [213] estimated the temperature-independent rate constant in the order of $6{\times}10^{13}$ (mol cm^{-3} s^{-1}), in the absence of any experimental or theoretical determination up to that point. More recently, experimental measurements by Bossolasco et al. [214] at sub-atmospheric pressures and at 294 K gave a rate faster than the estimated one by Tsang and Hampson [213]. Here, the reaction is presumed to be pressure- and temperature-independent and the rate constant from Bossolasco et al. [214] is extrapolated for the conditions of this study.

For the reaction of methylperoxyl with HO_2 and CH_3,

$$CH_3OO + HO_2 = CH_3OOH + O_2 \quad \text{(R30)}$$
$$CH_3OO + CH_3 = CH_3O + CH_3O \quad \text{(R31)}$$

we rely on the suggestions by Tyndall et al. [215] and Keiffer et al. [216], respectively. Another sink of the methylperoxyl radicals is its self-reaction giving either methoxy radicals,

$$CH_3OO + CH_3OO = CH_3O + CH_3O + O_2 \quad \text{(R32)}$$

or formaldehyde.

$$CH_3OO + CH_3OO = CH_3OH + CH_2O + O_2 \quad \text{(R33)}$$

The rate constants for these reactions are taken from Tyndall et al. [215] who evaluated existing low-temperature data.

The methylperoxyl radical can also abstract hydrogen from stable molecules such as CH_4 (R34) and CH_2O (R35),

$$CH_3OO + CH_4 = CH_3OOH + CH_3 \quad \text{(R34)}$$

$$CH_3OO + CH_2O = CH_3OOH + HCO \quad \text{(R35)}$$

to form CH_3OOH [32]. The rate constants for these reactions are estimated by analogy to HO_2 reactions. The most important reaction of CH_3OOH at the temperatures of interest is its dissociation [206].

$$CH_3OOH(+M) = CH_3O + OH(+M) \quad \text{(R36)}$$

The preferred rate constant for this reaction is taken from a theoretical calculation by Zhu and Lin [206].

The major removal mechanisms of the methoxy radical at combustion temperatures are dissociation (R37), isomerization (R38), and reactions with other stable components such as oxygen (R39).

$$CH_3O(+M) = CH_2O + H(+M) \quad \text{(R37)}$$

$$CH_3O(+M) = CH_2OH(+M) \quad \text{(R38)}$$

$$CH_3O + O_2 = CH_2O + HO_2 \quad \text{(R39)}$$

The rate constants of these reactions are given by a theoretical study by Aranda et al. [179].

Methanol is an important by-products of the partial oxidation of methane at intermediate temperatures [32]. At the conditions of this work, methanol is mainly formed in fuel-rich mixtures via R40.

$$CH_3O + CH_4 = CH_3OH + CH_3 \quad \text{(R40)}$$

For this reaction we rely on the results of Wantuck et al. [217] who combined measurements and RRKM calculations to derive the rate constant.

Table 6.1: Selected reactions from the chemical kinetic model. The rate constants are in the form of $k = AT^n \exp(-E/(RT))$. Units are *mol*, *cm*, *K*, *s*, and *cal*.

	Reaction	A	n	E	Note/Ref.
R1	$H + O_2 = O + OH$	1.04E+14	0.00	15286	[127]
R2	$HO_2 + HO_2 = H_2O_2 + O_2$	1.18E+9	0.77	-1825	[134]
	duplicate rate constant	1.25E+12	0.295	7397	
R3	$HCO(+M) = H + CO(+M)$	4.93E+16	-0.93	19724	[a], [190]
	Low-pressure limit:	7.43E+21	-2.36	19383	
	Troe parameters: 0.103 139.0 10900.0	4550.0			
R4	$HCO + O_2 = CO + HO_2$	6.92E+6	1.90	-1369	[183]
R5	$CH_2O(+M) = HCO + H(+M)$	8.00E+15	0.00	87726	[191]
	Low-pressure limit:	1.26E+36	-5.50	93932	
R6	$CH_2O(+M) = CO + H_2(+M)$	3.70E+13	0.00	71969	[191]
	Low-pressure limit:	4.40E+38	-6.10	93932	
R7	$CH_2O + H = HCO + H_2$	5.86E+03	3.13	1510	[192]
R8	$CH_2O + OH = HCO + H_2O$	2.39E+07	1.83	-1116	[193]
R9	$CH_2O + HO_2 = HCO + H_2O_2$	4.10E+04	2.50	10206	[194]
R10	$CH_3 + H(+M) = CH_4(+M)$	2.26E+14	0.03	144	[a], [198]
	Low-pressure limit:	2.74E+35	-5.35	3380	
	Troe parameters: 0.395 163.5 4250.3	1253676.0			
R11	$CH_4 + H = CH_3 + H_2$	4.10E+03	3.16	8755	[32]
R12	$CH_4 + O = CH_3 + OH$	4.40E+05	2.50	6577	[136]
R13	$CH_4 + OH = CH_3 + H_2O$	1.00E+06	2.18	2506	[200]
R14	$CH_4 + HO_2 = CH_3 + H_2O_2$	4.70E+04	2.50	21000	[136]
R15	$CH_3 + OH = CH_2 + H_2O$	4.30E+04	2.57	3997	[201]
R16	$CH_3 + OH = CH_2(S) + H_2O$	6.09E+10	0.60	2923	[b], [201]
R17	$CH_3 + OH = CH_3OH$	1.30E+22	-2.66	2451	[b], [201]
R18	$CH_3 + OH = CH_2OH + H$	2.53E+10	0.91	6402	[b], [201]
R19	$CH_3 + OH = CH_3O + H$	3.07E+09	0.92	12981	[b], [201]
R20	$CH_3 + OH = H_2 + HCOH$				[c], [201]
R21	$CH_3 + OH = H_2 + CH_2O$	2.36E+09	0.45	3791	[b], [201]
	duplicate rate constant	9.40E+07	1.29	2424	
R22	$CH_3 + HO_2 = CH_3O + OH$	1.00E+12	0.27	-687	[205]
R23	$CH_4 + O_2 = CH_3 + HO_2$	2.03E+05	2.75	51714	[208]
R24	$CH_3 + O_2 = CH_3OO$	1.05E+19	-2.30	1800	[d], [210]
	duplicate rate constant	4.10E+30	-5.70	8750	
R25	$CH_3 + O_2 = CH_3O + O$	7.50E+12	0.00	28297	[211]
R26	$CH_3 + O_2 = CH_2O + OH$	1.90E+11	0.00	9842	[211]
R27	$CH_3OO + H = CH_3O + OH$	1.00E+14	0.00	0	[213]

Continued on next page

Table 6.1 – *continued from previous page*

		Arrhenius data			
R28	$CH_3OO + O = CH_3O + O_2$	2.85E+10	1.00	-724	$HO_2 + O$
R29	$CH_3OO + OH = CH_3OH + O_2$	1.70E+14	0.00	0	[214]
R30	$CH_3OO + HO_2 = CH_3OOH + O_2$	2.50E+11	0.00	-1490	[215]
R31	$CH_3OO + CH_3 = CH_3O + CH_3O$	5.10E+12	0.00	-1411	[216]
R32	$CH_3OO + CH_3OO = CH_3O + CH_3O + O_2$	1.10E+18	-2.40	1800	[215]
	duplicate rate constant	7.00E+10	0.00	800	
R33	$CH_3OO + CH_3OO = CH_3OH + CH_2O + O_2$	2.00E+11	-0.55	-1600	[215]
R34	$CH_3OO + CH_4 = CH_3OOH + CH_3$	4.70E+04	2.50	21000	$HO_2 + CH_4$
R35	$CH_3OO + CH_2O = CH_3OOH + HCO$	4.10E+04	2.50	10206	$HO_2 + CH_2O$
R36	$CH_3OOH = CH_3O + OH$	2.22E+17	-0.42	44622	[d], [206]
R37	$CH_3O = CH_2O + H$	4.70E+93	-24.61	57200	[d], [179]
R38	$CH_3O = CH_2OH$	3.60E+89	-23.64	57920	[d], [179]
R39	$CH_3O + O_2 = CH_2O + HO_2$	4.80E-01	3.60	-1055	[179]
R40	$CH_3O + CH_4 = CH_3OH + CH_3$	1.30E+14	0.00	15073	[217]
R41	$CH_3OH + OH = CH_2OH + H_2O$	1.50E+08	1.44	113	[180]
R42	$CH_2OH + O_2 = CH_2O + HO_2$	7.20E+13	0.00	3736	[136]
	duplicate rate constant	2.90E+16	-1.50	0	

[a] : for enhanced third-body efficiencies see the mechanism file in the supplementary materials.

[b] : at 132 atm pressure, for other pressures see the mechanism file in the supplementary materials.

[c] : combined in R21

[d] : at 100 atm pressure, for other pressures see the mechanism file in the supplementary materials.

6.3.1 Thermodynamic and transport data

Thermodynamic and transport data are mainly taken from the earlier model in ref [32]. Important components were checked for any refinement in renowned databases (e.g. Burcat et al. [113]).

6.4 Results and discussion

6.4.1 Methane oxidation in the flow reactor

As outlined in the introduction, the major aim of this work was to provide novel data from methane oxidation at high pressures and intermediate temperatures. In this section, the results from the laminar flow reactor at 100 bar and 700–900 K are presented. For the simulations, a plug flow reactor with constrained temperature and pressure is used in Chemkin [109].

Figure 6.4 presents the gas composition at the reactor outlet under reducing conditions (Φ=19.7) at different isotherms. The consumption of reactants starts at 725 K and the major product of the partial oxidation of methane is CO at all investigated temperatures. Upon ignition, considerable amounts of formaldehyde and methanol are formed but their fractions decline gradually at higher temperatures. Instead, C_2H_6 and C_2H_4 are produced to greater extents at higher temperatures. At 900 K, the major products are CO and C_2H_6.

The model can predict the onset of reaction as well as the concentrations of CH_4, O_2, CO, C_2H_6 and C_2H_4 very well. Although CO_2 and CH_3OH are underpredicted and CH_2O is overpredicted, the model can reproduce well the trends of their changes and also the temperatures of their maximum yield.

Under stoichiometric conditions, the fuel conversion starts at a slightly higher temperature of 750 K (see figure 6.5). The major products are CO and CO_2 and trace amounts of C_2H_4 and C_2H_6 are formed too. Above 800 K, further conversion of fuel is retarded and the methane conversion is limited to 88% at 900 K.

For the stoichiometric mixture, the model reproduces accurately the onset of reaction as well as the relative changes in the fractions of stable components. However, the model predicts a slightly lower conversion for methane and oxygen at high temperatures which is accompanied by the underprediction of CO_2.

The methane oxidation under very oxidizing conditions (Φ=0.06) starts at 750 K. The major detected products are CO and CO_2 (see figure 6.6). The CO fraction peaks at 775 K but declines gradually at higher temperatures, likely due to oxidation to CO_2. The model predicts well the onset of reaction and the methane consumption upon ignition. The CO fraction is slightly overpredicted while CO_2 fraction is slightly underestimated at medium temperatures.

In an earlier work from the same laboratory by Rasmussen et al. [32], the onset of methane reaction under reducing conditions was reported to be 725–775 K (Φ=25–99, P=90–100 bar). They found the onset temperature of reaction at 775–800 K under stoichiometric (P=90–100 bar) and oxidizing (Φ=0.04, P=90–100 bar) conditions, while we detected the ignition at slightly lower temperatures of 723–750 K. This small difference can be due to the shorter gas residence time in [32].

The reaction pathways of methane are analyzed and the results are shown in figure 6.7. The analysis at a very early stage of reaction shows that methane conversion

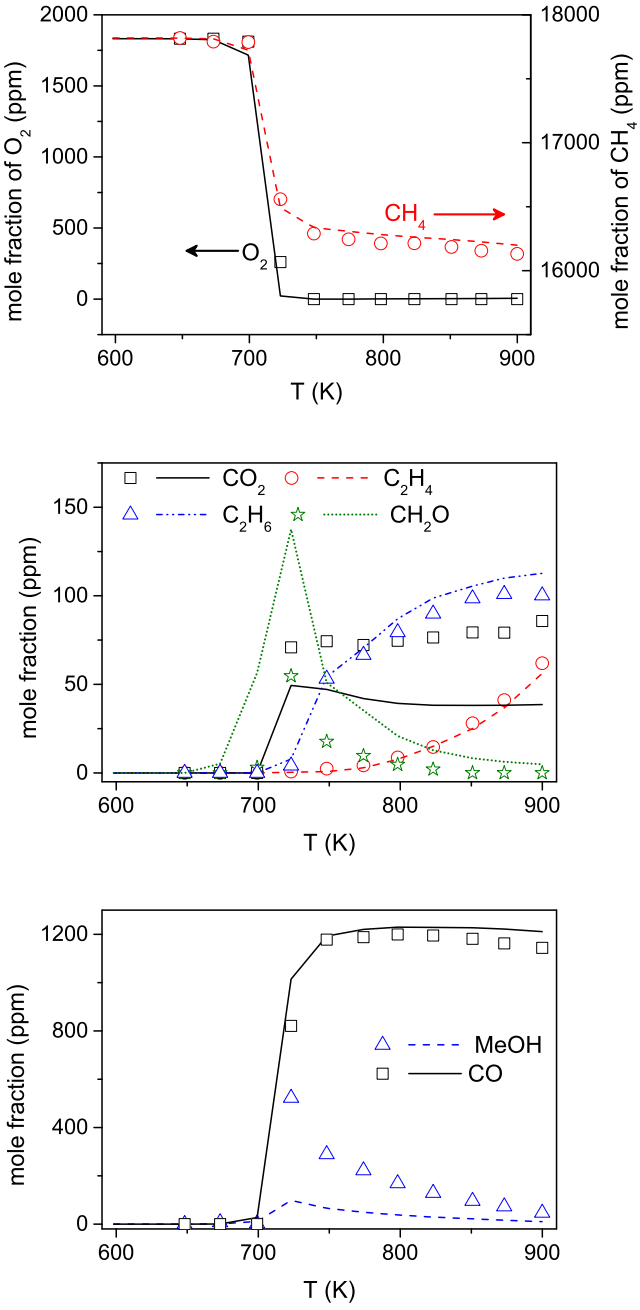

Figure 6.4: Results of experiments under reducing conditions (0.18% O_2 and 1.75% CH_4 in N_2, Φ=19.7) at 100 bar pressure. Symbols mark the experimental results and lines denote the predictions of the present model.

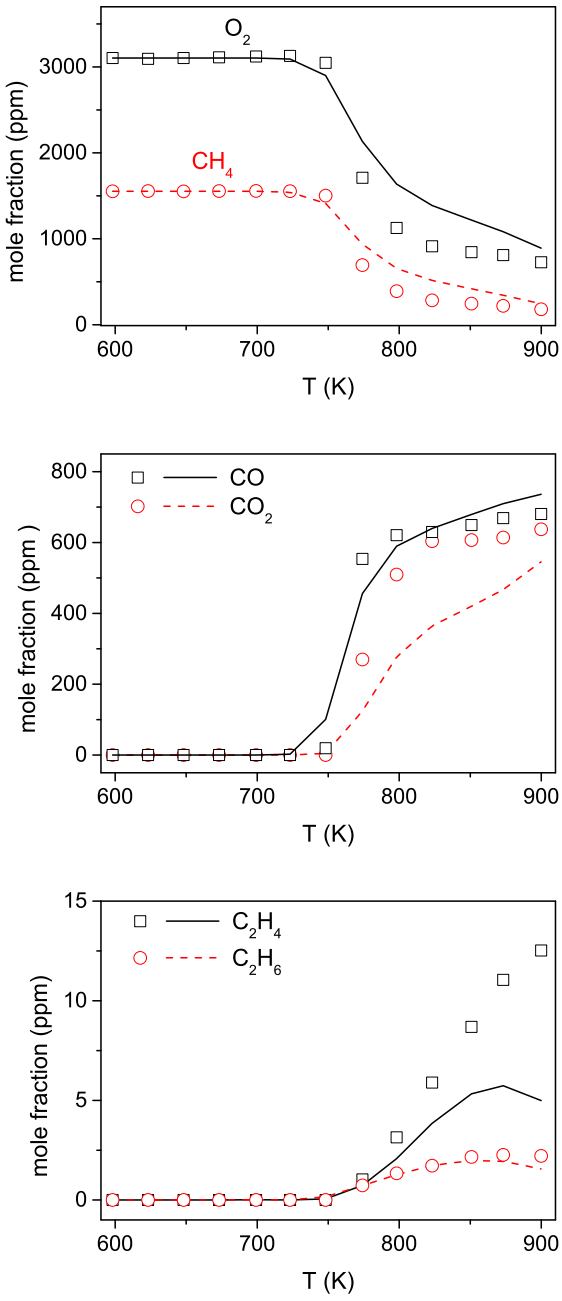

Figure 6.5: Results of experiments under stoichiometric conditions (0.31% O_2 and 0.16% CH_4 in N_2, Φ=1.0) at 100 bar pressure. Symbols mark the experimental results and lines denote the predictions of the present model.

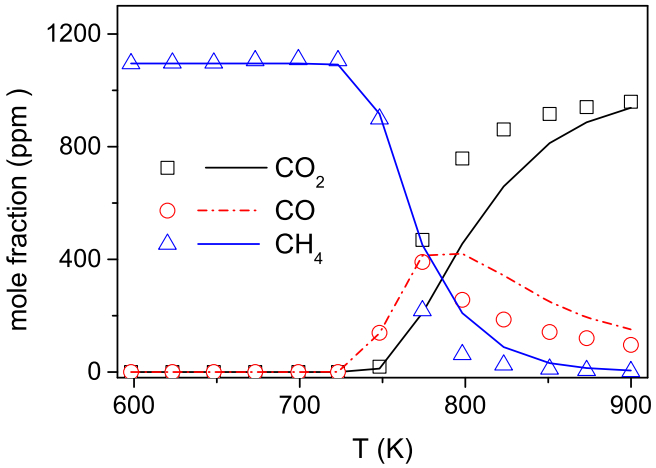

Figure 6.6: Results of experiments under oxidizing conditions (3.96% O_2 and 0.11% CH_4 in N_2, Φ=0.06) at 100 bar pressure. Symbols mark the experimental results and lines denote the predictions of the present model.

is initiated by its reaction with molecular oxygen,

$$CH_4 + O_2 = CH_3 + HO_2 \qquad \text{(R23)}$$

The formed methyl radical then combines with molecular oxygen to give either CH_3OO (R24) or CH_2O + OH (R26). The branch to CH_3OO (R24) is dominant at the initiation stage of methane oxidation, which results in the accumulation of CH_3OO radicals. The branch to CH_2O + OH (R26) retains a small but important share of CH_3 consumption, since it is the main source of OH radicals for a while. The formed OH radicals attack methane molecules,

$$CH_4 + OH = CH_3 + H_2O \qquad \text{(R13)}$$

and starts the main path of the fuel oxidation. In later stages, the required OH radicals are provided by the dissociations of H_2O_2 (R45) and CH_3OOH (R36).

$$H_2O_2(+M) = OH + OH(+M) \qquad \text{(R45)}$$

$$CH_3OOH(+M) = CH_3O + OH(+M) \qquad \text{(R36)}$$

Around 900 K, the reaction between the methyl and hydroperoxyl radicals,

$$CH_3 + HO_2 = CH_3O + OH \quad \text{(R22)}$$

also plays an important role in the production of OH.

The hydroperoxyl radical, the other product of the initiation reaction (R23), attacks methane molecules (R14) to produce H_2O_2.

$$CH_4 + HO_2 = CH_3 + H_2O_2 \quad \text{(R14)}$$

In a later stage of oxidation, reactions R9 and R2 become the major sources of H_2O_2.

$$CH_2O + HO_2 = H_2O_2 + HCO \quad \text{(R9)}$$
$$HO_2 + HO_2 = H_2O_2 + O_2 \quad \text{(R2)}$$

When a sufficient number of radicals is produced, the methane consumption proceeds by its reaction with the OH radical (R13) which gives $CH_3 + H_2O$. At low temperatures (~775 K), the methyl radical mainly reacts with oxygen to form CH_3OO.

$$CH_3 + O_2(+M) = CH_3OO(+M) \quad \text{(R24)}$$

The stability of the methylperoxyl radical (CH_3OO) is enhanced with increasing pressure whereas its thermal dissociation accelerates at elevated temperatures [218]. At high temperatures (~900 K) the reaction R22 becomes the dominant path in removing methyl radicals.

$$CH_3 + HO_2 = CH_3O + OH \quad \text{(R22)}$$

In fact, shifting from the low-temperature pathways to the high-temperature ones is mainly controlled by the competition between reactions R22 and R24 over methyl radicals.

The methylperoxyl radical can combine with HO_2 (R30) or CH_3 (R31) radicals. Depending on stoichiometry and temperature, the reaction between CH_3OO and CH_2O

(R35) can also plays a role in removing CH_3OO.

$$CH_3OO + HO_2 = CH_3OOH + O_2 \quad \text{(R30)}$$

$$CH_3OO + CH_3 = CH_3O + CH_3O \quad \text{(R31)}$$

$$CH_3OO + CH_2O = CH_3OOH + HCO \quad \text{(R35)}$$

The CH_3O radical mainly decomposes to formaldehyde and hydrogen atom (R37). The major sink of formaldehyde under stoichiometric conditions is its reaction by OH (R8).

Under reducing conditions, considerable amounts of methanol is formed via R40.

$$CH_3O + CH_4 = CH_3OH + CH_3 \quad \text{(R40)}$$

The reactions R41 and R42 make the main removing mechanism of methanol for all investigated conditions, in line with previous findings by Aranda et al. [179] in a study dedicated to the oxidation of methanol.

$$CH_3OH + OH = CH_2OH + H_2O \quad \text{(R41)}$$

$$CH_2OH + O_2 = CH_2O + HO_2 \quad \text{(R42)}$$

For methane oxidation at medium temperatures (~775 K), the reactions involving methylperoxyl radicals (CH_3OO) are found to be important which is in agreement with findings in [32, 119, 218, 219].

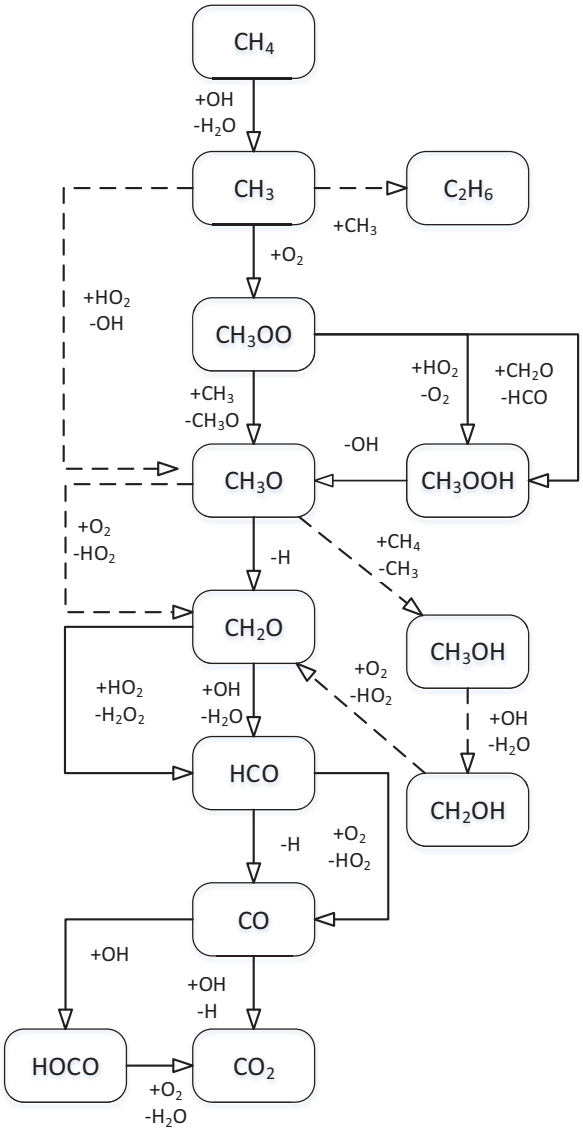

Figure 6.7: Major consumption path for methane at conditions investigated in the flow reactor. The dashed lines are active only under specific conditions. See the text for more details.

The sensitivity of selected reactions in predicting methane conversion as well as methanol formation is analyzed using a brute-force method in which the sensitivity coefficients are calculated as

$$S_{X,i} = \frac{\Delta X / X}{\Delta k_i / k_i}$$

The results of the analysis is shown in figure 6.8. Among the tested reactions, the

reaction R23,

$$CH_4 + O_2 = CH_3 + HO_2 \quad \text{(R23)}$$

inhibits the fuel conversion considerably, especially at higher temperatures. Although this reaction initiates the oxidation process, in the later stages of oxidation when the radical concentrations increases, it proceeds in the reverse direction and becomes a major terminating path of the radicals. R22, a competitor for R23, promotes the ignition by propagating the radical chain.

$$CH_3 + HO_2 = CH_3O + OH \quad \text{(R22)}$$

The reaction between methane and hydroxyl radicals,

$$CH_4 + OH = CH_3 + H_2O \quad \text{(R13)}$$

also plays a key role in methane oxidation.

The formaldehyde chemistry is important in the methane oxidation. While the H-abstraction by the HO_2 radical from formaldehyde (R9),

$$CH_2O + HO_2 = HCO + H_2O \quad \text{(R9)}$$

promotes the ignition, the abstraction reactions by hydroxyl (R8) and methyl radicals (R43),

$$CH_2O + OH = HCO + H_2O \quad \text{(R8)}$$
$$CH_2O + CH_3 = HCO + CH_4 \quad \text{(R43)}$$

inhibit the fuel conversion as the later reactions take out the demanded OH and CH_3 radicals.

Methanol is underpredicted by the model at 723 K under reducing conditions. According to the sensitivity analysis (figure 6.8), its prediction is highly sensitive to the rate of

$$CH_3O + CH_4 = CH_3OH + CH_3 \quad \text{(R40)}$$

which is the main path of methanol formation. The methanol yield is also sensitive to the reactions of the methylperoxyl radicals with CH_4 (R34), CH_3 (R31), CH_2O (R35), and HO_2 (R30), in agreement with the results of Arutyunov et al. [219]. Considering the large uncertainty in the rate constants of CH_3OO reactions, the model prediction may improve by the advent of more reliable data for methylperoxyl chemistry.

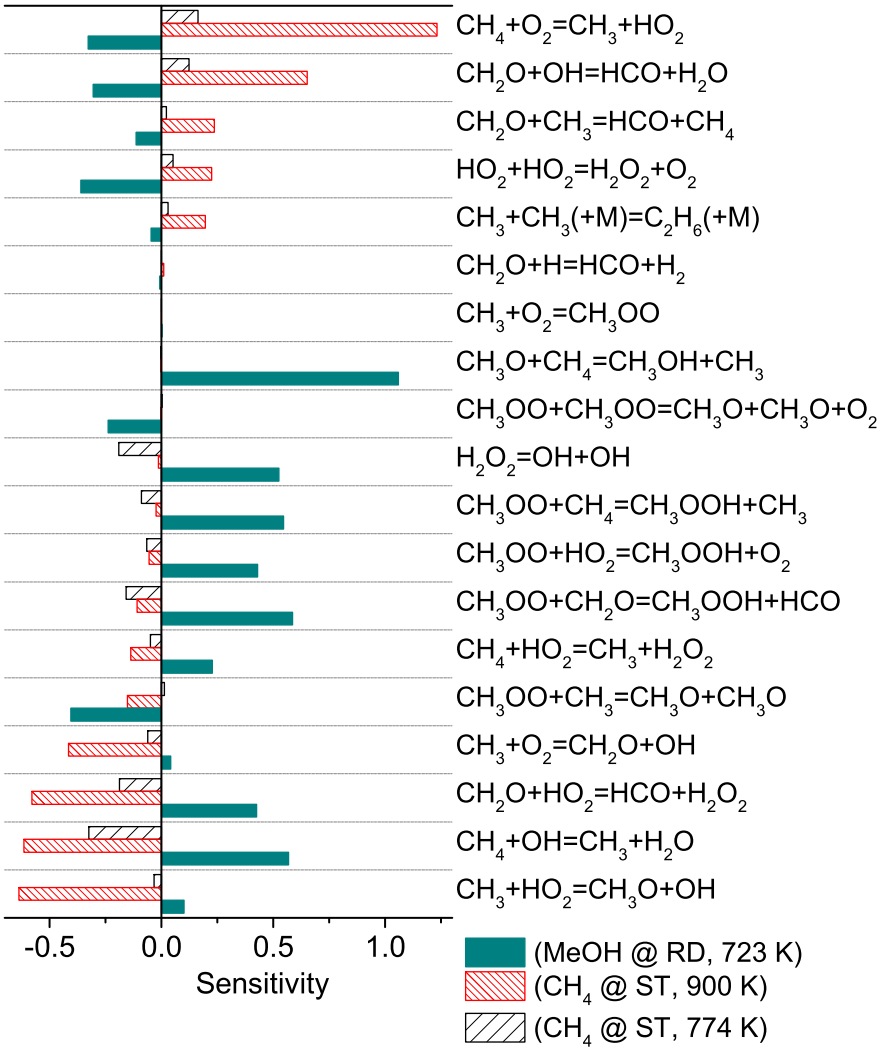

Figure 6.8: Sensitivity of CH_4 (under stoichiometric conditions) and methanol (under reducing conditions) mole fractions to the rate constants of selected reactions under the flow-reactor conditions. Pressure was 100 bar and only the isothermal part of the reactor was considered in simulations.

6.4.2 Comparison with literature data

The present chemical kinetic model is further evaluated by comparison to data available in literature. The model is used to reproduce the flow-reactor species profiles from earlier experiments in [32]. Ignition delay times and flame speeds are also used to assess the performance of the model at different temperatures and pressures.

6.4.2.1 Earlier results from the flow reactor

Rasmussen et al. [32] investigated the methane conversion in the same flow reactor used here. Figure 6.9 shows the results from their experiments under reducing conditions. The experiments gave the start of oxygen consumption at 775 K. The present model predicts the onset temperature of fuel conversion around 25 K lower than the experiments, but it reproduces well the concentrations of stable components above 800 K. Under stoichiometric (figure 6.10) and oxidizing (figure 6.11) conditions, the experiments gave the onset of fuel conversion at 785 and 775 K, respectively. The model predicts the ignition at 750 K for both stoichiometries. This premature ignition in simulations was also observed by Rasmussen et al. [32]. To address that, they included the effect of surface reactions by introducing a terminating reaction for CH_3OO radical over the wall surface. As the present model can reproduce well our recent results from the flow reactor, we refrain to implement a similar reaction in our model.

6.4.2.2 Ignition delay time in shock tubes

The oxidation of methane has been investigated for several years in shock tubes [21, 29–31, 33–35, 38, 75, 139, 220–224]. The residence time of gas in shock tubes is relatively short which makes it difficult to study ignition at low temperatures. Consequently, most of the measurements have been conducted at temperatures higher than those of this study. To evaluate the model at higher temperatures, selected experiments are simulated here.

Davidson and Hanson [33] measured the ignition delays of methane at pressures up to 156 atm and temperatures of 1137–1536 K. A selection of their results is shown in figure 6.12. As expected, ignition delay decreases by increasing pressure or temperature, and it is more sensitive to temperature. The ignition is faster in fuel-lean mixtures although they were diluted more (77% Ar) compared to the fuel-rich mixtures (67% Ar). The model compares well with the experimental results, especially at higher pressures.

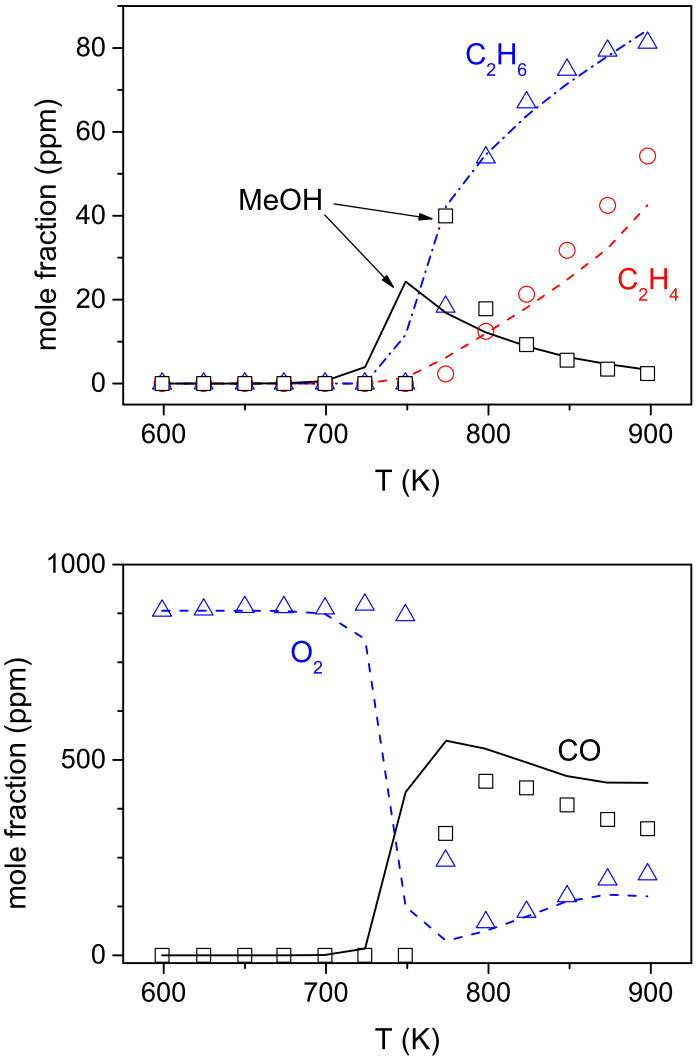

Figure 6.9: Comparison of the results from the experiments by Rasmussen et al. [32] and the prediction of the present model under reducing conditions (889 ppm O_2 + 1.12% CH_4 in N_2, Φ=25.2, 90 bar). The temperature profiles are inputted in the simulations.

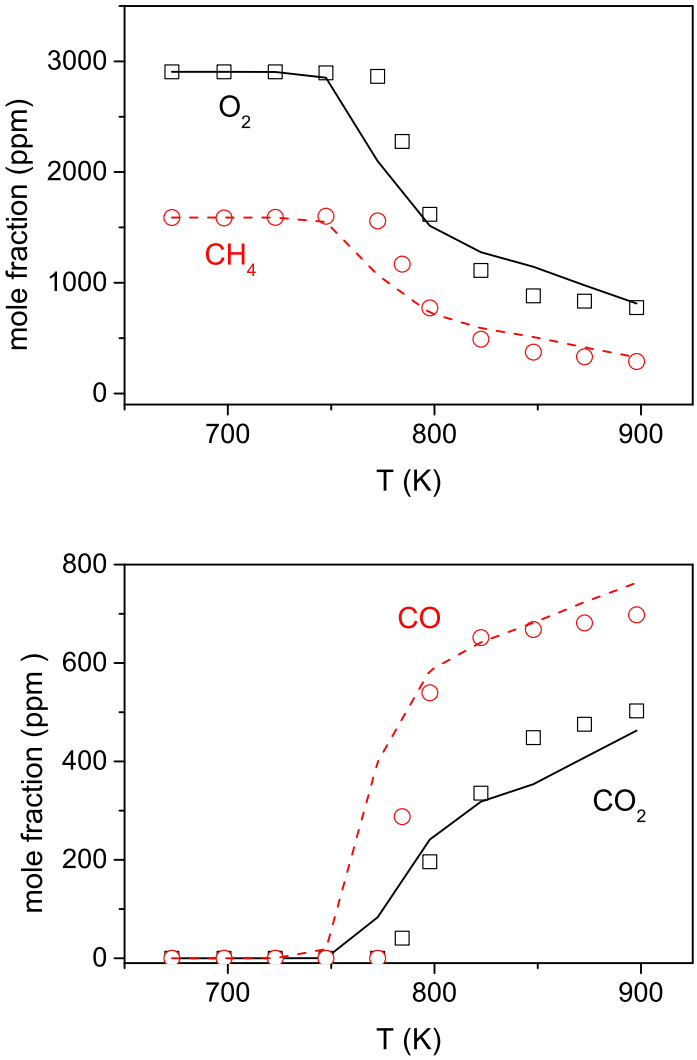

Figure 6.10: Comparison of the results from the experiments by Rasmussen et al. [32] and the prediction of the present model under stoichiometric conditions (2903 ppm O_2 + 1587 ppm CH_4 in N_2, Φ=1.09, 100 bar).

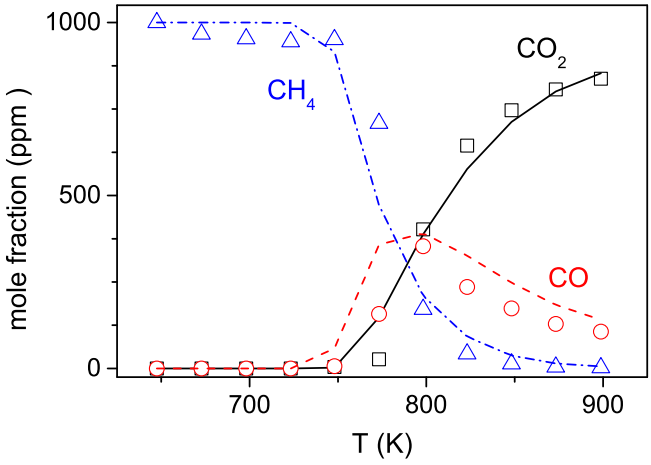

Figure 6.11: Comparison of the results from the experiments by Rasmussen et al. [32] and the prediction of the present model under oxidizing conditions (4.57% O_2 + 964 ppm CH_4 in N_2, Φ=0.042, 100 bar).

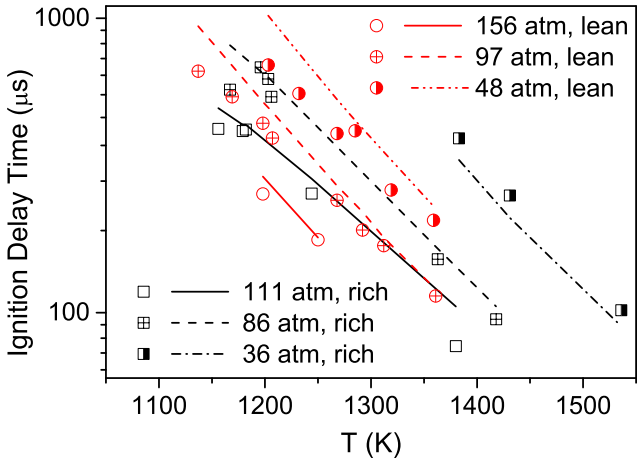

Figure 6.12: Ignition delay times of fuel-lean (3.8% CH_4+19.2% O_2 in Ar, Φ=0.4) and fuel-rich (20.0% CH_4+13.3% O_2 in Ar, Φ=3) mixtures. Symbols mark experimental results from Davidson and Hanson [33] and lines denotes the predictions of the present model. The simulations are conducted at fixed pressures while the pressure in the experiments fluctuated within ±10%.

The model prediction is compared against ignition delay data at higher pressure upon 456 atm, reported from shock-tube measurements by Zhukov et al. [29]. As shown in figure 6.13, increasing pressure accelerates ignition. The modeling results agree well with the measured data at 456 atm while the ignition delays are slightly over-predicted at 156 atm. Figure 6.13 also includes ignition delays measured at much lower pressures (6.9–8 atm) by Levy et al. [31]. There, the ignition is promoted by increasing the oxygen fraction in the mixture, as it was seen in the results of Davidson and Hanson [33]. Levy et al. [31] argued that excess oxygen accelerates the ignition by promoting the chain-branching reaction of R25 which is followed by another chain-branching reaction, R12. In contrast, redundant CH_4 inhibits ignition by promoting reaction R11 which competes over H radicals with the branching reaction of R1.

$$CH_3 + O_2 = CH_3O + O \quad \text{(R25)}$$

$$CH_4 + O = CH_3 + OH \quad \text{(R12)}$$

$$CH_4 + H = CH_3 + H_2 \quad \text{(R11)}$$

$$H + O_2 = O + OH \quad \text{(R1)}$$

Although the model overpredicts the ignition delays slightly, it can predict well the sensitivity to the stoichiometries.

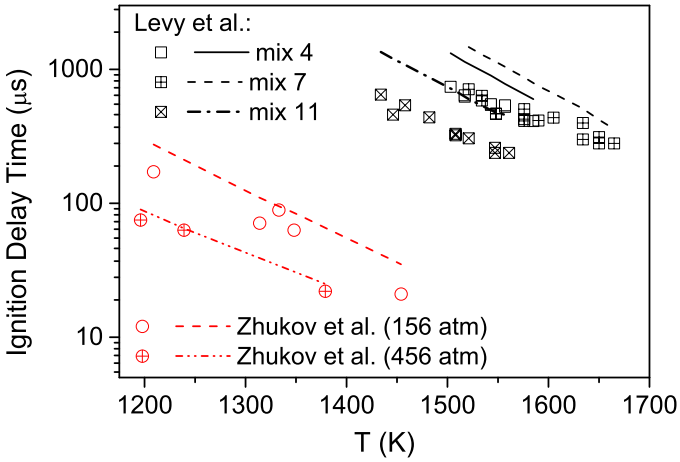

Figure 6.13: Ignition delay times of CH_4/air (Φ=0.5, from Zhukov et al. [29]) and CH_4/O_2 mixtures (from Levy et al. [31], mix 4: 3.53% CH_4 in N_2, 8 atm, Φ=1.01; mix 7: 4.0% CH_4 in N_2, 6.9 atm, Φ=1.33; mix 11: 1.99% CH_4 + 3.72% CO_2 in N_2, 7.7 atm, Φ=0.32). The simulations are conducted at fixed pressures while the pressure in the experiments fluctuated within ±10%.

The model is assessed at lower temperatures by comparing with data reported by Huang et al. [30] from shock-tube measurements over 1000–1350 K. According to figure 6.14, the model overpredicts the ignition delays, especially at lower temperatures. Generally the model prediction improves at higher pressures and higher temperatures, where ignition is faster. Simulating long ignition delay times (in order of millisecond) measured in shock tubes are vulnerable to non-idealities caused by neglecting the effects of flow compression and mixing [125]. Usually pressure and temperature increases gradually behind the shock wave. Such pressure/temperature rises are believed to be a result of fluid dynamic non-idealities, as they have been observed even for non-reactive mixtures [121]. To compensate for these device-dependent variations, the measured pressure history behind the shock wave should be included in simulations [121]. However, such data are not available for the measurements in [30].

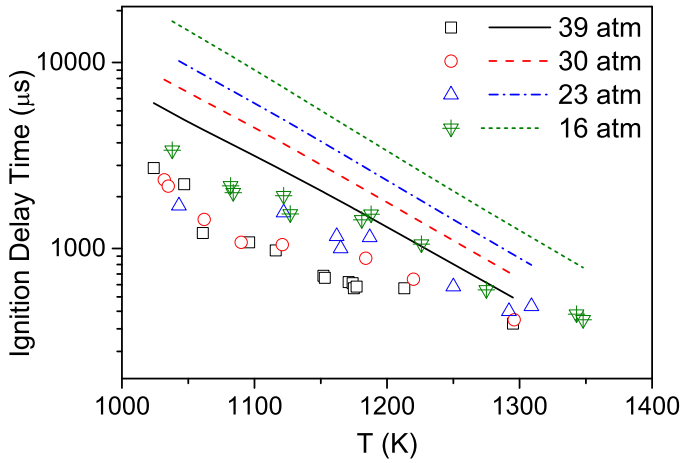

Figure 6.14: Ignition delay times of 9.5% CH_4 in N_2 (Φ=1) at different pressures. Symbols mark experimental results from Huang et al. [30] and lines denotes the predictions of the present model. The simulations are conducted at fixed pressures while the pressure in the experiments fluctuated within ±10%.

6.4.2.3 Flame speed

The laminar burning velocity of methane has been measured in several studies [11, 196, 225–229], but most of the published data have been limited to low pressures. Figure 6.15 shows the results of our simulations compared to the experimental data from literature. The flame speed decreases at elevated pressures. The model prediction is within the uncertainties of the measurements. The maximum of burning velocity was

measured in a slightly fuel-rich (Φ ~1.1) mixture for all pressures, and is well generated by using the present model.

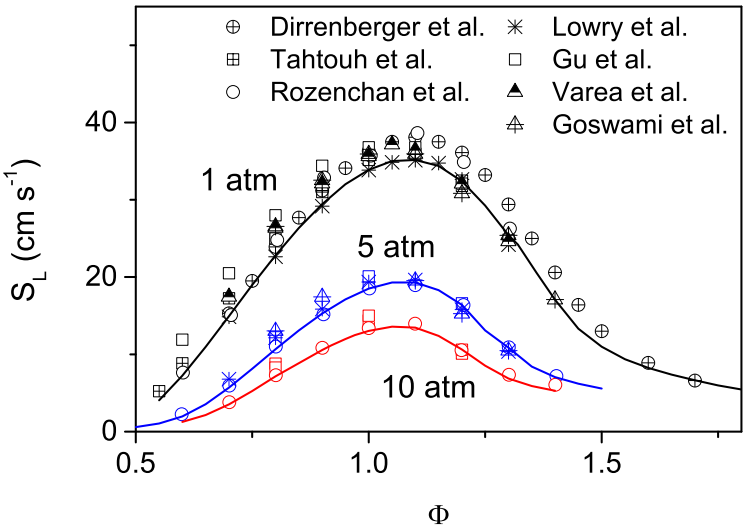

Figure 6.15: Laminar burning velocity of methane/air mixture at 1, 5, and 10 atm and initial temperature of 298–300 K. Symbols mark experimental results from Gu et al. [11], Dirrenberger et al. [225], Rozenchan et al. [196], Varea et al. [226], Goswami et al. [227], Tahtouh et al. [228], and Lowry et al. [229]. Lines denote the model prediction at specified pressures.

To identify sensitive reactions in predicting flame speed, the sensitivity of mass flow rate is calculated using the built-in functions of Chemkin [109]. Since the conditions at the inlet of the system is fixed, the mass flow rate sensitivity is linearly related to the flame speed sensitivity. Figure 6.16 shows the results of the analysis. The chain-branching reaction of

$$H + O_2 = O + OH \tag{R1}$$

controls the prediction of the methane flame speed to a great extent. This reaction is very efficient in branching radical chains, so competitor reactions in consuming H radicals show negative sensitivities.

The decomposition of HCO (R3) increases the flame speed whereas its reactions with one of H, OH, or O_2, slow down the flame propagation due to terminating the radical chain. The CO oxidation by OH (R44), the major source of heat release, is

among the reactions controlling the flame speed.

$$CO + OH = CO_2 + H \tag{R44}$$

Among methane reactions, the terminating reaction of

$$CH_3 + H(+M) = CH_4(+M) \tag{R10}$$

is the most sensitive one.

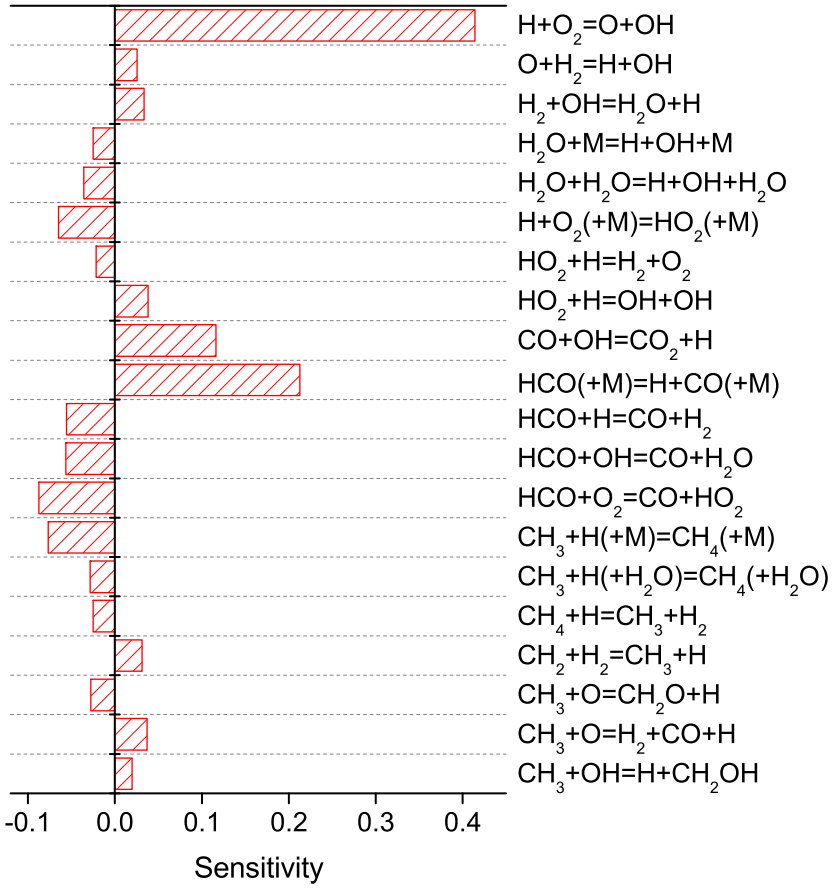

Figure 6.16: Sensitivity of laminar flame speed of methane/air at atmospheric pressure and initial temperature of 300 K under stoichiometric conditions.

Conclusion

Methane oxidation at high pressure (100 bar) and intermediate temperatures (600–900 K) has been investigated in a flow reactor. The onset temperature of methane reaction was found at 725–750 K, slightly depended on stoichiometry. A chemical kinetic model was developed and tested against the measurements. The model was able to predict well the onset temperature of reaction and the fractions of major stable species upon ignition. The results of sensitivity analyses showed that the partial oxidation of methane to methanol was highly sensitive to the oxidation chemistry of the methylperoxyl radical (CH_3OO) while the current data for this component are highly uncertain. The model compared well with measured ignition delay times and flame speeds from literature. The presented measurements extend the existing data for methane oxidation at high pressure and intermediate temperatures. Such data are vital in evaluating chemical kinetic models. Models validated at this range of temperatures and pressure are more likely to be useful in the design and optimization of engines and other devices involving combustion at high pressures. Further studies on methylperoxyl reactions are necessary for better understanding methane oxidation at high pressures and intermediate temperatures.

Chapter 7

Ethane

Abstract

Ethane oxidation at intermediate temperatures (600–900 K) and high pressures (20–100 bar) has been investigated in a laminar flow reactor. The measurements revealed the onset temperature of ethane reaction between 700 K and 825 K, depending on pressure and stoichiometry. At 20 bar, the fuel conversion was detected above 775 K under reducing conditions and above 825 K for stoichiometric and oxidizing conditions. Increasing pressure to 50 bar facilitated ignition at 750, 775, and 800 K for reducing, stoichiometric, and oxidizing conditions, respectively. Further increase of pressure to 100 bar gave ignition at 700 K for reducing and 750 K for other conditions. A detailed chemical kinetic model was developed and evaluated against data from the present work as well as from literature. The modeling results agreed well with most measurements but the onset of reaction in the flow reactor was predicted prematurely at high pressure under reducing conditions. Future work should be focused on improving the model prediction of ignition delay time as well as the flame speed of ethane.

7.1 Introduction

The investigation of ethane oxidation at high pressure and intermediate temperature is important from fundamental as well as practical perspectives. From a practical point of view, knowledge about the combustion behavior of ethane is essential because ethane is the major non-methane component in natural gas, and variations in ethane fraction in natural gas may result in significant changes in the ignition properties of the fuel [36]. These changes can result in undesired autoignition of the end gas in spark–

ignited engines, known as knock, leading to damage to the engine and increase in pollutant emissions. Moreover, information about the oxidation behavior is relevant to the performance and development of HCCI engines [230] and gas turbines [231]. From a fundamental perspective, the oxidation of C_2H_6 plays an important role in the hierarchical structure of the reaction mechanisms of hydrocarbon fuels. In order to verify and develop these chemical kinetic models for hydrocarbon oxidation, measurements of combustion characteristics at high pressure are essential.

Figure 7.1 represents a selection of available data for ethane oxidation at high pressures and intermediate temperatures. While the hydrocarbons ignition even at high temperatures relies on medium–temperature chemistry, this range of temperature was rarely covered by previous work.

Measured species profiles are useful as benchmarks in evaluating chemical kinetic models. Flow and jet-stirred reactors are suitable devices to measure species profiles, especially for relatively slow oxidation when long residence times are needed. Hunter et al. [46] studied ethane oxidation over temperatures of 915–966 K and pressures up to 10 atm in a flow reactor. A jet-stirred reactor was used by Dagaut et al. [232] to study ethane oxidation at temperatures of 800–1200 K and pressures of 1–10 atm. Beerer and McDonell [233] evaluated the ignition delay of ethane in a flow reactor over temperatures of 785–935 K and pressures of 7–15 atm.

The species profiles can also be measured in shock tubes. Tranter et al. [44] studied the pyrolysis and oxidation of ethane behind a reflected shock at pressures as high as 340 and 613 bar over temperatures of 1050–1450 K. Using a GC, they measured major stable products, i.e. C_2H_6, C_2H_4, C_2H_2 and CO. In other work from the same laboratory [45, 234] the measurements were extended to 40 and 1000 bar.

The ignition delay time, another useful tool to evaluate models, has been measured for ethane for years [21, 37–43, 84, 233], but few of the studies were under conditions relevant to engines. Bowman [37] measured the ignition delay of ethane for the first time by monitoring infrared emission from CO_2, CO, and H_2O. Later, Burcat et al. [38] measured the autoignition delay of ethane over 1204–1690 K and 8–10 bar in a shock tube. In a later work by Burcat et al. [39], temperatures of 1235–1660 K and pressures of 2–8 bar were covered. Lamoureux et al. [42] quantified ignition delays in a wide range of temperatures (1200–2700 K), pressures (1–18 bar), and equivalence ratios. Vries et al. [43] explored ignition delays at 1218–1860 K and 0.6–3.0 atm. More recently, Aul et al. [21] collected the ignition delays of ethane over 1082–1304 K at pressures below

~16 atm. Tests by Zhang et al. [84] at 1216–1360 K and 21 atm extended the benchmark to higher pressures, which are still far below the pressure in many devices involving combustion.

There have been a few chemical kinetic models for ethane oxidation. Nötzold and Algermissen [235] developed a model for ethane oxidation and tested it against high temperature data. Dagaut et al. [232] interpreted their results from a jet-stirred reactor into a chemical kinetic model. Naik and Dean [236] suggested a model for the oxidation of ethane at high pressure and evaluated it against available data up to that date. In a previous study from this laboratory [32], a kinetic model for the oxidation of CH_4 and C_2H_6 was suggested and evaluated against the results of high-pressure flow-reactor experiments while the C_2H_6 to CH_4 ratio was limited to 13% at maximum.

To extend the existing data toward conditions relevant to engines and gas turbines, this paper reports the results of ethane oxidation experiments in a laminar flow reactor at pressures of 20–100 bar and temperatures of 600–900 K under a wide range of stoichiometries. A chemical kinetic model based on previous work from the same laboratory in ref [1, 32, 102, 178, 179, 237] is proposed and evaluated by comparison to the present data as well as to data published in literature.

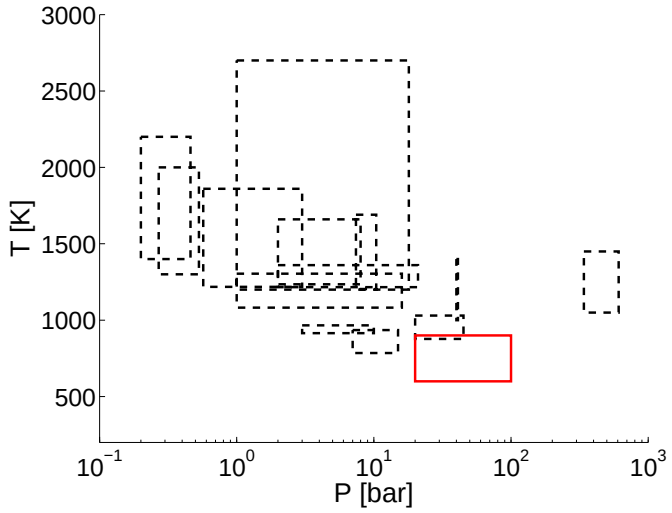

Figure 7.1: The temperature- and pressure-coverage of earlier experiments and the present ones. Dashed lines: the previous measurements in ref [37–46], red dash–dotted lines: the present measurement of species profile in the flow reactor.

7.2 Experimental approach

The experimental setup was a laboratory-scale high-pressure laminar-flow reactor designed to approximate plug flow. The setup was described in detail elsewhere [102] and only a brief description is provided here. The system was used here for the investigations of ethane oxidation chemistry at pressures from 20 to 100 bar, temperatures up to 900 K, and flow rate of ~ 3 Nliter/min (STP; 1 atm and 273.15 K).

The reactions took place in a tubular quartz reactor (inner diameter of 8 mm), enclosed in a stainless steel tube that acted as a pressure shell. Using a quartz tube and conducting experiments at high pressure are expected to minimize the contribution from heterogeneous reactions at the reactor wall. The steel tube was placed in a tube oven with three individually controlled electrical heating elements that produced an isothermal reaction zone in the middle of the reactor. A moving thermocouple was used to measure the temperature profile inside the pressure shell wall after stabilizing the system. The system was pressurized from the feed gas cylinders. The reactor pressure was monitored upstream of the reactor by a differential pressure transducer and controlled by a pneumatic pressure valve positioned after the reactor. The pressure fluctuations were less than 0.2 % during the experiments. The reactant gases were premixed before entering the reactor. All gases used in the present experiments were high purity gases or mixtures with certified concentrations (±2% uncertainty). Downstream of the reactor, the system pressure was reduced to atmospheric level prior to product analysis, which was conducted by an on-line *6890N Agilent Gas Chromatograph* (GC-TCD/FID from Agilent Technologies). All GC sampling and measurements were repeated at least two times to reduce measurement uncertainties. Distinguishing methanol from acetaldehyde was not possible due to signal overlapping in the GC. The signal areas corresponding to the sum of these components were measured and quantified by using the response factor of methanol, but the reported quantity was less accurate especially when a considerable acetaldehyde yield was expected.

The plug flow assumption was shown by Rasmussen et al. [102] to be a good approximation for the present operating conditions. Figure 7.2 shows the measured temperature profiles for different isotherms while the flow was pure nitrogen. It was found that considering the temperature profiles promote the accuracy of simulations. Therefore, a plug flow model with constrained temperature and pressure was used for simulations in Chemkin [109]. Temperature profiles measured at different pressures

revealed the sensitivity of temperature profiles to the system pressure, most likely due to fluctuations in nitrogen supply of the pressure shell at higher pressures. Therefore separate temperature profiles for each pressure are provided in supplementary materials. A source of uncertainty in determining gas temperature was the exothermicity of reactions. Due to the high level of dilution, this effect was limited. Simulations in Chemkin [109] with a constant pressure and enthalpy (adiabatic) model lead to maximum 22 K temperature rise. However, because of the fast heat transfer from hot gases to the pressure shell, especially in such a narrow reactor, the deviation of the gas temperature from the measured temperature should be even smaller.

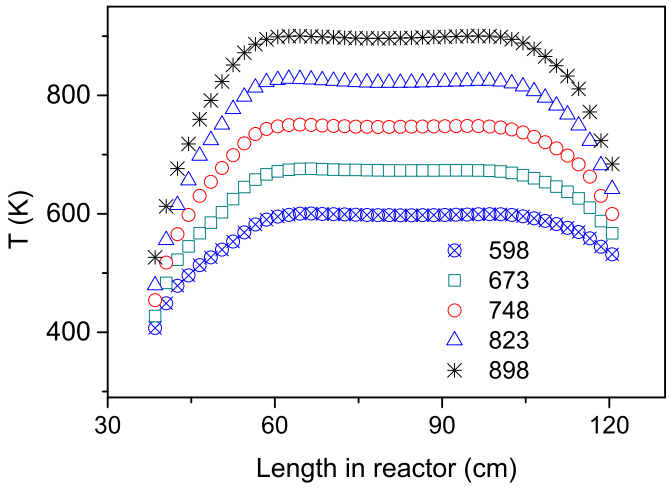

Figure 7.2: Measured temperature profiles across the reaction zone. The flow rate was 3 NL/min at pressure of 30 bar. The isothermal zone shrunk slightly at higher pressures.

7.3 Chemical kinetic model

In a previous study from this laboratory [32], a chemical kinetic model for combustion of CH_4 and C_2H_6 was suggested and evaluated against the experimental data at high pressures for the mixtures of C_2H_6 and CH_4. The present experiments on the oxidation of neat ethane make further evaluation of the model possible. Moreover, recent advances in the oxidation chemistry of hydrogen as well as C_1 species encouraged the authors to update the model thoroughly in ref [1, 237]. Here, the reactions of ethane subset which are important under investigated conditions, are reviewed and more accurate rate constants are implemented whenever possible.

The dissociation of ethane (R1) can initiate pyrolysis/oxidation at high tempera-

tures. At the temperatures of this study, this reaction is more favored in the reverse direction and it acts as a chain-termination path.

$$CH_3 + CH_3(+M) = C_2H_6(+M) \quad \text{(R1)}$$

At pressures of this study, the rate constant of this reaction approaches its high-pressure limit. A theoretical calculation of the high-pressure limit of this reaction by Klippenstein et al. [238] yielded a slight negative temperature dependency, it decreased by 30% as temperature rose from 700 to 1000 K. This trend is in line with most of earlier measurements (see details in ref [238]), so we replace the earlier temperature-independent rate constant from Baulch et al. [136] by this recent one.

The H-abstraction by a hydrogen atom from ethane (R2) has a relatively large barrier (~5.1 kcal/mol [239]), so it is mostly favored at high temperatures.

$$C_2H_6 + H = C_2H_5 + H_2 \quad \text{(R2)}$$

For this reaction, we rely on the results of Sivaramakrishnan et al. [239] who measured the rate of this reaction in a shock tube at 1128–1299 K and extrapolated the rate constant to 300–2000 K using transition-state theory calculations and earlier measurements. The adopted rate constant has a higher sensitivity to temperature comparing to an earlier one by Baulch et al. [136]. Whereas both rate constants are close at 600 K, the value in [239] is 4.6 times larger than the other one, at 2000 K.

Ethane oxidation at intermediate temperatures highly depends on the H-abstraction by OH radicals (R3).

$$C_2H_6 + OH = C_2H_5 + H_2O \quad \text{(R3)}$$

The lower barrier of this reaction (~0.7 kcal/mol [240]) compared to R2 facilitates its progress at medium temperatures. Here, the rate of this reaction is taken from a study by Krasnoperov and Michael [240] whose rate constant agrees well to earlier determinations.

Ethane oxidation at intermediate temperatures is initiated by the reaction between ethane and molecular oxygen (R5).

$$C_2H_6 + O_2 = C_2H_5 + HO_2 \quad \text{(R5)}$$

For this reaction, we relied on calculations by Sharipov and Starik [241] giving a rate constant around 40% lower (at 700 K) than the Baulch et al. [136] estimation.

The reaction between ethane and methyl radicals can be important under reducing conditions.

$$C_2H_6 + CH_3 = C_2H_5 + CH_4 \quad \text{(R6)}$$

Our preferred rate constant for this reaction is taken from shock tube measurements by Peukert et al. [242] at 1153–1297 K. Presuming immediate dissociation of C_2H_5 to C_2H_4 + H at investigated temperatures, Peukert et al. [242] quantified the rate of the title reaction by measuring H-atom concentration and using TST calculations.

The ethyl radical mainly combines with other radicals or adds to molecular oxygen. The ethyl reactions with hydroxyl radicals (R9, R10) as well as with HCO (R11) were studied theoretically by Labbe et al. [243] and their calculated pressure-dependent rate constants are adopted in this work.

$$C_2H_5 + OH(+M) = C_2H_4 + H_2O(+M) \quad \text{(R9)}$$
$$C_2H_5 + OH(+M) = CH_3 + CH_2OH(+M) \quad \text{(R10)}$$
$$C_2H_5 + HCO(+M) = CH_3 + CH_2CHO(+M) \quad \text{(R11)}$$

The main consumption path of the ethyl radical at intermediate temperatures is its addition to molecular oxygen.

$$C_2H_5 + O_2(+M) = CH_3CH_2OO(+M) \quad \text{(R12)}$$
$$= CH_2CH_2OOH(+M) \quad \text{(R13)}$$
$$= C_2H_4 + HO_2(+M) \quad \text{(R14)}$$
$$= cC_2H_4O + OH(+M) \quad \text{(R15)}$$

For this reaction, we rely on calculations by Klippenstein [244] who derived pressure-dependent rate constants for different branches of this reaction.

The ethylperoxyl radicals (CH_3CH_2OO) may isomerize internally to CH_2CH_2OOH

or dissociate to either $C_2H_4 + HO_2$ or $cC_2H_4O + OH$ [244].

$$CH_3CH_2OO(+M) = CH_2CH_2OOH(+M) \quad \text{(R16)}$$
$$= C_2H_4 + HO_2(+M) \quad \text{(R17)}$$
$$= cC_2H_4O + OH(+M) \quad \text{(R18)}$$

The rate constants for these steps are taken from calculations by Klippenstein [244].

The ethylperoxyl radical (CH_3CH_2OO) may abstract hydrogen from stable molecules e.g. CH_4 and CH_3OH, or combine with other radicals. In the absence of measurements or theoretical determinations, these steps are estimated by analogy to the reactions of CH_3OO.

Hydroxyalkyl radicals (QOOH) generally add to molecular oxygen to give OOQOOH at medium temperatures [119], so a probable reaction for CH_2CH_2OOH is

$$CH_2CH_2OOH + O_2(+M) = OOCH_2CH_2OOH(+M)$$

where CH_2CH_2OOH is mainly produced from isomerization of CH_3CH_2OO in R16. However, for small alkyls such as methyl and ethyl, it is not an important route in oxidation [176]. In fact, the hydroxyethyl radical (CH_2CH_2OOH) mainly dissociates to oxirane (cC_2H_4O) via R20 or ethene via R19.

$$CH_2CH_2OOH(+M) = C_2H_4 + HO_2(+M) \quad \text{(R19)}$$
$$= cC_2H_4O + OH(+M) \quad \text{(R20)}$$

Both channels for CH_2CH_2OOH dissociation are taken from a theoretical study by Klippenstein [244].

H-abstraction by CH_3CH_2OO from stable molecules gives ethyl hydroperoxide radical (CH_3CH_2OOH). The ethyl hydroperoxide radical can combine with other radicals or dissociate. For combination with radicals, we estimated the rate constant by analogy to CH_3OOH reactions. For the decomposition of ethyl hydroperoxide (R21), the preferred rate constant is from a theoretical determination by Chen et al. [245]. Among the investigated channels by Chen et al. [245], only CH_3CH_2O+OH is important under combustion related conditions and is implemented in this work.

$$CH_3CH_2OOH(+M) = CH_3CH_2O + OH(+M) \quad \text{(R21)}$$

Ethene is mainly produced from R14 and R17. The reaction between ethene and a hydroxyl radical was investigated theoretically by Senosiain et al. [246] who found that the direct hydrogen abstraction (R22) to form vinyl radicals (C_2H_3) should be the major channel at medium to high temperatures.

$$C_2H_4 + OH(+M) = C_2H_3 + H_2O(+M) \quad \text{(R22)}$$
$$= CH_3 + CH_2O(+M) \quad \text{(R23)}$$
$$= CH_3CHO + H(+M) \quad \text{(R24)}$$
$$= CH_2CHOH + H(+M) \quad \text{(R25)}$$
$$= CH_2CH_2OH(+M) \quad \text{(R26)}$$

More recently, Vasu et al. [247] measured the overall rate of the title reaction over 973–1438 K and pressures of 2–10 atm. At temperatures as high as in [247], the branch to C_2H_3 is expected to be dominant, so the decay rate of OH should give the rate of this branch. Adjusting TST calculations according to their measured values of OH decay, Vasu et al. [247] suggested a rate constant for C_2H_3 branch around 50 % higher (at 800 K) than Senosiain et al. [246]. However, the experiments in [247] could not determine the contribution of other channels. Here we adopt the pressure-dependent rate constants by Senosiain et al. [246] while measurements clarifying the branching ratio of the title reaction are warranted.

One of consumption pathways of vinyl radicals is its reaction with formaldehyde.

$$C_2H_3 + CH_2O(+M) = C_2H_4 + HCO(+M) \quad \text{(R27)}$$

The rate constants of this reaction is taken from a work by Goldsmith et al. [248].

Table 7.1: Selected reactions from ethane oxidation mechanism. The rate constants are in the form of $k = AT^n \exp\left(\frac{-E}{RT}\right)$. Units are *mol*, *cm*, *K*, *s*, and *cal*.

	Reaction	A	n	E	Note/Ref.
R1	$CH_3 + CH_3(+ M)=C_2H_6(+ M)$	9.46E+14	-0.54	179	[238]
	Low-pressure limit:	1.27E+41	-7.00	2762	
	Troe parameters: 0.62 73 1180 1.E30				
R2	$C_2H_6 + H=C_2H_5 + H_2$	7.35E+03	3.10	5340	[239]
	duplicate rate constant	3.26E+14	0.00	13667	
R3	$C_2H_6 + OH=C_2H_5 + H_2O$	1.61E+06	2.22	741	[240]
R4	$C_2H_6 + HO_2=C_2H_5 + H_2O_2$	1.10E+05	2.50	16850	[136]
R5	$C_2H_6 + O_2=C_2H_5 + HO_2$	2.92E+07	1.90	49548	[238]
R6	$C_2H_6 + CH_3=C_2H_5 + CH_4$	3.45E+01	3.44	10384	[238]
R7	$CH_3 + CH_3=C_2H_5 + H$	5.40E+13	0.00	16055	[136]
R8	$C_2H_4 + H(+ M)=C_2H_5(+ M)$	1.40E+09	1.46	1355	[249]
	Low-pressure limit:	2.00E+39	-6.64	5769	
	Troe parameters: -0.569 299 9147 152.4				
R9	$C_2H_5 + OH=C_2H_4 + H_2O$	4.70E+18	-1.58	7999	[243] , [a]
R10	$C_2H_5 + OH=CH_3 + CH_2OH$	6.50E+22	-2.44	12647	[243] , [a]
R11	$C_2H_5 + HCO=CH_3 + CH_2CHO$	6.50E+22	-2.44	12647	[243] , [a]
R12	$C_2H_5 + O_2=CH_3CH_2OO$	2.91E+27	-4.72	5184	[244] , [a]
R13	$C_2H_5 + O_2=CH_2CH_2OOH$	2.78E+13	-1.14	7725	[244] , [a]
R14	$C_2H_5 + O_2=C_2H_4 + HO_2$	1.35E+10	0.49	6247	[244] , [a]
R15	$C_2H_5 + O_2=cC_2H_4O + OH$	6.44E+13	-0.87	12430	[244] , [a]
R16	$CH_3CH_2OO=CH_2CH_2OOH$	3.36E+08	0.53	28900	[244] , [a]
R17	$CH_3CH_2OO=C_2H_4 + HO_2$	6.69E+23	-3.62	34110	[244] , [a]
R18	$CH_3CH_2OO=cC_2H_4O + OH$	6.66E+28	-5.29	43880	[244] , [a]
R19	$CH_2CH_2OOH=C_2H_4 + HO_2$	3.73E+22	-3.15	19180	[244] , [a]
R20	$CH_2CH_2OOH=cC_2H_4O + OH$	4.86E+20	-2.71	16440	[244] , [a]
R21	$CH_3CH_2OOH=CH_3CH_2O + OH$	1.38E+33	-5.27	48696	[245], [a]
R22	$C_2H_4 + OH=C_2H_3 + H_2O$	1.30E-01	4.20	-860	[246] , [a]
R23	$C_2H_4 + OH=CH_3 + CH_2O$	2.76E+13	-0.50	11455	[246] , [a]
R24	$C_2H_4 + OH=CH_3CHO + H$	6.80E+09	0.81	13867	[246] , [a]
R25	$C_2H_4 + OH=CH_2CHOH + H$	8.55E+10	0.75	11491	[246] , [a]
R26	$C_2H_4 + OH=CH_2CH_2OH$	6.02E+37	-7.44	14269	[246] , [a]
	duplicate rate constant	2.79E+19	-2.41	1011	
R27	$C_2H_3 + CH_2O=C_2H_4 + HCO$	3.31E+14	-0.87	10966	[248] , [a]

[a] at 100 atm pressure. For other pressures see the mechanism file in the supplementary materials.

7.4 Results and Discussion

7.4.1 Ethane oxidation in the flow reactor

The major aim of this work was to characterize ethane oxidation at high pressures and intermediate temperatures. The results from the flow-reactor measurements at temperatures of 600–900 K and pressures of 20–100 bar are presented in this section. The volumetric flow rate was ~3 Nl/min in all experiments. The gas residence time at the isothermal part of the reactor was estimated to be 3–4 s, 7–10 s, and 14–22 s for pressures of 20, 50, and 100 bar, respectively. For simulations, the temperature profiles (provided as supplementary materials) were implemented to improve accuracy.

The tests were carried out on stoichiometric, strong reducing, and very oxidizing mixtures. Evaluating models under intense fuel-rich and fuel-lean conditions can reveal the deficiency of reaction rate constants which are only sensitive under specific circumstances. Ignition under reducing conditions can also be practically important since in diesel engines combustion starts in a fuel-rich zone.

Figure 7.3 presents the results of experiments for fuel-rich mixtures (ϕ=37–47) at the pressures of 20, 50, and 100 bar. The fuel consumption starts at 775 K at 20 bar pressure. Ethene and to a lesser extent CO and CH_4 are major products. Increasing pressure to 50 and then 100 bar gives the onset temperatures of fuel conversion as 750 and 700 K, respectively. While the gas residence time at the isothermal zone of the reactor increases ~5 times when pressure is increased from 20 to 100 bar, the high-temperature fuel conversion is inhibited by increasing pressure, which is also reflected in the lower yield of C_2H_4. As outlined earlier, separating methanol and acetaldehyde is not possible due to GC signals overlapping, so the total yield of methanol plus acetaldehyde is quantified. The yield of methanol plus acetaldehyde first increases but soon decreases with increasing temperature and it is independent of pressure at high temperatures.

The model predictions under reducing conditions are also shown in figure 7.3. The model yields the onset temperature of the fuel conversion slightly lower (~25 K) than that by the measurements at 20 and 50 bar. At 100 bar, this gap between the model and the experiments grows to 50 K. However, the model prediction improves at higher temperatures at all investigated pressures. Above 775 K, the model agrees reasonably with the measurements of major species except CO, which is overpredicted twofold

by the model. Although the model underestimates the oxygenates (methanol plus acetaldehyde) at 100 bar, it captures well their variations at lower pressures.

For stoichiometric mixtures (ϕ=0.81–0.91), the onset of fuel oxidation is shifted to higher temperatures of 825, 775, and 750 K for pressures of 20, 50, and 100 bar, respectively (figure 7.4). The major products are measured as CO, CO_2 and C_2H_4, while C_2H_4 disappears by increasing temperature. In contrast to reducing conditions, here increasing pressure (and gas residence time) enhances oxidation at high temperatures. The model compares well with measurements under stoichiometric conditions and the onset of reaction as well as the fractions of the major products are predicted accurately.

For fuel-lean mixtures (ϕ= 0.034–0.038), the fuel oxidation starts at temperatures close to those found for stoichiometric mixtures (figure 7.5). Here, the major products are CO and CO_2, and the fuel oxidation is enhanced by increasing pressure (and consequently gas residence time). Similar to stoichiometric conditions, C_2H_4 peaks at intermediate temperatures and disappears at higher temperatures. The model predicts accurately the onset temperature of oxidation as well as the products composition.

From the present experiments, it can be seen that when pressure is increased the fuel oxidation starts at lower temperatures. This is in line with earlier results by Hunter et al. [46] who studied ethane oxidation at pressures up to 10 atm and temperatures ~925 K. The same trend was also found by Rasmussen et al. [32] for mixtures of methane and ethane.

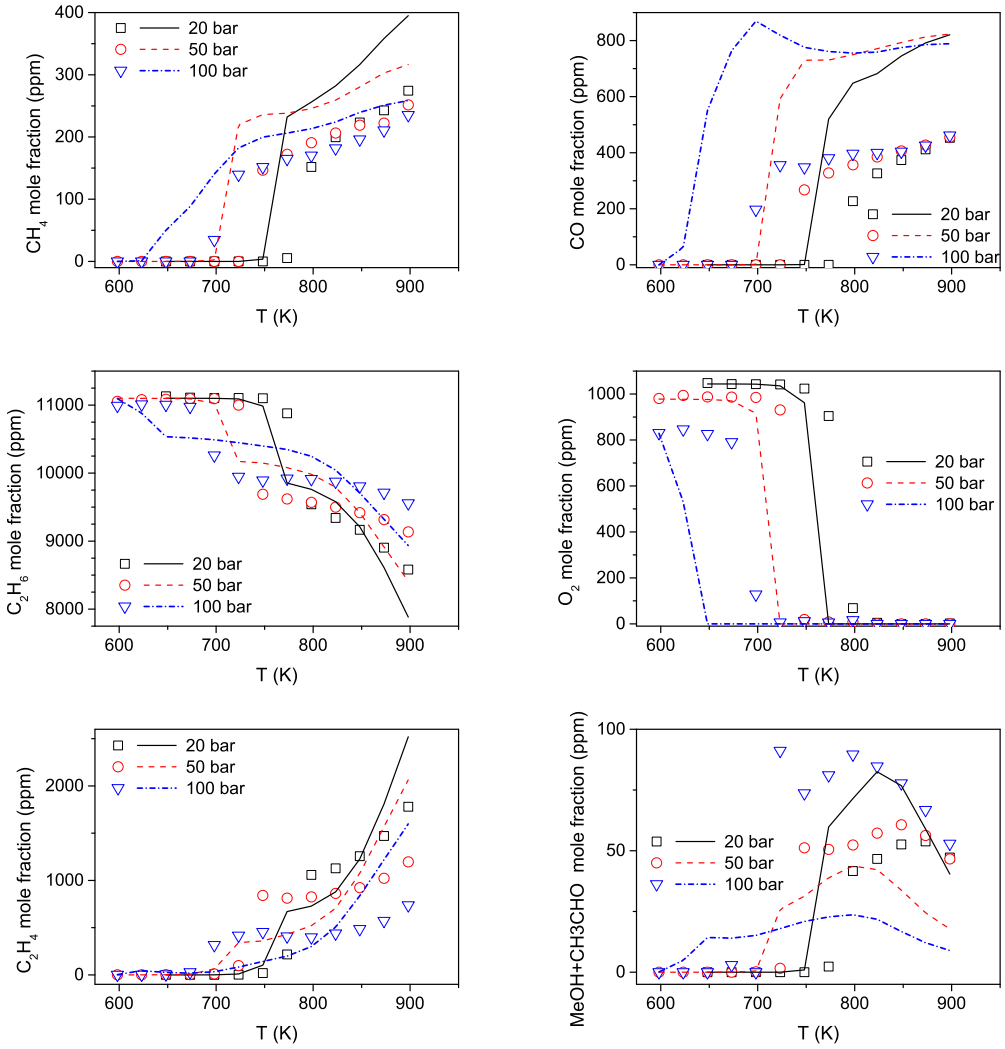

Figure 7.3: Results of experiments under reducing conditions at 20 bar (ϕ=37.2, 11130/1044 ppm of C_2H_6/O_2), 50 bar (ϕ=39.7, 11055/978 ppm of C_2H_6/O_2), and 100 bar (ϕ=46.6, 10990/834 ppm of C_2H_6/O_2). All mixtures are diluted in nitrogen. Symbols mark experimental results and lines denote predictions of the present model.

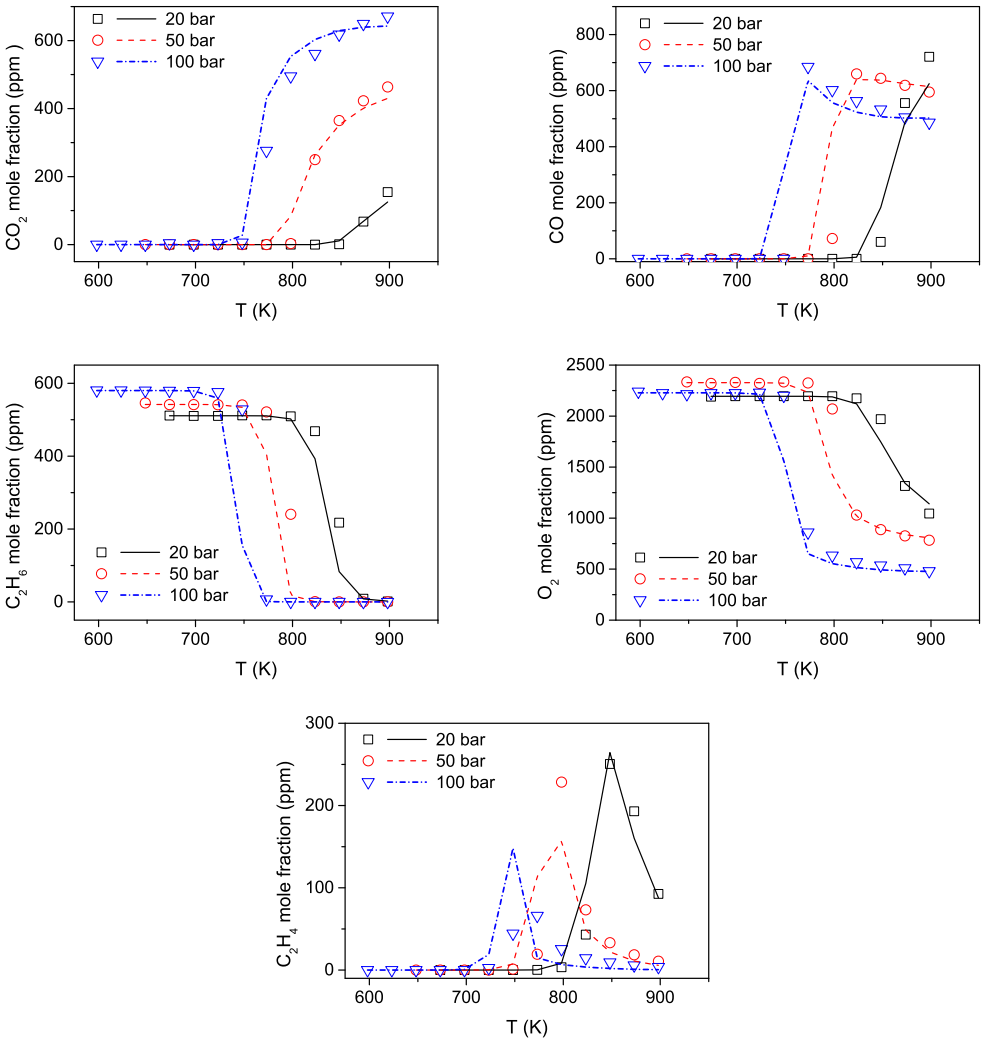

Figure 7.4: Results of experiments under stoichiometric conditions at 20 bar (ϕ=0.82, 511/2194 ppm of C_2H_6/O_2), 50 bar (ϕ=0.81, 542/2328 ppm of C_2H_6/O_2), and 100 bar (ϕ=0.91, 580/2228 ppm of C_2H_6/O_2). All mixtures are diluted in nitrogen. Symbols mark experimental results and lines denote predictions of the present model.

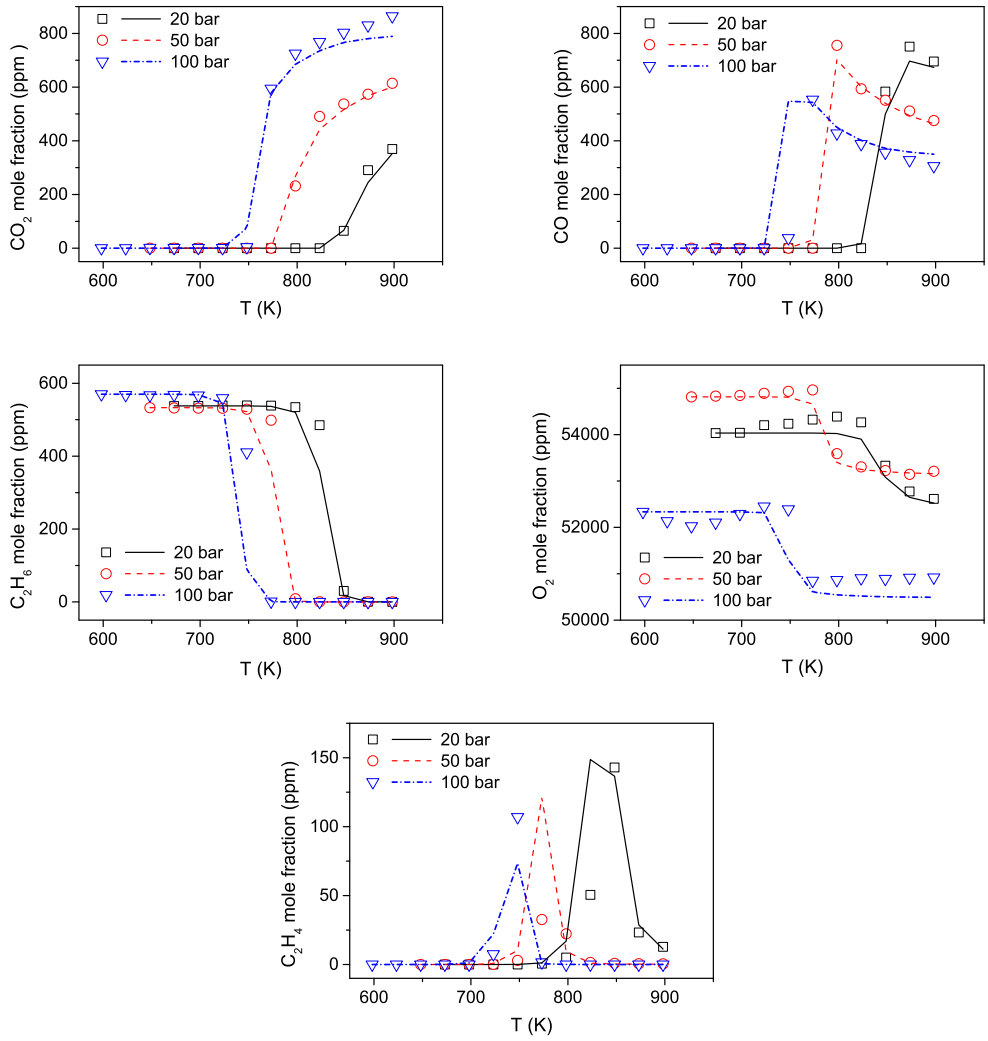

Figure 7.5: Results of experiments under oxidizing conditions at 20 bar (ϕ=0.035, 538/54035 ppm of C_2H_6/O_2), 50 bar (ϕ=0.034, 533/54815 ppm of C_2H_6/O_2), and 100 bar (ϕ=0.038, 570/52335 ppm of C_2H_6/O_2). All mixtures are diluted in nitrogen. Symbols mark experimental results and lines denote predictions of the present model.

The reaction pathways for ethane consumption at 100 bar and 600–900 K are shown in figure 7.6. The first step in ethane oxidation is H-abstraction by OH (R3) to form an ethyl radical, as expected at intermediate temperatures. At the early stages of oxidation, the abstraction by HO_2 (R4) is important too.

$$C_2H_6 + OH = C_2H_5 + H_2O \quad \text{(R3)}$$

$$C_2H_6 + HO_2 = C_2H_5 + H_2O_2 \quad \text{(R4)}$$

Under reducing conditions, the produced ethyl radical abstracts hydrogen from HO_2 to form an ethoxy radical (CH_3CH_2O).

$$C_2H_5 + HO_2(+M) = CH_3CH_2O + OH(+M) \quad \text{(R28)}$$

The ethoxy radical then dissociates to give formaldehyde.

$$CH_3CH_2O(+M) = CH_2O + CH_3(+M) \quad \text{(R29)}$$

For other stoichiometries, the ethyl radical adds to molecular oxygen (R12) to give CH_3CH_2OO which dissociates (R17) to ethene and a hydroperoxyl radical.

$$C_2H_5 + O_2(+M) = CH_3CH_2OO(+M) \quad \text{(R12)}$$

$$CH_3CH_2OO(+M) = C_2H_4 + HO_2(+M) \quad \text{(R17)}$$

Ethene mainly reacts with OH to give either CH_2CH_2OH or C_2H_3,

$$C_2H_4 + OH(+M) = CH_2CH_2OH(+M) \quad \text{(R26)}$$

$$C_2H_4 + OH(+M) = C_2H_3 + H_2O(+M) \quad \text{(R22)}$$

Then CH_2CH_2OH and the vinyl radical (C_2H_3) react with molecular oxygen,

$$CH_2CH_2OH + O_2(+M) = HOCH_2CH_2OO(+M) \quad \text{(R30)}$$

$$C_2H_3 + O_2(+M) = CH_2O + HCO(+M) \quad \text{(R31)}$$

while $HOCH_2CH_2OO$ dissociates to give formaldehyde.

$$HOCH_2CH_2OO(+M) = CH_2O + CH_2O + OH(+M) \quad \text{(R32)}$$

Another path for ethene consumption becomes important at higher temperatures and under reducing conditions,

$$C_2H_4 + HO_2(+ M) = CH_2CH_2OOH(+ M) \qquad \text{(R33-rev)}$$

which gives CH_2CO after a few intermediate steps.

The reaction pathways found here are different from the general pathways suggested for alkanes [119], as the isomerization of CH_3CH_2OO to CH_2CH_2OOH (R16) is not favored here. Instead, CH_3CH_2OO dissociates to $C_2H_4 + HO_2$ (R17). In fact, the CH_2CH_2OOH radical is only formed under reducing conditions and around 900 K from the combination of ethene and a hydroperoxyl radical (R33-rev). The consumption of CH_2CH_2OOH also does not follow the general pathways, as CH_2CH_2OOH dissociates (via R19 and R20) instead of the expected oxygen addition.

The sensitivities of selected reactions are analyzed via a brute-force method in which the sensitivity coefficient (S_i) is defined as

$$S_i = \frac{\left(\Delta X_{C_2H_6}/X_{C_2H_6}\right)}{(\Delta k_i/k_i)} \qquad (7.1)$$

where k_i is the rate constant of the i^{th} reaction. Figure 7.7 shows the results of the analysis for a couple of reactions. The reaction R17 shows a relatively large sensitivity for ethane conversion under reducing conditions.

$$CH_3CH_2OO(+ M) = C_2H_4 + HO_2(+ M) \qquad \text{(R17)}$$

At 650 K and 100 bar, there is no sign of fuel conversion in the measurements but the model predicts considerable amount of products. Increasing the rate constant of R17 inhibits the fuel oxidation, so it can improve the model prediction. The fuel conversion starts at 700 K (at 100 bar) according to the experiments. At this temperatures, the sensitivity coefficient of R17 changes the sign, now increasing R17 promotes the oxidation while the reaction proceeds in the forward direction at both 650 and 700 K.

Figure 7.8 includes the results of the analyses for oxidizing and stoichiometric mixtures. Increasing the rates of H-abstraction from ethane by hydroperoxyl (R3) and hydroxyl (R4) radicals promote the fuel oxidation at different pressures and stoichiome-

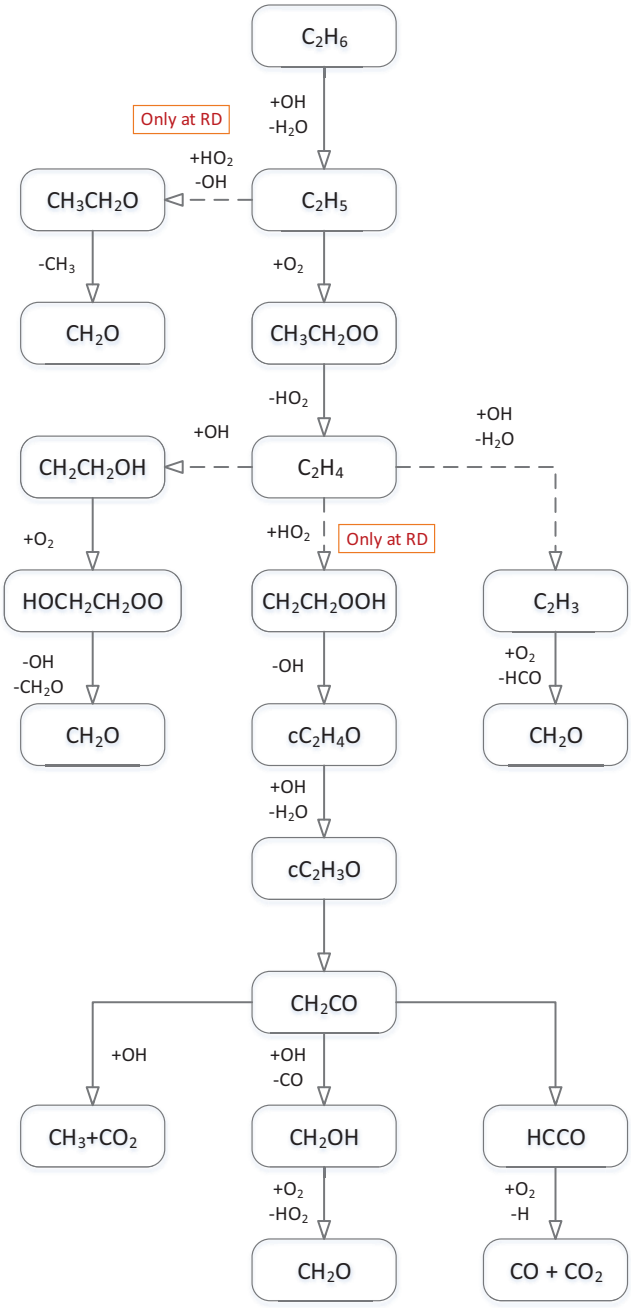

Figure 7.6: The major consumption path of ethane in the flow reactor at 100 bar pressure under reducing, stoichiometric, and oxidizing conditions.

tries.

$$C_2H_6 + OH = C_2H_5 + H_2O \quad \text{(R3)}$$

$$C_2H_6 + HO_2 = C_2H_5 + H_2O_2 \quad \text{(R4)}$$

Under oxidizing conditions and at a high temperature of 900 K, the reactions R22 and R26 emerge among the sensitive reactions.

$$C_2H_4 + OH(+ M) = C_2H_3 + H_2O(+ M) \quad \text{(R22)}$$

$$C_2H_4 + OH(+ M) = CH_2CH_2OH(+ M) \quad \text{(R26)}$$

Both of these reactions inhibit the fuel consumption by removing hydroxyl radicals from the system.

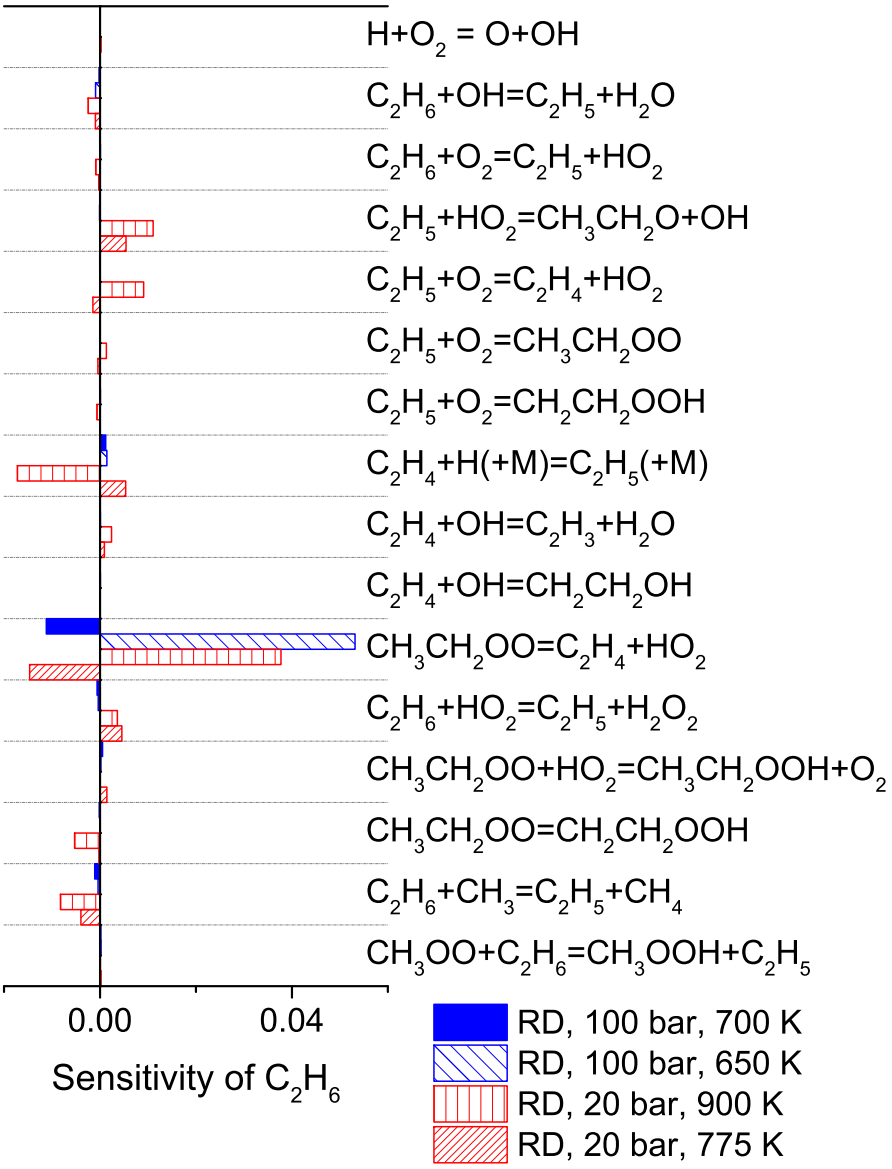

Figure 7.7: Sensitivity coefficients of C_2H_6 molar fraction at different pressures and temperatures under reducing conditions. The coefficients are calculated at the end of the nominal residence time of the flow reactor.

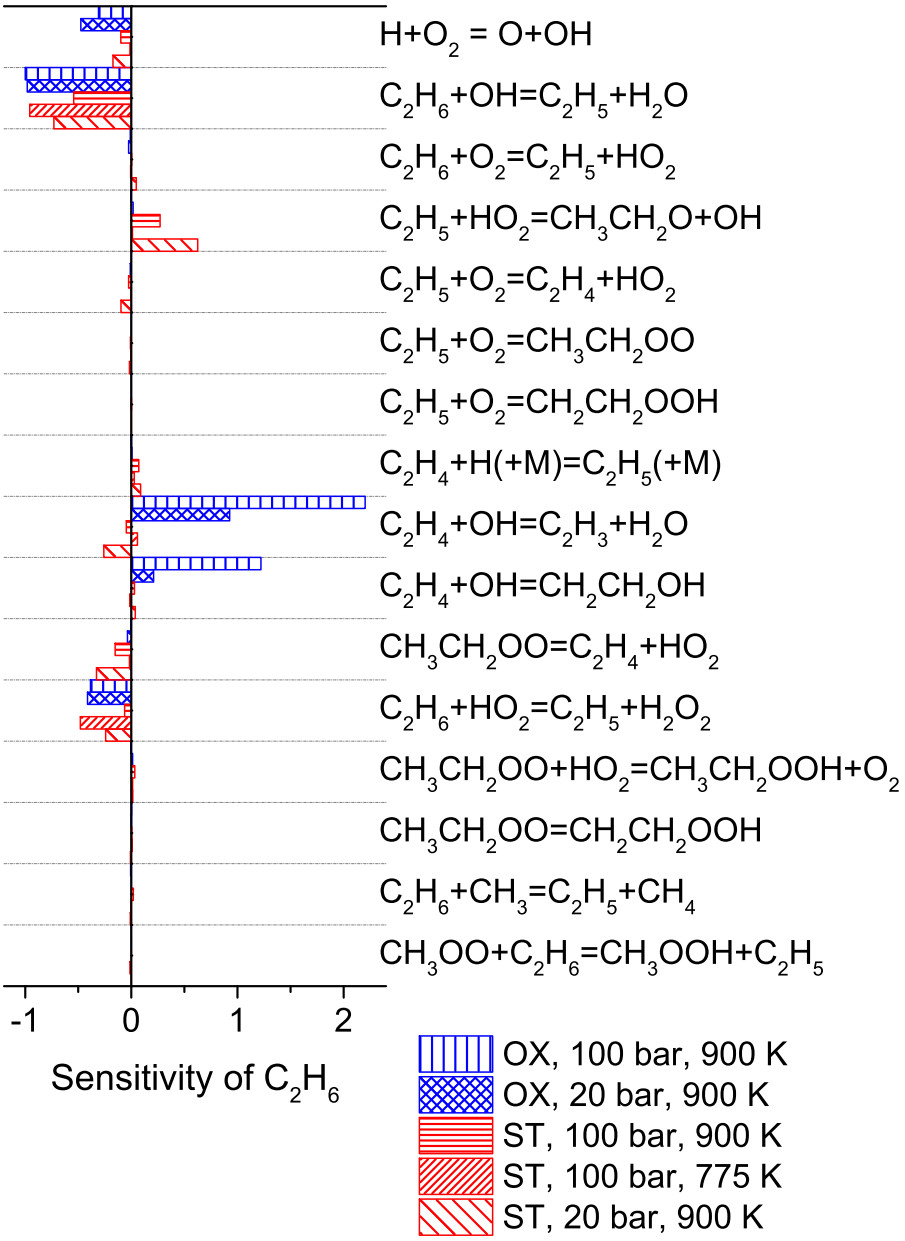

Figure 7.8: Sensitivity coefficients of C_2H_6 at different pressures, temperatures, and stoichiometries. The coefficients are calculated at the end of the nominal residence time of the flow reactor.

7.4.2 Comparison with literature data

The chemical kinetic model was evaluated against data from the flow reactor experiments at pressures of 20–100 bar and temperatures of 600–900 K. The assessment is extended to higher temperatures by comparison to data from shock tubes and flame speed measurements in the following sections.

7.4.2.1 Ignition at higher temperatures

The ignition delay time of ethane has been measured at pressures greater than 10 atm by Aul et al. [21], Zhang et al. [84], and Pan et al. [250]. Figure 7.9 shows the measured ignition delay times and the predictions by the present model. The ignition delays decrease monotonically by increasing temperature over the investigated conditions. Apart from fuel-lean data from Aul et al. [21], which are underestimated by the model, the model compare well with the measurements.

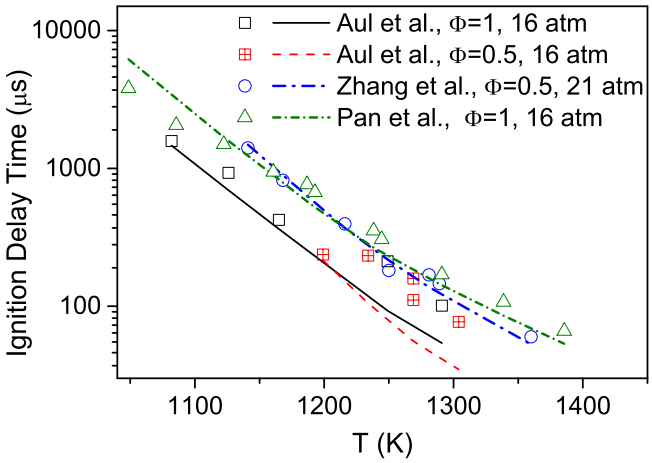

Figure 7.9: Ignition delay time of $C_2H_6/O_2/Ar$ mixtures calculated by the present model. Symbols mark experimental results from Aul et al. [21] (85% dilution in Ar), Zhang et al. [84] (95% dilution in Ar), and Pan et al. [250] (95% dilution in Ar).

7.4.2.2 Species profiles from shock tubes

Tranter and coworkers [44, 45] have measured the concentration of stable components in shock tube at high pressures of 40, 340, and 613 bar. The post-shock composition was measured by a GC. By recording pressure and calculating temperature accordingly, they were able to simulate the post-shock conditions. Data for the nominal pressure of 40 bar were reported in ref [45]. To simulate the data, here a fixed pressure of 40 bar

and a residence time of 1.7 ms were implemented in the model. As shown in figure 7.10, the fuel conversion starts around 1150 K and is accompanied by the gradual rise of CO and C_2H_4. Above 1250 K, the C_2H_4 concentration declines and it almost disappears around 1400 K. The model prediction agrees fairly well with the measurements.

Another study by Tranter et al. [44] reported data at higher pressures of 340 and 613 bar. As shown in figures 7.11 and 7.12, the fuel conversion is detected above 1075 K. Ethene peaks around 1200 K and then declines gradually. To simulate the data, two examples of pressure profiles provided in the original article are inputted into the model. As can be seen, the model predictions agree well with the measurements.

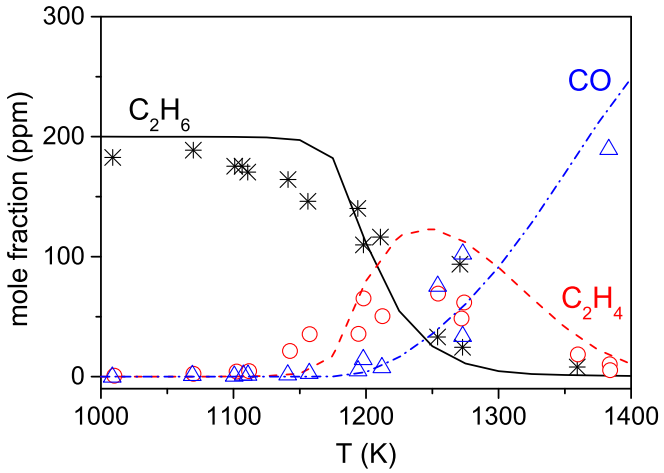

Figure 7.10: Post–shock concentration profiles at different temperatures. Symbols mark experimental results measured in a shock tube with initial mole fractions of 200 ppm of C_2H_6 (Φ=1, in N_2) at pressures of 40 bar, from ref [45]. Lines denote the prediction of the present model.

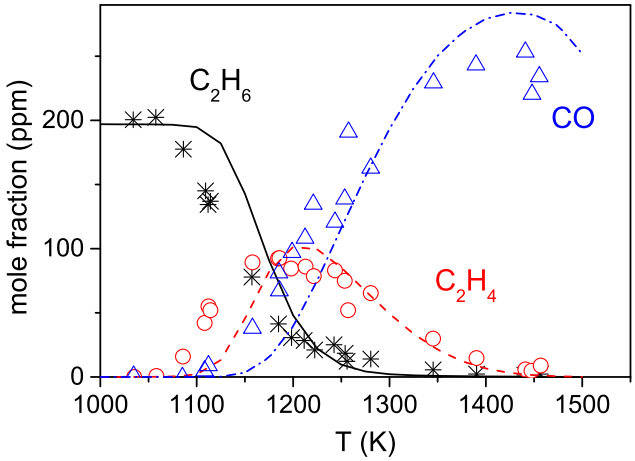

Figure 7.11: Post–shock concentration profiles at different temperatures. Symbols mark experimental results measured in a shock tube with initial mole fractions of 200 ppm of C_2H_6 (Φ=1, in N_2) at pressures of ~340 bar, from ref [44]; Lines denote the prediction of the present model.

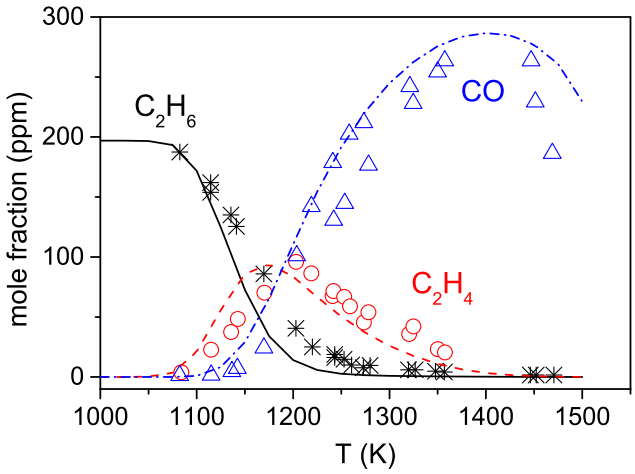

Figure 7.12: Post–shock concentration profiles at different temperatures. Symbols mark experimental results measured in a shock tube with initial mole fractions of 200 ppm of C_2H_6 (Φ=1, in N_2) at pressures of ~613 bar, from ref [44]. Lines denote the prediction of the present model.

7.4.2.3 Flame speed

Laminar flame speeds of combustible mixtures are widely used to evaluate kinetic models. For ethane/air mixtures, the flame speed has been measured at pressures up to 10 atm [12, 229, 251–254]. Figure 7.13 compares the model prediction with measurements at 1, 5, and 10 atm. The model overpredicts the flame speed at atmospheric pressure, but its accuracy improves at higher pressures.

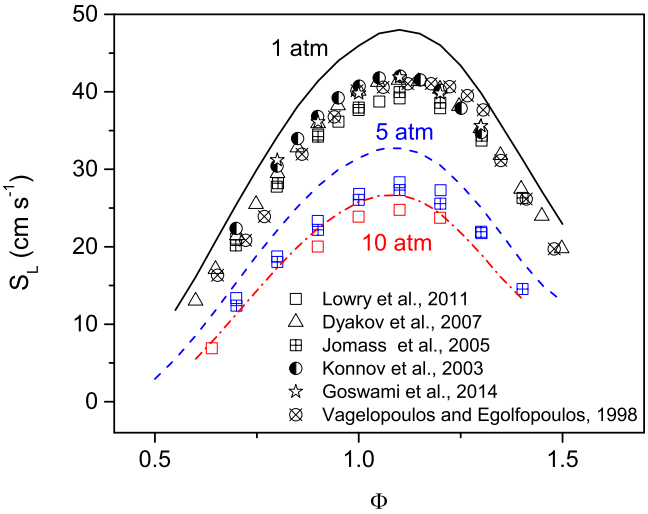

Figure 7.13: The unstretched laminar burning velocity of ethane/air mixtures versus equivalence ratio for an initial temperature of 300 K and at different pressures. Lines denote the present model predictions and symbols mark experimental results from Vagelopoulos and Egolfopoulos [12], Lowry et al. [229], Konnov et al. [251], Jomaas et al. [252], Dyakov et al. [253], and Goswami [254].

The present model predicts the flame speed of methane very well [237]. The flame speed of ethene is also calculated for an atmospheric flame and the results are within the uncertainty range of experimental measurements as shown in figure 7.14. Sensitivity analyses are conducted using built-in functions of Chemkin [109] for mass flow rate sensitivity, which represents well the sensitivity of flame speed to reaction rate constants. Figure 7.15 shows the results of the analyses for both ethane and ethene flames. Reactions involved in the production/ consumption of H radicals are crucial in determining flame speed. The hydrogen radical can diffuse from high-temperature zone of the flames to colder zones and initiates the reactions there. Most of the sensitive reactions are common between ethene and ethane. However, two reactions are

sensitive for ethane but not so sensitive for ethene:

$$CH_3 + CH_3(+M) = C_2H_5 + H(+M) \quad \text{(R1)}$$

$$C_2H_4 + H(+M) = C_2H_5(+M) \quad \text{(R8)}$$

Both reactions generally proceed in the reverse direction under ethane flame conditions so R1 consumes H radicals while R8 produces H. Earlier, Park et al. [197] examined three chemical kinetic models and found that all of them overpredicted the flame speed of ethane. In agreement to our findings here, Park et al. [197] concluded that reactions R1 and R8 are likely involved in the disagreement between the models and measurements for ethane flame speed.

The rate constant for reaction R1 is taken from a review by Baulch et al. [136], and for R8 we rely on a theoretical study by Miller and Klippenstein [249] which benefited from earlier measurements. In the absence of any advance in determining the rates of these reactions, we retained the rate constants here while further studies of these reactions are warranted.

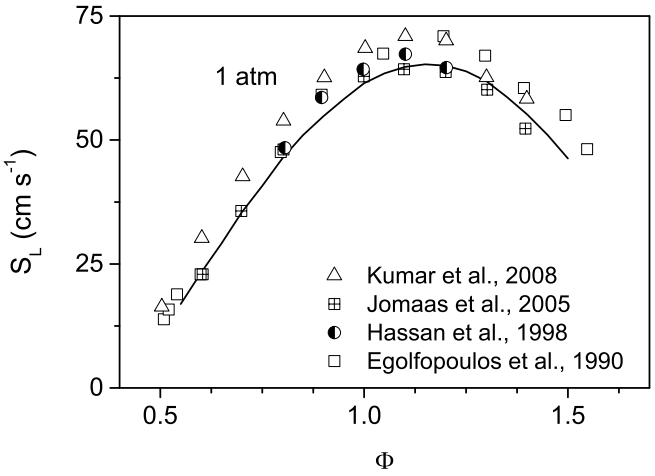

Figure 7.14: The unstretched laminar burning velocity of ethene/air mixtures versus equivalence ratio for an initial temperature of 300 K and at atmospheric pressure. Lines denote the present model predictions and symbols mark experimental results from Jomaas et al. [252], Egolfopoulos et al. [255], Hassan et al. [256], and Kumar et al. [257].

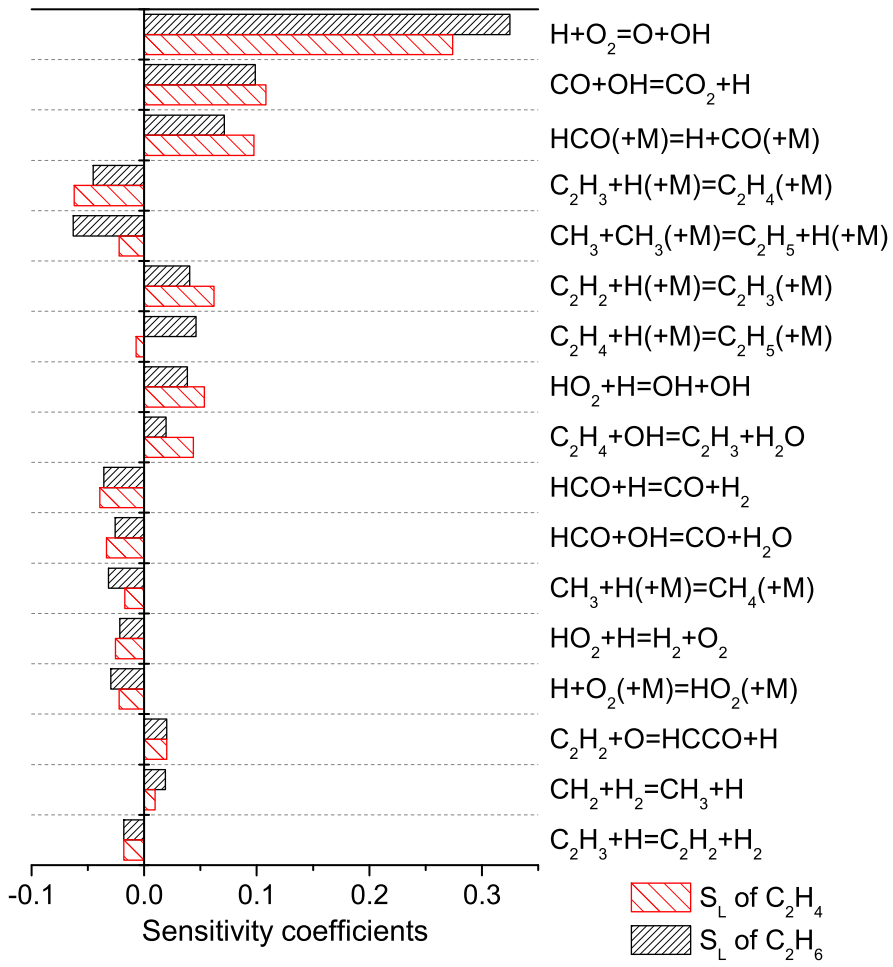

Figure 7.15: The sensitivity of the mass flow rate of ethane/air and ethene/air stoichiometric mixtures at atmospheric pressure and initial temperature of 300 K.

Conclusions

Ethane oxidation was investigated in a laminar flow reactor at intermediate temperatures of 600–900 K and high pressures of 20–100 bar. Through the experiments, the concentrations of stable species were measured at the reactor outlet while temperature was varied. The results revealed the onset temperatures of reaction between 700 K and 825 K, depending on pressure and stoichiometry. It was also found that increasing pressure and consequently the gas residence time reduced the onset temperature while stoichiometry had only a slight effect.

A detailed chemical kinetic model for ethane oxidation has been developed and evaluated against the data from the present experiments as well as from literature. The model predicted well the species concentrations from the flow reactor experiments. However, for high-pressure reducing conditions, the fuel conversion was predicted prematurely. The model could reproduce ignition delay times and post-shock concentrations from shock-tube experiments in literature, but it overpredicted flame speed at atmospheric pressure.

The provided data extend the ethane oxidation benchmark at high pressures and intermediate temperatures. Models validated against such data can be used more safely in the optimization of engines and gas turbines. Further work should address the premature ignition of the model at certain circumstances and the overprediction of ethane flame speed.

Chapter 8

Ethanol

Abstract

The pyrolysis and oxidation of ethanol has been investigated at temperatures of 600–900 K and a pressure of 50 bar in a laminar flow reactor. The experiments covered a wide range of fuel-air equivalence ratios (Φ=0.1, 1, 43, ∞), all highly diluted in nitrogen. The results, collected as the composition of the exhaust gas from the reactor as a function of the nominal temperature, extend the ethanol oxidation database at high pressures and intermediate temperatures. The onset temperature of ethanol oxidation was at 700–725 K over a wide range of stoichiometries. A considerable yield of aldehydes was detected at intermediate temperatures. Ethanol pyrolysis was observed at temperatures above 850 K. A detailed chemical kinetic model has been developed and evaluated against the present data as well as ignition delay times and flame speed measurements from literature. The developed model was able to predict the onset of fuel conversion and the composition of products from the flow reactor experiments fairly well. The model performed well in simulating ignition delays above 900 K whereas it overpredicted the flame speeds slightly. The results of sensitivity analyses revealed the importance of the reaction between ethanol and a hydroperoxyl radical for ignition at high pressure and intermediate temperatures. Future work should improve the accuracy of the model by providing more accurate rate constants for the key reactions identified here.

8.1 Introduction

In recent years, ethanol has attracted much research and commercial attention as an additive to conventional liquid fuels or even as an alternative for them. Ethanol addition to gasoline promotes the overall octane number of the fuel while it potentially reduces the emission of particulate matter [50] and CO [51]. In Brazil and many other places gasoline doped by ethanol is widely used in spark-ignited (SI) engines [49]. Ethanol addition to diesel fuel has also been studied [52, 53] and a positive effect on fuel economy was found [52]. The relatively high energy density of ethanol makes it attractive as a neat fuel too. Using ethanol-based fuels produced from bio-sources can reduce pressure on fossil fuels resources and reduce CO_2 release to atmosphere. However, the widespread usage of ethanol fuel may increase the emission of aldehydes [49, 51, 54] which can cause health risks.

Ethanol fuel, either neat or in blends, is mainly used in internal combustion engines. The next generation of internal combustion engines is likely to work based on the concept of homogeneous-charge compression-ignition (HCCI) engines which promises to combine the best features of conventional compression- and spark-ignited engines [258]. Ignition in such engines as well as any combustion device working at intermediate temperatures (below 1000 K) and elevated pressures is strongly affected by chemical kinetics. Furthermore, the reaction mechanism of ethanol is a crucial part in models for heavier alcohols often found in complicated biofuels [49]. The reaction mechanism of hydrocarbon fuels has been studied over decades, but the oxidation chemistry of oxygenated fuels is recent and many links in intermediate steps may be missing.

Despite its importance, detailed data for ethanol oxidation at high pressures and intermediate temperatures are scare. Tests at these conditions can be carried out in flow reactors. Li et al. [62] investigated ethanol pyrolysis at 950 K and pressures of 3–12 atm in a turbulent flow reactor. They found that the widely used mechanism by Marinov [259] underpredicted the fuel consumption under the investigated conditions. In their succeeding work [63], the rate constants for the thermal decomposition of ethanol was extracted. The same device was used by Haas et al. [61] to explore ethanol oxidation over 523–903 K and at 12.5 atm.

Ignition delay times at intermediate temperatures are commonly measured in rapid compression machines (RCM). Relatively short ignition delays of ethanol make it pos-

sible to conduct such experiments in shock tubes too. Lee et al. [55] measured the ignition delays of ethanol in an RCM at 750–1000 K and 20–40 atm. Noorani et al. [59] measured the ignition delay times of ethanol in a shock tube at 1070–1760 K and 2–12 atm and found a good agreement between the measurements and the prediction of the Marinov mechanism [259]. Mittal et al. [65] reported ignition delays of ethanol from RCM experiments at 10–50 bar and 825–985 K. Heufer and Olivier [34] measured ethanol ignition delays in a shock tube at 800–1400 K and pressures up to 40 bar. The same device was used by Lee et al. [60] to study ethanol ignition over 775–1300 K and at 80 bar. Lee et al. [60] further extended the data to 705 K by conducting RCM experiments. Cancino et al. [56] measured the ignition delay of ethanol in a shock tube over 650–1220 K and pressures of 10–50 bar. Some of the listed work partly cover the pressure and temperatures of the current study, but they only report ignition delay times as an overall characteristic of combustion. Additional valuable insight into the combustion chemistry can be obtained by measuring more detailed characteristics such as species profiles.

Early versions of ethanol oxidation mechanism by Dunphy et al. [58] and Norton and Dryer [260] and Norton and Dryer [261] were mainly developed for atmospheric pressure. Marinov [259] conducted a comprehensive analysis on ethanol oxidation and estimated unknown rate constants by analogy to well determined reactions. Whereas most of the data used by Marinov [259] were collected at low pressures and high temperatures, his model has been used widely in high-pressure studies. Dryer and coworkers [61, 63] developed a kinetic model and validated it against flow-reactor data at 12.5 bar as well as against ignition delays up to 50 bar. Lee et al. [60] modified a few key reactions of the model in [61, 63] and validated the model against ignition delays at pressures up to 77 bar. Frassoldati et al. [262] published a kinetic model for ethanol, heavier alcohols, and their mixtures with gasoline surrogates. This model and those by Saxena and Williams [263] and Leplat et al. [264] were not validated at high pressures. Cancino et al. [56] modified earlier kinetic models to address ethanol oxidation chemistry at high pressures and intermediate temperatures. However, their model was solely validated against shock tube data. Mittal et al. [65] optimized a model for ethanol oxidation at intermediate temperatures. By the advent of more reliable data for the key reactions in ethanol oxidation, a thorough reevaluation of reactions focusing on medium temperatures and high pressure seems necessary.

In this paper we present species concentration profiles from ethanol pyrolysis and

oxidation in a flow reactor at high pressure and intermediate temperatures. A detailed chemical kinetic model based on earlier studies from the same laboratory [1, 32, 102, 178–180, 237, 265] is further developed and evaluated against the data from the present work as well as from literature.

8.2 Experimental approach

The experimental setup was a laboratory-scale high-pressure laminar-flow reactor designed to approximate plug flow [102]. The setup was described in detail elsewhere [102] and only a brief description is provided here. The system was used here for the investigation of ethanol oxidation chemistry at a pressure of 50 bar, temperatures up to 900 K, and a flow rate of 4.78 Nliter/min (4.42 Nliter/min for the pyrolysis experiments, STP: 1 atm and 273.15 K).

The reactions took place in a tubular quartz reactor (inner diameter of 8 mm) to minimize the effects of surface reactions. The quartz reactor was enclosed in a stainless steel tube that acted as a pressure shell. The system was pressurized from the feed gas cylinders and the reactor pressure was monitored upstream of the reactor by a differential pressure transducer and controlled by a pneumatically operated pressure control valve positioned after the reactor. The pressure fluctuations of the reactor were limited to ±0.2%. The pressure in the shell-side of the reactor was retained close to that inside the reactor in order to prevent breaking the quartz tube.

The steel tube was placed in a tube oven with three individually controlled electrical heating elements that produced an isothermal reaction zone (±6 K) of ~42–48 cm in the middle of the reactor. A moving thermocouple was used to measure the temperature profile inside the pressure shell at the external surface of the quartz tube after stabilizing the system.

The flow rates were regulated by mass-flow controllers. The gases were mixed at ambient temperature well before entering the reactor so a complete mixing was expected before the high temperature zone of the reactor.

The liquid feeding system was described in detail in [103]. The liquid was pressurized by an HPLC pump and its flow to the reactor was controlled by a liquid mass flow controller. The liquid then evaporated at temperatures around 520 K and mixed with the incoming gaseous feed before entering the reactor. A long stabilization period before each test was employed to limit the fluctuations of the liquid feeding system to ±5%.

Downstream of the reactor, the system pressure was reduced to atmospheric level prior to product analysis, which was conducted by an on-line *6890N Agilent Gas Chromatograph* (GC-TCD/FID from Agilent Technologies) calibrated according to the procedure in [237]. The GC allowed detecting O_2, CO, CO_2, C_2H_4 and C_2H_6 with estimated uncertainties around 5%. CH_4 could not be quantified accurately due to signal overlapping with CO. A higher uncertainty for ethanol measurement was estimated due to its calibration procedure. Distinguishing methanol from acetaldehyde was not possible due to signal overlapping for the GC configuration used. However, it was possible to measure the signal areas corresponding to sum of these components. Using the response factor of methanol, the sum of acetaldehyde and methanol was reported quantitatively but a relatively large uncertainty must be acknowledged. Moreover, due to the small signal to noise ratio of formaldehyde, a larger uncertainty especially in measuring low quantities of formaldehyde was expected.

All gases used in the present experiments were high purity gases or mixtures with certified concentrations (±2% uncertainty) and the ethanol purity was above 99.8 %. The total flow rate was also measured by a bubble flow meter downstream of the reactor. Using a quartz tube and conducting experiments at high pressures were expected to minimize the contribution from heterogeneous reactions at the reactor wall.

For each set of experiments, the concentration of reactants as well as the pressure of the system were maintained while temperature of the isothermal zone was increased in small steps which simultaneously shortened gas residence time at the isothermal zone of the reactor.

Figure 8.1 shows the measured temperature profiles for different isotherms in pure nitrogen. The residence time of the gases at the isothermal zone of the reactor can be estimated as τ[s]=3840/T [K] (±8%) for all the oxidizing experiments and τ[s]=4098/T [K] (±8%) for the pyrolysis tests. A model with constrained temperature and pressure was used for modeling in Chemkin [109].

A potential source of uncertainty in interpreting data from the flow reactor was temperature rise due to exothermic reactions. The reactants were strongly diluted in inert gases to limit the undesired temperature rise. When the mixture has the highest exothermicity, measuring the temperature profile indicated a marginal difference compared to the flow of pure nitrogen. The narrow quartz tube used here also accelerated the thermal equilibrium between the reactive gas inside the reactor and the heating bath gas surrounding it. A constant pressure and enthalpy (adiabatic) model

leads to maximum 107 K temperature rise in the most critical situation. However, in the absence of any indication of temperature rise, the deviation of the gas temperature from the measured temperatures was expected to be significantly smaller due to the fast heat transfer between the quartz reactor and its surrounding.

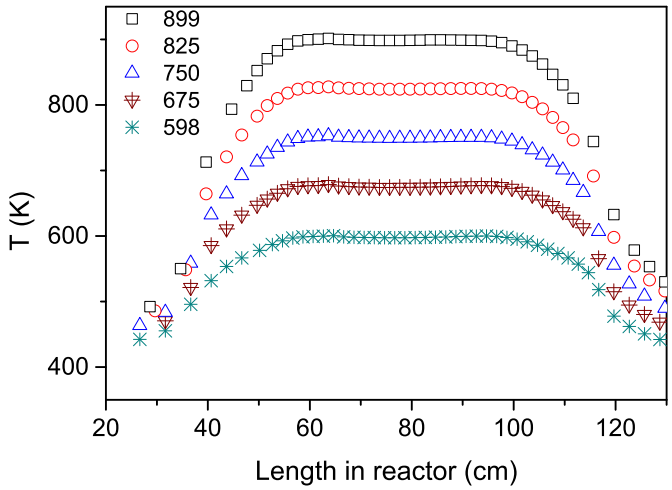

Figure 8.1: Measured temperature profiles across the reaction zone. The nitrogen flow rate was 4.78 NL/min at a pressure of 50 bar. The flow rate and temperature profiles were slightly different for the ethanol pyrolysis experiments.

8.3 Chemical kinetic model

The reaction mechanism and corresponding thermodynamic and transport data were drawn from previous work from the same laboratory in [32, 102, 178, 180]. The methanol subset has been revisited and improved by Aranda et al. [179]. Recently, we have reevaluated hydrogen, methane, and ethane subsets in [1, 237, 265]. Here, the reactions important for ethanol oxidation at high pressure and moderate temperatures are discussed.

The thermal decomposition of ethanol (R1) plays a key role in the oxidation process at high temperatures [61] and is believed to proceed in three channels [266]:

$$\mathrm{CH_3CH_2OH(+M)} = \mathrm{C_2H_4 + H_2O(+M)} \quad \text{(R1a)}$$

$$= \mathrm{CH_3 + CH_2OH(+M)} \quad \text{(R1b)}$$

$$= \mathrm{C_2H_5 + OH(+M)} \quad \text{(R1c)}$$

Sivaramakrishnan et al. [266] measured ethanol dissociation over 1392–1663 K and by

employing theoretical calculations suggested rate constants for 800–2000 K. At high pressures and temperatures, the derived rate constants are close to those calculated by Park et al. [267], but they differ more at low pressures and temperatures. Ethanol dissociation were also measured by Wu et al. [268] at 1450–1760 K in shock-tube tests with very low ethanol concentrations of 1–3 ppm. Data from Wu et al. [268] support branching ratios which are less sensitive to pressure, compared to those by Sivaramakrishnan et al. [266]. More recently, Kiecherer et al. [269] extracted the rate of $C_2H_4 + H_2O$ branch by measuring the concentration of H_2O at 1300–1510 K under atmospheric pressure. Their measured rate for $C_2H_4 + H_2O$ branch is in line with those concluded in [266, 268]. In the absence of any measurements at the elevated pressure of this study, we rely on the results from Sivaramakrishnan et al. [266].

Ethanol combustion is controlled by H-abstraction reactions forming isomers of C_2H_5O radicals, i.e. α-hydroxyethyl (CH_3CHOH), β-hydroxyethyl (CH_2CH_2OH), and ethoxy (CH_3CH_2O) radicals. One of the key abstraction reactions is the reaction between ethanol and an H atom (R2).

$$CH_3CH_2OH + H = CH_3CHOH + H_2 \quad \text{(R2a)}$$
$$= CH_2CH_2OH + H_2 \quad \text{(R2b)}$$
$$= CH_3CH_2O + H_2 \quad \text{(R2c)}$$

At high temperatures, ethanol dissociation also becomes active, so only measuring H-decay cannot give the rate of R2 accurately [266]. To overcome this problem, Sivaramakrishnan et al. [266] measured D atom concentration in reaction $CH_3CH_2OH + D$ over 1054–1359 K and then eliminated the isotope effect via theoretical calculations. Their calculations show that the dominant channels are CH_3CHOH and CH_2CH_2OH, which are consistent with an earlier study by Park et al. [267]. A more recent theoretical study by Meana-Paneda and Fernandez-Ramos [270] yielded an overall rate constant 4–6 times higher than those by Sivaramakrishnan et al. [266] at combustion temperatures. However, due to the lack of experimental evidence for such higher rates, we adopt the rate constants from Sivaramakrishnan et al. [266].

The reaction between ethanol and hydroxyl radical is the dominant H-abstraction reaction of ethanol at intermediate temperatures [61, 271]. The dominant channels

under combustion related conditions are [266]:

$$CH_3CH_2OH + OH = CH_3CHOH + H_2O \quad \text{(R3a)}$$
$$= CH_2CH_2OH + H_2O \quad \text{(R3b)}$$
$$= CH_3CH_2O + H_2O \quad \text{(R3c)}$$

The CH_2CH_2OH radical produced from the second channel (R3b) is expected to dissociate to C_2H_4 + OH at temperatures above 550 K [266]. Above 650 K, the dissociation further accelerates, so it is considered instantaneous compared to other chemical time scales. Sivaramakrishnan et al. [266] studied the title reaction over 857–1297 K by monitoring OH decay rate, which only represents the overall rate of R3a + R3c due to the dissociation of CH_2CH_2OH. Theoretical calculations by Sivaramakrishnan et al. [266] gave an overall rate for R3a + R3c larger than the measured values so they adjusted the barrier heights of all the branches in their calculations to compensate for it. Their adjusted rate constants indicate negligible contributions from R3b and R3c in the overall rate of CH_3CH_2OH + OH at combustion temperatures.

The title reaction was investigated at lower temperatures of 298–523 K by Carr et al. [271] who used isotopic labeling to distinguish different channels below 523 K, where CH_2CH_2OH decomposition is negligible. Carr et al. [271] found an overall rate of R3 in agreement to that in [266] at low temperatures but with a stronger temperature dependence. Moreover, the two studies differ in determining branching ratios. Data from Carr et al. [271] support minor contributions of α and β channels at high temperatures which makes R3c the dominant path. However, the branching to β channel at the upper limit of temperatures studied by Carr et al. [271] was determined with a larger uncertainty which makes conclusion difficult.

A theoretical study by Zheng and Truhlar [272] yielded an overall rate for R3 in line with the majority of the earlier measurements. However, a higher dependence on temperature was predicted above 1000 K compared to ref [266]. Over a wide range of temperature, the branching ratios of α and β channels were calculated to be around 0.6 and 0.2, higher than those found in [266].

More recently, Stranic et al. [273] measured the overall rate as well as the rate of the β branch of the title reaction over 900–1270 K. Isotopic labeling of OH radicals enabled Stranic et al. [273] to prevent interference from CH_2CH_2OH dissociation on the measured rate. The branching ratio of the β channel was reported to be 0.2–0.25

over 900–1200 K whereas distinction between R3a and R3c was not possible in [273].

All in all, the major difference between most studies is in allocating branching ratios. The overall rate of Zheng and Truhlar [272] lies within the uncertainty range of the listed measurements over a wide range of temperature. The β branching ratio calculated in [272] is close to the only reliable measurement of the β branch from Stranic et al. [273]. Therefore, the rate constants of Zheng and Truhlar [272] are used here. To implement the calculated rate (using *M08-SO/6-31+G(d,p)* potential surface) in Chemkin [109], a modified Arrhenius equation is fitted to the data over 300–2500 K. The fitted equation reproduces the original complicated equation with an error of 10% at maximum.

Ignition at intermediate temperatures depends strongly on hydroperoxyl radical reactions [1, 237, 265]. In the absence of any measurement or theoretical calculation for the reaction between ethanol and the hydroperoxyl radical, Marinov [259] estimated the rate constant by analogy to methanol reactions.

$$\begin{aligned} CH_3CH_2OH + HO_2 &= CH_3CHOH + H_2O && \text{(R4a)} \\ &= CH_2CH_2OH + H_2O && \text{(R4b)} \\ &= CH_3CH_2O + H_2O && \text{(R4c)} \end{aligned}$$

For the reaction between ethanol and a methyl radical, the most reliable data are those from a theoretical study by Xu et al. [274] who found a smaller overall rate of $CH_3CH_2OH + CH_3$ compared to the estimation by Marinov [259].

$$\begin{aligned} CH_3CH_2OH + CH_3 &= CH_3CHOH + CH_4 && \text{(R5a)} \\ &= CH_2CH_2OH + CH_4 && \text{(R5b)} \\ &= CH_3CH_2O + CH_4 && \text{(R5c)} \end{aligned}$$

The α-hydroxyethyl radical (CH_3CHOH) is presumably the major product of H-abstraction reactions from ethanol. For the decomposition of CH_3CHOH, the rate constants are taken from an RRKM study by Dames [275] who predicted the major branch (R6a) to be faster up to one order of magnitude compared to an earlier calculation by

Xu et al. [276].

$$\begin{aligned} CH_3CHOH(+M) &= CH_3CHO + H(+M) && \text{(R6a)} \\ &= CH_2CHOH + H(+M) && \text{(R6b)} \\ &= CH_3 + CH_2O(+M) && \text{(R6c)} \end{aligned}$$

The abstraction by a hydrogen atom is expected to be important only at low pressures [243]. The rate constants for different branches of this reaction are taken from a theoretical study by Labbe et al. [243].

$$\begin{aligned} CH_3CHOH + H(+M) &= CH_2CHOH + H_2(+M) && \text{(R7a)} \\ &= C_2H_4 + H_2O(+M) && \text{(R7b)} \\ &= CH_3 + CH_2OH(+M) && \text{(R7c)} \\ &= C_2H_5 + OH(+M) && \text{(R7d)} \\ &= CH_3CH_2OH(+M) && \text{(R7e)} \end{aligned}$$

For the reaction between CH_3CHOH and molecular oxygen, we rely on a theoretical study by Silva et al. [277] who found the major products to be $CH_3CHO + HO_2$ under combustion conditions.

$$\begin{aligned} CH_3CHOH + O_2(+M) &= CH_3CHO + HO_2(+M) && \text{(R8a)} \\ &= CH_2CHOH + HO_2(+M) && \text{(R8b)} \end{aligned}$$

The other possible products, $CH_2CHOH + HO_2$, were formed in small amounts and only at high temperatures. The high pressure limit of this reaction was also studied by Zador et al. [278] who predicted an overall rate larger within a factor of two. However, the pressure dependence of the reaction was not explored in [278].

The β-hydroxyethyl radical (CH_2CH_2OH) is another isomer of C_2H_5O formed by hydrogen abstraction from ethanol. The dissociation of CH_2CH_2OH is expected to yield either $C_2H_4 + OH$ (R9a) or $CH_2CHO + H$ (R9b) [276].

$$\begin{aligned} CH_2CH_2OH(+M) &= C_2H_4 + OH(+M) && \text{(R9a)} \\ &= CH_2CHO + H(+M) && \text{(R9b)} \end{aligned}$$

The branch to C_2H_4 was studied theoretically [246, 276, 279] and experimentally [280]. The theoretical derivations by Xu et al. [276] and Senosiain et al. [246] differed within a factor of six at atmospheric pressure over 700–1000 K. Senosiain et al. [246] predicted a larger sensitivity to temperature which was also confirmed with experiments by Srinivasan et al. [280]. Therefore, the $C_2H_4 + OH$ (R9a) branch is taken from Senosiain et al. [246] who fitted pressure-dependent rate constants for the reverse direction of this reaction. The rate constant of the other branch to $CH_2CHO + H$ (R9b) is adopted from the calculations of Yamada et al. [279].

The rate constants for the reaction between CH_2CH_2OH and hydrogen atoms are taken from a study by Labbe et al. [243].

$$\begin{aligned} CH_2CH_2OH + H(+M) &= C_2H_4 + H_2O(+M) && \text{(R10a)} \\ &= CH_2OH + CH_3(+M) && \text{(R10b)} \\ &= C_2H_5 + OH(+M) && \text{(R10c)} \end{aligned}$$

For the reactions between CH_2CH_2OH and other radicals, the rate constants are estimated by analogy to C_2H_5 reactions.

Lopez et al. [178] analyzed the consumption paths of β-hydroxyethyl radical (CH_2CH_2OH) and estimated the major sink of this radical to be its reaction with molecular oxygen. They estimated the rate constant of this reaction by analogy to C_2H_5 reactions.

$$\begin{aligned} CH_2CH_2OH + O_2(+M) &= CH_2CHOH + HO_2(+M) && \text{(R11a)} \\ &= HOCH_2CH_2OO(+M) && \text{(R11b)} \end{aligned}$$

Zador et al. [278] derived the high pressure limit of this reaction by high-level ab initio calculations and found an overall high-pressure rate around five times larger than those in Lopez et al. [178]. Three branches of this reaction is found to be important [278]:

$$\begin{aligned} CH_2CH_2OH + O_2(+M) &= CH_2CHOH + HO_2(+M) && \text{(R11a)} \\ &= HOCH_2CH_2OO(+M) && \text{(R11b)} \\ &= CH_2O + CH_2O + OH(+M) && \text{(R11c)} \end{aligned}$$

However, the branching ratios could not be determined accurately in their work. Another theoretical study by Silva et al. [281] using density functional theory and ab ini-

tio methods gave rate constant 2–3 orders of magnitude lower than the high-pressure limit of Zador et al. [278]. Due to the inconsistency in the two studies and lack of data for branching ratios in [278], we estimated the rate constants and the major products based on analogy to C_2H_5 reactions, while further study of this reaction is warranted.

Another isomer of C_2H_5O formed via H-abstraction reactions from ethanol is the ethoxy radical (CH_3CH_2O). Caralp et al. [282] measured the ethoxy radical decomposition at 391–471 K. Later Dames [275] used an RRKM equation simulation to extrapolate the rate constant to higher temperatures of 406–1200 K and pressures of 0.001–100 atm. Dames [275] found that the decomposition to $CH_3 + CH_2O$ is the only favored channel under combustion conditions.

$$CH_3CH_2O(+M) = CH_3 + CH_2O(+M) \tag{R13}$$

Another RRKM study by Xu et al. [276] agreed well with the experimental results of Caralp et al. [282]. However, outside the range of temperature and pressure of the experiments in [282], the two theoretical calculations predict substantially different pressure and temperature dependencies. Here, we adopt the rate from Dames [275] while measurements at medium temperatures are desired.

The ethoxy radical isomerization was also studied by Dames [275].

$$CH_3CH_2O(+M) = CH_2CH_2OH(+M)$$

According to Dames [275], this path is unimportant so it is omitted from the present model.

For the reactions between ethoxy and hydrogen radicals, the preferred rate constants are taken from a theoretical study by Xu et al. [283]

$$\begin{aligned} CH_3CH_2O + H(+M) &= CH_3CH_2OH(+M) && \text{(R14a)} \\ &= CH_2OH + CH_3(+M) && \text{(R14b)} \\ &= CH_3CHO + H_2(+M) && \text{(R14c)} \end{aligned}$$

Acetaldehyde is a major undesired by-product from ethanol oxidation [49, 51, 54]. At high temperatures, acetaldehyde is expected to dissociate mainly to CH_3 + HCO [284]. Yasunaga et al. [285] studied acetaldehyde pyrolysis behind a reflected shock wave over 1000–1700 K and fitted rate constants for the dissociation of acetaldehyde by

trial and error. Sivaramakrishnan et al. [284] measured the overall rate of acetaldehyde pyrolysis as well as its branching ratio in a shock tube and identified major branches as

$$\mathrm{CH_3CHO(+M)} = \mathrm{CH_3 + HCO(+M)} \quad \text{(R15a)}$$
$$= \mathrm{CH_4 + CO(+M)} \quad \text{(R15b)}$$

Since at high temperatures the formyl radical (HCO) decomposes rapidly to CO + H, measuring hydrogen atom concentration can give the rate of the branch to $\mathrm{CH_3}$ + HCO (R15a). According to Sivaramakrishnan et al. [284] the branch to $\mathrm{CH_3}$ + CHO accounted for 77% of the total conversion, independent from pressure and temperature under the investigated conditions. In combination with theoretical calculations, Sivaramakrishnan et al. [284] extracted the rate constants over 600–2500 K and pressures up to 130 atm, which are adopted here.

The isomerization of acetaldehyde to vinyl alcohol was studied theoretically by Shao et al. [286]. Here, the rate constant for the reverse direction (R15c-rev) is taken from an Arrhenius fitting by Dames [275] to the rate in [286].

$$\mathrm{CH_2CHOH(+M)} = \mathrm{CH_3CHO(+M)} \quad \text{(R15c-rev)}$$

The reaction between acetaldehyde and a hydrogen atom was studied by Sivaramakrishnan et al. [284] who derived rate constants over 200–2500 K from shock-tube tests and theoretical calculations. The dominant branch of the title reaction is expected to be $\mathrm{CH_3CO + H_2}$, but at the upper-limit temperature of this study the $\mathrm{CH_2CHO + H_2}$ branch can also contribute considerably.

$$\mathrm{CH_3CHO + H(+M)} = \mathrm{CH_3CO + H_2(+M)} \quad \text{(R17a)}$$
$$= \mathrm{CH_2CHO + H_2(+M)} \quad \text{(R17b)}$$
$$= \mathrm{CH_3CH_2O(+M)} \quad \text{(R17c)}$$
$$= \mathrm{CH_3CHOH(+M)} \quad \text{(R6a-r)}$$

The branch to $\mathrm{CH_3CHOH}$ was also studied by Dames [275] and the rate constant were expressed for the reverse direction, the dissociation of $\mathrm{CH_3CHOH}$. For $\mathrm{CH_3CHOH}$ dissociation at 50 atm, the pressure-dependent rate constants by Dames [275] depend less on temperature compared to pressure-independent rate constants from Sivaramakrish-

nan et al. [284]. We adopt the rate constants for R17a–R17c from Sivaramakrishnan et al. [284] while the rate constant for CH_3CHOH branch is taken from Dames [275], due to the potential importance of pressure.

The reaction between the hydroxyl radical and acetaldehyde is expected to be the primary acetaldehyde removal pathway during combustion [193].

$$CH_3CHO + OH = CH_2CHO + H_2O \quad \text{(R18a)}$$
$$= CH_3CO + H_2O \quad \text{(R18b)}$$

The overall rate of this reaction was measured by Taylor et al. [287] in a shock tube at temperatures up to 860 K. According to theoretical analyses in [287], $CH_3CO + H_2O$ should be the major branch at low temperatures while $CH_2CHO + H_2O$ is dominant at intermediate temperatures.

A more recent shock tube measurement by Wang et al. [193] extended the data to temperatures of 1000–1388 K and revealed a positive temperature dependence at combustion temperatures [193]. However, determining the branching ratio was not possible experimentally. Earlier studies at low temperatures of 220–298 K suggested the contribution of CH_3CO channel to be around 93–95% [288, 289]. The fitted rate constants in Wang et al. [193] are biexponential. Here, one exponential term of the fitted rate is assigned to CH_3CO and the other one to CH_2CHO, depending on their temperature dependence. This gives the contribution of CH_3CO channel to be 88–94% (over 500–1200 K). However, a more accurate determination of the branching ratio would be beneficial.

The reaction between acetaldehyde and the hydroperoxyl radical is presumably important at temperatures investigated in this work. Marinov [259] estimated major products of this reaction and its rate constants by analogy to formaldehyde and propane reactions.

$$CH_3CHO + HO_2 = CH_3CO + H_2O_2 \quad \text{(R19a)}$$
$$= CH_2CHO + H_2O_2 \quad \text{(R19b)}$$

According to his analysis, the CH_3CO branch is dominant at temperatures below 1300 K but the CH_2CHO branch takes over at higher temperatures. A single point measurement by Morajkar et al. [290] yielded 9×10^9 ($cm^3\ mol^{-1}\ s^{-1}$) at 294 K which is within 30% of the overall rate estimated by Marinov [259]. In contrast, a theoretical

study by Altarawneh et al. [291] derived an overall rate considerably smaller below 1000 K compared to that in [259]. As the only available experimental data agree better with the estimation by Marinov [259], we adopt the rate constants in Marinov [259] while further study of this reaction is recommended.

Vinyl alcohol is expected to be an important intermediate in ethanol oxidation. For the reactions between vinyl alcohol and either hydrogen or oxygen atoms, the rate constants are taken from a theoretical study by Labbe et al. [243].

$$CH_2CHO + H(+M) = CH_3 + HCO(+M) \quad \text{(R20a)}$$

$$CH_2CHO + H(+M) = CH_3CO + H(+M) \quad \text{(R20b)}$$

$$CH_2CHO + O = CH_2O + HCO \quad \text{(R21)}$$

Table 8.1: Reactions from ethanol reaction mechanism. The rate constants are in the form of $k = AT^n \exp(-E/(RT))$. Units are *mol*, *cm*, *K*, *s*, and *cal*.

	Reaction	A	n	E	Note/Ref.
R1a	$CH_3CH_2OH=C_2H_4 + H_2O$	3.84E+20	-2.06	69426	[a], [266]
R1b	$CH_3CH_2OH=CH_3 + CH_2OH$	6.17E+51	-10.34	109879	[a], [266]
R1c	$CH_3CH_2OH=C_2H_5 + OH$	1.78E+47	-8.96	101002	[a], [266]
R2a	$CH_3CH_2OH + H=CH_3CHOH + H_2$	8.79E+03	2.68	2913	[266]
R2b	$CH_3CH_2OH + H=CH_2CH_2OH + H_2$	5.31E+03	2.81	7491	[266]
R2c	$CH_3CH_2OH + H=CH_3CH_2O + H_2$	9.45E+02	3.14	8696	[266]
R3a	$CH_3CH_2OH + OH=CH_3CHOH + H_2O$	4.46E+02	3.11	-2666	pw, [272]
R3b	$CH_3CH_2OH + OH=CH_2CH_2OH + H_2O$	9.43E+03	2.67	-1004	pw, [272]
R3c	$CH_3CH_2OH + OH=CH_3CH_2O + H_2O$	2.37E+03	2.82	-691	pw, [272]
	duplicate rate constant	7.91E+07	1.18	-303	
R4a	$CH_3CH_2OH + HO_2=CH_3CHOH + H_2O$	8.20E+03	2.55	10750	[259]
R4b	$CH_3CH_2OH + HO_2=CH_2CH_2OH + H_2O$	1.20E+04	2.55	15750	[259]
R4c	$CH_3CH_2OH + HO_2=CH_3CH_2O + H_2O$	2.50E+12	0.00	24000	[259]
R5a	$CH_3CH_2OH + CH_3=CH_3CHOH + CH_4$	1.99E+01	3.37	7630	[259]
R5b	$CH_3CH_2OH + CH_3=CH_2CH_2OH + CH_4$	2.04E+00	3.57	7717	[259]
R5c	$CH_3CH_2OH + CH_3=CH_3CH_2O + CH_4$	3.30E+02	3.30	12283	[259]
R6a	$CH_3CHOH(+M)=CH_3CHO + H(+M)$	6.17E+09	1.31	33778	[276]
	Low-pressure limit:	1.77E+16	0.00	20782	
	Troe parameters: 0.187 65.2 2568	41226			
R6b	$CH_3CHOH(+M)=CH_2CHOH + H(+M)$	6.36E+09	1.33	35974	[276]

Continued on next page

Table 8.1 – *continued from previous page*

		Arrhenius data			
	Low-pressure limit:	8.18E+14	0.00	21517	
	Troe parameters: 0.473 10 2218 2615				
R6c	$CH_3CHOH(+ M)=CH_3 + CH_2O(+ M)$	2.22E+09	1.18	33987	[276]
	Low-pressure limit:	5.86E+15	0.00	21333	
	Troe parameters: 0.124 1 1729 50000				
R7a	$CH_3CHOH + H=CH_2CHOH + H_2$	3.14E+12	0.27	-334	[243]
R7b	$CH_3CHOH + H=C_2H_4 + H_2O$	1.65E+20	-1.81	9448	[a], [243]
R7c	$CH_3CHOH + H=CH_3 + CH_2OH$	4.03E+23	-2.53	13637	[a], [243]
R7d	$CH_3CHOH + H=C_2H_5 + OH$	6.27E+21	-2.11	15269	[a], [243]
R7e	$CH_3CHOH + H=CH_3CH_2OH$	1.63E+40	-7.82	12916	[a], [243, 292]
R8a	$CH_3CHOH + O_2=CH_3CHO + HO_2$	3.78E+20	-2.43	3090	[a], [277]
R8b	$CH_3CHOH + O_2=CH_2CHOH + HO_2$	4.38E+05	1.70	2330	[a], [277]
R9a$_{rev}$	$C_2H_4 + OH=CH_2CH_2OH$	2.79E+19	-2.41	1011	[a], [246]
R9b	$CH_2CH_2OH=CH_2CHO + H$	2.20E+05	2.84	32920	[279]
R10a	$CH_2CH_2OH + H=C_2H_4 + H_2O$	3.64E+16	-0.72	8767	[a], [243]
R10b	$CH_2CH_2OH + H=CH_2OH + CH_3$	7.47E+20	-1.69	13429	[a], [243]
R10c	$CH_2CH_2OH + H=C_2H_5 + OH$	8.07E+19	-1.51	15534	[a,b], [243]
R11a	$CH_2CH_2OH + O_2=CH_2CHOH + HO_2$	1.35E+10	0.49	6247	[a], $C_2H_5 + O_2$
R11b	$CH_2CH_2OH + O_2=HOCH_2CH_2OO$	2.91E+27	-4.72	5184	[a], $C_2H_5 + O_2$
R12	$HOCH_2CH_2OO=CH_2O + CH_2O + OH$	9.40E+08	0.99	22250	[293]
R13	$CH_3CH_2O(+ M)=CH_3 + CH_2O(+ M)$	6.31E+10	0.93	17100	[275]
	Low-pressure limit:	4.70E+25	-3.00	16001	
	Troe parameters: 0.426 0.3 2278 100000				
R14a	$CH_3CH_2O + H(+ M)=CH_3CH_2OH(+ M)$	3.08E+11	0.89	13	[283]
	Low-pressure limit:	3.77E+51	-15.55	11101	
R14b	$CH_3CH_2O + H(+ M)=CH_2OH + CH_3(+ M)$	2.56E+18	-1.05	5128	[283]
	Low-pressure limit:	2.99E+11	0.89	17	
R14c	$CH_3CH_2O + H=CH_3CHO + H_2$	7.47E+09	1.15	673	[283]
R15a	$CH_3CHO(+ M)=CH_3 + HCO(+ M)$	2.09E+22	-1.74	86355	[c], [284]
	Low-pressure limit:	8.81E+58	-11.30	95912	
R15b	$CH_3CHO(+ M)=CH_4 + CO(+ M)$	8.98E+21	-1.74	86355	[c], [284]
	Low-pressure limit:	3.78E+58	-11.30	95912	
	Troe parameters: 0.183 462 167734 1.58E+06				
R15c$_{rev}$	$CH_2CHOH(+ M)=CH_3CHO(+ M)$	9.66E+23	-3.29	59994	[275, 286]
	Low-pressure limit:	2.87E+45	-8.12	52204	
	Troe parameters: 0.5 863 320 100000				

Continued on next page

Table 8.1 – *continued from previous page*

		Arrhenius data			
R16a	$CH_3CHO + H = CH_3CO + H_2$	1.31E+05	2.58	1219	[284]
R16b	$CH_3CHO + H = CH_2CHO + H_2$	2.72E+03	3.10	5203	[284]
R16c	$CH_3CHO + H = CH_3CH_2O$	4.61E+07	1.71	7090	[284]
R17a	$CH_3CHO + OH = CH_2CHO + H_2O$	8.49E+13	0.00	5310	[193]
R17b	$CH_3CHO + OH = CH_3CO + H_2O$	2.76E+12	0.00	-709	[193]
R18a	$CH_3CHO + HO_2 = CH_3CO + H_2O_2$	2.40E+19	-2.20	14030	[259]
R18b	$CH_3CHO + HO_2 = CH_2CHO + H_2O_2$	2.30E+11	0.40	14864	[259]
R19	$CH_2CHOH(+ M) = CH_3CHO(+ M)$	9.66E+23	-3.29	59994	[275, 286]
	Low-pressure limit:	2.87E+45	-8.12	52204	
	Troe parameters: 0.5 863 320 100000				
R20a	$CH_2CHO + H = CH_3 + HCO$	7.47E+20	-1.69	13429	[a], [243]
R20b	$CH_2CHO + H = CH_3CO + H$	8.07E+19	-1.51	15534	[a], [243]
R21	$CH_2CHO + O = CH_2O + HCO$	5.00E+13	0.00	0	[243]
R22	$CH_2CHOH + HO_2 = CH_3CHO + HO_2$	1.49E+05	1.67	6810	[294]

[a] : at 100 atm pressure, for other pressures see the mechanism file in the supplementary materials.

[b] : for reactions between CH_2CH_2OH and other radicals, estimated by analogy to C_2H_5 reactions, see the mechanism file in the supplementary materials.

[c] : enhanced third-body efficiencies: H_2: 2.86, H_2O: 8.57, CH_4: 4.23, CO: 2.14, CO_2: 2.86, C_2H_6: 4.23, N_2: 1.43, HE: 1.00, AR: 1.00

8.4 Results and Discussion

8.4.1 Ethanol oxidation in the flow reactor

The aim of this work was to characterize the pyrolysis and oxidation of ethanol at high pressure and intermediate temperatures. Here, results from the flow reactor experiments are presented and the developed model is evaluated against them.

Figure 8.2 shows the results of pyrolysis experiments in which ethanol conversion starts around 825 K. The maximum of fuel conversion is 18% and occurs at 900 K. CH_4, CO, and C_2H_4 are the major detected products. The ethanol mole fraction fluctuates below the onset temperature of reaction, but these fluctuations are within the ±5% uncertainty of the liquid feeding system discussed earlier. Carbon is balanced within the maximum scatter of ±8%. This small gap can be due to the fluctuations of the liquid feeding system as well as the uncertainties in measuring aldehydes and ethanol.

The present model predicts the onset temperature of ethanol decomposition well but it slightly overestimates the chemical reactivity of ethanol at higher temperatures. As discussed earlier, the GC configuration does not allow quantifying acetaldehyde and methanol separately. According to the model, methanol is only formed in negligible quantities in all experiments conducted here, so it is expected that the measured quantity represents only acetaldehyde. The acetaldehyde yield from the model agrees well with the measurements at temperature below 875 K. However it should be noted that the relation between GC detector signals and acetaldehyde concentration is established by using the methanol response factor, so the measurement of acetaldehyde is more uncertain than those of other components.

Ethanol conversion starts around 700 K for the fuel-rich mixture (Φ=43, see figure 8.3). Acetaldehyde and CO are the major detected products of ethanol partial oxidation. It is not possible to quantify the methane concentration since the GC signals for CH_4 and CO overlap partly which may also slightly deteriorate the accuracy of CO measurement. Similar to the pyrolysis test, the model predicts a negligible methanol yield so the sum of methanol and acetaldehyde measured by GC is interpreted as acetaldehyde. The maximum conversion of ethanol is 36% while oxygen is fully consumed at high temperatures

The model predicts well the onset temperature of reaction but it marginally underestimates the fuel conversion at high temperatures. Although the model overpredicts the formation of ethane and formaldehyde to some extent, it reproduces well the fractions of O_2, C_2H_4, CO, and CH_3CHO. By adopting methane concentration from the model, the carbon loss in the experiments is 15% at maximum.

Under stoichiometric conditions, ethanol oxidation starts around 725 K. CO and CO_2 are the major detected products, as shown in figure 8.4. The CO concentration peaks around 750 K and drops gradually at higher temperatures. Aldehydes are detected around 725 K, which is the onset temperature of oxidation, but they soon disappear at higher temperatures. Ethene, detected in a few ppm, changes non-monotonically versus temperature.

The model reproduces fairly well the onset of fuel conversion as well as the concentration of major products. Notwithstanding CO is overestimated at high temperatures, the non-linear changes in aldehydes and ethene profiles are well predicted by the model. Balancing carbon reveals a maximum loss of 22%.

For the fuel-lean mixture (Φ=0.10), the fuel oxidation is observed at temperatures

above 725 K, the similar temperature to those found for stoichiometric and reducing mixtures. Again, aldehydes peak at 725 K, but they soon disappear at higher temperatures. The model yields a satisfactory agreement to the measurements and the carbon is balanced by a maximum loss of 18% which occurs at 725 K.

The data presented here are in line with the results by Haas et al. [61] who studied ethanol ignition at a lower pressure of 12.5 atm and found the ignition temperatures of 750–775 K under stoichiometric ($\Phi = 0.91$, 0.27% ethanol) and fuel–lean ($\Phi = 0.43$, 0.28% ethanol) conditions. No sign of negative temperature coefficient (NTC) behavior was observed neither in [61] nor in the present study.

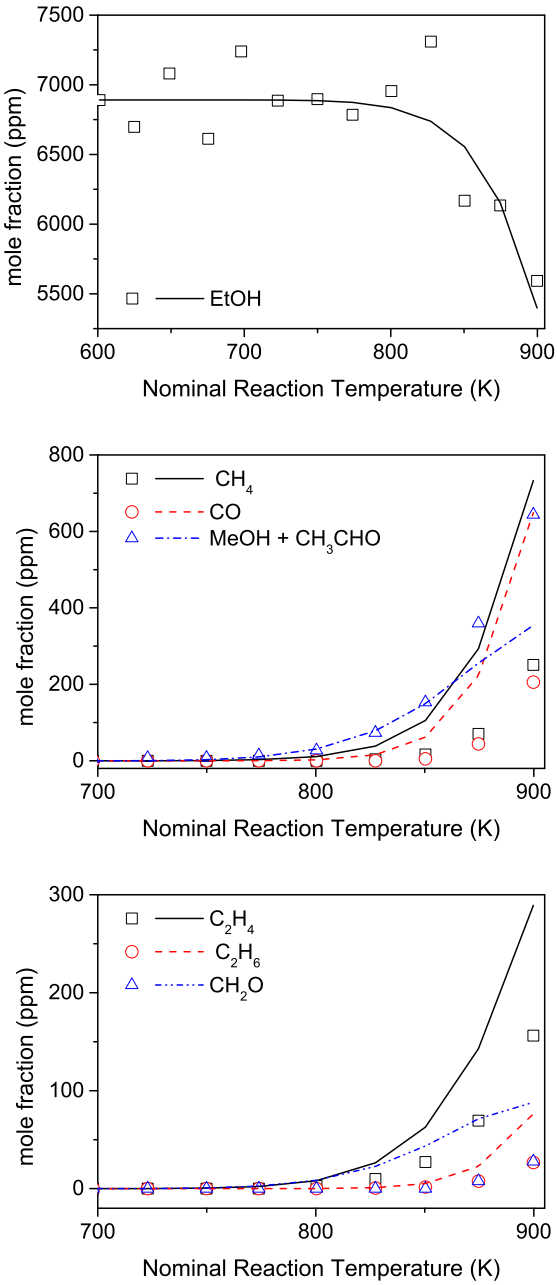

Figure 8.2: Results of pyrolysis experiments (0.689% ethanol in N_2) at 50 bar. Gas residence time is given by τ[s]=4098/T[K] (±8%).

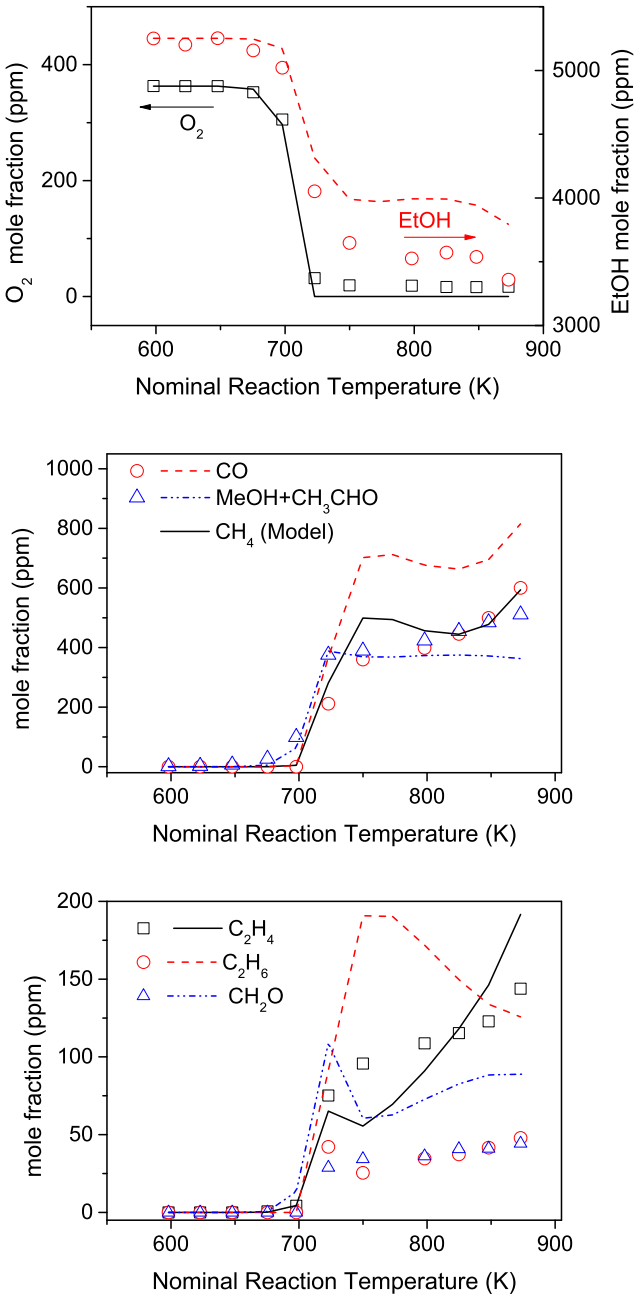

Figure 8.3: Results of experiments under reducing conditions (0.525% ethanol and 0.0363% O_2 in N_2, Φ=43) at 50 bar. Gas residence time is given by τ[s]=3840/T[K] (±8%).

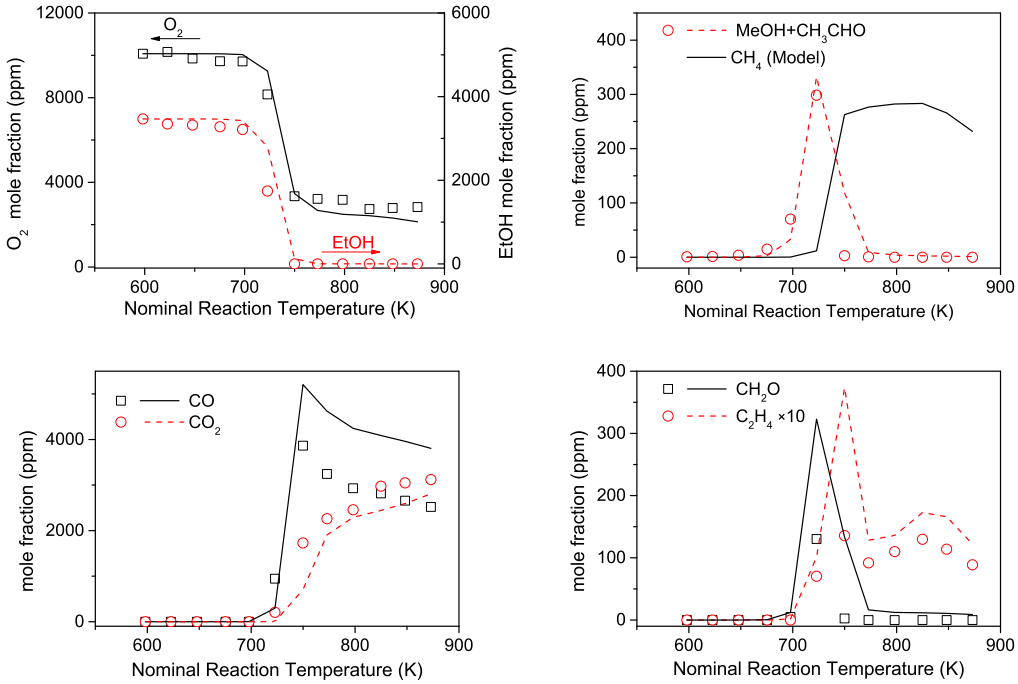

Figure 8.4: Results of experiments under stoichiometric conditions (0.525% ethanol and 0.0363% O_2 in N_2, Φ=1.0) at 50 bar. Gas residence time is given by τ[s]=3840/T[K] (±8%).

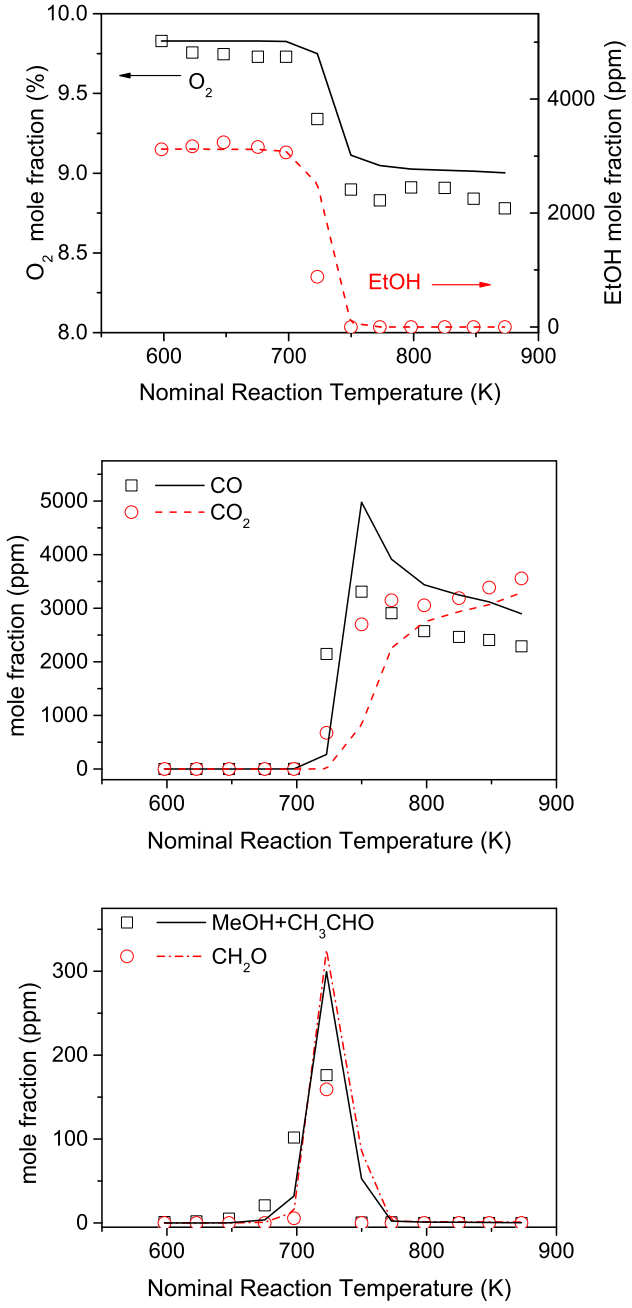

Figure 8.5: Results of experiments under oxidizing conditions (0.312% ethanol and 9.830% O_2 in N_2, Φ=0.10) at 50 bar. Gas residence time is given by τ[s]=3840/T[K] (±8%).

The consumption path of ethanol under the flow reactor conditions is shown in figure 8.6. Under all investigated conditions, ethanol is mainly consumed via conversion to the α-hydroxyethyl radical (CH_3CHOH). In the absence of oxygen, ethanol pyrolysis to CH_3CHOH is mainly governed by H-abstractions by H (R2a) and CH_3 (R5a). For ethanol oxidation, the H-abstraction reactions by OH (R3a) and HO_2 (R4a) take over the other abstraction reactions.

$$CH_3CH_2OH + H = CH_3CHOH + H_2 \quad \text{(R2a)}$$
$$CH_3CH_2OH + OH = CH_3CHOH + H_2O \quad \text{(R3a)}$$
$$CH_3CH_2OH + HO_2 = CH_3CHOH + H_2O \quad \text{(R4a)}$$
$$CH_3CH_2OH + CH_3 = CH_3CHOH + CH_4 \quad \text{(R5a)}$$

The formed α-hydroxyethyl radical (CH_3CHOH) either reacts with an oxygen molecule (R8a) or dissociates (R6a), depending on oxygen availability in the system.

$$CH_3CHOH(+M) = CH_3CHO + H(+M) \quad \text{(R6a)}$$
$$CH_3CHOH + O_2 = CH_3CHO + HO_2 \quad \text{(R8a)}$$

Both paths give acetaldehyde which is then dehydrogenated to the acetyl radical (CH_3CO).

$$CH_3CHO + H = CH_3CO + H_2 \quad \text{(R16a)}$$
$$CH_3CHO + OH(+M) = CH_3CO + H_2O(+M) \quad \text{(R17b)}$$
$$CH_3CHO + HO_2 = CH_3CO + H_2O_2 \quad \text{(R18a)}$$

The acetyl radical (CH_3CO) then dissociates to CO and CH_3.

$$CH_3CO(+M) = CH_3 + CO(+M) \quad \text{(R23)}$$

The H-abstraction from ethanol may also give CH_3CH_2O or CH_2CH_2OH, but these paths are less important in ethanol conversion. The path to CH_3CH_2O (R5c) is more favored under reducing conditions.

$$CH_3CH_2OH + CH_3 = CH_3CH_2O + CH_4 \quad \text{(R5c)}$$

The ethoxy radical (CH_3CH_2O) then dissociates to formaldehyde which finally gives HCO.

$$CH_3CH_2O(+M) = CH_2O + CH_3(+M) \quad \text{(R13)}$$
$$CH_2O + OH = HCO + H_2O \quad \text{(R24)}$$
$$CH_2O + HO_2 = HCO + H_2O_2 \quad \text{(R25)}$$

The HCO radical mainly reacts with molecular oxygen to give CO.

$$HCO + O_2 = CO + HO_2 \quad \text{(R26)}$$

The other product of H-abstraction from ethanol is β-hydroxyethyl radical (CH_2CH_2OH), which is more favored under stoichiometric and oxidizing conditions.

$$CH_3CH_2OH + OH = CH_2CH_2OH + H_2O \quad \text{(R3b)}$$

The CH_2CH_2OH radical either adds to molecular oxygen (R11b) or dissociates (R9a).

$$CH_2CH_2OH + O_2(+M) = HOCH_2CH_2OO(+M) \quad \text{(R11b)}$$
$$CH_2CH_2OH(+M) = C_2H_4 + OH(+M) \quad \text{(R9a)}$$

Then $HOCH_2CH_2OO$ dissociates to give two formaldehyde molecules.

$$HOCH_2CH_2OO(+M) = CH_2O + CH_2O + OH(+M) \quad \text{(R12)}$$

The reaction pathways presented here agree with a general pathway for ethanol oxidation suggested by Frassoldati et al. [262]. However, the lower temperatures of the current study favors oxygen association to CH_2CH_2OH (R11b) in addition to its dissociation (R9a) predicted in [262].

The sensitivities of selected reactions are analyzed via a brute-force method in which the sensitivity coefficient (S_i) is defined as

$$S_i = \frac{(\Delta X_{\mathrm{EtOH}}/X_{\mathrm{EtOH}})}{(\Delta k_i/k_i)} \quad (8.1)$$

Figures 8.7 and 8.8 show the results of the analysis for selected reactions under the flow reactor conditions. Ethanol pyrolysis is mainly affected by the reactions between

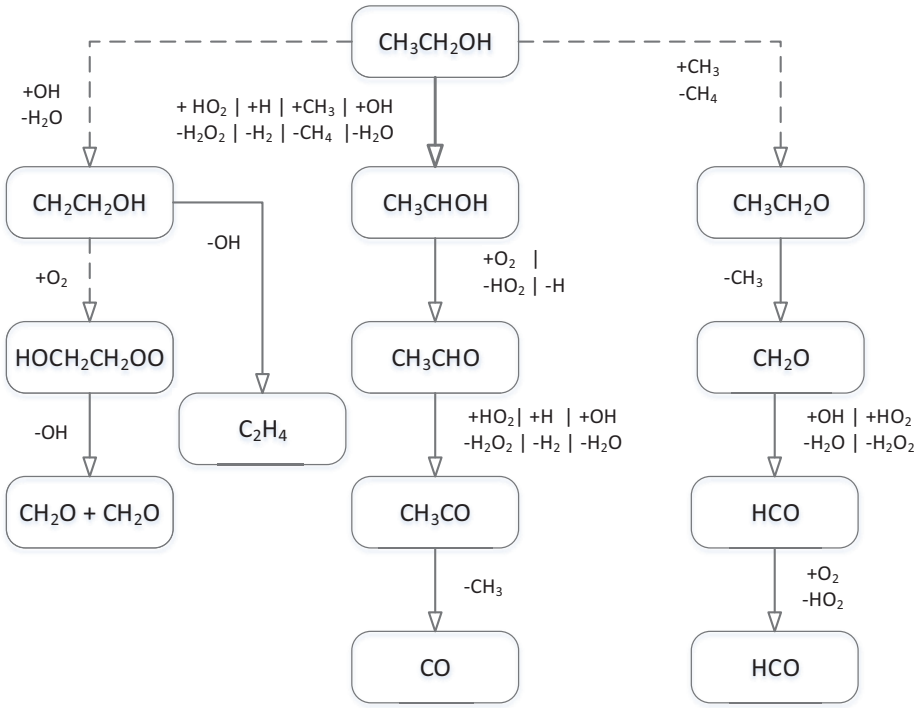

Figure 8.6: Consumption path for ethanol at 50 bar and 750–900 K under the flow reactor conditions.

ethanol and methyl radicals (R5).

$$\mathrm{CH_3CH_2OH + CH_3 = CH_3CHOH + CH_4} \quad \text{(R5a)}$$

$$\mathrm{= CH_2CH_2OH + CH_4} \quad \text{(R5b)}$$

$$\mathrm{= CH_3CH_2O + CH_4} \quad \text{(R5c)}$$

The ethanol dissociation to CH_2OH is also important in ethanol pyrolysis.

$$\mathrm{CH_3CH_2OH(+M) = CH_3 + CH_2OH(+M)} \quad \text{(R1b)}$$

Under reducing conditions and at 723 K, the reactions R27 and R28 also become

controlling steps.

$$HO_2 + HO_2 = H_2O_2 + O_2 \quad \text{(R27)}$$

$$H_2O_2(+M) = OH + OH(+M) \quad \text{(R28)}$$

Increasing R27 inhibits the fuel oxidation as HO_2 may be consumed by another sensitive abstraction reaction, R4a

$$CH_3CH_2OH + HO_2 = CH_3CHOH + H_2O \quad \text{(R4a)}$$

R28 promotes the oxidation by providing much needed hydroxyl radicals. Under the same conditions but at a temperature 150 K higher, the abstraction by hydroxyl radicals becomes important too.

$$CH_3CH_2OH + OH = CH_2CH_2OH + H_2O \quad \text{(R3b)}$$

For stoichiometric and oxidizing conditions, the reactions R28 and R4a are important over 723–900 K. At 900 K, formaldehyde reaction with the hydroxyl radical inhibits the fuel oxidation, as this reaction takes out hydroxyl radicals.

$$CH_2O + OH = HCO + H_2O \quad \text{(R24)}$$

The other path for formaldehyde conversion enhances the oxidation:

$$CH_2O + HO_2 = HCO + H_2O_2 \quad \text{(R25)}$$

Higher temperatures also promote the ethanol reaction with hydroxyl radicals.

$$CH_3CH_2OH + OH = CH_3CHOH + H_2O \quad \text{(R3a)}$$

$$= CH_2CH_2OH + H_2O \quad \text{(R3b)}$$

$$= CH_3CH_2O + H_2O \quad \text{(R3c)}$$

Again, the abstractions by HO_2 (R4, R25) promote the fuel oxidation whereas HO_2 conversion to H_2O_2 (R27) restrains ethanol oxidation.

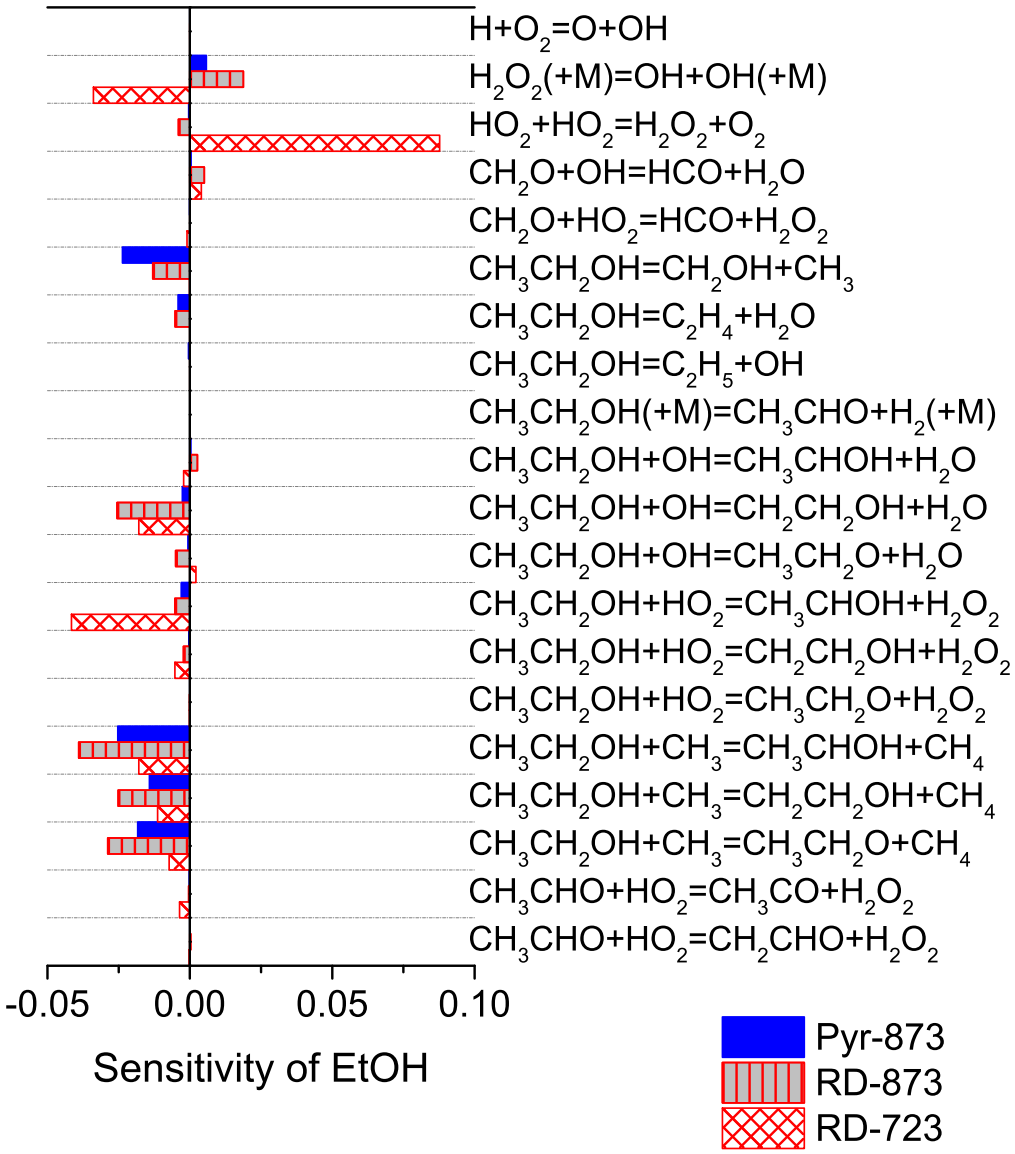

Figure 8.7: Sensitivity of ethanol prediction by the model at 50 bar and under the flow reactor conditions.

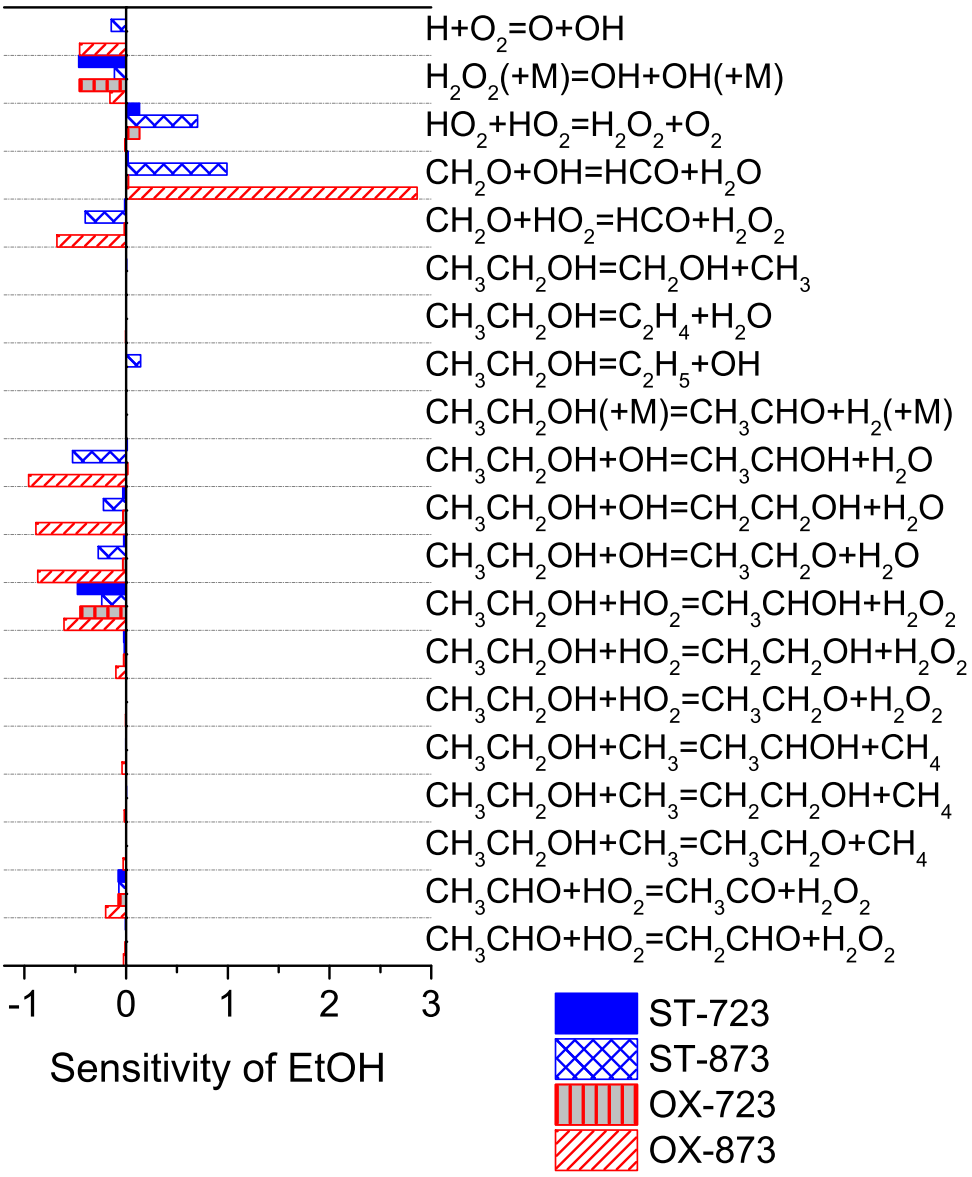

Figure 8.8: Sensitivity of ethanol prediction by the model at 50 bar and under the flow reactor conditions.

8.4.2 Comparison with literature data

8.4.2.1 Ignition at higher temperatures

Figure 8.9 presents selected ethanol ignition delays measured in shock tubes which make further evaluation of the model at higher temperatures possible. The ignition delays decrease monotonically by increasing temperature. The model can predict the ignition delays fairly well above 900 K. At lower temperatures, ignition delays are overpredicted.

The overprediction of models for long ignition delays (~ms) measured in shock tubes was reported and discussed earlier in [121, 125]. Over long residence times, pressure and temperature increase gradually behind the shock wave, even in non-reactive mixtures. To compensate for it, a pressure rise of 2% (per ms) is considered in simulating data from Cancino et al. [56]. A method suggested by Chaos and Dryer [121] is used to input the pressure variation in Chemkin [109], which improves the prediction of ignition delays. It is likely that inputting post-shock pressure history improves the model prediction against other low-temperature data as well. However, the model still overpredicts the ignition delays measured by Cancino et al. [56] by a factor of four at low temperatures.

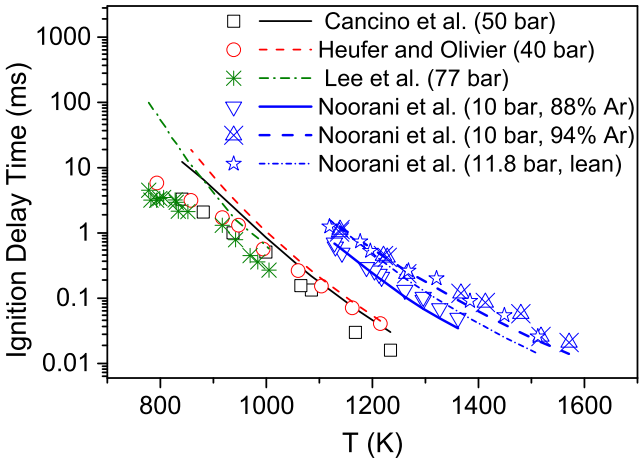

Figure 8.9: Ignition delay time of stoichiometric ethanol/air (from Cancino et al. [56], Lee et al. [60], and Heufer and Olivier [34]) and ethanol/O_2/Ar (Φ=0.5 and 1, from Noorani et al. [59]). The lines mark the present model prediction. In simulating data from Cancino et al. [56], a post-shock pressure rise of 2% (per ms) is included.

The sensitivity of ignition-delay prediction to selected reactions are calculated with

a brute-force method in which the coefficients are calculated as

$$S_i = \frac{(\Delta\tau/\tau)}{(\Delta k_i/k_i)} \tag{8.2}$$

where τ is the ignition delay time and k_i is the rare constant of i^{th} reaction. The results of the analyses for selected reactions are shown in figure 8.10. Among the evaluated reactions, the H-abstraction by HO_2 from ethanol is sensitive over temperatures of 800–1400 K.

$$CH_3CH_2OH + HO_2 = CH_3CHOH + H_2O \tag{R4a}$$

By increasing temperature, the importance of this reaction decreases while R29 becomes a bottleneck step in ignition.

$$H + O_2 = O + OH \tag{R29}$$

Both reactions R4a and R29 promote ignition and shorten the ignition delay time. At low temperature, the HO_2 radical is even more important when its conversion to H_2O_2 (R27) inhibits the ignition considerably, similar to the flow reactor conditions.

$$HO_2 + HO_2 = H_2O_2 + O_2 \tag{R27}$$

The importance of the H-abstraction reaction by HO_2 (R4a) in ethanol ignition at medium temperature has been noted earlier in [56, 60, 65, 295]. Here, the rate of this reaction is taken from Marinov [259] who estimated the rate constants by analogy to methanol reactions, something which naturally gives a rise in the uncertainty. To improve model predictions at temperatures below 1000 K, the rate constant of this reaction was modified in [56, 60, 65]. In the work by Cancino et al. [56], the overall rate of $CH_3CH_2OH + HO_2$ increased by orders of magnitude. Here, we refrain from optimizing the rate constant of $CH_3CH_2OH + HO_2$, but a more accurate description of this reaction could potentially improve the agreement at intermediate temperatures.

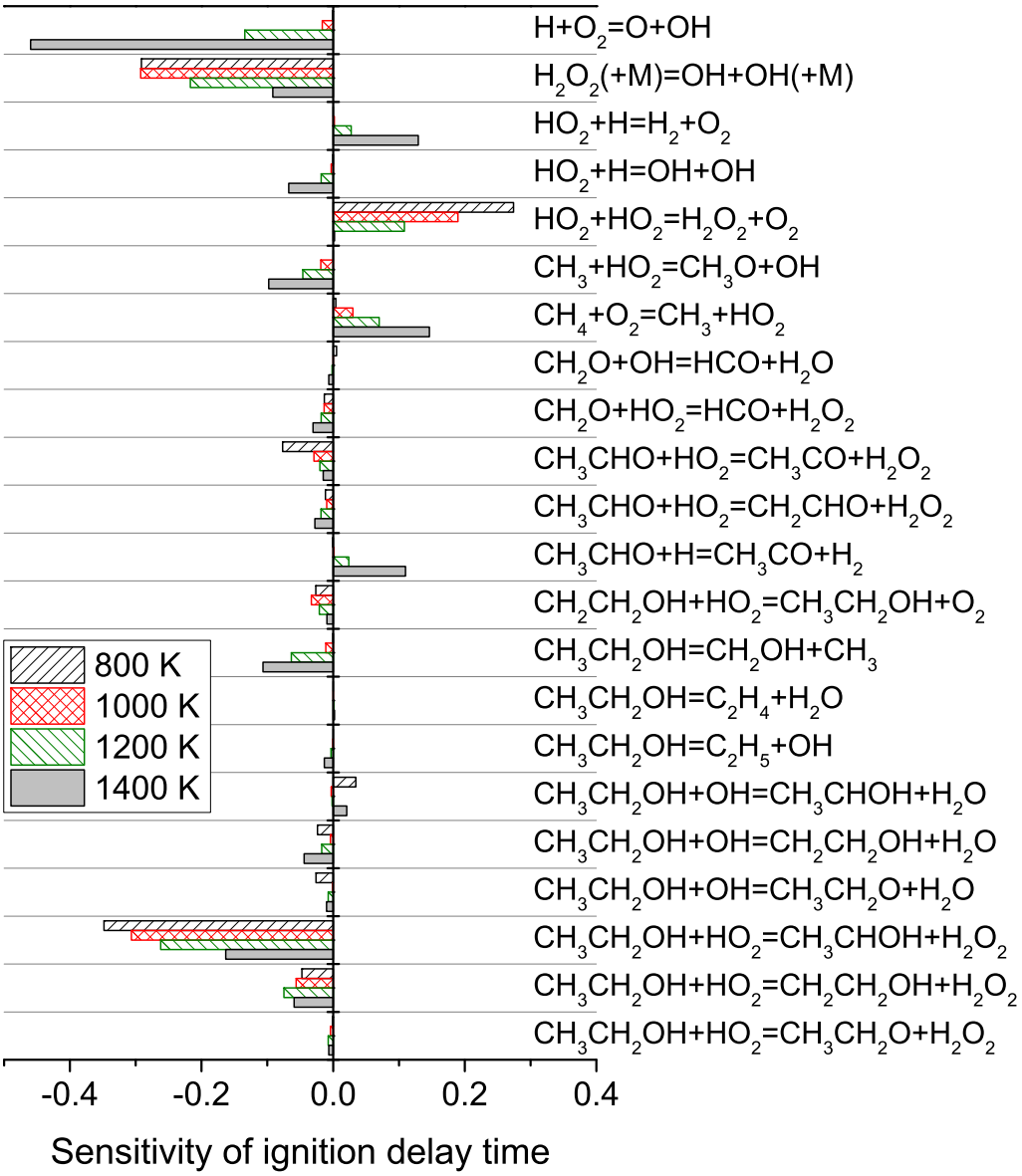

Figure 8.10: Sensitivity of ignition delay time prediction to selected reactions. The coefficients were calculated as $S_i = (\Delta\tau/\tau)/(\Delta k_i/k_i)$ for a stoichiometric ethanol/air mixtures at 50 bar.

8.4.2.2 Flame speed

Figure 8.11 compares the laminar flame speed of ethanol/air mixtures calculated by the model with those measured in [296–301]. At atmospheric pressure, the model slightly overpredicts the burning velocity but its prediction improves for fuel-rich mixtures. The trend of changes as well as the fuel-air equivalence ratio corresponding to the maximum flame speed are also predicted well.

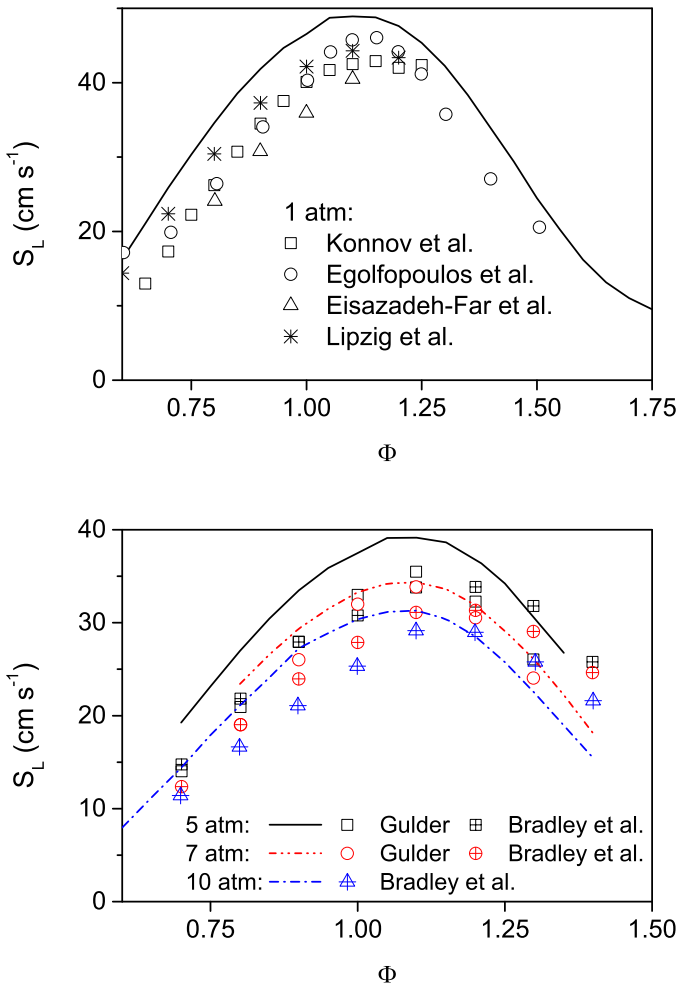

Figure 8.11: Laminar flame speed of ethanol/air mixture at (a) atmospheric pressure and initial temperature of 300 K; (b) 5, 7, and 10 bar and initial temperatures of 350, 350, and 358 K, respectively. Experimental results are from Gulder [296], Konnov et al. [297], Bradley et al. [298], Lipzig et al. [299], Egolfopoulos et al. [300], and Eisazadeh-Far et al. [301].

The model is further tested against data at higher pressures of 5, 7, and 10 bar. Experimental data for high pressures are taken from Gulder [296] and Bradley et al.

[298]. To avoid ethanol condensation in the mixtures, the initial temperature had to be increased at higher pressures. While the maximum flame speed at 5 and 7 bar occurred at Φ=1.1 according to Gulder [296], it was reported at Φ=1.2 by Bradley et al. [298]. This difference shifted the whole profiles and made noticeable scattering between the data, specially in the fuel-rich side. Although the model overestimates the flame speed for fuel–lean mixtures, its prediction improves for fuel-rich mixtures.

The sensitivity of gas flow rate (in mass unit) to reaction rate constants is analyzed with the built-in functions of Chemkin [109] and the results are shown in figure 8.12. Since the initial temperature and pressure are fixed, the mass flow rate sensitivity necessarily correlates to the sensitivity of flame speed. As expected, the reactions involving hydrogen atoms are far more sensitive in determining the burning velocity, e.g. the chain-branching reaction of R29.

$$H + O_2 = O + OH \tag{R29}$$

The CO oxidation which is the major source of heat in the system, influences significantly the calculation of flame speed.

$$CO + OH = CO_2 + H \tag{R30}$$

Whereas the decomposition of HCO promotes the burning rate noticeably, its reactions with any of H, OH, or O_2 slow down the burning rate.

The C_2 subset is relatively less important in determining the burning velocity. Its most important reactions are

$$C_2H_5 + HCO(+M) = CH_3 + CH_2CHO(+M) \tag{R31}$$
$$C_2H_3 + H(+M) = C_2H_4(+M) \tag{R32}$$
$$C_2H_2 + H(+M) = C_2H_3(+M) \tag{R33}$$

The most sensitive reaction from ethanol subset is R3a:

$$CH_3CH_2OH + OH = CH_3CHOH + H_2O \tag{R3a}$$

The deviation of model predictions from measurements of ethanol flame speed has been reported earlier in [297, 302]. Konnov et al. [297] showed that both mechanisms

by Konnov [303] and Saxena and Williams [263] significantly overpredict ethanol laminar burning velocities in lean and near-stoichiometric mixtures. Another model by Leplat et al. [264] generally underestimated burning velocities under fuel-rich conditions. Christensen et al. [302] found that in addition to ethanol, the flame speed of acetaldehyde is also generally overpredicted by the chemical kinetic models in [263, 303]. Christensen et al. [302] analyzed the sensitivity of the mechanism by Leplat et al. [264] and found R29 and R30 to be controlling for both ethanol and acetaldehyde flames, similar to the finding here for ethanol flames. However, Christensen et al. [302] found that the flame speed of ethanol is not sensitive to the acetaldehyde subset.

The calculation of burning velocity is highly affected by high temperature chemistry, so achieving a perfect agreement is not within the scope of this paper. However, a more thorough analysis of the model to improve the prediction of burning velocity can be interesting.

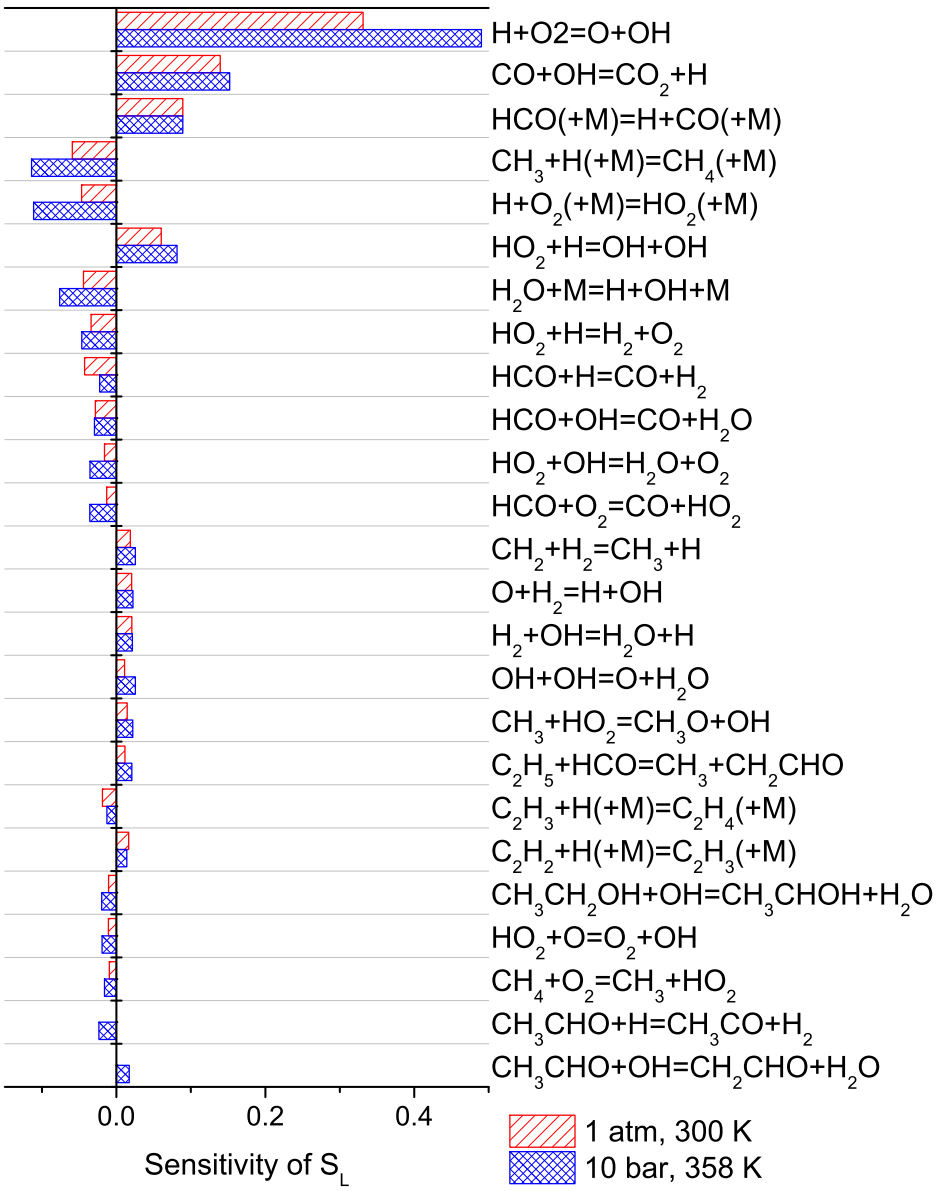

Figure 8.12: Sensitivity of flame speed of ethanol/air mixture at 1 atm and 10 bar pressures and the initial temperatures of 300 and 358 K.

Conclusion

Ethanol pyrolysis and oxidation were investigated in a laminar flow reactor at 50 bar pressure and temperatures of 700–900 K. The onset temperature of ethanol oxidation was found to be 700–725 K for a wide range of stoichiometries (Φ=0.1–43). In pyrolysis experiments, the decomposition of ethanol was detected above 850 K. A detailed chemical kinetic model was developed for ethanol oxidation and pyrolysis. The modeling results agreed well with the measured onset temperature of reaction as well as the concentration of most components upon initiation. The model was also manipulated to predict the ignition delay time and flame speed of ethanol measured in literature. Modeling results agreed well with the measured ignition delays above 900 K. Below 900 K, the model overpredicted ignition delays which might be due to the uncertainty in the rate constants of the reaction between ethanol and hydroperoxyl radicals. The flame speed were slightly overpredicted but the model prediction improved for fuel-rich mixtures. The presented data can be used to validate kinetic models at intermediate temperature and elevated pressures. More accurate determination of the key reactions identified here might be helpful in utilizing the model for industrial applications.

Chapter 9

Dimethyl ether (DME) and DME/Methane

Abstract

The pyrolysis and oxidation of dimethyl ether (DME) and its mixtures with methane were investigated at high pressures (50 and 100 bar) and intermediate temperatures (450–900 K). Mixtures highly diluted in nitrogen with different fuel-air equivalence ratios ($\Phi = \infty$, ~20, 1, ~0.05) were studied in a laminar flow reactor. At 50 bar, the DME pyrolysis started at 825 K and the major products were CH_4, CH_2O, and CO. For the DME oxidation at 50 bar, the onset temperature of reaction was 525 K, independent of fuel-air equivalence ratio. The DME oxidation was characterized by a negative temperature coefficient (NTC) zone which was found sensitive to changes in the mixture stoichiometry but always including temperatures of 575–625 K. The oxidation of methane doped by DME was studied in the flow reactor at 100 bar. The fuel-air equivalence ratio (Φ) was varied from 0.06 to 20, and the DME to CH_4 ratio changed over 1.8–3.6%. A profound promoting effect of DME addition on methane ignition was observed as the onset of reaction shifted to lower temperatures by 50–150 K. A detailed chemical kinetic model based on previous work from the same laboratory was developed by adding a DME subset from Zhao and coworkers and updating a few reactions. The model was evaluated against the present data as well as high temperature data from literature. The model predicted fairly well the onset temperature of the fuel conversion as well as the gas composition upon ignition. However, further studies of the interactions between DME and methane are needed.

9.1 Introduction

Combustion will remain the major source of energy for decades [2, 3]. The steady increase in the global energy demand as well as the release of carbon dioxide and harmful pollutants from the combustion of most fossil fuels are the major motivations to seek alternative sources of energy. In medium term, fossil-derived fuels which produce less pollutants and have a higher energy efficiency may relieve the environmental problems to some extent. Among the alternative fuels, dimethyl ether (DME) has attracted interest, especially for engines. DME can be produced from different feedstocks, e.g. oil, natural gas, coal, waste products, and biomass. Bio-derived DME fuel can potentially reduce the release of CO_2 to the environment. Lower ignition temperature, shorter ignition delay time, and easier evaporation compared to conventional diesel fuels make DME an attractive alternative. Replacing diesel fuel by DME reduces the emission of particulate matter (PM) and nitrogen oxides (NOx) from slightly modified compression-ignition (CI) engines [67–71]. The absence of a C – C bond in the molecular structure of DME, as well as its high oxygen content, are believed to suppress soot formation [69]. Using DME fuel in gas turbines has also been demonstrated and DME could replace natural gas in slightly modified gas turbines [72]. However, low energy density and potentially high emission of aldehydes and CO may challenge widespread usage of DME as a fuel [69].

DME has also been considered as an additive to improve combustion properties of various fuels, e.g. natural gas. Adding DME to natural gas accelerates ignition [73–76] and its addition to methane increases flame speed [74, 77]. DME addition to methane, ethane, and propane can suppress the formation of polycyclic aromatic hydrocarbons (PAHs) and soot [304]. Doping LPG by DME reduces NOx emissions [78]. DME is also an effective additive in ethanol-fueled CI and SI (spark-ignition) engines [79, 80]. DME was considered as an additive to methanol for use in CI engines in early studies [81–83]. Whereas DME accelerates methane ignition, its effect on ethane oxidation is more complicated [84]. Therefore it is vital to understand interactions between DME and the components of natural gas, especially since local variations in the composition of natural gas can be noticeable.

The DME ignition and oxidation show a complicated behavior of negative temperature coefficient (NTC) at intermediate temperatures [86, 90, 95, 98]. Ignition in engines and many industrial processes is greatly affected by combustion chemistry at high pressure and intermediate temperature. Despite this fact, the DME oxidation has

rarely been investigated at this range of temperature and pressure. This regime usually can be studied in flow reactors and rapid compression machines (RCM), but for DME shock tubes are also useful due to its short ignition delay time. Shock-tube measurements of ignition delays by Pfahl et al. [86] at pressures up to 40 bar reasserted the two-stage ignition of DME. Dagaut and coauthors [98, 99] used a jet-stirred reactor (JSR) to study DME oxidation at pressures up to 10 atm. Dryer and coauthors [90, 91, 95, 100] explored DME oxidation in flow reactors and RCM's at pressures below 20 atm. Their results were interpreted in terms of a chemical kinetic model in [95]. Other shock-tube studies by Li et al. [87], Hu et al. [76], Tang et al. [75], and Burke et al. [85] reported ignition delays at pressures below 25 bar. DME flame-measurements were conducted at pressures as high as 10–20 bar [305–307], but they mostly reflect the high-temperature oxidation-chemistry of DME. Ignition delays and flame speeds are valuable as benchmarks in studying combustion, but details of the oxidation chemistry cannot be drawn from them. Species profiles upon ignition from flow reactors can offer additional detailed insight into the involved chemistry.

Despite its importance, DME interactions with natural gas components were rarely characterized. Amano and Dryer [73] reported flow-reactor measurements of CH_4/DME oxidation at 10–18 atm and 800–1060 K. Burke et al. [85] measured ignition delays of CH_4/ DME mixtures over 10–30 atm and 600–1400 K. Other studies of DME addition to natural gas components [74–77] were limited to temperatures above 1000 K. Extending data to high pressure and intermediate temperature is beneficial in understanding CH_4 /DME interactions.

Developing chemical kinetic models for combustion of methane and DME is a vital step in utilizing their mixtures practically. Alzueta et al. [308] developed a model for DME oxidation based on their data from an atmospheric flow reactor. Dagaut and coauthors [98, 99] suggested a model for DME oxidation from their experiments in a jet-stirred reactor (JSR). Curran et al. [309] suggested a model which later has been extended to low temperatures in [90, 91]. Zhao et al. [95] improved the earlier models in [90, 91] by comparing with data from a flow reactor. More recently, Burke et al. [85] suggested an optimized model for DME oxidation.

In this work, we present the results of DME pyrolysis and oxidation at 50 bar and 450–900 K as well as results of tests on methane doped with DME at 100 bar pressure and 450–900 K. All experiments are conducted in a flow reactor. In addition to stoichiometric conditions, oxidation data are collected at strongly reducing (Φ=~20) and very

oxidizing conditions (Φ=0.04–0.06). The DME oxidation subset from Zhao et al. [95] is added to a reaction mechanism developed in our laboratory [1, 179, 237, 265, 310, 311] and reaction rate constants are modified according to recent updates. The developed model is evaluated against the present data and those available from the literature.

9.2 Experimental approach

The experimental setup was a laboratory-scale high-pressure laminar-flow reactor designed to approximate plug flow [102]. The setup was described in detail elsewhere [102] and only a brief description is provided here. The system was used here to study the oxidation chemistry of DME as well as its mixtures with methane. The temperature of the reactor was varied between 450–900 K. DME experiments were conducted at 50 bar pressure and with a constant flow rate of 4.53 Nliter/min (STP; 1 atm and 273.15 K). The oxidation of methane doped by DME was studied at 100 bar and at a flow rate of 3.23 Nliter/min (STP).

The reactions took place in a tubular quartz reactor (inner diameter of 8 mm) to minimize the effects of surface reactions. The quartz reactor was enclosed in a stainless steel tube that acted as a pressure shell. The system was pressurized from the feed gas cylinders and the reactor pressure was controlled by a pneumatically operated pressure control valve positioned after the reactor. The pressure fluctuations of the reactor were limited to ±0.2%.

The steel tube was placed in a tube oven with three individually-controlled electrical heating-elements that produced an isothermal reaction zone (±6 K) of ~37–41 cm in the middle of the reactor. A moving thermocouple was used to measure the temperature profile inside the pressure shell at the external surface of the quartz tube after stabilizing the system.

The flow rates of different gases were regulated by mass-flow controllers. The gases were mixed at ambient temperature well before entering the reactor, so a complete mixing was expected before the reactor.

All gases used in the present experiments were high purity gases or mixtures with certified concentrations (±2% uncertainty). The total flow rate was measured by a bubble flow meter downstream of the reactor. Using a quartz tube and conducting experiments at high pressures were expected to minimize the contribution from heterogeneous reactions at the reactor wall.

Downstream of the reactor, the system pressure was reduced to atmospheric level

prior to product analysis, which was conducted by an on-line *6890N Agilent Gas Chromatograph* (GC-TCD/FID from Agilent Technologies) calibrated according to the procedure in [237]. The GC allowed detection of O_2, CO, CO_2, CH_4, C_2H_4, and C_2H_6 with estimated uncertainties around 5%. Distinguishing methanol from acetaldehyde was not possible due to signal overlapping in the GC detector. However, it was possible to measure the signal areas corresponding to the sum of these components. According to simulations, no yield of acetaldehyde was expected in the present experiments, so the sum of acetaldehyde and methanol could be interpreted and quantified as methanol. Moreover, due to the small signal to noise ratio of formaldehyde, a larger uncertainty especially in measuring low quantities of formaldehyde was expected.

For each set of experiment, the mole fractions of reactants as well as the gas pressure were constrained while temperature of the isothermal zone was increased in small steps which simultaneously shortened gas residence time in the reactor.

Figure 9.1 shows the measured temperature profiles of nitrogen flow with flow rate and pressure corresponding to the DME experiments. The tabulated temperature profiles for the DME experiments can be found in supplementary data. For the doped methane experiments, the temperature profiles were similar to those given in [237]. Over this work, it was found that considering only the isothermal zone of the reactor in interpreting and simulating the data can be misleading, due to the high reactivity of DME at the low temperatures in the heating zone of the reactor. Therefore, a plug flow approximation with constrained temperature according to the measured profiles was used for modeling in Chemkin [109].

A potential source of uncertainty in interpreting data from the flow reactor was the temperature rise due to exothermic reactions. The reactants were strongly diluted in inert gas to limit the undesired temperature change. When the mixture has the highest exothermicity, a measured temperature profile indicated a marginal difference compared to the flow of pure nitrogen. Simulations with a constant pressure and enthalpy (adiabatic) model lead to a maximum temperature rise of 5 K for neat DME experiments and 25 K for the mixtures of methane and DME. The narrow quartz tube used here accelerated the thermal equilibrium between the reactive gas inside the reactor and the heating bath gas surrounding it, so the deviation of the gas temperature from the measured profiles is estimated to be even smaller.

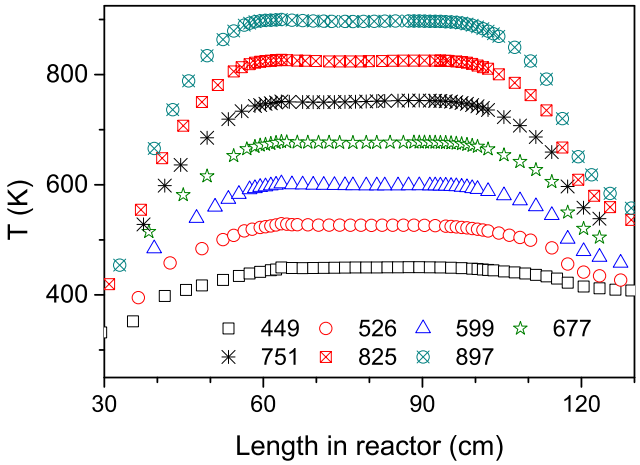

Figure 9.1: Measured temperature profiles across the reaction zone. The flow was pure nitrogen with a flow rate of 4.53 NL/min at a pressure of 50 bar.

9.3 Chemical kinetic model

The present reaction scheme consists of $H_2/C_1/C_2$/alcohols submodels developed in [1, 179, 237, 265, 310]. The DME submodel is taken from Zhao et al. [95] with some modifications discussed below. The oxidation subset for formic acid is taken from a recent study by Marshall and Glarborg [311].

An accurate description of the thermal decomposition of DME,

$$\begin{aligned} CH_3OCH_3(+M) &= CH_3 + CH_3O(+M) && \text{(R1)} \\ &= CH_4 + CH_2O(+M) && \text{(R1b)} \end{aligned}$$

is needed in modeling its high temperature oxidation [95]. Zhao et al. [95] calculated the dissociation rate of DME by using RRKM/master equation simulations. Sivaramakrishnan et al. [312] combined shock-tube measurements with theoretical calculations to derive pressure-dependent rate constants of DME dissociation over 500–2000 K and at pressures of 0.01–300 bar. The major channel of DME dissociation gave $CH_3 + CH_3O$ (R1) while a roaming channel to $CH_4 + CH_2O$ (R1b) contributed importantly at temperatures high enough, according to the experiments by Sivaramakrishnan et al. [312]. In contrast, the theoretical calculation in [312] predicted negligible branching to the roaming channel (R1b). More recently, Tranter et al. [313] measured the title reaction over temperatures of 1500–2450 K and at low pressures. Above 2000 K,

the total rate of DME dissociation by Tranter et al. [313] was smaller than that in [312]. Moreover, Tranter et al. [313] found the contribution of the roaming channel to be negligible, in line with the theory in [312]. We thus adopt the pressure-dependent rate constants derived by Sivaramakrishnan et al. [312] but we assign the total rate to the major channel (CH_3 + CH_3O).

The reaction between DME and a hydrogen atom (R2) was investigated experimentally by Sivaramakrishnan et al. [312] at 1149–1465 K.

$$CH_3OCH_3 + H = CH_3OCH_2 + H_2 \tag{R2}$$

Combining their results with available data from literature, Sivaramakrishnan et al. [312] suggested a rate constant for temperatures of 273–1465 K which is employed here.

The initial propagation reaction in combustion of DME at low-medium temperature is the H-abstraction by the hydroxyl radical [314]:

$$CH_3OCH_3 + OH = CH_3OCH_2 + H_2O \tag{R4}$$

In a recent measurement using laser flash-photolysis by Carr et al. [314], this reaction was explored at the temperatures of 200–850 K. Utilizing theoretical calculations and adding data at lower and higher temperatures from literature enabled Carr et al. [314] to derive a rate constant over 200–1400 K which is adopted in the present model.

The hydrogen abstraction by the HO_2 radical (R5) is an important step in low-temperature oxidation.

$$CH_3OCH_3 + HO_2 = CH_3OCH_2 + H_2O_2 \tag{R5}$$

Zhao et al. [95] increased the estimated rate of R5 by Curran et al. [309] to fit their model to experimental data. For this reaction we rely on a more recent calculation by Mendes et al. [315] over 500–2000 K which yielded a rate constant considerably smaller than that in [95].

The abstraction by the methyl radical from DME (R6) is an important step in DME consumption in flow reactors and shock tubes [95].

$$CH_3OCH_2 + CH_3 = CH_3OCH_2 + CH_4 \tag{R6}$$

For this reaction we rely on measurements by Tranter et al. [316] in a shock tube at low pressures and over 1163–1629 K.

The hydrogen abstraction by CH_3OO was found to be sensitive at low temperature combustion of methane [237]. A similar reaction (R10) for DME oxidation was not included in the model by Zhao et al. [95].

$$CH_3OCH_3 + CH_3OO = CH_3OCH_2 + CH_3OOH \quad \text{(R10)}$$

Recently Burke et al. [85] estimated the rate constant for this reaction. In the absence of any measurement or calculation, we adopt this estimation.

The dissociation of methoxymethyl radical (R11) is important in predicting ignition delay time [85].

$$CH_3OCH_2(+M) = CH_2O + CH_3(+M) \quad \text{(R11)}$$

For this reaction the most reliable data are those advocated by Burke et al. [85] who investigated its pressure dependence by RRKM calculations.

Methyl formate is an important intermediate in DME oxidation [243]. The major product of H-abstraction from methyl formate (R17–R23) is CH_3OCO. The CH_3OCO reactions with methyl and hydrogen radicals (R26–R30) are taken from a theoretical study by Labbe et al. [243].

$$\begin{aligned} CH_3OCO + H(+M) &= CH_3OH + CO(+M) && \text{(R26)} \\ &= CH_2O + CH_2O(+M) && \text{(R27)} \\ &= CH_4 + CO_2(+M) && \text{(R28)} \\ CH_3OCO + CH_3(+M) &= CH_3OH + CH_2CO(+M) && \text{(R29)} \\ &= CH_3CHO + CH_2O(+M) && \text{(R30)} \end{aligned}$$

Formic acid (HOCHO) is a major reaction intermediate in the oxidation of DME at medium temperatures [90]. Curran et al. [90] suggested two main pathways for the production of formic acid. The first one started with the decomposition of HO_2CH_2OCHO to OCH_2OCHO (R42) and then isomerization via R43. The $HOCH_2OCO$ radical decomposed to $HOCH_2O + CO$ (R44) and the $HOCH_2O$ radical

dissociated to the formic acid and a hydrogen radical (R46).

$$HO_2CH_2OCHO = OCH_2OCHO + OH \quad \text{(R42)}$$

$$OCH_2OCHO(+M) = HOCH_2OCO(+M) \quad \text{(R43)}$$

$$HOCH_2OCO(+M) = HOCH_2O + CO(+M) \quad \text{(R44)}$$

$$HOCH_2O(+M) = HOCHO + H(+M) \quad \text{(R46)}$$

In the second pathway, $HOCH_2O$ was formed from a reaction between formaldehyde and hydroxyl radical (R47).

$$CH_2O + OH = HOCH_2O \quad \text{(R47)}$$

We maintain these two pathways for the generation of the formic acid in our model, but the rate constant for R47 is taken from theoretical calculations by Xu et al. [317] instead of the estimation by Curran et al. [90]. For the oxidation of formic acid, we adopt the entire submodel from a recent study by Marshall and Glarborg [311].

Table 9.1: Reactions from DME chemical kinetic model. The rate constants are in the form of $k = AT^n\ exp(-E\ /\ (RT))$. Units are *mol*, *cm*, *K*, *s*, and *cal*.

	Reaction	A	n	E	Note/Ref.
R1	$CH_3OCH_3(+M)=CH_3 + CH_3O(+M)$	2.33E+19	−0.66	84092	[312]
	Low-pressure limit:	1.72E+59	−11.4	93243.0	
	Troe parameters: 1 1 880				
R2	$CH_3OCH_3 + H=CH_3OCH_2 + H_2$	3.94E+00	4.13	1779	[312]
R3	$CH_3OCH_3 + O=CH_3OCH_2 + OH$	1.86E−03	5.29	−109	‡
R4	$CH_3OCH_3 + OH=CH_3OCH_2 + H_2O$	1.95E+07	1.89	−365	[314]
R5	$CH_3OCH_3 + HO_2=CH_3OCH_2 + H_2O_2$	3.17E−03	4.64	10556	[315]
R6	$CH_3OCH_3 + CH_3=CH_3OCH_2 + CH_4$	1.02E+01	3.78	9687	[316]
R7	$CH_3OCH_3 + O_2=CH_3OCH_2 + HO_2$	4.10E+13	0.00	44910	‡
R8	$CH_3OCH_3 + CH_3O=CH_3OCH_2 + CH_3OH$	6.02E+11	0.00	4074	‡
R9	$CH_3OCH_3 + CH_3OCH_2O_2=CH_3OCH_2 + CH_3OCH_2O_2H$	5.00E+12	0.00	17690	‡
R10	$CH_3OCH_3 + CH_3OO=CH_3OCH_2 + CH_3OOH$	1.27E−03	4.64	10556	[85]
R11	$CH_3OCH_2=CH_2O + CH_3$	2.66E+29	−4.94	31786	[a], [85]
R12	$CH_3OCH_2 + CH_3O=CH_3OCH_3 + CH_2O$	2.41E+13	0.00	0	‡
R13	$CH_3OCH_2 + CH_2O=CH_3OCH_3 + HCO$	5.49E+03	2.80	5862	‡
R14	$CH_3OCH_2 + HO_2=CH_3OCH_2O + OH$	9.00E+12	0.00	0	‡

Continued on next page

Table 9.1 – *continued from previous page*

		Arrhenius data			
	Methyl formate (CH3OCHO) subset				
R15	$CH_3OCH_2O=CH_3OCHO + H$	1.75E+16	−0.66	11720	‡
R16	$CH_3OCHO=CH_3 + OCHO$	1.39E+18	−0.99	79140	‡
R17	$CH_3OCHO + O_2=CH_3OCO + HO_2$	1.00E+13	0.00	49700	‡
R18	$CH_3OCHO + OH=CH_3OCO + H_2O$	2.34E+07	1.61	35	‡
R19	$CH_3OCHO + HO_2=CH_3OCO + H_2O_2$	1.22E+12	0.00	17000	‡
R20	$CH_3OCHO + O=CH_3OCO + OH$	2.35E+05	2.5	2230	‡
R21	$CH_3OCHO + H=CH_3OCO + H_2$	4.55E+06	2	5000	‡
R22	$CH_3OCHO + CH_3=CH_3OCO + CH_4$	7.55E−01	3.46	5481	‡
R23	$CH_3OCHO + CH_3O=CH_3OCO + CH_3OH$	5.48E+11	0.00	5000	‡
R24	$CH_3OCO=CH_3O + CO$	7.45E+12	−1.76	17150	‡
R25	$CH_3OCO=CH_3 + CO_2$	1.51E+12	−1.78	13820	‡
R26	$CH_3OCO + H=CH_3OH + CO$	4.06E+20	−1.75	8027	[a], [243]
R27	$CH_3OCO + H=CH_2O + CH_2O$	8.11E+14	−0.68	8112	[a], [243]
R28	$CH_3OCO + H=CH_4 + CO_2$	3.40E+14	−0.40	9188	[a], [243]
R29	$CH_3OCO + CH_3=CH_3OH + CH_2CO$	2.22E+15	−0.45	16410	[a], [243]
R30	$CH_3OCO + CH_3=CH_3CHO + CH_2O$	3.79E+14	−0.63	18985	[a], [243]
	Low temperature sequence				
R31	$CH_3OCH_2 + O_2=CH_3OCH_2O_2$	2.00E+12	0.00	0	‡
R32	$CH_3OCH_2O_2 + CH_2O=CH_3OCH_2O_2H + HCO$	1.00E+12	0.00	11670	‡
R33	$CH_3OCH_2O_2 + CH_3OCH_2O_2=O_2 + CH_3OCH_2O + CH_3OCH_2O$	1.60E+23	−4.50	0	‡
R34	$CH_3OCH_2O_2 + CH_3OCH_2O_2=O_2 + CH_3OCHO + CH_3OCH_2OH$	6.84E+22	−4.50	0	‡
R35	$CH_3OCH_2O_2H=CH_3OCH_2O + OH$	2.11E+22	−2.12	43830	‡
R36	$CH_3OCH_2O=CH_3O + CH_2O$	9.72E+15	−1.10	20640	‡
R37	$CH_3OCH_2O + O_2=CH_3OCHO + HO_2$	5.00E+10	0.00	500	‡
	Isomerization				
R38	$CH_3OCH_2O_2=CH_2OCH_2O_2H$	6.00E+10	0.00	21500	‡
R39	$CH_2OCH_2O_2H=OH + CH_2O + CH_2O$	1.50E+13	0.00	20500	‡
R40	$CH_2OCH_2O_2H + O_2=O_2CH_2OCH_2O_2H$	7.00E+11	0.00	0	‡
R41	$O_2CH_2OCH_2O_2H=HO_2CH_2OCHO + OH$	4.00E+10	0.00	18500	‡
R42	$HO_2CH_2OCHO=OCH_2OCHO + OH$	3.00E+16	0.00	40000	‡
R43	$OCH_2OCHO=HOCH_2OCO$	1.00E+11	0.00	14000	‡
R44	$HOCH_2OCO=HOCH_2O + CO$	2.18E+16	−2.69	17200	‡
R45	$HOCH_2OCO=CH_2OH + CO_2$	5.31E+15	−2.61	20810	‡

Continued on next page

Table 9.1 – *continued from previous page*

		Arrhenius data			
	Formic acid (HOCHO) formation				
R46	$HOCH_2O$=HOCHO + H	1.00E+14	0.00	14900	‡
R47	CH_2O + OH=$HOCH_2O$	6.30E+06	1.63	4282	[317]

‡ according to Zhao et al. [95]

[a] at 100 atm pressure, for other pressures see the mechanism file in the supplementary data.

9.4 Results and Discussion

Species profiles from DME pyrolysis and oxidation in the flow reactor at intermediate temperatures (450–900 K) and high pressure (50 bar) are presented in this section. Later, the results of the oxidation experiments of methane doped by DME over 450–900 K and at 100 bar are presented and compared with the neat methane oxidation published in [237]. To simulate the flow reactor results, a plug flow approximation with constrained temperature (according to provided temperature profiles) and pressure is used in Chemkin [109].

9.4.1 Oxidation of neat DME in the flow reactor

Figure 9.2 gives results from DME pyrolysis experiments. The DME dissociation starts around 825 K, where a trace amount of methane is detected. At higher temperatures, CH_2O and CO are detected as well. Carbon is balanced well within ±3%. Although the model overpredicts slightly the conversion at high temperatures, it predicts the experimentally observed changes in the concentrations fairly well.

Under reducing conditions (Φ=20, figure 9.3), the DME consumption starts around 525 K, and CO is detected above 550 K. Between 575 K and 675 K, the concentration of DME remains almost constant which is an indication of the expected NTC behavior. The NTC trend is more pronounced in the oxygen profile in which two inflection points characterizing the NTC zone can be identified at 575 and 625 K. Between these points, the oxygen fraction increases with increasing temperature. DME oxidation resumes at higher temperatures and oxygen is completely consumed. Below 725 K, the major detected product is formaldehyde. Above 725 K, CO and CH_4 become the major products while formaldehyde is still non-negligible. Trace amounts of ethene and ethane are also measured above 700 K.

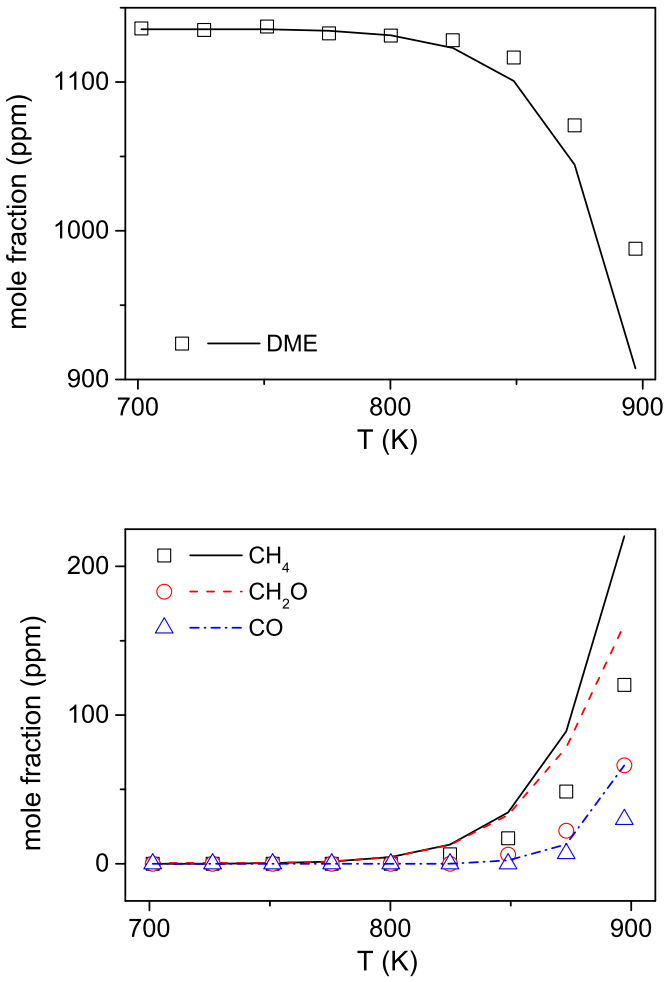

Figure 9.2: Results of DME pyrolysis experiments (1136 ppm of DME in N_2) at 50 bar.

The model predicts well the complicated non-monotonic changes in species fraction against temperature. The concentrations of CH_4, CO, and C_2H_6 are also well reproduced by the model. Although formaldehyde fraction is overpredicted, the trend of its change is reasonably predicted by the model.

Balancing carbon in the fuel-rich experiments reveals 12% carbon loss in the worst case. According to the simulations, formic acid (HOCHO) and methyl formate (CH_3OCHO) should be formed in trace amounts under current conditions, but our measuring facility does not allow us to quantify these components. Adopting the concentrations of formic acid and methyl formate from the model, the carbon balance is improved to 10%.

The NTC behavior of DME is more pronounced under stoichiometric conditions (figure 9.4). The onset of DME reaction is found around 525 K, where trace amounts of CO and CO_2 are detected. The first inflection point can be identified at 575 K; above this point the fraction of reactants increases as temperature is raised. This NTC trend continues until 650 K, the second inflection point. Above 650 K, the DME consumption is accelerated as temperature rises and DME disappears completely above 775 K. The oxygen consumption is confined to maximum 60%, likely due to the slow oxidation of CO at these temperatures. The inflection points can also be identified in the CO and CO_2 profiles. Withing these points, product formation is retarded. An interesting trend in the CO_2 fraction is seen at 800–900 K, where it falls but soon rises by elevating temperature. Methane increases monotonically with temperature and is formed in trace amounts above 725 K. Formaldehyde peaks around 700 K and disappears above 750 K.

The model predicts well the onset of reaction, the inflection points, and the fractions of DME, O_2, CO, and CH_4. However, it slightly overpredicts formaldehyde, and underpredicts CO_2 in the NTC zone. The simulations show that methyl formate (CH_3OCHO) and formic acid (HOCHO) are produced up to 40 and 84 ppm, respectively. Adopting their fractions from the model, carbon is balanced within ±6%.

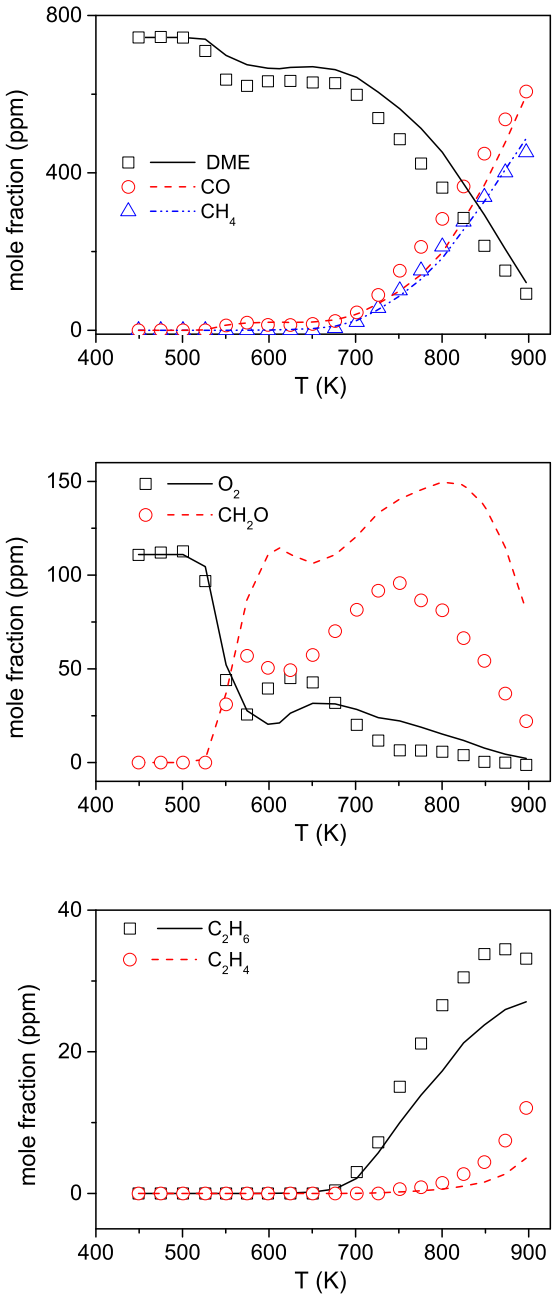

Figure 9.3: Results of DME reducing experiments at 50 bar (744/111 ppm of DME/O_2 in N_2, Φ=20.2).

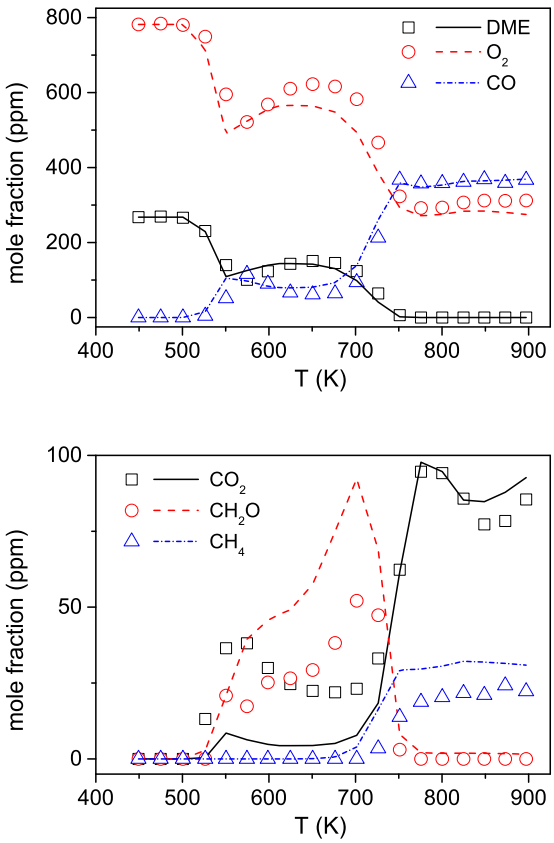

Figure 9.4: Results of DME experiments under stoichiometric conditions and at 50 bar (268/782 ppm of DME/O_2 in N_2, Φ=1.0).

For the fuel-lean mixtures (Φ=0.04), oxidation starts around 525 K. The NTC inflection points can be positioned at 575 and 675 K. Between these points, DME fraction remains almost constant but it disappears completely above 700 K. A similar plateau can be seen in the CO and CO_2 profiles over the same temperatures. Interestingly, the CO fraction is almost independent of temperature and it stays around 90 ppm over 575–900 K.

The model predicts well the onset of oxidation, the shapes of the profiles, and the fractions of the major components. However, it slightly underpredicts CO_2 formation at NTC zone, similar to that for stoichiometric conditions. The model predicts the maximum formation of methyl formate and formic acid in considerable amounts of 30 and 86 ppm, respectively. Adopting these concentrations from the model, the carbon loss in the experiments is less than 14%.

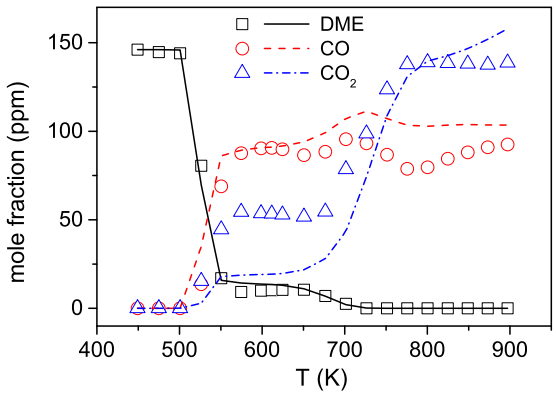

Figure 9.5: Results of DME oxidizing experiments at 50 bar (146/10774 ppm of DME/O_2 in N_2, Φ=0.04).

In the DME oxidization experiments, the onset temperature of DME reaction is around 525 K, independent of the fuel-air equivalence ratio. The inflection points corresponding to the NTC regime are slightly sensitive to changes in the stoichiometry, but generally NTC zone includes temperatures of 575–625 K. The present results are in line with the results of earlier jest-stirred reactor [98] and flow reactor [90, 92] experiments where DME ignition was reported around 525–550 K and the NTC zone included temperatures of 600–700 K, despite differences in their initial reactant concentrations and pressure.

As outlined earlier, the current experimental facility does not allow quantifying formic acid and methyl formate whereas the model predicts a considerable yield of

them, especially under stoichiometric and oxidizing conditions. Measuring these components in future studies can be beneficial for better evaluation of models. Moreover, the GC is not configured for quantifying C_3 components, and the model also does not include C_3 subset. Therefore, it is likely that the observed carbon loss in the experiments is partly due to the formation of C_3 components.

A better insight into DME oxidation in the flow reactor can be obtained from simulations. Figure 9.6 shows simulated DME conversion profiles against the length in the reactor under stoichiometric conditions. At 550 K, the conversion starts at the beginning of the isothermal zone of the reactor while the fuel conversion starts well before the isothermal zone at higher temperatures. This explains the necessity of including the temperature profiles to simulate the experimental results. Since the total flow rate (in mole) is constant, increasing temperature shortens the reactor residence time as well. To separate the effect of the residence time from the temperature variations, the DME conversion is simulated using an isothermal model with initial gas composition same as those in stoichiometric conditions. As shown in figure 9.7, the conversion starts well earlier at 650 K compared to 550 K, but the fuel consumption is retarded after a while at 650 K. At 750 K, DME conversion is slow and the final fuel conversion is less than that at 550 K, but more than at 650 K. Above 800 K, the fuel conversion is further accelerated by elevating temperature.

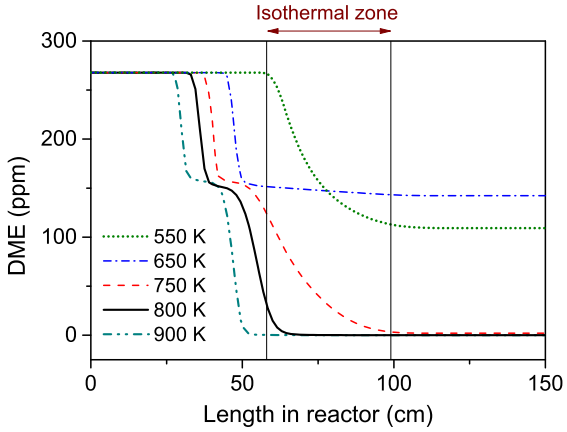

Figure 9.6: DME conversion versus the length in the reactor at different temperatures under conditions same as those in figure 9.4. The temperature profiles are implemented in the simulations.

Figure 9.8 shows the fractions of radicals in conditions corresponding to figure 9.7. At 550 K, radicals are formed later compared to other temperatures and their fraction

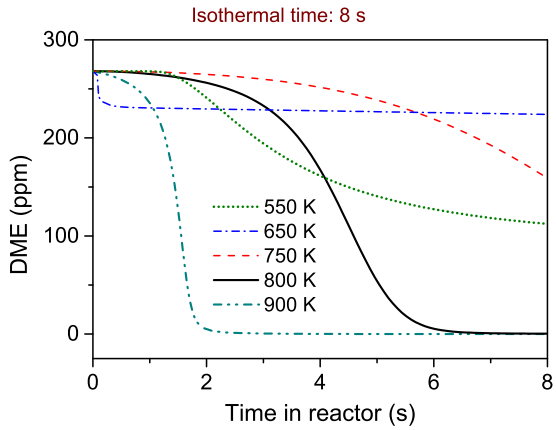

Figure 9.7: DME conversion versus time for initial conditions as those in figure 9.4. The conversion profile is shown for different isotherms.

stays high. The major reactivity at 800 and 900 K can be identified with local peaks in the radical concentrations.

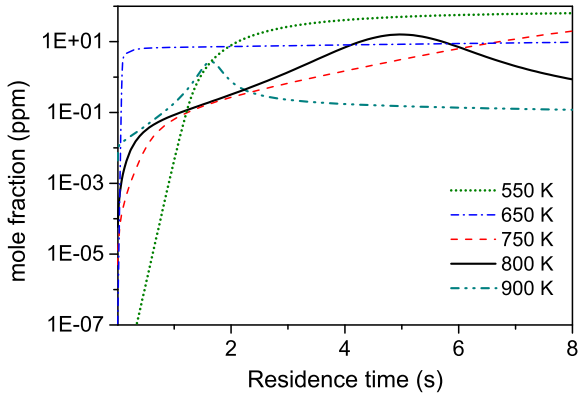

Figure 9.8: Radicals growth in the DME stoichiometric oxidation under conditions similar to those in figure 9.4. Simulations are conducted at constant temperatures. The number of radicals represents the summation of H, O, OH, HO_2, H_2O_2, CH_3, CH_3OO, C_2H_5, and CH_3OCH_2.

The model is used to analyze the reaction pathways of DME pyrolysis and oxidation under the flow reactor conditions. The analysis (figure 9.9) shows that in the absence of oxygen the pyrolysis of DME initiates by its dissociation (R1),

$$CH_3OCH_3(+M) = CH_3O + CH_3(+M) \qquad \text{(R1)}$$

and followed by CH_3O dissociation (R48).

$$CH_3O(+ M) = CH_2O + H(+ M) \quad \text{(R48)}$$

The produced hydrogen radical can attack another DME molecule (R2) to give a methoxy-methyl radical (CH_3OCH_2).

$$CH_3OCH_3 + H = CH_3OCH_2 + H_2 \quad \text{(R2)}$$

The CH_3OCH_2 radical dissociates to formaldehyde and a methyl radical (R11),

$$CH_3OCH_2(+ M) = CH_2O + CH_3(+ M) \quad \text{(R11)}$$

and the formed methyl radicals can attack another DME molecule,

$$CH_3OCH_3 + CH_3 = CH_3OCH_2 + CH_4 \quad \text{(R6)}$$

so the chain-propagating continues. When the concentrations of the methyl and hydrogen radicals increase enough, the major consumption of DME is governed by its reactions with CH_3 (R6) and H (R2). More production of formaldehyde activates its consumption path via reaction with the methyl radical,

$$CH_2O + CH_3 = HCO + CH_4 \quad \text{(R49)}$$

where HCO eventually decomposes to CO and a hydrogen atom.

For DME oxidation, however the process is more complicated. DME reaction with molecular oxygen,

$$CH_3OCH_3 + O_2 = CH_3OCH_2 + HO_2 \quad \text{(R7)}$$

and to a lesser extent the thermal decomposition of DME (R1) initiate the reactions at 550–800 K. Around 900 K, DME dissociation takes over the initiation process. As shown in figure 9.9 for the temperatures of 550–900 K, DME is mainly consumed with H-abstraction by OH radicals (R4). The abstraction reactions by H (R2) and CH_3 (R6)

also contribute, especially for fuel-rich conditions at relatively high temperatures.

$$CH_3OCH_3 + OH = CH_3OCH_2 + H_2O \quad \text{(R4)}$$
$$CH_3OCH_3 + H = CH_3OCH_2 + H_2 \quad \text{(R2)}$$
$$CH_3OCH_3 + CH_3 = CH_3OCH_2 + CH_5 \quad \text{(R6)}$$

At temperatures as high as 900 K, the CH_3OCH_2 radical dissociates directly to formaldehyde (R11) which eventually yields CO. At lower temperature of 750 K, almost half of the CH_3OCH_2 radicals add to molecular oxygen (R31) to form $CH_3OCH_2O_2$ which itself isomerizes to $CH_2OCH_2O_2H$ via R38.

$$CH_3OCH_2 + O_2(+M) = CH_3OCH_2O_2(+M) \quad \text{(R31)}$$
$$CH_3OCH_2O_2(+M) = CH_2OCH_2O_2H(+M) \quad \text{(R38)}$$

The $CH_2OCH_2O_2H$ radical dissociates and gives two formaldehyde molecules and a hydroxyl radical:

$$CH_2OCH_2O_2H(+M) = OH + CH_2O + CH_2O(+M) \quad \text{(R39)}$$

Below 700 K, the direct conversion of CH_3OCH_2 to formaldehyde (R11) disappears from the reaction path and CH_3OCH_2 removal is overtaken by oxygen addition (R31). As temperature decreases furthermore, the fuel conversion becomes even more complicated, as $CH_2OCH_2O_2H$ does not dissociate to CH_2O via R39 anymore. Instead, it adds to another oxygen molecule to form $O_2CH_2OCH_2O_2H$ (R40) which dissociates to HO_2CH_2OCHO(R41). The later radical isomerizes (R42) and gives OCH_2OCHO.

$$CH_2OCH_2O_2H + O_2(+M) = O_2CH_2OCH_2O_2H(+M) \quad \text{(R40)}$$
$$O_2CH_2OCH_2O_2H(+M) = HO_2CH_2OCHO + OH(+M) \quad \text{(R41)}$$
$$HO_2CH_2OCHO(+M) = OCH_2OCHO + OH(+M) \quad \text{(R42)}$$

These steps (R41–R42) produce two hydroxyl radicals per each $O_2CH_2OCH_2O_2H$ radical consumed. This path eventually yields formic acid that oxidizes to CO_2.

The path favored at 550–650 K produces more radicals than it consumes, so even at such low temperatures it accelerates the ignition considerably, because of chain-branching. The paths followed at higher temperatures are also chain-branching, but

less efficient in generating radicals. As the temperature rises to around 900 K, the hydrogen peroxide dissociation becomes the major source of OH production hence accelerating the ignition considerably. The presented pathways are generally independent of the stoichiometries investigated here.

The reaction path demonstrated here agrees well with analyses by Guo et al. [318] and by Curran et al. [90] although they were mainly focused on pressures lower than the present work.

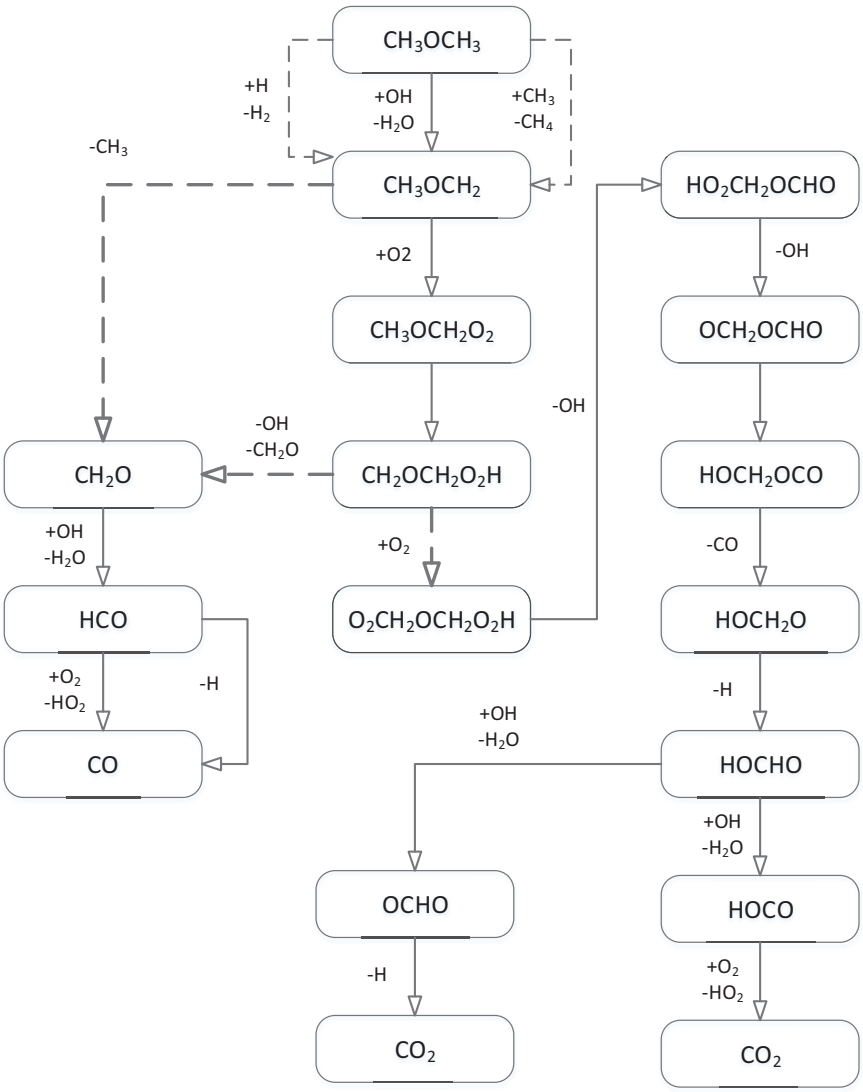

Figure 9.9: The reaction pathways of DME at different stoichiometries under the flow reactor conditions at 50 bar and 550–900 K.

The sensitivities of predicted DME fraction under the flow reactor conditions are analyzed via a brute-force method in which the sensitivity coefficient (S_i) is defined as

$$S_i = \frac{(\Delta X_{\mathrm{DME}}/X_{\mathrm{DME}})}{(\Delta k_i/k_i)} \tag{9.1}$$

According to figures 9.10 and 9.11, the abstraction reaction from DME by CH_3 (R6) as well as DME thermal decomposition (R1) are sensitive in the pyrolysis of DME.

$$CH_3OCH_3(+M) = CH_3 + CH_3O(+M) \tag{R1}$$
$$CH_3OCH_3 + CH_3 = CH_3OCH_2 + CH_4 \tag{R6}$$

In the presence of a small amount of oxygen, under reducing conditions and at high temperatures, the abstraction steps by H (R2) and HO_2 (R5) radicals also become important.

$$CH_3OCH_3 + H = CH_3OCH_2 + H_2 \tag{R2}$$
$$CH_3OCH_3 + HO_2 = CH_3OCH_2 + H_2O_2 \tag{R5}$$

While R2 inhibits the fuel conversion, the reaction between a hydrogen atom and molecular oxygen (R50) promotes the fuel conversion.

$$H + O_2(+M) = HO_2(+M) \tag{R50}$$

Formaldehyde conversion to the formyl radical is another step promoting fuel conversion.

$$CH_2O + CH_3 = HCO + CH_4 \tag{R49}$$

Under reducing conditions but at lower temperatures of 550–650 K, oxygen addition to $CH_2OCH_2O_2H$ (R40) becomes a critical step.

$$CH_2OCH_2O_2H + O_2(+M) = O_2CH_2OCH_2O_2H(+M) \tag{R40}$$

The sensitivity coefficients for reactions R2 and R50 change their signs compared to the high-temperature reducing conditions.

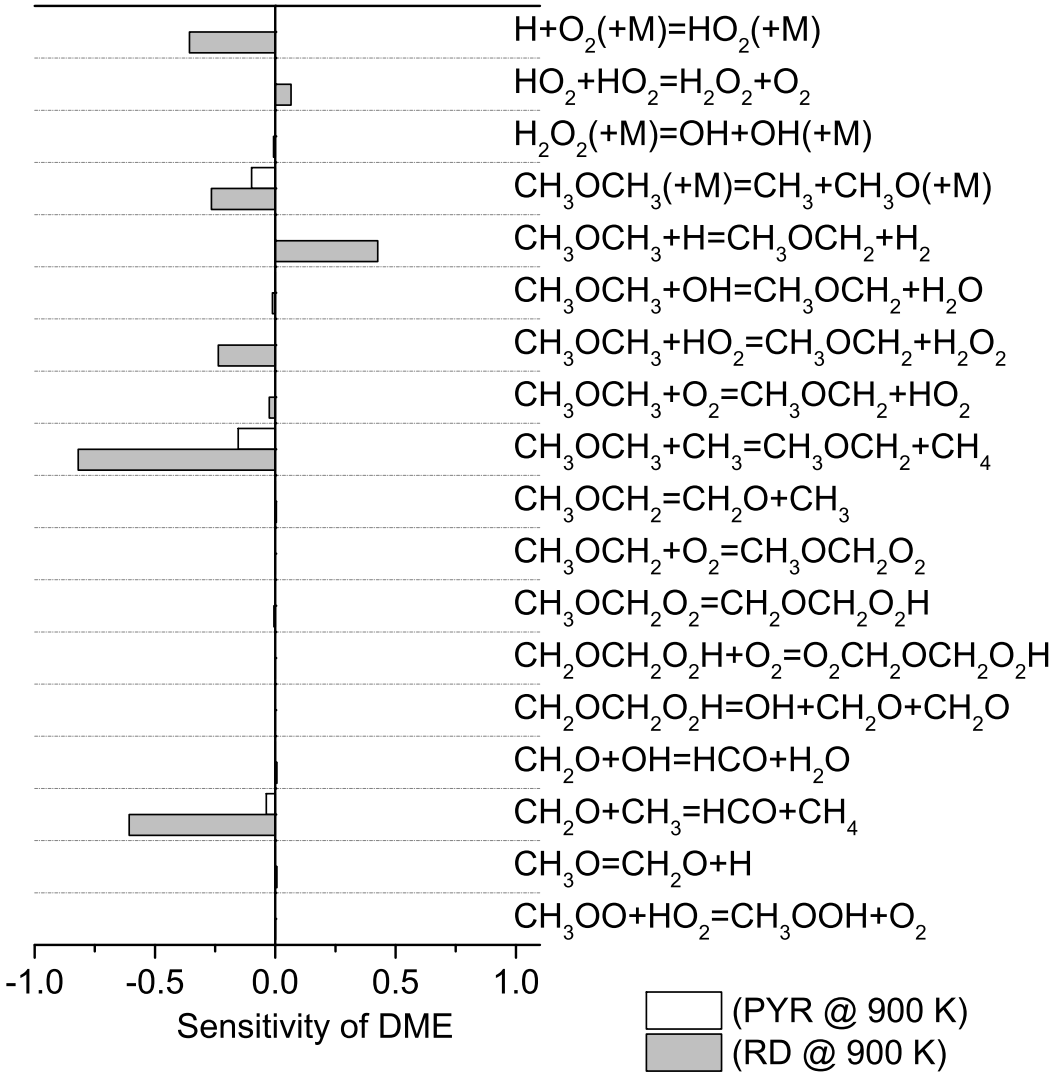

Figure 9.10: Sensitivity coefficients for DME pyrolysis and reduction under conditions similar to those in figures 9.2 and 9.3. The coefficients are calculated by considering only the isothermal part of the reactor (the gas residence time as τ[s] = 3534 / T[K]).

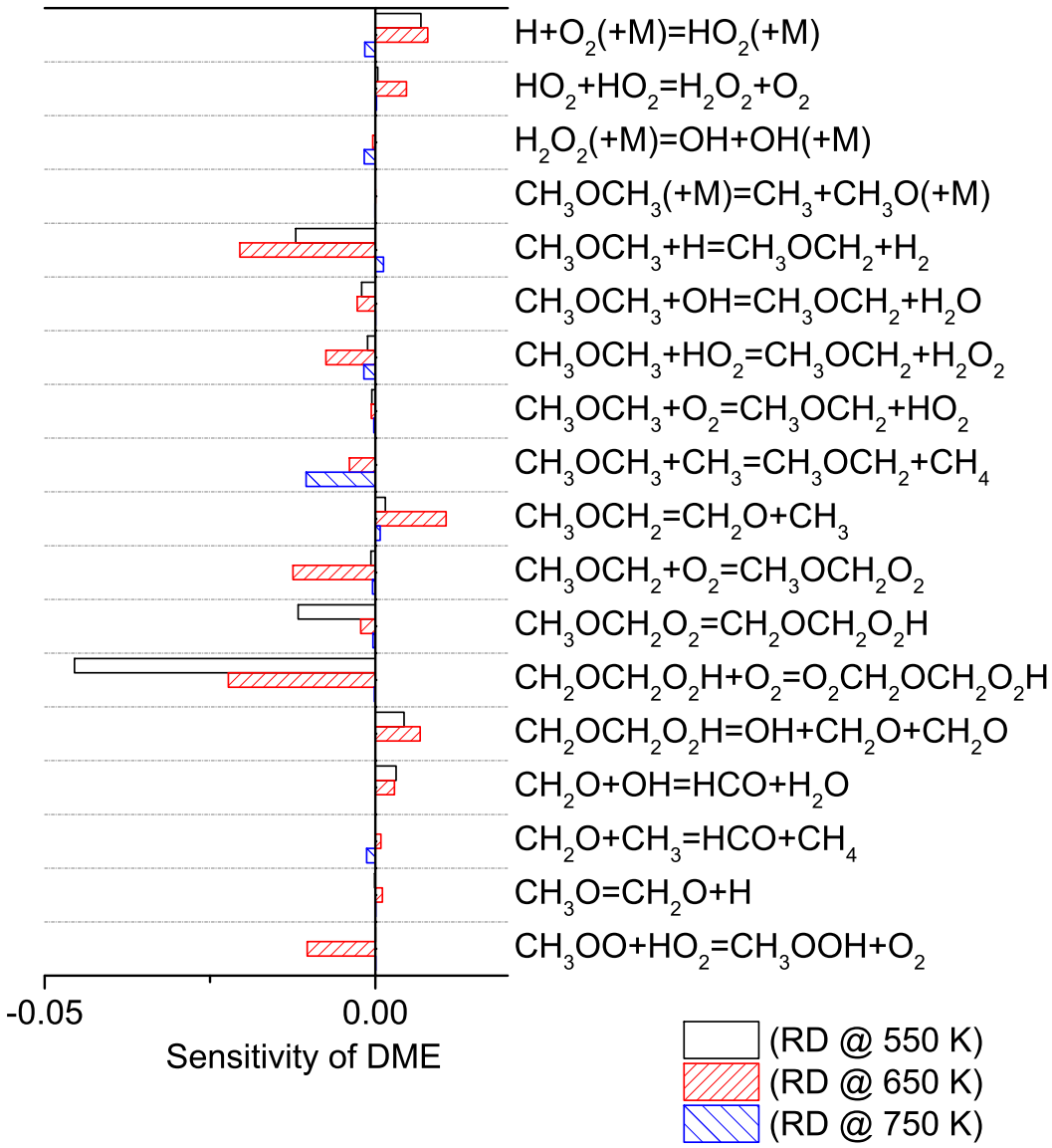

Figure 9.11: Sensitivity coefficients for DME pyrolysis and reduction under conditions similar to those in figures 9.2 and 9.3. The coefficients are calculated by considering only the isothermal part of the reactor (the gas residence time as τ[s] = 3534 / T[K]).

Figures 9.12 and 9.13 show the results of sensitivity analyses under stoichiometric and oxidizing conditions. For the stoichiometric mixture, the fuel conversion at high temperature is extensively affected by the rate constant of the reaction between formaldehyde and a hydroxyl radical,

$$CH_2O + OH = HCO + H_2O \quad \text{(R51)}$$

This reaction inhibits the fuel oxidation by removing much needed hydroxyl radicals. DME conversion at this temperature is also sensitive to the abstraction by OH,

$$CH_3OCH_3 + OH = CH_3OCH_2 + H_2O \quad \text{(R4)}$$

Furthermore, the chain-terminating reaction R52 inhibits substantially the fuel conversion.

$$HO_2 + HO_2 = H_2O_2 + O_2 \quad \text{(R52)}$$

At the lower temperature of 550 K and under stoichiometric conditions, the formaldehyde reaction with the hydroxyl radical (R51) is not so sensitive. Instead, the oxygen addition to $CH_2OCH_2O_2H$ (R40) becomes important. The isomerization of $CH_3OCH_2O_2$ to $CH_2OCH_2O_2H$ (R38) is also sensitive at 550 K, whereas the rate of this step turns to be less important at higher temperatures.

$$CH_3OCH_2O_2(+M) = CH_2OCH_2O_2H(+M) \quad \text{(R38)}$$

For the fuel-lean mixture, high temperature oxidation is controlled considerably by the reaction between formaldehyde and a hydroxyl radical (R51), similar to high-temperature stoichiometric conditions. At 750 K, the dissociation of $CH_2OCH_2O_2H$ (R39) also retards the DME oxidation to a great extend.

$$CH_2OCH_2O_2H(+M) = OH + CH_2O + CH_2O(+M) \quad \text{(R39)}$$

At this temperature, according to the reaction pathways, the path to formaldehyde (R39) and the path to $O_2CH_2OCH_2O_2H$ (R40) contribute almost equally in removing the $CH_2OCH_2O_2H$ radical. In other words, the transition from low-temperature route to the high-temperature one occurs around 750 K. This can explain the large negative

sensitivity coefficient of R39, as enhancing R39 favors the high-temperature path which is less efficient in generating radicals.

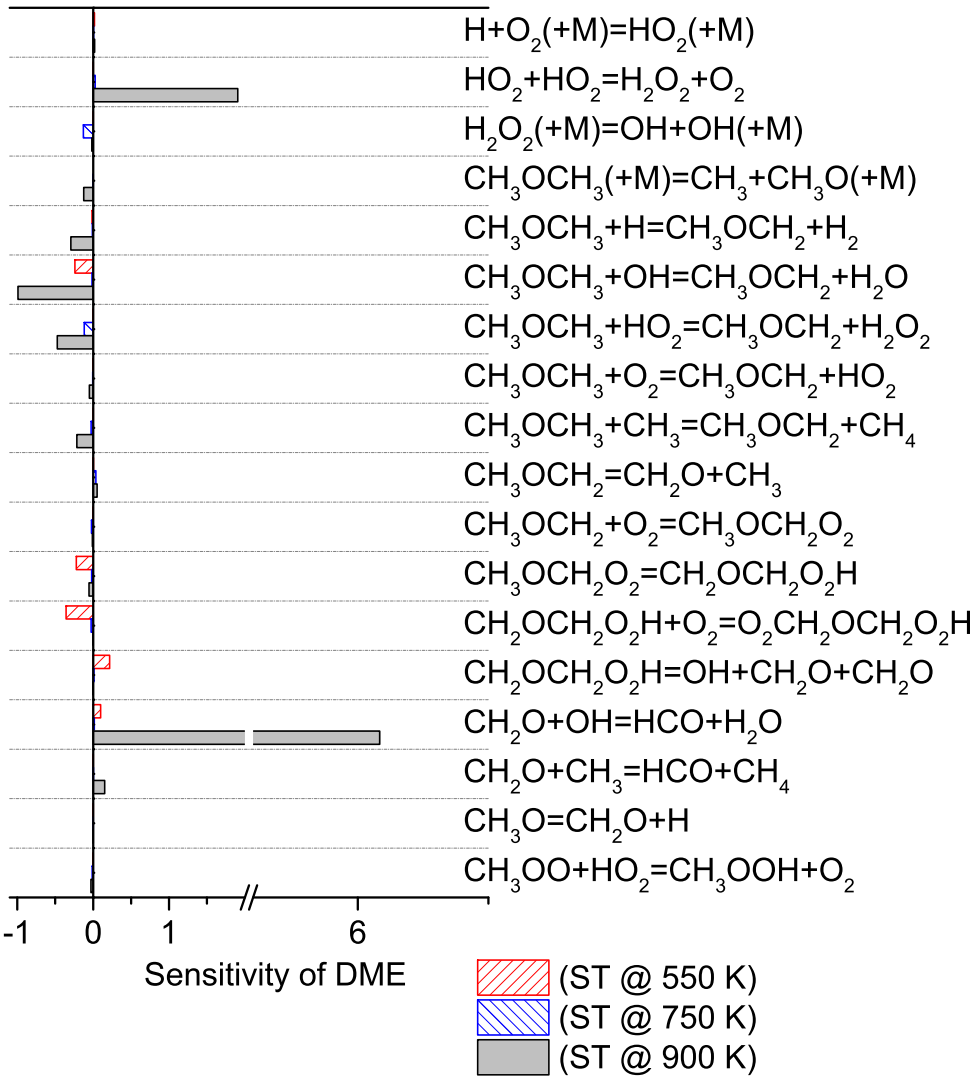

Figure 9.12: Sensitivity coefficients for DME conversion under stoichiometric and oxidizing conditions similar to those in figures 9.4 and 9.5. The coefficients are calculated considering only the isothermal part of the reactor (τ[s] = 3534 / T[K]).

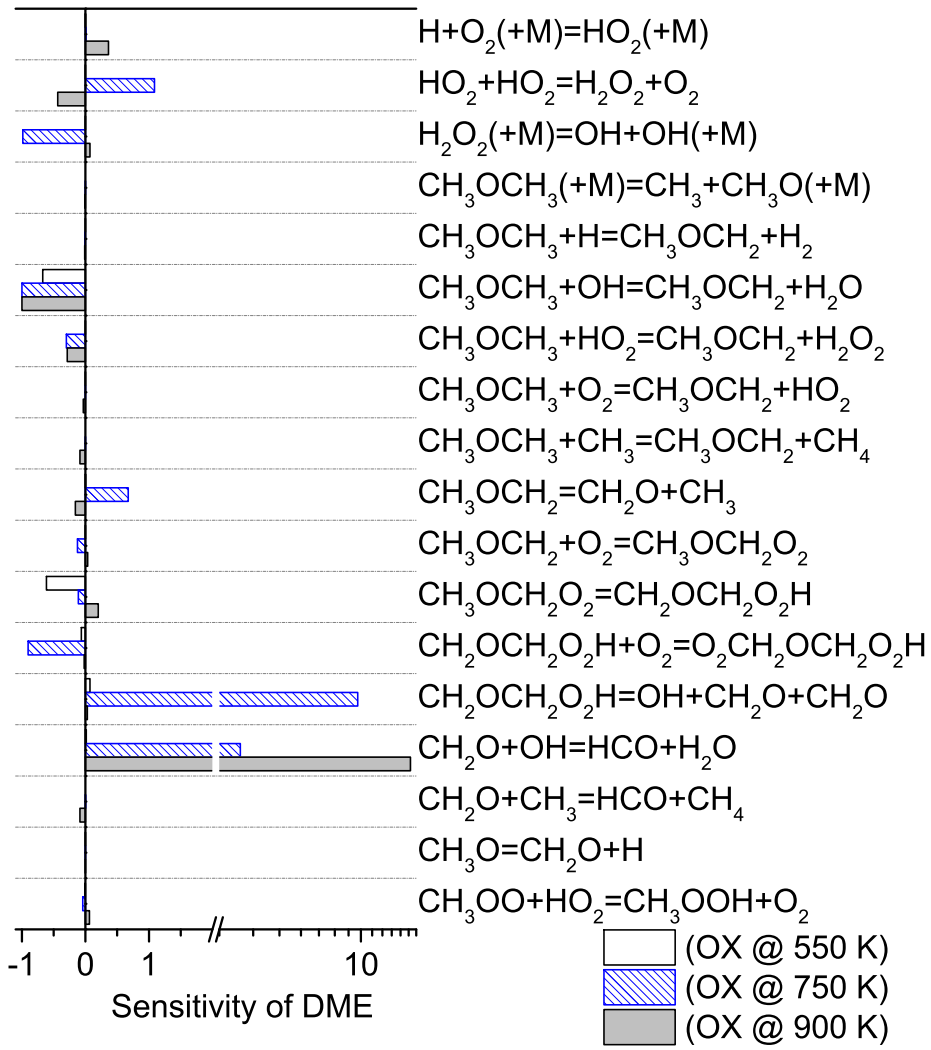

Figure 9.13: Sensitivity coefficients for DME conversion under stoichiometric and oxidizing conditions similar to those in figures 9.4 and 9.5. The coefficients are calculated considering only the isothermal part of the reactor (τ[s] = 3534 / T[K]).

9.4.2 Oxidation of Methane doped with DME

The effect on the fuel oxidation of doping methane with small amounts of DME is investigated in the flow reactor at a pressure of 100 bar. Neat methane oxidation data were published previously [237] and are shown here for comparison. For neat as well as the doped methane experiments, the isothermal residence time is given by $\tau[s] = 9550/T\,[K]$. However, implementing the temperature profiles provided in [237] improves the accuracy of the simulation.

Figure 9.14 presents the results of experiments under reducing conditions (Φ=19.5–20.0). Constraining the fuel-air equivalence ratio, DME is added to the mixture with the DME to CH_4 ratio of 3.2%. Such a small amount of DME has a striking effect, as the onset temperature of the fuel conversion shifts from ~725 K for the neat methane to ~575 K for the doped methane.

The effect of DME addition is not only on the ignition temperature, but also on the shapes of species profiles. For the neat DME experiment under reducing conditions, a plateau was observed in the DME profile over 575–675 K. Such a plateau now can be identified around 600–650 K for the doped experiments, not only in DME profile, but also in the O_2, CO, and CH_4 profiles. It seems that the doped mixture inherits the two-stage ignition from DME. The first stage of ignition takes place around 575 K, a temperature higher than that of neat DME at 50 bar (525 K). The second one is around 675 K, a temperature lower than the ignition temperature of neat methane (725 K). The earlier ignition triggered by adding DME promotes the formation of CO_2 and CO at high temperatures. In contrast, C_2H_4 and C_2H_6 yields are slightly suppressed in the presence of DME.

According to figure 9.14, almost the same yield of methanol can be achieved when temperature is reduced from 750 K to 600 K but DME is added at the same time. Therefore DME may be useful as a promoting agent in the direct conversion of methane to methanol. The DME fraction fluctuated slightly (±3%) before the ignition, but that is within the uncertainty range of our experiments.

Whereas the onset of reaction under reducing conditions is predicted accurately by the model for both neat DME and neat methane [237], the ignition of methane mixed with DME is predicted slightly premature. This results in the slight underpredictions of DME and oxygen over 550–700 K. However, the model accurately reproduces the changes observed experimentally in the DME, O_2, CO, CH_4 and CO_2 profiles. Formaldehyde is overpredicted noticeably in the presence of DME.

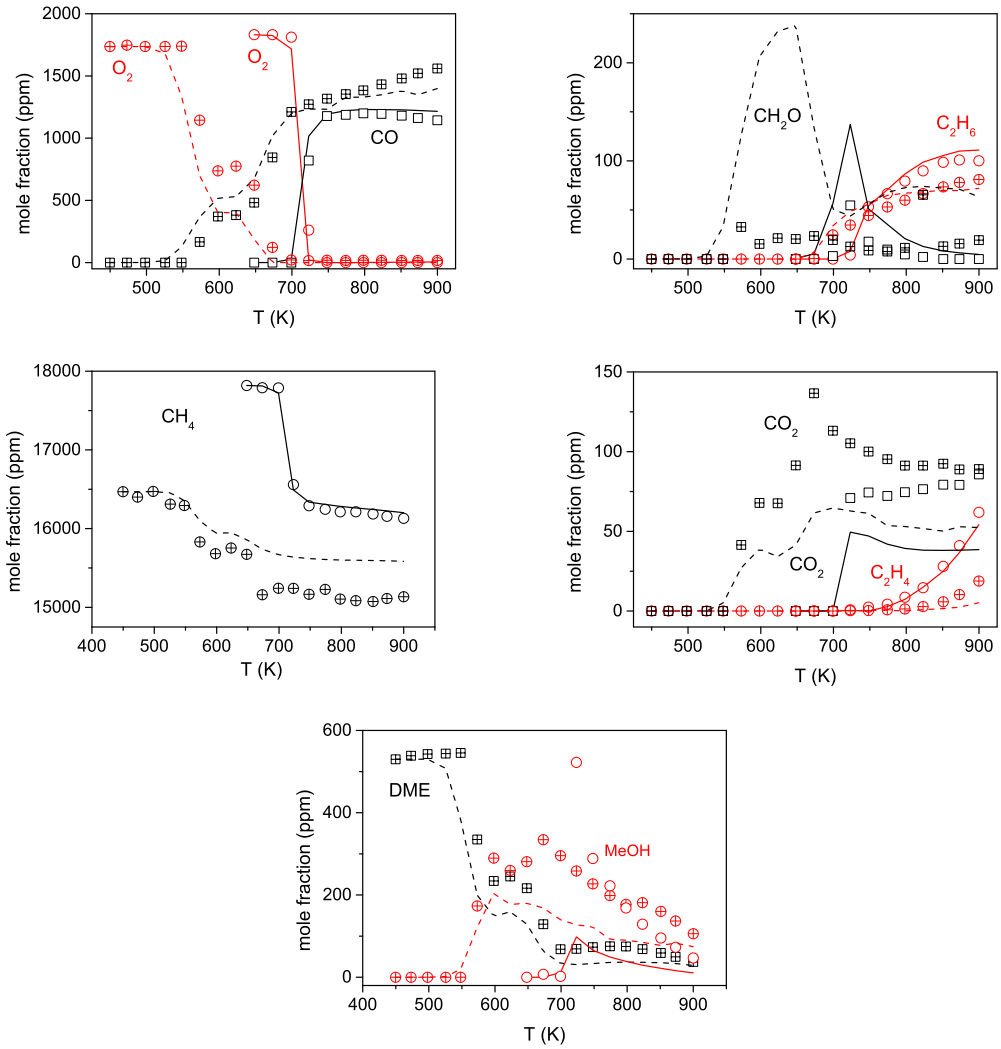

Figure 9.14: Results of DME addition to methane under reducing conditions (Φ=19.5–20.0) and at 100 bar. Open symbols/solid lines: the neat CH_4 experiment [237] with 1832/17819 ppm of O_2/CH_4; Crossed symbols/dashed lines: the doped experiment with 1736/16469/530 ppm of O_2/CH_4/DME; all diluted in N_2.

Under stoichiometric conditions (Φ=0.99–1.02), two sets of experiments are conducted with the DME to CH_4 ratios of 1.8% and 3.2%. For both cases, the DME conversion starts around 675 K, but there is no consumption of CH_4 and O_2 below 700–725 K (see figure 9.15). As neat methane ignites at 750 K, the addition of DME triggers methane oxidation at temperatures 25–50 K lower. The NTC behavior can be identified only in the DME profiles over 725–750 K. Apart from that, the species profiles show a monotonic sensitivity to temperature. The concentrations of the major products at

high temperatures are not sensibly affected by DME addition.

The model predicts well the onset of methane conversion as well as the fractions of O_2, CH_4, CO, and CO_2, but it underestimates the ignition temperature of DME in both doped mixtures, i.e. 550–575 K instead of 650 K. This premature DME conversion affects the DME profiles at higher temperatures. The predictions of methane and oxygen fractions have not been affected by the premature ignition of DME.

Neat DME ignites at 525 K (at 50 bar) for a wide range of stoichiometries, so it seems that methane suppresses the ignition of DME in the mixture. Methane might activate some chain-terminating paths in DME oxidation at low temperatures. Noting that the model was able to predict accurately the ignition of neat DME and neat methane under a wide range of stoichiometries, it is likely that the potential inhibiting effect of methane on DME ignition is not well covered in the model.

For the fuel-lean mixture (Φ=0.06), the oxidation of neat methane starts around 750 K, according to figure 9.16. Doping with a DME to CH_4 ratio of 3.6% gives methane oxidation at 700 K, but DME itself ignites around 650 K. Oxygen abundance promotes CO oxidation.

The model estimates well the methane oxidation temperature as well as the fractions of CH_4, CO_2, and CO. However, DME ignition is predicted at lower temperatures than the experimental observations, i.e. 550 K instead of 650 K.

Calculations show that heat released from DME oxidation in the doped mixture is negligible, so the promoting effect of DME addition is probably related to a dramatic growth in the concentrations of radicals.

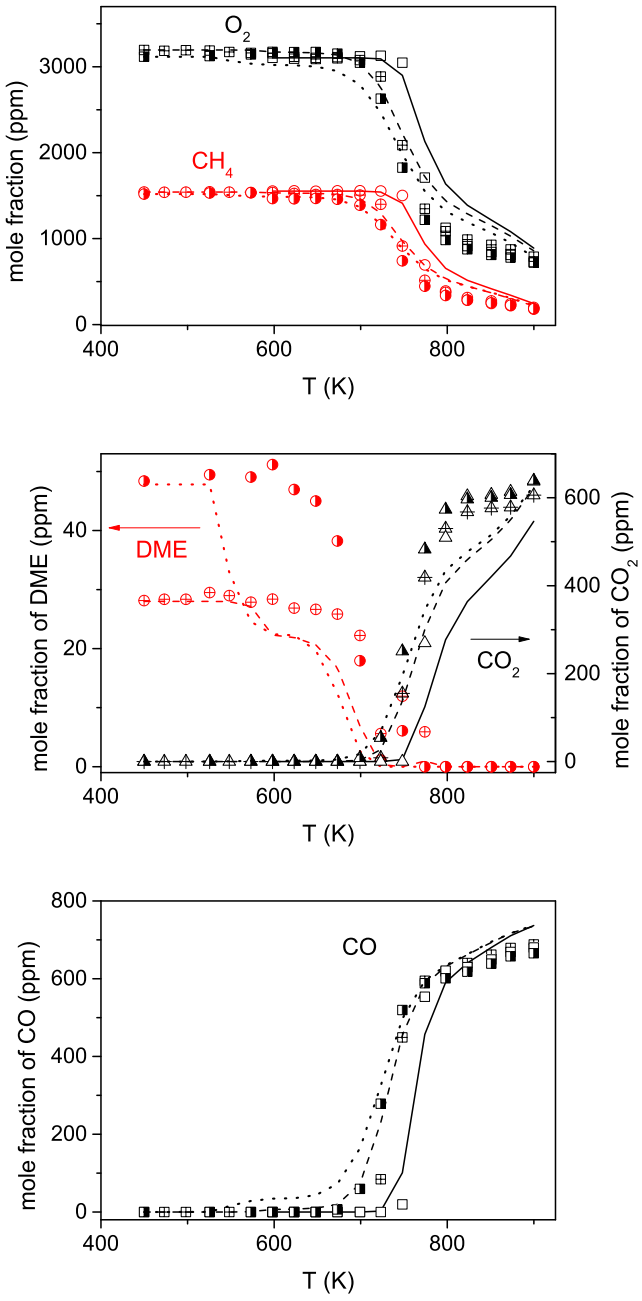

Figure 9.15: Results of DME addition to methane under stoichiometric conditions (Φ=0.99–1.02) and at 100 bar. Open symbols/solid lines: the neat CH_4 experiment [237] with 3104/1553 ppm of O_2/CH_4; Crossed symbols/dashed lines: the doped experiment (1.8%) with 3195/1542/28 ppm of O_2/CH_4/DME; Half-open symbols/dotted lines: the doped experiment (3.2%) with 3117/1519/48 ppm of O_2/CH_4/DME; all diluted in N_2.

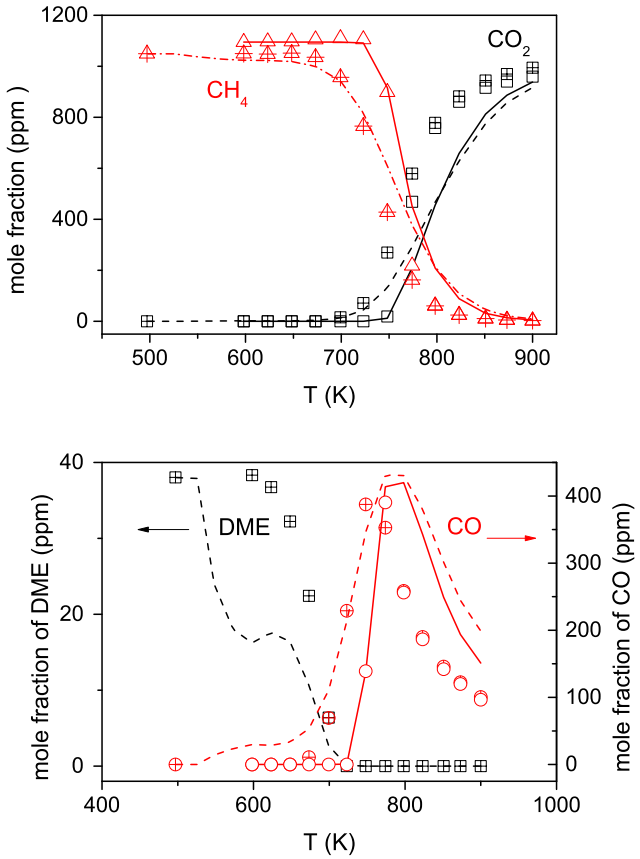

Figure 9.16: Results of experiments of DME addition to methane under oxidizing conditions (Φ=0.06) and at 100 bar. Open symbols/solid lines: the neat CH_4 experiment [237] with 39573/1095 ppm of O_2/CH_4; Crossed symbols/dashed lines: the doped experiment with 36849/1049/38 ppm of O_2/CH_4/DME; all diluted in N_2.

Under stoichiometric conditions and at 725 K, ignition is only observed in the doped experiments (3.2% doping) and not in the neat methane experiments. The reaction pathways analysis under such conditions reveals that the DME conversion initiates by the reaction between DME and molecular oxygen, similar to neat DME (figure 9.9). The produced CH_3OCH_2 radical then follows the consumption path of neat DME, yielding OH radicals, especially from the dissociation of $CH_2OCH_2O_2H$ at this temperature. At an early stage of ignition, around two-thirds of the produced OH radicals are consumed in the abstracting hydrogen from methane,

$$CH_4 + OH = CH_3 + H_2O \tag{R53}$$

which starts the major path of methane oxidation [237]. After ignition, methane follows the consumption path of neat methane as in [237].

Previously, Tang et al. [75] argued that the ignition promotion of DME addition to methane was due to the growth of the methyl radical fraction at the beginning of oxidation. Chen et al. [74] also attributed the promoting effect to the rapid build-up of HO_2 and CH_3 over the ignition delay time. However, their analyses were conducted at temperatures higher than this study, where the ignition regime is expected to be different from the ones investigated here.

The sensitivity of DME prediction at 600 K for the stoichiometric mixture of the doped methane (3.2% doping) is shown in figure 9.17. At this temperature, DME should not be converted according to the measurements, but the model predicts a considerable consumption of DME. The total fuel to oxygen ratio is in agreement with stoichiometric balance, but DME reacts in a very oxidizing environment since methane does not participate in the oxidation at such low temperatures. The sensitivity of reactions are analogous to the sensitivity of neat DME under oxidizing conditions and at a lower pressure of 50 bar (figures 9.12 and 9.13). However, the results of brute-force sensitivity analyses conducted in this work should be interpreted with caution, as the sensitivity coefficients are calculated only for selected reactions, and consequently other important reactions might be left out.

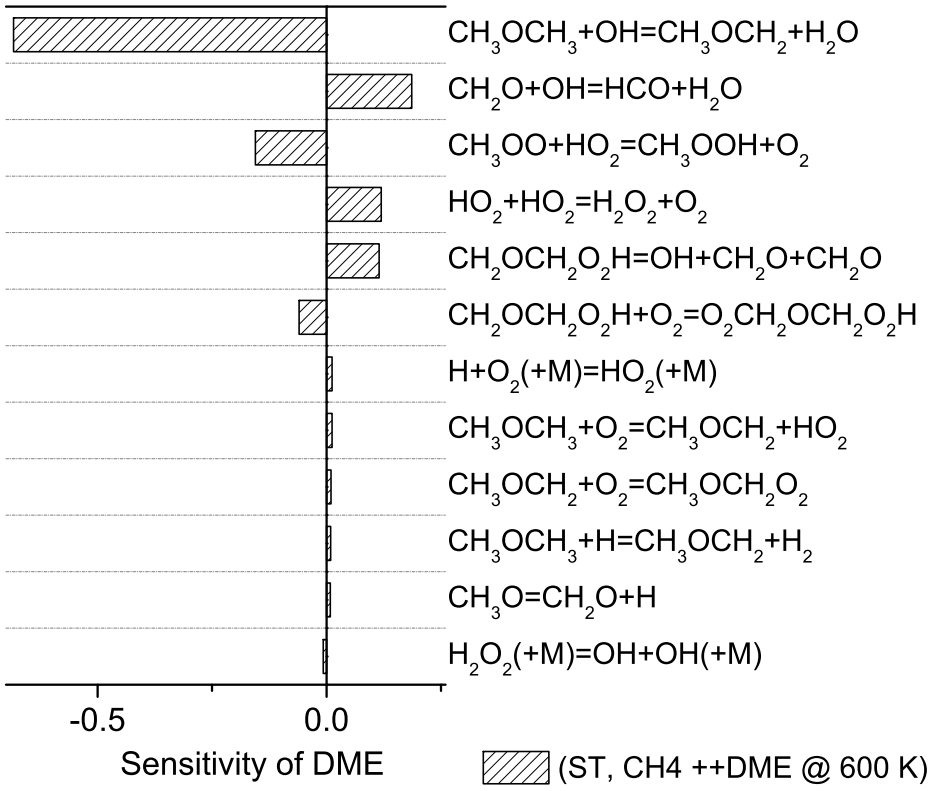

Figure 9.17: Sensitivity coefficients (brute-force) of DME in its mixture with methane (DME / CH_4 =3.2%) under stoichiometric conditions and at a pressure of 100 bar in the flow reactor. The coefficients were calculated by implementing the temperature profiles.

9.4.3 Comparison with literature data

9.4.3.1 Ignition at higher temperatures

The model can be evaluated at higher temperatures by comparing its prediction with available ignition delays measured in shock tubes. The ignition delay times of stoichiometric DME/air and DME/O_2/Ar at pressures of 1–40 bar are shown in figure 9.18. As expected, DME/air ignites considerably faster than the highly diluted mixtures of DME/O_2 in Ar. The ignition delays of DME/air are characterized by two inflection points. Between these points, the ignition delay represents the NTC behavior, similar to flow-reactor results for onset temperature of reaction. The first inflection point is slightly affected by pressure as it moves from 790 K to 830 K when pressure is increased from 13 bar to 40 bar. The sensitivity of ignition delays to pressure is higher over the NTC region and increasing pressure reduces the ignition delays considerably.

The model reproduces well the ignition delays of DME/air and the corresponding inflection points.

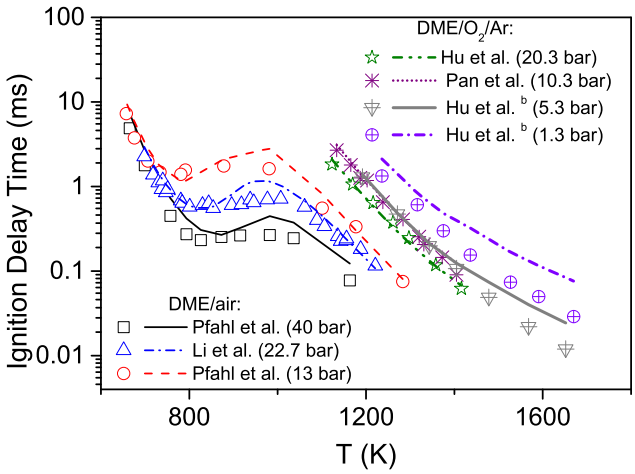

Figure 9.18: Ignition delay times of stoichiometric DME/air (data from Pfahl et al. [86] and Li et al. [87]) and DME/O_2/Ar (data from Hu et al. [76], Pan et al. [88], Hu et al.^{b} [89]). Lines denote the prediction of the present model assuming constant u,v.

The ignition delay times of stoichiometric mixtures highly diluted in argon are measured at temperatures above 1100 K, so the NTC behavior is not expected. It seems that the ignition delay shortens by increasing pressure over 1100–1600 K too. Although the agreement between the modeled and the measured delay times deteriorates slightly at high temperatures, the model performs well below 1400 K at different pressures.

The model is further evaluated against ignition delays under fuel-rich and fuel-lean conditions for the mixtures of DME/O_2 diluted either in argon or nitrogen (figure 9.19). The ignition delays are longer for the fuel-lean mixtures. Same as for stoichiometric conditions, the model predicts well the ignition delays.

Previously we observed that the model was able to estimate accurately the onset temperature of the major reaction in the mixtures of methane and DME in the flow reactor although it predicted premature ignition of DME in the mixtures. To further evaluate the interaction of methane and DME in the model, the ignition delays of mixtures of methane and DME are calculated and compared to the available data in figure 9.20. Here, the DME to methane ratio is varied from 0% to 100%, and as can be seen the model follows very well the experimental results for mixtures in air. For the mixtures in argon, however the model estimates a little longer ignition delays compared to the measurements.

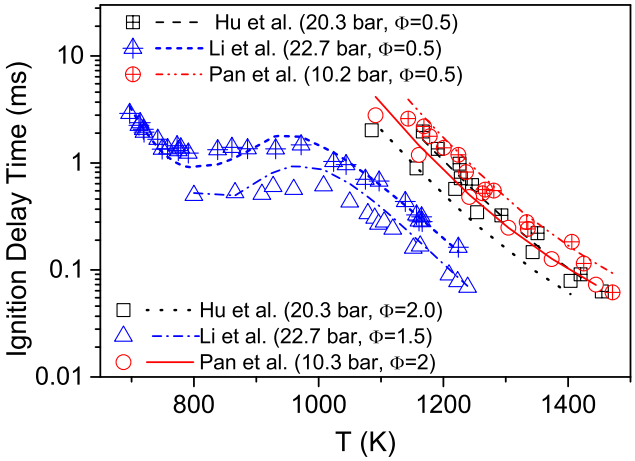

Figure 9.19: Ignition delay times of fuel-lean (Hu et al. [76]: 0.68% DME in O_2/Ar, Li et al. [87]: 3.38% DME in O_2/N_2, Pan et al. [88]: 0.68% DME in O_2/Ar) and fuel-rich (Hu et al. [76]: 2.46% DME in O_2/Ar, Li et al. [87]: 9.51% DME in O_2/N_2, Pan et al. [88]: 2.46% DME in O_2/Ar) mixtures at different pressures. Lines denote the prediction of the present model.

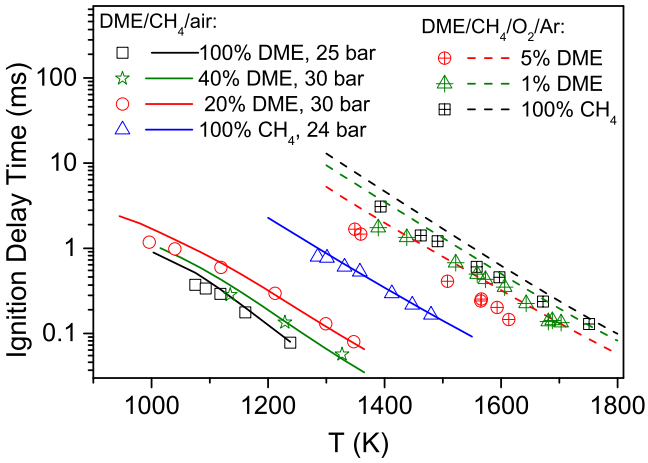

Figure 9.20: Effect of replacing methane by DME on the ignition delay times of stoichiometric mixtures. Symbols present the measurements in shock tubes for mixtures in air by Burke et al. [85] and for mixtures in argon (94% Ar) by Tang et al. [75]. Lines denote the prediction of the present model.

After evaluating the present model under different conditions, we use it to study the effects of pressure on the ignition delay time of DME/air. Figure 9.21 presents the results of the simulations over 600–1100 K and pressures of 1–200 bar. The ignition delay seems to be independent of the pressure at temperatures as low as 600 K. In fact, this trend was already observed in the experimental data where the measured ignition delays at different pressures converged below the first inflection temperature (see figure 9.18). On the other side, the ignition at 1100 K is accelerated strongly by increasing pressure from 1 to 200 bar. For intermediate temperatures between 600 and 1100 K, the ignition delay initially drops but later it levels off at higher pressures.

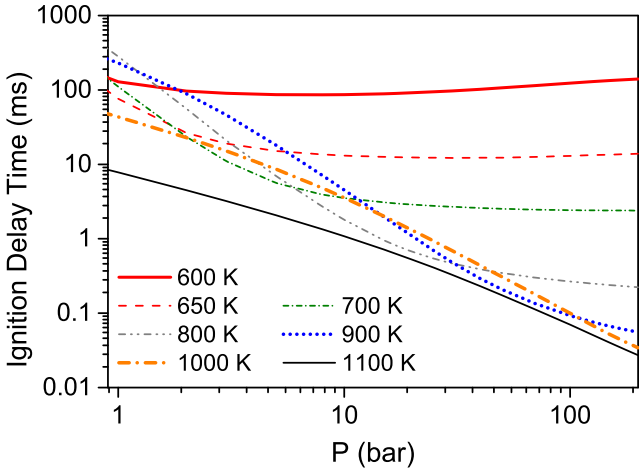

Figure 9.21: Effect of pressure and temperature on ignition delay times of stoichiometric DME/air mixture.

9.4.3.2 Flame speed

The variations of laminar flame speed can represent the net effect of the mixture diffusivity, exothermicity, and reactivity [319]. The flame speed thus has widely been used to evaluate chemical kinetic models, especially regarding high temperature chemistry. Figure 9.22 compares modeled flame speeds with measured data at pressures up to 10 atm. As expected, the flame speed decreases with increasing pressure. The maximum of the flame speed at 1–6 atm was measured at $\Phi \simeq 1.2$, which is well predicted by the model. The model slightly underestimates the flame speed of fuel-rich mixtures.

The sensitivity of flow rate (in mass) to the reaction rate constants can be calculated by the built-in functions in Chemkin [109]. Since pressure, temperature, and composition are fixed at the inlet, the sensitivity of the flow rate represents the sensitivity of

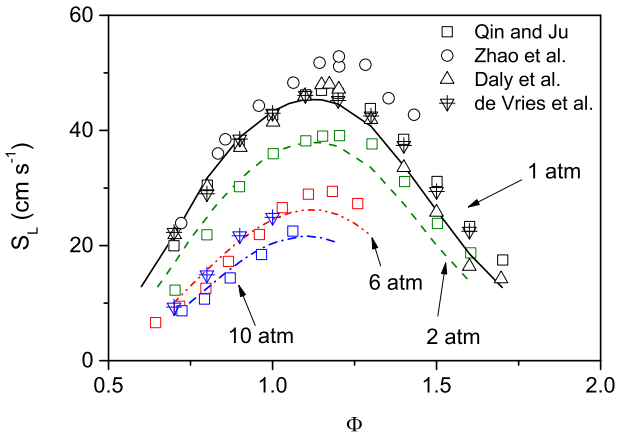

Figure 9.22: Laminar flame speed of DME/air at initial temperature of 298 K and different pressures. Experimental results are taken from Qin and Ju [306], Daly et al. [13], Vries et al. [307], and Zhao et al. [320]. Lines denote the predictions of the present model.

the flame speed too. As shown in figure 9.23, the flame speed of DME is determined strongly by reactions involved hydrogen atom. Especially, the chain-branching reaction of R54 and the chain-propagating reactions of R55 and R56 affect the flame speed of DME extensively.

$$H + O_2 = O + OH \tag{R54}$$

$$HCO(+ M) = H + CO(+ M) \tag{R55}$$

$$CO + OH = CO_2 + H \tag{R56}$$

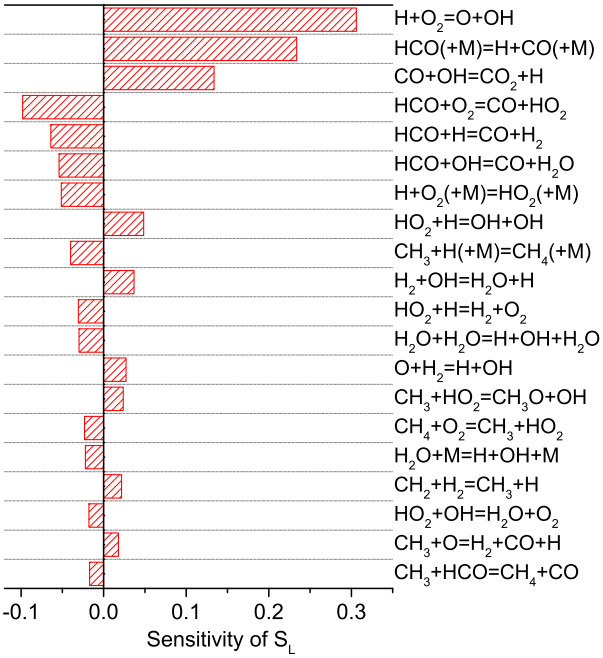

Figure 9.23: The sensitivity of flame speed of stoichiometric DME/air at initial temperature and pressure of 298 K and 1 atm, respectively. The coefficients are calculated and normalized using the built-in functions of Chemkin [109].

Conclusion

The pyrolysis and oxidation of DME and its effect on methane oxidation as an additive have been investigated in a flow reactor at high pressures and intermediate temperatures. It was found that DME pyrolysis started around 825 K at 50 bar pressure. The DME oxidation experiments at 50 bar gave the onset temperature of reaction at 525 K, independent of fuel-air equivalence ratio. Further experiments at 100 bar showed that by adding a small amount of DME to methane its ignition could effectively be accelerated. A model was developed for DME/CH_4 oxidation and was evaluated at a wide range of pressure, temperature, and stoichiometries. The model compared well with the data of neat DME oxidation from the flow reactor. Both onset temperature of reaction and the fractions of major components were reproduced fairly well by the model. The model agreed reasonably with ignition delays and flame speeds of DME. The model could also outline the onset temperature of major reactions in CH_4/DME mixtures. Further work is needed to focus on the interactions between DME and CH_4 in the model to address the premature DME depletion in CH_4/DME mixtures. The

presented species profiles of DME and DME/CH_4 conversion extended the experimental benchmark for oxidation at high pressures and intermediate temperatures. Such benchmark are vital in validating chemical kinetic models developed for addressing problems in real conditions.

Chapter 10

Comparison across the Fuels

In this chapter, combustion characteristics of investigated fuels are compared. In addition to species profiles, calculated ignition delay times of the fuels are presented. These data are discussed in details in the corresponding chapters and they are presented here only to provide a wider perspective of the results.

10.1 Species profiles for the flow reactor

Figure 10.1 shows the results from the flow-reactor experiments under reducing conditions and at different pressures. The fuel-air equivalence ratio (Φ) varies from 12 to 47. The fuel and oxygen fractions are shown as normalized by their initial values. The CO and CO_2 fractions are normalized by the carbon content of the fuel at the inlet of the reactor. Under investigated conditions, DME is chemically reactive above 525 K, and it gives a considerable fraction of CO at high temperatures. Ethanol is the second most reactive fuel which converts around 675 K. However, ethane (at 100 bar) is more reactive compared to ethanol (at 50 bar) regarding the oxygen consumption.

As stoichiometry, pressure, gas residence time, and the extent of dilution vary among experiments, fuel-reactivity should be compared with caution. Ideally, the experiments should be conducted under similar conditions to facilitate comparison of different fuels, but it was not possible due to practical and technical limitations. Instead, the strategy followed in this project is first to evaluate the model against collected results under different conditions. If the model compares well with the experimental observations, then the species profiles of all fuels will be extrapolated to certain fixed conditions using the model.

In corresponding chapters for each fuel, it is shown that the model generally agrees well with the measured data. Consequently, the model is used here to predict the

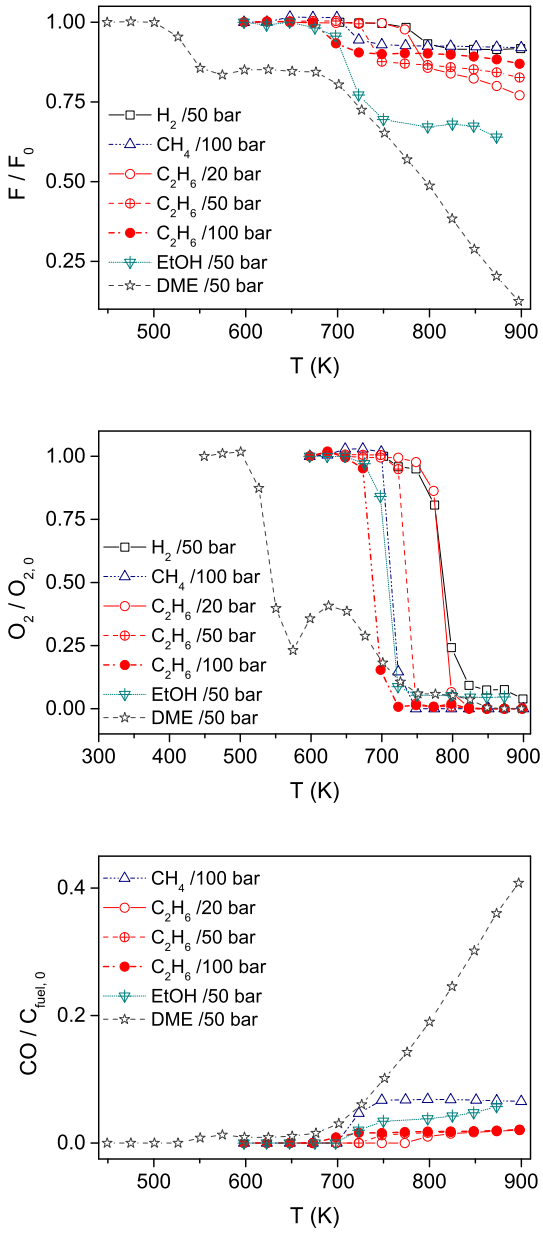

Figure 10.1: The normalized species profiles from the flow-reactor experiments on fuel-rich mixtures (Φ=12–47). The initial mole fractions of the fuels were 0.953 / 1.753 / 1.113 / 1.106 / 1.1 / 0.525 / 0.074 (in %) and the initial mole fractions of oxygen were 395 / 1781 / 1048 / 981 / 830 / 363 / 112 (in ppm) for H_2, CH_4, C_2H_6 (20 bar), C_2H_6 (50 bar), C_2H_6 (100 bar), ethanol, and DME experiments, respectively. All gases were strongly diluted in nitrogen. Symbols are connected by lines for eye guidance. Note that gas residence time varied among tests with pressure and the isothermal length of the reactor.

species profiles from oxidation in an ideal constant-pressure and -temperature reactor with a residence time of 10 s, a pressure of 100 bar, and a fuel-air equivalence ratio of 25 (in air). It should be acknowledged that when the mixtures of fuel in air are studied, the concentrations of reactants, e.g. $[O_2]$, are several times larger than the concentration studied in the flow reactor experiments, due to high dilution with inert gas (usually more than 90%) in the experiments. However, whenever data were available from experiments in mixtures with air, the model has been evaluated against them and has been shown to give reliable predictions.

Figure 10.2 shows the results of the extrapolation by the model. At low temperatures, ethane is more reactive compared to ethanol. In contrast, ethanol is converted more at high temperatures. Hydrogen is the least reactive fuel at intermediate temperatures. Methane reactivity lies within those of ethanol and hydrogen.

Comparing the rate of the thermal dissociation of the different fuels (R1–R5) may explain this behavior. Figure 10.3 shows the rate constants for the thermal dissociation of the investigated fuels (R1–R5) in nitrogen atmosphere at 100 bar.

$$C_2H_6(+M) = CH_3 + CH_3(+M) \quad \text{(R1)}$$

$$CH_3CH_2OH(+M) = CH_2OH + CH_3(+M) \quad \text{(R2a)}$$

$$= C_2H_4 + H_2O(+M) \quad \text{(R2b)}$$

$$= C_2H_5 + OH(+M) \quad \text{(R2c)}$$

$$CH_3OCH_3(+M) = CH_3 + CH_3O(+M) \quad \text{(R3)}$$

$$CH_4(+M) = CH_3 + H(+M) \quad \text{(R4)}$$

$$H_2(+M) = H + H(+M) \quad \text{(R5)}$$

The rate constants for the dissociation of DME and ethanol are much higher than those of other fuels, explaining their faster consumption. However, it should be noted that even in the complete absence of oxygen, the dissociation is not the only reaction converting the fuels. In fact, the reaction between the fuel molecule and radicals produced from dissociation can be important as well. For example, in DME pyrolysis the reaction between the methyl radical and DME (R6) also contributes significantly.

$$CH_3OCH_3 + CH_3 = CH_3OCH_2 + CH_4 \quad \text{(R6)}$$

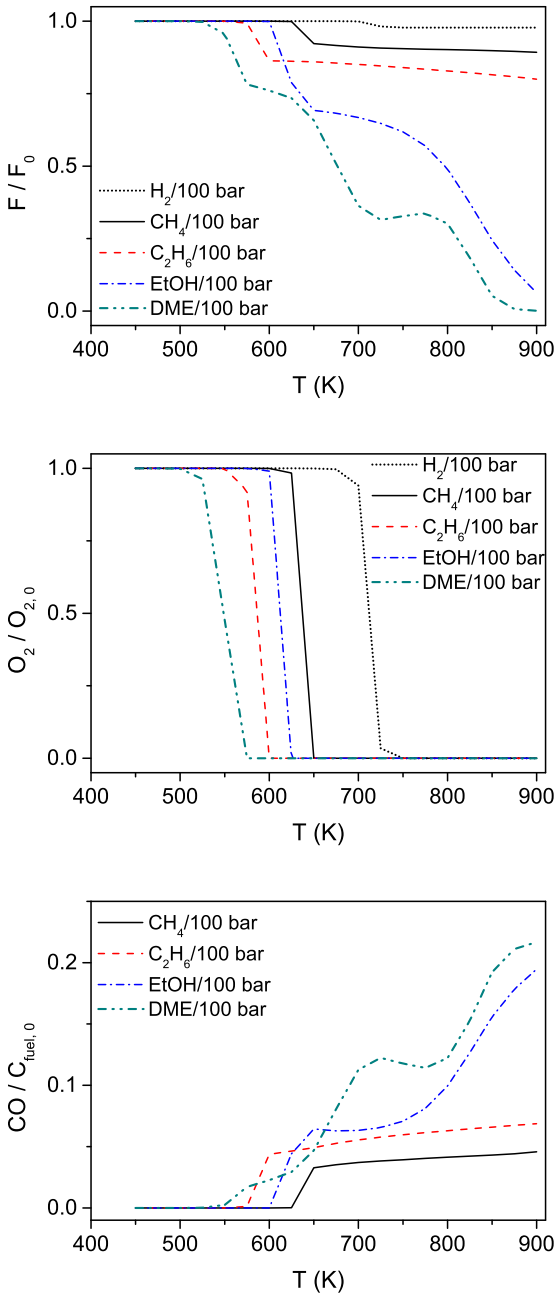

Figure 10.2: The species profiles extrapolated by the model for fuel-rich mixtures (Φ=25) in air. The isothermal gas residence time is fixed at 10 s and pressure is 100 bar.

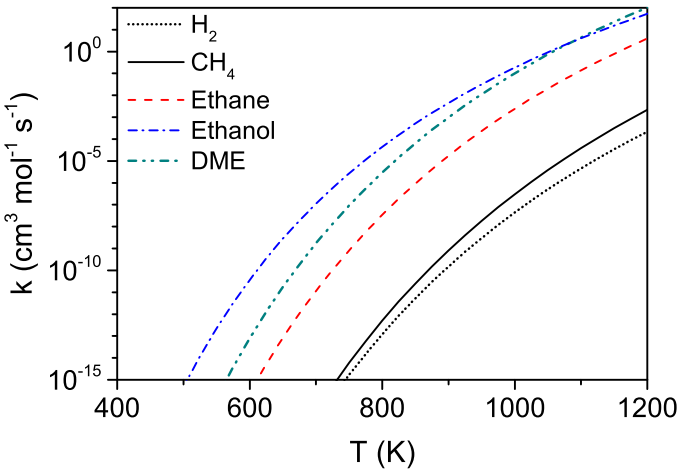

Figure 10.3: The rate constants of the dissociation of studied fuels in nitrogen atmosphere at 100 bar.

After the ignition, DME and ethanol profiles show a non-linear sensitivity to temperature. In chapter 9 the Negative Temperature Coefficient (NTC) behavior of DME at intermediate temperatures has been discussed in detail. As shown in figure 10.1 for highly diluted mixtures, the NTC behavior has not been observed for ethanol. Instead, it seems that ethanol conversion in figure 10.2 has two stages, ethanol fraction drops sharply by increasing temperature up to 650 K, but above that it changes slowly against temperature. Such behavior in the ethanol profile might be an artifact of the model, so further experiments on ethanol oxidation in air are interesting, both fundamentally and practically. When oxygen is fully consumed in the mixture, further conversion of hydrogen, methane, and ethane is stopped. In contrast, the conversion of oxygenated fuels (ethanol and DME) continues after oxygen depletion.

For a better perspective, the conversion profiles are plotted for all fuels as a function of time in the reactor (figure 10.4). The first drop in DME concentration coincides with the complete consumption of oxygen, but DME conversion continues gradually afterwards. Ethanol conversion also continues for a short interval after oxygen depletion.

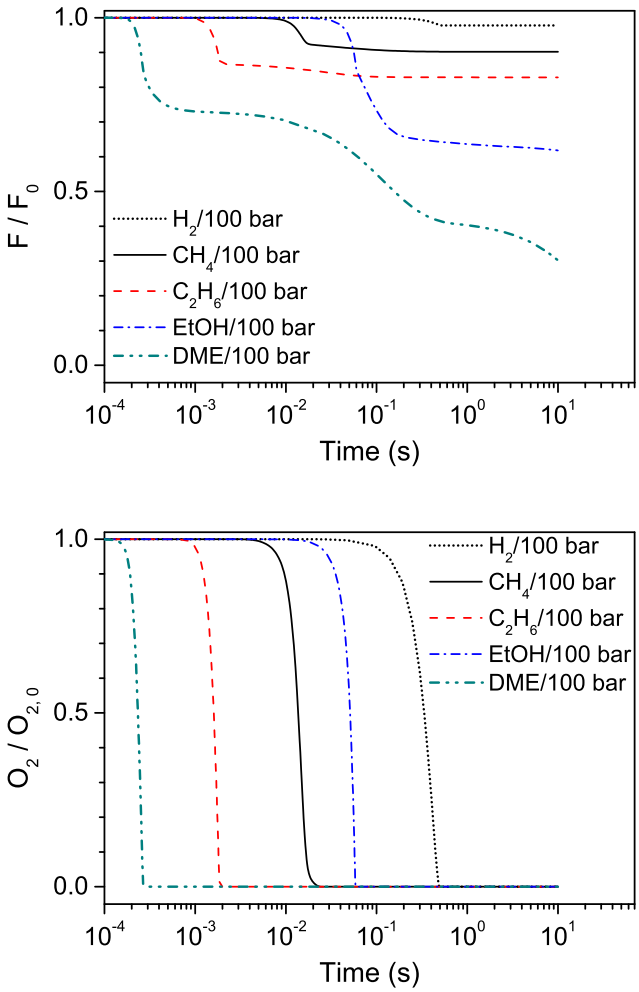

Figure 10.4: The normalized fractions of fuel and oxygen as a function of time for oxidation at 800 K under conditions similar to those in figure 10.2.

Figures 10.5 and 10.6 show the results of the tests on stoichiometric mixtures. The most reactive fuel is DME, with conversion starting from 525 K. Fuel oxidation starts at 700–725 K for ethanol (at 50 bar) and at 750 K for ethane (at 100 bar). The NTC behavior of DME is more profound under conditions investigated here, and the major part of DME carbon converts to CO. Whereas DME, ethanol, and ethane are consumed completely at 900 K, a considerable amount of oxygen still remains in the system, in line with the high ratio of CO to CO_2 fractions.

To eliminate the effects of pressure, dilution, and gas residence time, the model is used to predict conversion in an ideal reactor under stoichiometric conditions (Φ=1.0).

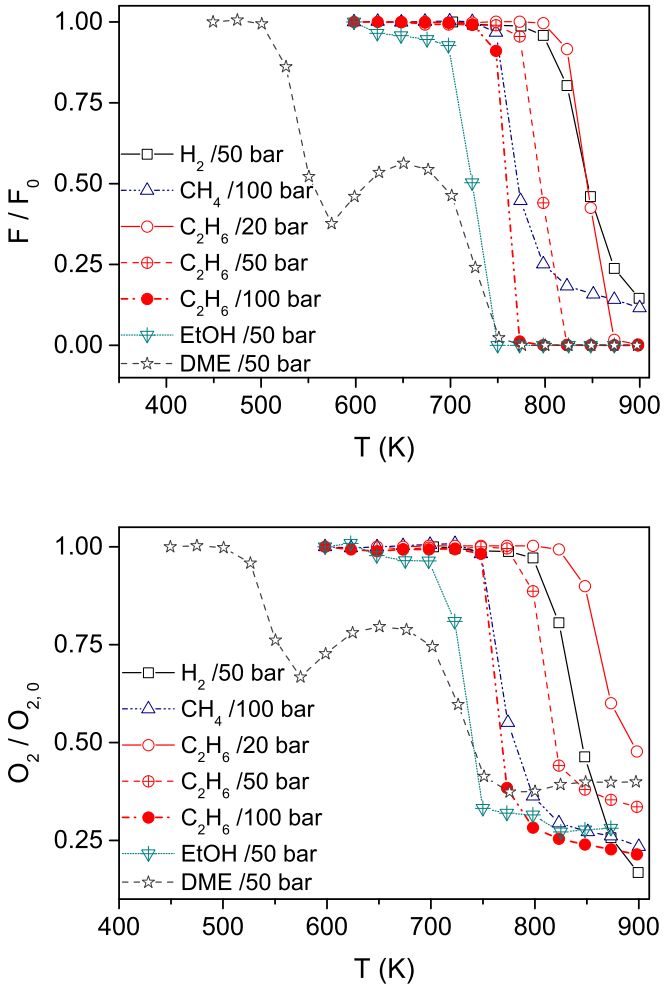

Figure 10.5: The normalized species profiles from the flow-reactor experiments on stoichiometric mixtures (Φ=0.8–1.0). The initial mole fractions of the fuels were 3104 / 1553 / 512 / 546 / 581 / 3467 / 268 (in ppm) and the initial mole fractions of oxygen were 1508 / 3104 / 2190 / 2335 / 2240 / 10076 / 782 (in ppm) for H_2, CH_4, C_2H_6 (20 bar), C_2H_6 (50 bar), C_2H_6 (100 bar), ethanol, and DME experiments, respectively. All gases were strongly diluted in nitrogen. Symbols are connected by lines for eye guidance. Note that gas residence time varied among tests with pressure and the isothermal length of the reactor.

As shown in figure 10.7, ethane is the most reactive fuel after DME. The onset temperatures of reaction are 525, 600, 625, 675, and 725 K for DME, ethane, ethanol, methane, and hydrogen, respectively. The CO formation is considerable up to 775 K in methane oxidation and until 825 K in the oxidation of other fuels. For all investigated fuels at 900 K, more than 92% of fuel carbon is eventually converted to CO_2.

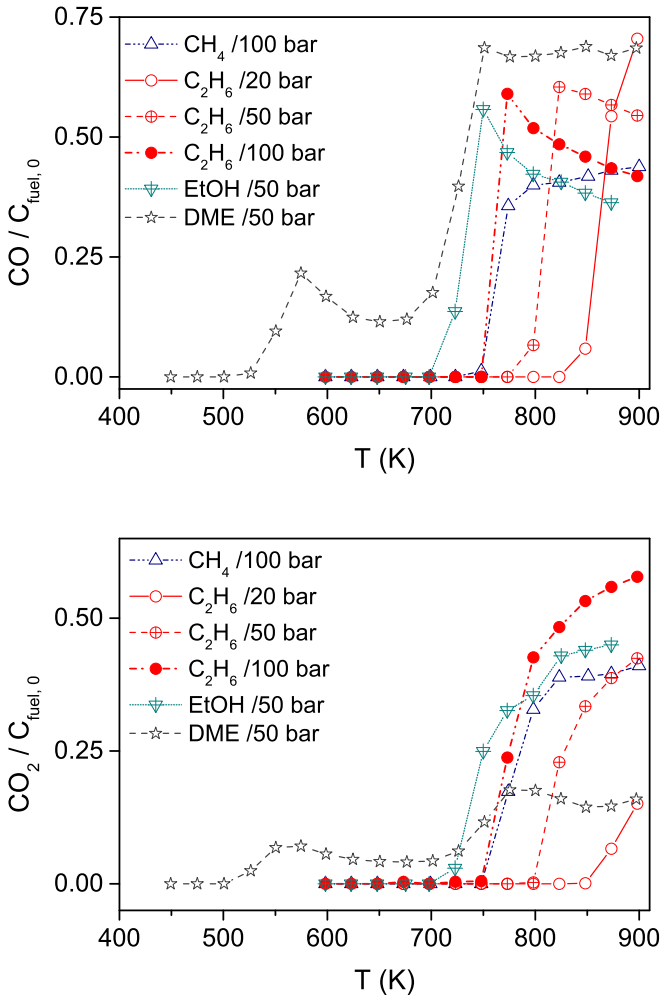

Figure 10.6: The normalized species profiles from the flow-reactor experiments under stoichiometric conditions given in figure 10.5.

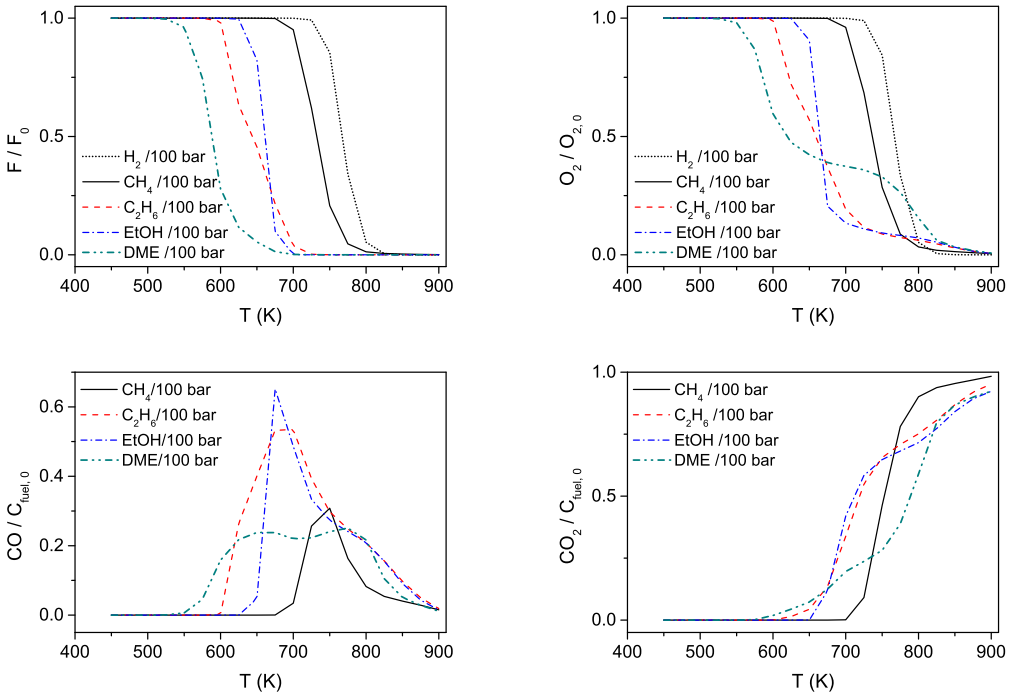

Figure 10.7: The normalized species profiles extrapolated by the model for stoichiometric mixtures (Φ=1.0) in air. The isothermal gas residence time is fixed as 10 s and pressure is 100 bar.

Figure 10.8 shows the effect of pressure on fuel conversion under stoichiometric conditions. For all fuels except DME, elevating pressure accelerates fuel conversion at low temperatures to some extent. For DME, the onset temperature of reaction is slightly retarded by increasing pressure. The highest sensitivity to pressure is seen for ethane, where the ignition temperature shifts around 75 K due to the changes in pressure.

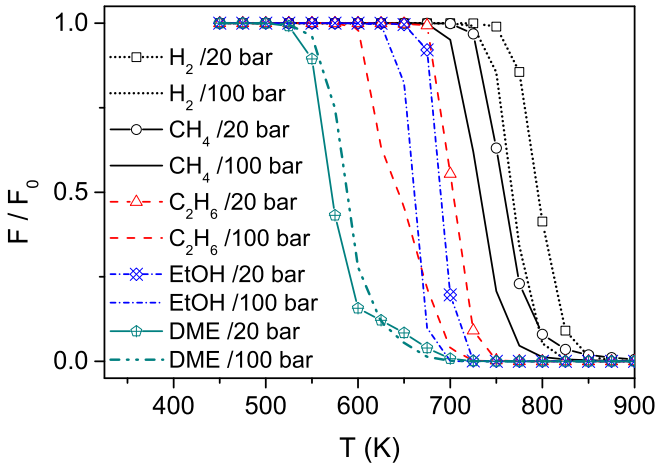

Figure 10.8: Effect of pressure on fuel conversion for stoichiometric mixtures (Φ=1.0) in air simulated by the present model. The isothermal gas residence time is 10 s.

The results of the tests on fuel-lean mixtures are shown in figure 10.9. Even at the highest temperature, hydrogen is not completely oxidized despite the high fraction of oxygen. In DME oxidation, the NTC trend is weakened, but CO fraction shows an interesting behavior where it levels off above 575 K. The CO_2 profile from DME oxidation has two plateaus, one over 550–675 K, and the other over 750–900 K. Figure 10.10 shows the results of simulations for the mixtures in air. Ethane is the most reactive fuel after DME at low temperatures. The fuel oxidation starts at 525, 675, 700, 725, and 750 K for DME, ethanol, ethane, methane, and hydrogen, respectively. For DME oxidation, the plateau in the CO_2 profile disappears, but CO still shows a non-monotonic trend.

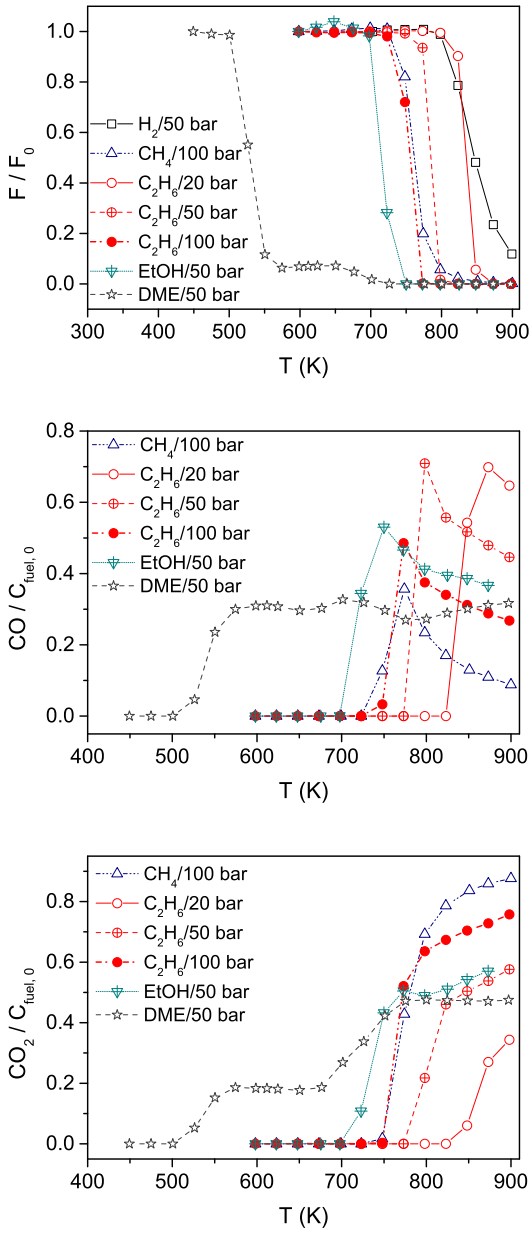

Figure 10.9: The normalized species profiles from the flow reactor experiments on fuel-lean mixtures (Φ=0.04–0.1). The initial mole fractions of the fuels were 1610 / 1095 / 538 / 533 / 570 / 3121 / 146 (in ppm) and the initial mole fractions of oxygen were 1.604 / 3.957 / 5.404 / 5.482 / 5.234 / 9.83 / 1.077 (in %) for H_2, CH_4, C_2H_6 (20 bar), C_2H_6 (50 bar), C_2H_6 (100 bar), ethanol, and DME experiments, respectively. All gases were strongly diluted in nitrogen. Symbols are connected by lines for eye guidance. Note that gas residence time varied among tests with pressure and the isothermal length of the reactor.

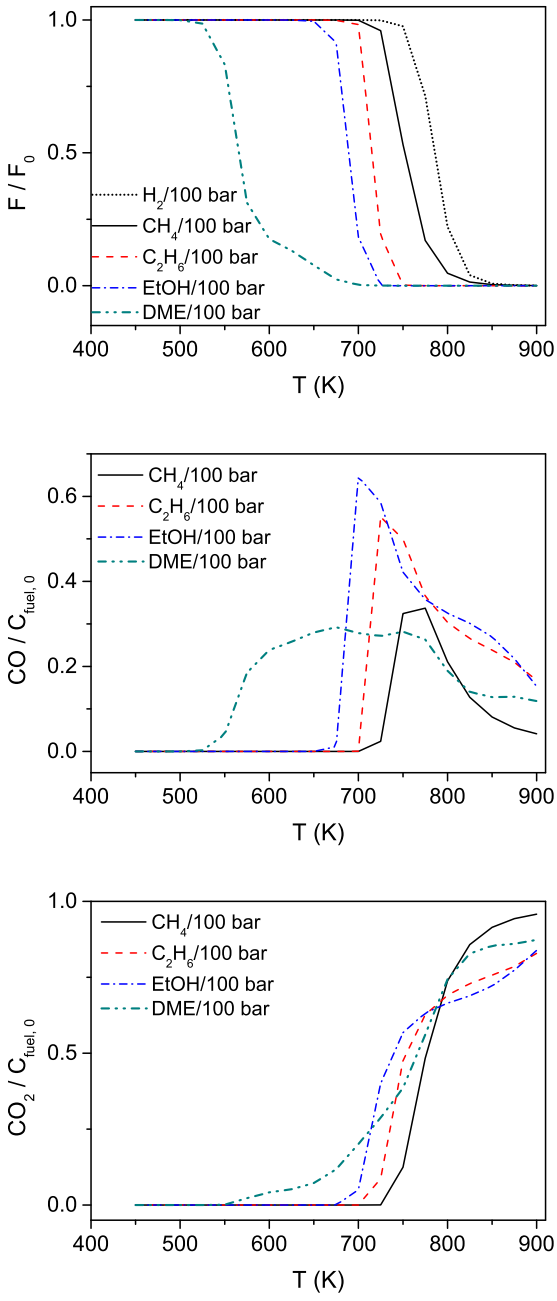

Figure 10.10: The normalized species profiles extrapolated by the model for fuel-lean mixtures (Φ=0.1) in air. The isothermal gas residence time is fixed as 10 s and pressure is 100 bar.

10.2 Ignition delay times of mixtures in air

The ability of the model in predicting ignition delay times of the investigated fuels is evaluated over a wide range of conditions in corresponding chapters. Here, the ignition delay times of stoichiometric mixtures of different fuels with air are calculated. As shown in figure 10.11, DME ignites considerably faster that the other fuels at temperatures around 800 K. Ethane, ethanol, methane, and hydrogen ignite later. Above 1200 K, ethanol precedes DME in ignition. While hydrogen ignites later than the other fuels at 800 K, it has the shortest delay time above 1400 K. The dramatic variations in the ignition delays of the fuels at different temperatures emphasize the necessity of reliable chemical kinetic models in the design and optimization of systems involved with ignition. The sensitivity of ignition delay to pressure and temperature is discussed in more detail for each fuel in its corresponding chapter.

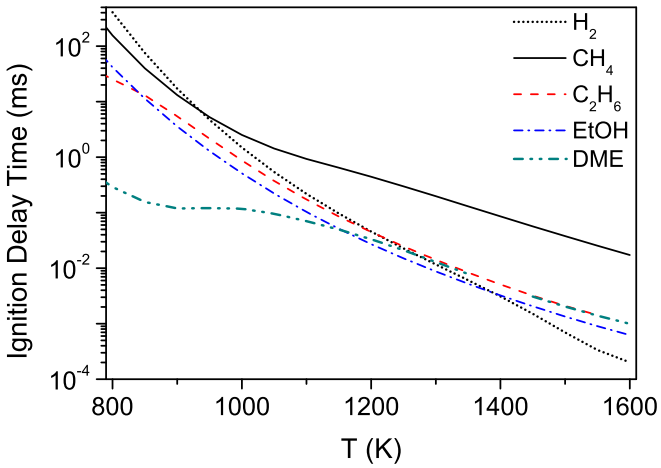

Figure 10.11: The ignition delay time calculated by the present model for stoichiometric fuel-air mixtures at 100 bar.

Conclusion and outlook

Combustion at high pressures and intermediate temperatures has generated research interest due to its importance in modern engines and energy plants. Alternative bio-derived fuels have attracted interest of policymakers mainly due to their environmental advantages. However, application of bio-derived fuels under the conditions of modern energy plants and engines has rarely been studied. In this project, the combustion of hydrogen, methane, ethane, ethanol, and dimethyl ether (DME) was characterized by measurements in a laminar flow reactor over a wide range of temperature, pressure, and stoichiometry. The measurements presented the onset temperature of reaction and mixture composition upon ignition for studied fuels. A detailed chemical kinetic model was evaluated against the present data as well as against flame speeds and ignition delays from literature. The results indicated that

- Hydrogen reaction started at 800 K (at 50 bar) under stoichiometric and oxidizing conditions and at 750 K under reducing conditions. The model compared well with the species profiles, flame speeds, and ignition delay times and it could clarify the complicated sensitivity of hydrogen ignition delay to pressure and temperature.

- Methane reaction started at 725–750 K (at 100 bar), almost independent of the stoichiometry. The model agreed well with the species profiles, flame speed, and ignition delay time measurements. Sensitivity analyses showed that methanol yield from the partial oxidation of methane at high pressures strongly depended on the thermochemistry data of CH_3OO which are quite uncertain.

- The onset temperature of ethane reaction was between 700 and 825 K, and depended on stoichiometry and pressure (20–100 bar). Elevating pressure generally promoted ethane oxidation. The developed model was able to predict the mixture composition from most experiments. However, the fuel conversion was pre-

dicted prematurely under reducing conditions and at high pressures. Moreover, the model overestimated flame speed. Via sensitivity analyses, the reactions potentially responsible for the disagreement were found for further studies.

– Ethanol dissociation was detected above 850 K while its oxidation was at 700–725 K and almost independent of fuel-air equivalence ratio (at 50 bar). The model compared well with the measurements of species profiles from the flow reactor. The flame speed of ethanol was slightly overpredicted. Ignition delay time of ethanol was well predicted by the model above 900 K, but it was overpredicted below 900 K. Sensitivity analyses revealed the reaction between ethanol and the hydroperoxyl radical as a critical factor in predicting ignition delay time at low temperatures, while this reaction has only been determined with a large uncertainty.

– DME pyrolysis and oxidation were investigated over 450–900 K and at 50 bar. DME pyrolysis started around 825 K while the onset of DME oxidation was around 525 K, independent of fuel-air equivalence ratio. In DME oxidation, the NTC temperatures always included the range of 575–625 K. Flame speed and ignition delays of DME were predicted well by the model. Further experiments at 100 bar on the mixtures of methane and DME showed that doping methane with a small amount of DME enhanced the oxidation considerably. The model predicts well the onset of major reactions, but DME conversion in the mixtures with methane was predicted prematurely. Further work on interactions between methane and DME is required.

– Using the model to extrapolate the results to fixed conditions for all fuels showed that DME is the most reactive fuel among the investigated ones at low temperatures (650 K). For all the fuels except DME, the oxidation of stoichiometric mixtures started at lower temperatures when the pressure was elevated. The ignition delay times of different fuels showed a complicated sensitivity to temperature, e.g. while hydrogen ignited later than the other fuels at 800 K, it ignited faster than the others at 1500 K.

Bibliography

[1] H. Hashemi, J. M. Christensen, S. Gersen, and P. Glarborg. "Hydrogen oxidation at high pressure and intermediate temperatures: Experiments and kinetic modeling". *Proc. Combust. Inst.* 35.1 (2015), pp. 553–560.

[2] International Energy Agency. *Key world energy statistics*. International Energy Agency, 2014.

[3] U.S. Energy Information Administration. *International Energy Outlook 2013*. Washington: EIA, 2013.

[4] J. N. Armor. "Emerging importance of shale gas to both the energy & chemicals landscape". *J. Energy Chem.* 22.1 (2013), pp. 21–26.

[5] A. M. Hochhauser. "Gasoline and Other Motor Fuels". In: *Kirk-Othmer Encycl. Chem. Technol.* John Wiley & Sons, Inc., 2000.

[6] F. Battin-Leclerc, E. Blurock, J. Simmie, M. Alzueta, A. S. Tomlin, and M. Olzmann. "Introduction". In: *Cleaner Combustion*. Ed. by F. Battin-Leclerc, J. M. Simmie, and E. Blurock. Springer London, 2013, pp. 1–14.

[7] D. L. Flowers, S. M. Aceves, J. Martinez-Frias, and R. W. Dibble. "Prediction of carbon monoxide and hydrocarbon emissions in iso-octane HCCI engine combustion using multizone simulations". *Proc. Combust. Inst.* 29.1 (2002), pp. 687–694.

[8] International Energy Agency. *CO_2 emissions from fuel combustion (2013 Edition)*. International Energy Agency, 2013.

[9] W. M. Haynes, ed. *CRC handbook of chemistry and physics*. CRC press, 2014.

[10] F. N. Egolfopoulos and C. K. Law. "An experimental and computational study of the burning rates of ultra-lean to moderately-rich $H_2/O_2/N_2$ laminar flames with pressure variations". *Symp. (Int.) Combust., [Proc.]* 23.1 (1991), pp. 333–340.

[11] X. J. Gu, M. Z. Haq, M. Lawes, and R. Woolley. "Laminar burning velocity and Markstein lengths of methane/air mixtures". *Combust. Flame* 121.1-2 (2000), pp. 41–58.

[12] C. M. Vagelopoulos and F. N. Egolfopoulos. "Direct experimental determination of laminar flame speeds". *Symp. (Int.) Combust., [Proc.]* 27.1 (1998), pp. 513–519.

[13] C. A. Daly, J. M. Simmie, J. Würmel, N. DjebaÏli, and C. Paillard. "Burning velocities of dimethyl ether and air". *Combust. Flame* 125.4 (2001), pp. 1329–1340.

[14] L. Sileghem, V. A. Alekseev, J. Vancoillie, K. M. Van Geem, E. J. K. Nilsson, S. Verhelst, and A. A. Konnov. "Laminar burning velocity of gasoline and the gasoline surrogate components iso-octane, n-heptane and toluene". *Fuel* 112 (2013), pp. 355–365.

[15] R. McCarthy and C. Yang. "Determining marginal electricity for near-term plug-in and fuel cell vehicle demands in California: Impacts on vehicle greenhouse gas emissions". *Journal of Power Sources* 195.7 (2010), pp. 2099–2109.

[16] G. Mittal, C.-J. Sung, and R. A. Yetter. "Autoignition of H_2/CO at elevated pressures in a rapid compression machine". *Int. J. Chem. Kinet.* 38.8 (2006), pp. 516–529.

[17] U. Maas and J. Warnatz. "Ignition processes in hydrogen- oxygen mixtures". *Combust. Flame* 74.1 (1988), pp. 53–69.

[18] C. K. Westbrook and F. L. Dryer. "Chemical kinetic modeling of hydrocarbon combustion". *Prog. Energy Combust. Sci.* 10.1 (1984), pp. 1–57.

[19] Z. Huang, Y. Zhang, K. Zeng, B. Liu, Q. Wang, and D. Jiang. "Measurements of laminar burning velocities for natural gas-hydrogen-air mixtures". *Combust. Flame* 146.1-2 (2006), pp. 302–311.

[20] D. Healy, H. J. Curran, J. M. Simmie, D. M. Kalitan, C. M. Zinner, A. B. Barrett, E. L. Petersen, and G. Bourque. "Methane/ethane/propane mixture oxidation at high pressures and at high, intermediate and low temperatures". *Combust. Flame* 155.3 (2008), pp. 441–448.

[21] C. J. Aul, W. K. Metcalfe, S. M. Burke, H. J. Curran, and E. L. Petersen. "Ignition and kinetic modeling of methane and ethane fuel blends with oxygen: A design of experiments approach". *Combust. Flame* 160.7 (2013), pp. 1153–1167.

[22] C. L. Rasmussen. "Direct Partial Oxidation of Natural Gas to Liquid Chemicals". PhD thesis. Technical University of Denmark (DTU), Department of Chemical Engineering, 2007.

[23] K. E. Woodcock and M. Gottlieb. "Gas, Natural". In: *Kirk-Othmer Encycl. Chem. Technol.* John Wiley & Sons, Inc., 2000.

[24] International Group of Liquefied Natural Gas Importers (GIIGNL). *The LNG Industry in 2013.* (GIIGNL), 2013.

[25] A. Melvin. "Spontaneous ignition of methane–air mixtures at high pressure I–the ignition delay preceding explosion". *Combust. Flame* 10.2 (1966), pp. 120–128.

[26] D. W. Rytz and A. Baiker. "Partial oxidation of methane to methanol in a flow reactor at elevated pressure". *Ind. Eng. Chem. Res.* 30.10 (1991), pp. 2287–2292.

[27] P. Dagaut, J.-C. Boettner, and M. Cathonnet. "Methane Oxidation: Experimental and Kinetic Modeling Study". *Combust. Sci. Technol.* 77.1-3 (1991), pp. 127–148.

[28] T. B. Hunter, H. Wang, T. A. Litzinger, and M. Frenklach. "The oxidation of methane at elevated pressures: Experiments and modeling". *Combust. Flame* 97.2 (1994), pp. 201–224.

[29] V. P. Zhukov, V. A. Sechenov, and A. Starikovskii. “Spontaneous Ignition of Methane-Air Mixtures in a Wide Range of Pressures”. *Combust., Explos. Shock Waves* 39.5 (2003), pp. 487–495.

[30] J. Huang, P. G. Hill, W. K. Bushe, and S. R. Munshi. “Shock-tube study of methane ignition under engine-relevant conditions: Experiments and modeling”. *Combust. Flame* 136.1-2 (2004), pp. 25–42.

[31] Y. Levy, E. Olchanski, V. Sherbaurn, V. Erenburg, and A. Burcat. “Shock-tube ignition study of methane in air and recirculating gases mixtures”. *J. Propul. Power* 22.3 (2006), pp. 669–676.

[32] C. L. Rasmussen, J. G. Jakobsen, and P. Glarborg. “Experimental Measurements and Kinetic Modeling of CH_4/O_2 and $CH_4/C_2H_6/O_2$ Conversion at High Pressure”. *Int. J. Chem. Kinet.* 40.12 (2008), pp. 778–807.

[33] D. F. Davidson and R. K. Hanson. *Fundamental Kinetics Database Utilizing Shock Tube Measurements, Volume 1: Ignition Delay Time Measurements*. Internal report. Mechanical Engineering Department, Stanford University, CA 94305, USA, 2005.

[34] K. A. Heufer and H. Olivier. “Determination of ignition delay times of different hydrocarbons in a new high pressure shock tube”. *Shock Waves* 20.4 (2010), pp. 307–316.

[35] Y. Zhang, X. Jiang, L. Wei, J. Zhang, C. Tang, and Z. Huang. “Experimental and modeling study on auto-ignition characteristics of methane/hydrogen blends under engine relevant pressure”. *Int. J. Hydrog. Energy* 37.24 (2012), pp. 19168–19176.

[36] J. Huang and W. Bushe. “Experimental and kinetic study of autoignition in methane/ethane/air and methane/propane/air mixtures under engine-relevant conditions”. *Combust. Flame* 144.1 (2006), pp. 74–88.

[37] C. T. Bowman. “An experimental and analytical investigation of the high-temperature oxidation mechanisms of hydrocarbon fuels”. *Combust. Sci. Technol.* 2.2–3 (1970), pp. 161–172.

[38] A. Burcat, K. Scheller, and A. Lifshitz. “Shock-tube investigation of comparative ignition delay times for C1-C5 alkanes”. *Combust. Flame* 16.1 (1971), pp. 29–33.

[39] A. Burcat, R. W. Crossley, K. Scheller, and G. B. Skinner. “Shock tube investigation of ignition in ethane-oxygen-argon mixtures”. *Combust. Flame* 18.1 (1972), pp. 115–123.

[40] D. F. Cooke and A. Williams. “shock-tube studies of methane and ethane oxidation”. *Combust. Flame* 24.2 (1975), pp. 245–256.

[41] Y. Hidaka, Y. Tanaka, H. Kawano, and M. Suga. “Mass spectrometric study of C2-hydrocarbons-Oxidation in shock waves”. *J. Mass Spectrom. Soc. Jpn.* 29.2 (1981), pp. 191–198.

[42] N. Lamoureux, C. E. Paillard, and V. Vaslier. “Low hydrocarbon mixtures ignition delay times investigation behind reflected shock waves”. *Shock waves* 11.4 (2002), pp. 309–322.

[43] J. de Vries, J. M. Hall, S. L. Simmons, M. J. A. Rickard, D. M. Kalitan, and E. L. Petersen. "Ethane ignition and oxidation behind reflected shock waves". *Combust. Flame* 150.1-2 (2007), pp. 137–150.

[44] R. S. Tranter, R. Sivaramakrishnan, K. Brezinsky, and M. D. Allendorf. "High pressure, high temperature shock tube studies of ethane pyrolysis and oxidation". *Phys. Chem. Chem. Phys.* 4.11 (2002), pp. 2001–2010.

[45] R. S. Tranter, H. R. Amoorthy, A. Raman, K. Brezinsky, and M. D. Allendorf. "High-pressure single-pulse shock tube investigation of rich and stoichiometric ethane oxidation". *Proc. Combust. Inst.* 29.1 (2002), pp. 1267–1275.

[46] T. B. Hunter, T. A. Litzinger, H. Wang, and M. Frenklach. "Ethane oxidation at elevated pressures in the intermediate temperature regime: Experiments and modeling". *Combust. Flame* 104.4 (1996), pp. 505–523.

[47] J. H. Mack, S. M. Aceves, and R. W. Dibble. "Demonstrating direct use of wet ethanol in a homogeneous charge compression ignition (HCCI) engine". *Energy* 34.6 (2009), pp. 782–787.

[48] S. Saxena, S. Schneider, S. Aceves, and R. Dibble. "Wet ethanol in HCCI engines with exhaust heat recovery to improve the energy balance of ethanol fuels". *Appl. Energy* 98 (2012), pp. 448–457.

[49] K. Kohse-Höinghaus, P. Oßwald, T. A. Cool, T. Kasper, N. Hansen, F. Qi, C. K. Westbrook, and P. R. Westmoreland. "Biofuel combustion chemistry: from ethanol to biodiesel". *Angew. Chem., Int. Ed.* 49.21 (2010), pp. 3572–3597.

[50] H. Chen, S. Shi-Jin, and W. Jian-Xin. "Study on combustion characteristics and PM emission of diesel engines using ester–ethanol–diesel blended fuels". *Proc. Combust. Inst.* 31.2 (2007), pp. 2981–2989.

[51] A. K. Agarwal. "Biofuels (alcohols and biodiesel) applications as fuels for internal combustion engines". *Prog. Energy Combust. Sci.* 33.3 (2007), pp. 233–271.

[52] Z. Bo, F. Weibiao, and G. Jingsong. "Study of fuel consumption when introducing DME or ethanol into diesel engine". *Fuel* 85.5-6 (2006), pp. 778–782.

[53] E. W. de Menezes, R. da Silva, R. Cataluña, and R. J. Ortega. "Effect of ethers and ether/ethanol additives on the physicochemical properties of diesel fuel and on engine tests". *Fuel* 85.5 (2006), pp. 815–822.

[54] C. Yao, X. Yang, R. Roy Raine, C. Cheng, Z. Tian, and Y. Li. "The Effects of MTBE/Ethanol Additives on Toxic Species Concentration in Gasoline Flame". *Energy Fuels* 23.7 (2009), pp. 3543–3548.

[55] D. Lee, S. Hochgreb, and J. C. Keck. "Autoignition of alcohols and ethers in a rapid compression machine". *SAE Tech. Pap. 932755* (1993).

[56] L. R. Cancino, M. Fikri, A. A. M. Oliveira, and C. Schulz. "Measurement and Chemical Kinetics Modeling of Shock-Induced Ignition of Ethanol-Air Mixtures". *Energy Fuels* 24.5 (2010), pp. 2830–2840.

[57] H. J. Curran, M. P. Dunphy, J. M. Simmie, C. K. Westbrook, and W. J. Pitz. "Shock tube ignition of ethanol, isobutene and MTBE: Experiments and modeling". *Symp. (Int.) Combust., [Proc.]* 24.1 (1992), pp. 769–776.

[58] M. P. Dunphy, P. M. Patterson, and J. M. Simmie. "High-temperature oxidation of ethanol. Part 2.-Kinetic modelling". *J. Chem. Soc., Faraday Trans.* 87.16 (1991), pp. 2549–2559.

[59] K. E. Noorani, B. Akih-Kumgeh, and J. M. Bergthorson. "Comparative high temperature shock tube ignition of C_1–C_4 primary alcohols". *Energy Fuels* 24.11 (2010), pp. 5834–5843.

[60] C. Lee, S. Vranckx, K. A. Heufer, S. V. Khomik, Y. Uygun, H. Olivier, and R. X. Fernandez. "On the Chemical Kinetics of Ethanol Oxidation: Shock Tube, Rapid Compression Machine and Detailed Modeling Study". *Zeitschrift fur Phys. Chemie* 226.1 (2012), pp. 1–28.

[61] F. M. Haas, M. Chaos, and F. L. Dryer. "Low and intermediate temperature oxidation of ethanol and ethanol - PRF blends: An experimental and modeling study". *Combust. Flame* 156.12 (2009), pp. 2346–2350.

[62] J. Li, A. Kazakov, and F. L. Dryer. "Ethanol pyrolysis experiments in a variable pressure flow reactor". *Int. J. Chem. Kinet.* 33.12 (2001), pp. 859–867.

[63] J. Li, A. Kazakov, and F. L. Dryer. "Experimental and Numerical Studies of Ethanol Decomposition Reactions". *J. Phys. Chem. A* 108.38 (2004), pp. 7671–7680.

[64] P. Dagaut and C. Togbé. "Experimental and modeling study of the kinetics of oxidation of ethanol- gasoline surrogate mixtures (E85 surrogate) in a jet-stirred reactor". *Energy Fuels* 22.5 (2008), pp. 3499–3505.

[65] G. Mittal, S. M. Burke, V. A. Davies, B. Parajuli, W. K. Metcalfe, and H. J. Curran. "Autoignition of ethanol in a rapid compression machine". *Combust. Flame* 161.5 (2014), pp. 1164–1171.

[66] T. Fleisch, C. McCarthy, A. Basu, C. Udovich, P. Charbonneau, W. Slodowske, S. E. Mikkelsen, and J. McCandless. "New clean diesel technology: Demonstration of ULEV emissions on a Navistar diesel engine fueled with dimethyl ether". *SAE Spec. Publ.* 1129 (1995), pp. 39–50.

[67] S. Sidhu, J. Graham, and R. Striebich. "Semi-volatile and particulate emissions from the combustion of alternative diesel fuels". *Chemosphere* 42.5–7 (2001), pp. 681–690.

[68] D. Cipolat. "Analysis of energy release and NO_x emissions of a CI engine fuelled on diesel and DME". *Appl. Therm. Eng.* 27.11-12 (2007), pp. 2095–2103.

[69] C. Arcoumanis, C. Bae, R. Crookes, and E. Kinoshita. "The potential of di-methyl ether (DME) as an alternative fuel for compression-ignition engines: A review". *Fuel* 87.7 (2008), pp. 1014–1030.

[70] L. Xinling and H. Zhen. "Emission reduction potential of using gas-to-liquid and dimethyl ether fuels on a turbocharged diesel engine". *Sci. Total Environ.* 407.7 (2009), pp. 2234–2244.

[71] G. Thomas, B. Feng, A. Veeraragavan, M. J. Cleary, and N. Drinnan. "Emissions from DME combustion in diesel engines and their implications on meeting future emission norms: A review". *Fuel Process. Technol.* 119 (2014), pp. 286–304.

[72] M. C. Lee, S. B. Seo, J. H. Chung, Y. J. Joo, and D. H. Ahn. "Industrial gas turbine combustion performance test of DME to use as an alternative fuel for power generation". *Fuel* 88.4 (2009), pp. 657–662.

[73] T. Amano and F. L. Dryer. "Effect of dimethyl ether, NO_x, and ethane on CH_4 oxidation: High pressure, intermediate-temperature experiments and modeling". *Symp. (Int.) Combust., [Proc.]* 1 (1998), pp. 397–404.

[74] Z. Chen, X. Qin, Y. Ju, Z. Zhao, M. Chaos, and F. L. Dryer. "High temperature ignition and combustion enhancement by dimethyl ether addition to methane-air mixtures". *Proc. Combust. Inst.* 31.1 (2007), pp. 1215–1222.

[75] C. Tang, L. Wei, J. Zhang, X. Man, and Z. Huang. "Shock Tube Measurements and Kinetic Investigation on the Ignition Delay Times of Methane/Dimethyl Ether Mixtures". *Energy Fuels* 26.11 (2012), pp. 6720–6728.

[76] E. Hu, Z. Zhang, L. Pan, J. Zhang, and Z. Huang. "Experimental and Modeling Study on Ignition Delay Times of Dimethyl Ether/Propane/Oxygen/Argon Mixtures at 20 bar". *Energy Fuels* 27.7 (2013), pp. 4007–4013.

[77] W. B. Lowry, Z. Serinyel, M. C. Krejci, H. J. Curran, G. Bourque, and E. L. Petersen. "Effect of methane-dimethyl ether fuel blends on flame stability, laminar flame speed, and Markstein length". *Proc. Combust. Inst.* 33.1 (2011), pp. 929–937.

[78] D. Lee, J. S. Lee, H. Y. Kim, C. K. Chun, S. C. James, and S. S. Yoon. "Experimental Study on the Combustion and NO_x Emission Characteristics of DME/LPG Blended Fuel Using Counterflow Burner". *Combust. Sci. Technol.* 184.1 (2012), pp. 97–113.

[79] D. Cipolat and N. Bhana. "Fuelling of a compression ignition engine on ethanol with DME as ignition promoter: Effect of injector configuration". *Fuel Process. Technol.* 90.9 (2009), pp. 1107–1113.

[80] C. Liang, C. Ji, B. Gao, X. Liu, and Y. Zhu. "Investigation on the performance of a spark-ignited ethanol engine with DME enrichment". *Energy Convers. Manag.* 58 (2012), pp. 19–25.

[81] C. J. Green, N. A. Cockshutt, and L. King. "Dimethyl ether as a methanol ignition improver: Substitution requirements and exhaust emissions impact". *SAE Tech. Pap. 902155* (1990).

[82] M. E. Karpuk, J. D. Wright, J. L. Dippo, and D. E. Jantzen. "Dimethyl ether as an ignition enhancer for methanol-fueled diesel engines". *SAE Tech. Pap. 912420* (1991).

[83] M. E. Karpuk and S. W. Cowley. "On board dimethyl ether generation to assist methanol engine cold starting". *SAE Tech. Pap. 881678* (1998).

[84] J. Zhang, E. Hu, L. Pan, Z. Zhang, and Z. Huang. "Shock-Tube Measurements of Ignition Delay Times for the Ethane/Dimethyl Ether Blends". *Energy Fuels* 27.10 (2013), pp. 6247–6254.

[85] U. Burke, K. P. Somers, P. Ó Toole, C. M. Zinner, N. Marquet, G. Bourque, E. L. Petersen, W. K. Metcalfe, Z. Serinyel, and H. J. Curran. "An ignition delay and kinetic modeling study of methane, dimethyl ether, and their mixtures at high pressures". *Combust. Flame* 162.2 (2015), pp. 315–330.

[86] U. Pfahl, K. Fieweger, and G. Adomeit. "Self-ignition of diesel-relevant hydrocarbon-air mixtures under engine conditions". *Symp. (Int.) Combust., [Proc.]* 26.1 (1996), pp. 781–789.

[87] Z. Li, W. Wang, Z. Huang, and M. A. Oehlschlaeger. "Dimethyl Ether Autoignition at Engine-Relevant Conditions". *Energy Fuels* 27.5 (2013), pp. 2811–2817.

[88] L. Pan, E. Hu, J. Zhang, Z. Zhang, and Z. Huang. "Experimental and kinetic study on ignition delay times of DME/H_2/O_2/Ar mixtures". *Combust. Flame* 161.3 (2014), pp. 735–747.

[89] E. Hu, X. Jiang, Z. Huang, J. Zhang, Z. Zhang, and X. Man. "Experimental and Kinetic Studies on Ignition Delay Times of Dimethyl Ether/n-Butane/O_2/Ar Mixtures". *Energy Fuels* 27.1 (2013), pp. 530–536.

[90] H. J. Curran, S. L. Fischer, and F. L. Dryer. "The reaction kinetics of dimethyl ether. II: Low-temperature oxidation in flow reactors". *Int. J. Chem. Kinet.* 32.12 (2000), pp. 741–759.

[91] S. L. Fischer, F. L. Dryer, and H. J. Curran. "The reaction kinetics of dimethyl ether. I: High-temperature pyrolysis and oxidation in flow reactors". *Int. J. Chem. Kinet.* 32.12 (2000), pp. 713–740.

[92] F. Herrmann, P. Oßwald, and K. Kohse-Höinghaus. "Mass spectrometric investigation of the low-temperature dimethyl ether oxidation in an atmospheric pressure laminar flow reactor". *Proc. Combust. Inst.* 34.1 (2013), pp. 771–778.

[93] N. Kurimoto, B. Brumfield, X. Yang, T. Wada, P. Diévart, G. Wysocki, and Y. Ju. "Quantitative measurements of HO_2/H_2O_2 and intermediate species in low and intermediate temperature oxidation of dimethyl ether". *Proc. Combust. Inst.* 35.1 (2015), pp. 457–464.

[94] A. Schonborn, P. Sayad, A. A. Konnov, and J. Klingmann. "Autoignition of Dimethyl Ether and Air in an Optical Flow-Reactor". *Energy Fuels* 28.6 (2014), pp. 4130–4138.

[95] Z. Zhao, M. Chaos, A. Kazakov, and F. L. Dryer. "Thermal decomposition reaction and a comprehensive kinetic model of dimethyl ether". *Int. J. Chem. Kinet.* 40.1 (2008), pp. 1–18.

[96] Y. Hidaka, K. Sato, and M. Yamane. "High-temperature pyrolysis of dimethyl ether in shock waves". *Combust. Flame* 123.1-2 (2000), pp. 1–22.

[97] R. D. Cook, D. F. Davidson, and R. K. Hanson. "Shock tube measurements of ignition delay times and OH time-histories in dimethyl ether oxidation". *Proc. Combust. Inst.* 32.1 (2009), pp. 189–196.

[98] P. Dagaut, C. Daly, J. M. Simmie, and M. Cathonnet. "The oxidation and ignition of dimethylether from low to high temperature (500-1600 K): Experiments and kinetic modeling". *Symp. (Int.) Combust., [Proc.]* 27.1 (1998), pp. 361–369.

[99] P. Dagaut, J.-C. Boettner, and M. Cathonnet. "Chemical kinetic study of dimethylether oxidation in a jet stirred reactor from 1 to 10 atm: Experiments and kinetic modeling". *Symp. (Int.) Combust., [Proc.]* 26.1 (1996), pp. 627–632.

[100] G. Mittal, M. Chaos, C.-J. Sung, and F. L. Dryer. "Dimethyl ether autoignition in a rapid compression machine: Experiments and chemical kinetic modeling". *Fuel Process. Technol.* 89.12 (2008), pp. 1244–1254.

[101] S. H. Pyun, W. Ren, K.-Y. Lam, D. F. Davidson, and R. K. Hanson. "Shock tube measurements of methane, ethylene and carbon monoxide time-histories in DME pyrolysis". *Combust. Flame* 160.4 (2013), pp. 747–754.

[102] C. L. Rasmussen, J. Hansen, P. Marshall, and P. Glarborg. "Experimental measurements and kinetic modeling of $CO/H_2/O_2/NO$, conversion at high pressure". *Int. J. Chem. Kinet.* 40.8 (2008), pp. 454–480.

[103] J. M. Christensen, P. A. Jensen, and A. D. Jensen. "Effects of Feed Composition and Feed Impurities in the Catalytic Conversion of Syngas to Higher Alcohols over Alkali-Promoted Cobalt-Molybdenum Sulfide". *Ind. Eng. Chem. Res.* 50.13 (2011), pp. 7949–7963.

[104] R. B. Bird, W. E. Stewart, and E. N. Lightfoot. *Transport Phenomena*. Wiley, 2007.

[105] D. R. Lide. *CRC handbook of chemistry and physics*. CRC press, 2004.

[106] C. N. Satterfield. *Mass transfer in heterogeneous catalysis*. M.I.T. Press, 1970.

[107] F. A. Holland and R. Bragg. *Fluid Flow for Chemical Engineers (Second Edition)*. Oxford: Butterworth-Heinemann, 1995, pp. 1–69.

[108] F. Monge, V. Aranda, A. Millera, R. Bilbao, and M. Alzueta. "Tubular Flow Reactors". In: *Cleaner Combustion*. Ed. by F. Battin-Leclerc, J. M. Simmie, and E. Blurock. Springer London, 2013, pp. 211–230.

[109] Reaction Design. *CHEMKIN-PRO 15131*. San Diego, USA, 2013.

[110] F. Lindemann, S. Arrhenius, I. Langmuir, N. Dhar, J. Perrin, and W. M. Lewis. "Discussion on "the radiation theory of chemical action"". *Trans. Faraday Soc.* 17 (1922), pp. 598–606.

[111] R. Gilbert, K. Luther, and J. Troe. "Theory of Thermal Unimolecular Reactions in the Fall-off Range. II. Weak Collision Rate Constants". *Berichte der Bunsengesellschaft für physikalische Chemie* 87.2 (1983), pp. 169–177.

[112] R. J. Kee, M. E. Coltrin, and P. Glarborg. *Chemically reacting flow: theory and practice*. Wiley-Interscience, 2003.

[113] E. Goos, A. Burcat, and B. Ruscic. *Ideal Gas Thermochemical Database with updates from Active Thermochemical Tables*. 2014.

[114] B. Ruscic. *Active Thermochemical Tables (ATcT) values based on ver. 1.112 of the Thermochemical Network*. 2013. URL: http://atct.anl.gov/.

[115] S. Li and L. Petzold. "Software and algorithms for sensitivity analysis of large-scale differential algebraic systems". *J. Comput. Appl. Math.* 125.1-2 (2000), pp. 131–145.

[116] L. Petzold, R. Serban, S. Li, S. Raha, and Y. Cao. "Sensitivity analysis and design optimization of differential-algebraic equation systems". *NATO Sci. Ser., Ser. III* 179 (2001), pp. 153–168.

[117] N. N. Semenov. *Chemical kinetics and chain reactions*. International series of monographs on physics. The Clarendon press, 1935.

[118] E. Blurock and F. Battin-Leclerc. "Modeling Combustion with Detailed Kinetic Mechanisms". In: *Cleaner Combustion*. Ed. by F. Battin-Leclerc, J. M. Simmie, and E. Blurock. Springer London, 2013, pp. 17–57.

[119] J. Zador, C. A. Taatjes, and R. X. Fernandes. "Kinetics of elementary reactions in low-temperature autoignition chemistry". *Prog. Energy Combust. Sci.* 37.4 (2011), pp. 371–421.

[120] K. Yasunaga and R. Tranter. "Speciation in Shock Tubes". In: *Cleaner Combustion*. Ed. by F. Battin-Leclerc, J. M. Simmie, and E. Blurock. Springer London, 2013, pp. 143–161.

[121] M. Chaos and F. L. Dryer. "Chemical-kinetic modeling of ignition delay: Considerations in interpreting shock tube data". *Int. J. Chem. Kinet.* 42.3 (2010), pp. 143–150.

[122] J. Warnatz, U. Maas, and R. W. Dibble. *Combustion : physical and chemical fundamentals, modeling and simulation, experiments, pollutant formation*. Springer, 2006.

[123] A. Kéromnés. "Rapid Compression Machines". In: *Cleaner Combustion*. Ed. by F. Battin-Leclerc, J. M. Simmie, and E. Blurock. Springer, 2013, pp. 163–181.

[124] E. J. K. Nilsson and A. A. Konnov. "Flame Studies of Oxygenates". In: *Cleaner Combustion*. Ed. by F. Battin-Leclerc, J. M. Simmie, and E. Blurock. Springer London, 2013, pp. 231–280.

[125] F. L. Dryer and M. Chaos. "Ignition of syngas/air and hydrogen/air mixtures at low temperatures and high pressures: Experimental data interpretation and kinetic modeling implications". *Combust. Flame* 152.1–2 (2008), pp. 293–299.

[126] Z. Hong, D. F. Davidson, and R. K. Hanson. "An improved H_2/O_2 mechanism based on recent shock tube/laser absorption measurements". *Combust. Flame* 158.4 (2011), pp. 633–644.

[127] M. P. Burke, M. Chaos, Y. Ju, F. L. Dryer, and S. J. Klippenstein. "Comprehensive H_2/O_2 kinetic model for high-pressure combustion". *Int. J. Chem. Kinet.* 44.7 (2012), pp. 444–474.

[128] A. Keromnes, W. K. Metcalfe, K. A. Heufer, N. Donohoe, A. K. Das, C.-J. Sung, J. Herzler, C. Naumann, P. Griebel, O. Mathieu, M. C. Krejci, E. L. Petersen, W. J. Pitz, and H. J. Curran. "An experimental and detailed chemical kinetic modeling study of hydrogen and syngas mixture oxidation at elevated pressures". *Combust. Flame* 160 (2013), pp. 995–1011.

[129] Z. Hong, S. S. Vasu, D. F. Davidson, and R. K. Hanson. "Experimental study of the rate of $OH+HO_2 \rightarrow H_2O+O_2$ at high temperatures using the reverse reaction". *J. Phys. Chem. A* 114.17 (2010), pp. 5520–5525.

[130] Z. Hong, D. Davidson, E. Barbour, and R. Hanson. "A new shock tube study of the $H+O_2 \rightarrow OH+O$ reaction rate using tunable diode laser absorption of H_2O near 2.5 μm". *Proc. Combust. Inst.* 33.1 (2011), pp. 309–316.

[131] Z. Hong, K.-Y. Lam, R. Sur, S. Wang, D. F. Davidson, and R. K. Hanson. "On the rate constants of $OH+HO_2$ and HO_2+HO_2: A comprehensive study of H_2O_2 thermal decomposition using multi-species laser absorption". *Proc. Combust. Inst.* 34.1 (2013), pp. 565–571.

[132] M. Sangwan, E. N. Chesnokov, and L. N. Krasnoperov. "Reaction OH + OH Studied over the 298–834 K Temperature and 1–100 bar Pressure Ranges". *J. Phys. Chem. A* 116.24 (2012), pp. 6282–6294.

[133] M. Sangwan and L. N. Krasnoperov. "Disproportionation Channel of Self-Reaction of Hydroxyl Radical, OH + OH = H_2O + O, Studied by Time-Resolved Oxygen Atom Trapping". *J. Phys. Chem. A* 116.48 (2012), pp. 11817–11822.

[134] D. D. Y. Zhou, K. Han, P. Zhang, L. B. Harding, M. J. Davis, and R. T. Skodje. "Theoretical Determination of the Rate Coefficient for the $HO_2 + HO_2 = H_2O_2 + O_2$ Reaction: Adiabatic Treatment of Anharmonic Torsional Effects". *J. Phys. Chem. A* 116.9 (2012), pp. 2089–2100.

[135] M. P. Burke, S. J. Klippenstein, and L. B. Harding. "A quantitative explanation for the apparent anomalous temperature dependence of $OH+HO_2=H_2O+O_2$ through multiscale modeling". *Proc. Combust. Inst.* 34.1 (2013), pp. 547–555.

[136] D. L. Baulch, C. T. Bowman, C. J. Cobos, R. A. Cox, T. Just, J. A. Kerr, M. J. Pilling, D. Stocker, J. Troe, W. Tsang, R. W. Walker, and J. Warnatz. "Evaluated Kinetic Data for Combustion Modeling: Supplement II". *J. Phys. Chem. Ref. Data* 34.3 (2005), pp. 757–1397.

[137] J. Herzler and C. Naumann. "Shock-tube study of the ignition of methane/ ethane/ hydrogen mixtures with hydrogen contents from 0% to 100% at different pressures". *Proc. Combust. Inst.* 32.1 (2009), pp. 213–220.

[138] G. A. Pang, D. F. Davidson, and R. K. Hanson. "Experimental study and modeling of shock tube ignition delay times for hydrogen–oxygen–argon mixtures at low temperatures". *Proc. Combust. Inst.* 32.1 (2009), pp. 181–188.

[139] Y. Zhang, Z. Huang, L. Wei, J. Zhang, and C. K. Law. "Experimental and modeling study on ignition delays of lean mixtures of methane, hydrogen, oxygen, and argon at elevated pressures". *Combust. Flame* 159.3 (2012), pp. 918–931.

[140] D. Lee and S. Hochgreb. "Hydrogen autoignition at pressures above the second explosion limit (0.6–4.0 MPa)". *Int. J. Chem. Kinet.* 30.6 (1998), pp. 385–406.

[141] A. K. Das, C.-J. Sung, Y. Zhang, and G. Mittal. "Ignition delay study of moist hydrogen/oxidizer mixtures using a rapid compression machine". *Int. J. Hydrog. Energy* 37.8 (2012), pp. 6901–6911.

[142] S. Gersen, H. Darmeveil, and H. Levinsky. "The effects of CO addition on the autoignition of H_2, CH_4 and CH_4/H_2 fuels at high pressure in an RCM". *Combust. Flame* 159.12 (2012), pp. 3472–3475.

[143] M. A. Mueller, R. A. Yetter, F. L. Dryer, and T. J. Kim. "Flow reactor studies and kinetic modeling of the H_2/O_2 reaction". *Int. J. Chem. Kinet.* 31.2 (1999), pp. 113–125.

[144] D. Beerer and V. McDonell. "Autoignition of hydrogen and air inside a continuous flow reactor with application to lean premixed combustion". *J. Eng. Gas Turbines Power* 130.5 (2008), p. 051507.

[145] Y. Bedjanian, G. Le Bras, and G. Poulet. "Kinetic Study of OH + OH and OD + OD Reactions". *J. Phys. Chem. A* 103.35 (1999), pp. 7017–7025.

[146] M. S. Wooldridge, R. K. Hanson, and C. T. Bowman. "A shock tube study of the OH + OH = H_2O + O reaction". *Int. J. Chem. Kinet.* 26.4 (1994), pp. 389–401.

[147] M.-K. Bahng and R. G. Macdonald. "Determination of the Rate Constant for the OH(X2Π) + OH(X2Π) = O(3P) + H_2O Reaction over the Temperature Range 293-373 K". *J. Phys. Chem. A* 111.19 (2007), pp. 3850–3861.

[148] G. Altinay and R. G. Macdonald. "Determination of the Rate Constant for the OH(X2Π) + OH(X2Π) = H_2O + O(3P) Reaction Over the Temperature Range 295 to 701 K". *J. Phys. Chem. A* 118.1 (2014), pp. 38–54.

[149] T. L. Nguyen and J. F. Stanton. “Ab Initio Thermal Rate Calculations of HO + HO = O(3P) + H_2O Reaction and Isotopologues”. *J. Phys. Chem. A* 117.13 (2013), pp. 202678–202686.

[150] L. F. Keyser. “Kinetics of the reaction OH + HO_2 = H_2O + O_2 from 254 to 382 K”. *J. Phys. Chem.* 92.5 (1988), pp. 1193–1200.

[151] C. Kappel, K. Luther, and J. Troe. “Shock wave study of the unimolecular dissociation of H_2O_2 in its falloff range and of its secondary reactions”. *Phys. Chem. Chem. Phys.* 4.18 (2002), pp. 4392–4398.

[152] J. Peeters and G. Mahnen. “Reaction mechanisms and rate constants of elementary steps in methane-oxygen flames”. *Symp. (Int.) Combust., [Proc.]* 14.1 (1973), pp. 133–146.

[153] J. M. Goodings and A. N. Hayhurst. “Heat release and radical recombination in premixed fuel-lean flames of H_2+ O_2+ N_2. Rate constants for H + OH + M = H_2O + M and HO_2+ OH = H_2O + O_2”. *J. Chem. Soc., Faraday Trans. 2* 84.6 (1988), pp. 745–762.

[154] N. K. Srinivasan, M.-C. Su, J. W. Sutherland, J. V. Michael, and B. Ruscic. “Reflected Shock Tube Studies of High-Temperature Rate Constants for OH + NO_2 = HO_2 + NO and OH + HO_2= H_2O + O_2”. *J. Phys. Chem. A* 110.21 (2006), pp. 6602–6607.

[155] H. Hippler, H. Neunaber, and J. Troe. “Shock wave studies of the reactions HO + H_2O_2 → H_2O + HO_2 and HO + HO_2 → H_2O + O_2 between 930 and 1680 K”. *J. Chem. Phys.* 103.9 (1995), pp. 3510–3516.

[156] R. Patrick and M. J. Pilling. “The temperature dependence of the HO_2 + HO_2 reaction”. *Chem. Phys. Lett.* 91.5 (1982), pp. 343–347.

[157] M. Brower, E. L. Petersen, W. Metcalfe, H. J. Curran, M. Fueri, G. Bourque, N. Aluri, and F. Guethe. “Ignition Delay Time and Laminar Flame Speed Calculations for Natural Gas/Hydrogen Blends at Elevated Pressures”. *J. Eng. Gas Turbines Power* 135.2 (2013), p. 21504.

[158] H. Sun and Z. Li. “Rate constant measurement for the OH + OH = H_2O + O reaction at 220–320 K using discharge flow/mass spectrometer/resonance fluorescence technique”. *Chem. Phys. Lett.* 399.1-3 (2004), pp. 33–38.

[159] J. W. Sutherland, P. M. Patterson, and R. B. Klemm. “Rate constants for the reaction, O(3P)+H_2O ⇆ OH+OH, over the temperature range 1053 K to 2033 K using two direct techniques”. *Symp. (Int.) Combust., [Proc.]* 23.1 (1991), pp. 51–57.

[160] P. D. Lightfoot, B. Veyret, and R. Lesclaux. “The rate constant for the HO_2+HO_2 reaction at elevated temperatures”. *Chem. Phys. Lett.* 150.1–2 (1988), pp. 120–126.

[161] S. Gersen, A. Mokhov, J. Darmeveil, H. Levinsky, and P. Glarborg. “Ignition-promoting effect of NO_2 on methane, ethane and methane/ethane mixtures in a rapid compression machine”. *Proc. Combust. Inst.* 33.1 (2011), pp. 433–440.

[162] A. E. Lutz, R. J. Kee, and J. A. Miller. *SENKIN: A FORTRAN Program for Predicting Homogeneous Gas Phase Chemical Kinetics with Sensitivity Analysis*. Tech. rep. MS-9051. Livermore: Sandia National Laboratories, 1988.

[163] K. T. Aung, M. I. Hassan, and G. M. Faeth. "Flame stretch interactions of laminar premixed hydrogen/air flames at normal temperature and pressure". *Combust. Flame* 109.1–2 (1997), pp. 1–24.

[164] E. Hu, Z. Huang, J. He, C. Jin, and J. Zheng. "Experimental and numerical study on laminar burning characteristics of premixed methane-hydrogen-air flames". *Int. J. Hydrog. Energy* 34.11 (2009), pp. 4876–4888.

[165] O. C. Kwon and G. M. Faeth. "Flame/stretch interactions of premixed hydrogen-fueled flames: Measurements and predictions". *Combust. Flame* 124.4 (2001), pp. 590–610.

[166] N. Lamoureux, N. Djebaili-Chaumeix, and C. Paillard. "Laminar flame velocity determination for H_2-air-steam mixtures using the spherical bomb method". In: *Journal de Physique IV (Proceedings)*. Vol. 12. 7. EDP sciences. 2002, pp. 445–452.

[167] C. Tang, Z. Huang, C. Jin, J. He, J. Wang, X. Wang, and H. Miao. "Laminar burning velocities and combustion characteristics of propane-hydrogen-air premixed flames". *Int. J. Hydrog. Energy* 33.18 (2008), pp. 4906–4914.

[168] S. D. Tse, D. L. Zhu, and C. K. Law. "Morphology and burning rates of expanding spherical flames in H_2/O_2/inert mixtures up to 60 atmospheres". *Proc. Combust. Inst.* 28.2 (2000), pp. 1793–1800.

[169] C. M. Vagelopoulos, F. N. Egolfopoulos, and C. K. Law. "Further considerations on the determination of laminar flame speeds with the counterflow twin-flame technique". *Symp. (Int.) Combust., [Proc.]* 25.1 (1994), pp. 1341–1347.

[170] S. Verhelst, R. Woolley, M. Lawes, and R. Sierens. "Laminar and unstable burning velocities and Markstein lengths of hydrogen-air mixtures at engine-like conditions". *Proc. Combust. Inst.* 30.1 (2005), pp. 209–216.

[171] International Energy Agency. *Are We Entering a Golden Age of Gas? (World energy outlook 2011)*. Paris: IEA, International Energy Agency OECD, 2011.

[172] G. P. Smith, D. M. Golden, M. Frenklach, N. W. Moriarty, B. Eiteneer, M. Goldenberg, C. T. Bowman, R. K. Hanson, S. Song, J. William C. Gardiner, V. V. Lissianski, and Z. Qin. *GRI-Mech Version 3.0*. 1999. URL: http://combustion.berkeley.edu/gri-mech/.

[173] E. L. Petersen, D. M. Kalitan, S. Simmons, G. Bourque, H. J. Curran, and J. M. Simmie. "Methane/propane oxidation at high pressures: Experimental and detailed chemical kinetic modeling". *Proc. Combust. Inst.* 31.1 (2007), pp. 447–454.

[174] F. H. V. Coppens, J. D. Ruyck, and A. A. Konnov. "The effects of composition on burning velocity and nitric oxide formation in laminar premixed flames of $CH_4 + H_2 + O_2 + N_2$". *Combust. Flame* 149.4 (2007), pp. 409–417.

[175] H. Jin, A. Cuoci, A. Frassoldati, T. Faravelli, Y. Wang, Y. Li, and F. Qi. "Experimental and kinetic modeling study of PAH formation in methane coflow diffusion flames doped with n-butanol". *Combust. Flame* 161.3 (2014), pp. 657–670.

[176] J. A. Miller, M. J. Pilling, and J. Troe. "Unravelling combustion mechanisms through a quantitative understanding of elementary reactions". *Proc. Combust. Inst.* 30.1 (2005), pp. 43–88.

[177] C. L. Rasmussen, A. E. Rasmussen, and P. Glarborg. "Sensitizing effects of NO_x on CH_4 oxidation at high pressure". *Combust. Flame* 154.3 (2008), pp. 529–545.

[178] J. G. Lopez, C. L. Rasmussen, M. U. Alzueta, Y. Gao, P. Marshall, and P. Glarborg. "Experimental and kinetic modeling study of C_2H_4 oxidation at high pressure". *Proc. Combust. Inst.* 32 (2009), pp. 367–375.

[179] V. Aranda, J. M. Christensen, M. U. Alzueta, P. Glarborg, S. Gersen, Y. Gao, and P. Marshall. "Experimental and Kinetic Modeling Study of Methanol Ignition and Oxidation at High Pressure". *Int. J. Chem. Kinet.* 45.5 (2013), pp. 283–294.

[180] C. L. Rasmussen, K. H. Wassard, K. Dam-Johansen, and P. Glarborg. "Methanol oxidation in a flow reactor: Implications for the branching ratio of the CH_3OH+OH reaction". *Int. J. Chem. Kinet.* 40.7 (2008), pp. 423–441.

[181] J. Li, Z. Zhao, A. Kazakov, M. Chaos, F. L. Dryer, and J. J. Scire. "A comprehensive kinetic mechanism for CO, CH_2O, and CH_3OH combustion". *Int. J. Chem. Kinet.* 39.3 (2007), pp. 109–136.

[182] M. Colberg and G. Friedrichs. "Room Temperature and Shock Tube Study of the Reaction HCO + O_2 Using the Photolysis of Glyoxal as an Efficient HCO Source". *J. Phys. Chem. A* 110.1 (2006), pp. 160–170.

[183] N. Fassheber, G. Friedrichs, P. Marshall, and P. Glarborg. "High Temperature Glyoxal Oxidation: Implications for HCO+O_2". *To be Submitted* (2015).

[184] F. L. Nesbitt, J. F. Gleason, and L. J. Stief. "Temperature Dependence of the Rate Constant for the Reaction HCO + O_2 = HO_2 + CO at T = 200–398 K". *J. Phys. Chem. A* 103.16 (1999), pp. 3038–3043.

[185] B. Veyret and R. Lesclaux. "Absolute rate constants for the reactions of the formyl radical HCO with oxygen and nitric oxide from 298 to 503 K". *J. Phys. Chem.* 85.13 (1981), pp. 1918–1922.

[186] R. S. Timonen, E. Ratajczak, and D. Gutman. "Kinetics of the reactions of the formyl radical with oxygen, nitrogen dioxide, chlorine, and bromine". *J. Phys. Chem.* 92.3 (1988), pp. 651–655.

[187] J. D. DeSain, L. E. Jusinski, A. D. Ho, and C. A. Taatjes. "Temperature dependence and deuterium kinetic isotope effects in the HCO (DCO)+O_2 reaction between 296 and 673 K". *Chem. Phys. Lett.* 347.1–3 (2001), pp. 79–86.

[188] H. Hippler, N. Krasteva, and F. Striebel. “The thermal unimolecular decomposition of HCO: Effects of state specific rate constants on the thermal rate constant”. *Phys. Chem. Chem. Phys.* 6.13 (2004), pp. 3383–3388.

[189] L. Krasnoperov, E. Chesnokov, H. Stark, and A. Ravishankara. “Elementary reactions of formyl (HCO) radical studied by laser photolysis–transient absorption spectroscopy”. *Proc. Combust. Inst.* 30.1 (2005), pp. 935–943.

[190] X. Yang, T. Tan, P. Diévart, E. A. Carter, and Y. Ju. “Theoretical assessment on reaction kinetics HCO and CH_2OH unimolecular decomposition”. In: *8th U. S. Combust. Meet.* 2013.

[191] J. Troe. “Refined Analysis of the Thermal Dissociation of Formaldehyde”. *J. Phys. Chem. A* 111.19 (2007), pp. 3862–3867.

[192] S. Wang, E. E. Dames, D. F. Davidson, and R. K. Hanson. “Reaction Rate Constant of CH_2O + H = HCO + H_2 Revisited: A Combined Study of Direct Shock Tube Measurement and Transition State Theory Calculation”. *J. Phys. Chem. A* 118.44 (2014), pp. 10201–10209.

[193] S. Wang, D. F. Davidson, and R. K. Hanson. “High temperature measurements for the rate constants of C_1–C_4 aldehydes with OH in a shock tube”. *Proc. Combust. Inst.* 35.1 (2015), pp. 473–480.

[194] B. Eiteneer, C.-L. Yu, M. Goldenberg, and M. Frenklach. “Determination of Rate Coefficients for Reactions of Formaldehyde Pyrolysis and Oxidation in the Gas Phase”. *J. Phys. Chem. A* 102.27 (1998), pp. 5196–5205.

[195] J. W. Sutherland, M.-C. Su, and J. V. Michael. “Rate constants for H + CH_4, CH_3 + H_2, and CH_4 dissociation at high temperature”. *Int. J. Chem. Kinet.* 33.11 (2001), pp. 669–684.

[196] G. Rozenchan, D. L. Zhu, C. K. Law, and S. D. Tse. “Outward propagation, burning velocities, and chemical effects of methane flames up to 60 atm”. *Proc. Combust. Inst.* 29.2 (2002), pp. 1461–1470.

[197] O. Park, P. S. Veloo, N. Liu, and F. N. Egolfopoulos. “Combustion characteristics of alternative gaseous fuels”. *Proc. Combust. Inst.* 33.1 (2011), pp. 887–894.

[198] J. Troe and V. G. Ushakov. “The dissociation/recombination reaction CH_4 (+M) = CH_3 + H (+M): A case study for unimolecular rate theory”. *J. Chem. Phys.* 136.21 (2012), p. 214309.

[199] J. Zador, S. J. Klippenstein, and J. A. Miller. “Pressure-Dependent OH Yields in Alkene + HO_2 Reactions: A Theoretical Study”. *J. Phys. Chem. A* 115.36 (2011), pp. 10218–10225.

[200] N. K. Srinivasan, M.-C. Su, J. W. Sutherland, and J. V. Michael. “Reflected Shock Tube Studies of High-Temperature Rate Constants for OH + CH_4 = CH_3 + H_2O and CH_3 + NO_2 = CH_3O + NO”. *J. Phys. Chem. A* 109.9 (2005), pp. 1857–1863.

[201] A. W. Jasper, S. J. Klippenstein, L. B. Harding, and B. Ruscic. "Kinetics of the Reaction of Methyl Radical with Hydroxyl Radical and Methanol Decomposition". *J. Phys. Chem. A* 111.19 (2007), pp. 3932–3950.

[202] M. Sangwan, E. N. Chesnokov, and L. N. Krasnoperov. "Reaction CH_3 + OH Studied over the 294–714 K Temperature and 1–100 bar Pressure Ranges". *J. Phys. Chem. A* 116.34 (2012), pp. 8661–8670.

[203] Z. Hong, D. F. Davidson, K.-Y. Lam, and R. K. Hanson. "A shock tube study of the rate constants of HO_2 and CH_3 reactions". *Combust. Flame* 159.10 (2012), pp. 3007–3013.

[204] V. P. Zhukov. "Kinetic model of alkane oxidation at high pressure from methane to n-heptane". *Combust. Theory Modell.* 13.3 (2009), pp. 427–442.

[205] A. W. Jasper, S. J. Klippenstein, and L. B. Harding. "Theoretical rate coefficients for the reaction of methyl radical with hydroperoxyl radical and for methylhydroperoxide decomposition". *Proc. Combust. Inst.* 32.1 (2009), pp. 279–286.

[206] R. Zhu and C. Lin. "The CH_3 + HO_2 Reaction: First-Principles Prediction of Its Rate Constant and Product Branching Probabilities". *J. Phys. Chem. A* 105.25 (2001), pp. 6243–6248.

[207] M. Sangwan and L. N. Krasnoperov. "Kinetics of the Gas Phase Reaction CH_3 + HO_2". *J. Phys. Chem. A* 117.14 (2013), pp. 2916–2923.

[208] N. K. Srinivasan, J. V. Michael, L. B. Harding, and S. J. Klippenstein. "Experimental and theoretical rate constants for CH_4 + O_2 = CH_3 + HO_2". *Combust. Flame* 149.1-2 (2007), pp. 104–111.

[209] N. K. Srinivasan, M.-C. Su, and J. V. Michael. "CH_3 + O_2 = H_2CO + OH Revisited". *J. Phys. Chem. A* 111.45 (2007), pp. 11589–11591.

[210] R. X. Fernandes, K. Luther, and J. Troe. "Falloff curves for the reaction CH_3+ O_2 (+ M) → CH_3O_2 (+ M) in the pressure range 2-1000 bar and the temperature range 300-700 K". *J. Phys. Chem. A* 110.13 (2006), pp. 4442–4449.

[211] N. K. Srinivasan, M.-C. Su, J. W. Sutherland, and J. V. Michael. "Reflected Shock Tube Studies of High-Temperature Rate Constants for CH_3 + O_2, H_2CO + O_2, and OH + O_2". *J. Phys. Chem. A* 109.35 (2005), pp. 7902–7914.

[212] F. Ewig, D. Rhäsa, and R. Zellner. "Kinetics, Energetics and OH Product Yield of the Reaction CH_3O+ O (3P) → $CH_3O^*_2$ → Products". *Berichte der Bunsengesellschaft für physikalische Chemie* 91.7 (1987), pp. 708–717.

[213] W. Tsang and R. F. Hampson. "Chemical Kinetic Data Base for Combustion Chemistry. Part I. Methane and Related Compounds". *J. Phys. Chem. Ref. Data* 15.3 (1986), pp. 1087–1279.

[214] A. Bossolasco, E. P. Faragó, C. Schoemaecker, and C. Fittschen. "Rate constant of the reaction between CH_3O_2 and OH radicals". *Chemical Physics Letters* 593 (2014), pp. 7–13.

[215] G. S. Tyndall, R. A. Cox, C. Granier, R. Lesclaux, G. K. Moortgat, M. J. Pilling, A. R. Ravishankara, and T. J. Wallington. "Atmospheric chemistry of small organic peroxy radicals". *J. Geophys. Res. Atmos.* 106.D11 (2001), pp. 12157–12182.

[216] M. Keiffer, A. J. Miscampbell, and M. J. Pilling. "A global technique for analysing multiple decay curves. Application to the CH_3+ O_2 system". *J. Chem. Soc., Faraday Trans. 2* 84.5 (1988), pp. 505–514.

[217] P. J. Wantuck, R. C. Oldenborg, S. L. Baughcum, and K. R. Winn. "Direct measurements of methoxy removal rate constants for collisions with CH_4, Ar, N_2, Xe, and CF4 in the temperature range 673-973 K". *Symp. (Int.) Combust., [Proc.]* 22.1 (1989), pp. 973–981.

[218] M. A. Deminskii, I. V. Chernysheva, S. Umanskii, M. I. Strelkova, A. E. Baranov, I. V. Kochetov, A. P. Napartovich, T. Sommerer, S. Saddoughi, J. Herbon, and B. V. Potapkin. "Low-temperature ignition of methane-air mixtures under the action of nonequilibrium plasma". *Russ. J. Phys. Chem. B* 7.4 (2013), pp. 410–423.

[219] V. S. Arutyunov, V. I. Vedeneev, and V. Y. Basevich. "Direct high-pressure gas-phase oxidation of natural gas to methanol and other oxygenates". *Russ. Chem. Rev.* 65.3 (1996), pp. 197–224.

[220] A. Lifshitz, K. Scheller, A. Burcat, and G. B. Skinner. "Shock-tube investigation of ignition in methane-oxygen-argon mixtures". *Combust. Flame* 16.3 (1971), pp. 311–321.

[221] E. K. Dabora. "Effect of NO_2 on the ignition delay of CH_4-air mixtures". *Combust. Flame* 24 (1975), pp. 181–184.

[222] L. J. Spadaccini and M. B. Colket. "Ignition delay characteristics of methane fuels". *Prog. Energy Combust. Sci.* 20.5 (1994), pp. 431–460.

[223] E. L. Petersen, M. Röhrig, D. F. Davidson, R. K. Hanson, and C. T. Bowman. "High-pressure methane oxidation behind reflected shock waves". *Symp. (Int.) Combust., [Proc.]* 26.1 (1996), pp. 799–806.

[224] E. L. Petersen, D. F. Davidson, and R. K. Hanson. "Kinetics modeling of shock-induced ignition in low-dilution CH_4/O_2 mixtures at high pressures and intermediate temperatures". *Combust. Flame* 117.1-2 (1999), pp. 272–290.

[225] P. Dirrenberger, H. Le Gall, R. Bounaceur, O. Herbinet, P.-A. Glaude, A. Konnov, and F. Battin-Leclerc. "Measurements of laminar flame velocity for components of natural gas". *Energy Fuels* 25.9 (2011), pp. 3875–3884.

[226] E. Varea, V. Modica, A. Vandel, and B. Renou. "Measurement of laminar burning velocity and Markstein length relative to fresh gases using a new postprocessing procedure: Application to laminar spherical flames for methane, ethanol and isooctane/air mixtures". *Combust. Flame* 159.2 (2012), pp. 577–590.

[227] M. Goswami, S. C. R. Derks, K. Coumans, W. J. Slikker, M. H. de Andrade Oliveira, R. J. M. Bastiaans, C. C. M. Luijten, L. P. H. de Goey, and A. A. Konnov. "The effect of elevated pressures on the laminar burning velocity of methane + air mixtures". *Combust. Flame* 160.9 (2013), pp. 1627–1635.

[228] T. Tahtouh, F. Halter, and C. Mounaim-Rousselle. "Measurement of laminar burning speeds and Markstein lengths using a novel methodology". *Combust. Flame* 156.9 (2009), pp. 1735–1743.

[229] W. Lowry, J. de Vries, M. Krejci, E. Petersen, Z. Serinyel, W. Metcalfe, H. Curran, and G. Bourque. "Laminar Flame Speed Measurements and Modeling of Pure Alkanes and Alkane Blends at Elevated Pressures". *J. Eng. Gas Turbines Power* 133.9 (2011), p. 91501.

[230] S. Tanaka, F. Ayala, J. C. Keck, and J. B. Heywood. "Two-stage ignition in HCCI combustion and HCCI control by fuels and additives". *Combust. Flame* 132.1-2 (2003), pp. 219–239.

[231] J. Y. Ren, F. N. Egolfopoulos, and T. T. Tsotsis. "NO_X emission control of lean methane-air combustion with addition of methane reforming products". *Combust. Sci. Technol.* 174.4 (2002), pp. 181–205.

[232] P. Dagaut, M. Cathonnet, and J.-c. Boettner. "Kinetics of ethane oxidation". *Int. J. Chem. Kinet.* 23.5 (1991), pp. 437–455.

[233] D. J. Beerer and V. G. McDonell. "An experimental and kinetic study of alkane autoignition at high pressures and intermediate temperatures". *Proc. Combust. Inst.* 33.1 (2011), pp. 301–307.

[234] R. S. Tranter, A. Raman, R. Sivaramakrishnan, and K. Brezinsky. "Ethane oxidation and pyrolysis from 5 bar to 1000 bar: Experiments and simulation". *Int. J. Chem. Kinet.* 37.5 (2005), pp. 306–331.

[235] D. Nötzold and J. Algermissen. "Chemical kinetics of the ethane-oxygen reaction part I: High temperature oxidation at ignition temperatures between 1400 K and 1800 K". *Combust. Flame* 40 (1981), pp. 293–313.

[236] C. V. Naik and A. M. Dean. "Modeling high pressure ethane oxidation and pyrolysis". *Proc. Combust. Inst.* 32.1 (2009), pp. 437–443.

[237] H. Hashemi, J. M. Christensen, and P. Glarborg. "Ignition of Methane at High Pressure and Medium Temperatures: Measurements and Kinetic Modeling". To be submitted, see Chapter 6. 2015.

[238] S. J. Klippenstein, Y. Georgievskii, and L. B. Harding. "Predictive theory for the combination kinetics of two alkyl radicals". *Phys. Chem. Chem. Phys.* 8.10 (2006), pp. 1133–1147.

[239] R. Sivaramakrishnan, J. V. Michael, and B. Ruscic. "High-temperature rate constants for H/D + C_2H_6 and C_3H_8". *Int. J. Chem. Kinet.* 44.3 (2012), pp. 194–205.

[240] L. N. Krasnoperov and J. V. Michael. “Shock Tube Studies Using a Novel Multipass Absorption Cell: Rate Constant Results For OH + H_2 and OH + C_2H_6”. *J. Phys. Chem. A* 108.26 (2004), pp. 5643–5648.

[241] A. S. Sharipov and A. M. Starik. “Theoretical Study of the Reaction of Ethane with Oxygen Molecules in the Ground Triplet and Singlet Delta States”. *J. Phys. Chem. A* 116.33 (2012), pp. 8444–8454.

[242] S. L. Peukert, N. J. Labbe, R. Sivaramakrishnan, and J. V. Michael. “Direct Measurements of Rate Constants for the Reactions of CH_3 Radicals with C_2H_6, C_2H_4, and C_2H_2 at High Temperatures”. *J. Phys. Chem. A* 117.40 (2013), pp. 10228–10238.

[243] N. J. Labbe, R. Sivaramakrishnan, and S. J. Klippenstein. “The role of radical + fuel-radical well-skipping reactions in ethanol and methylformate low-pressure flames”. *Proc. Combust. Inst.* 35.1 (2015), pp. 447–455.

[244] S. J. Klippenstein. “Personal Communication”. 2015.

[245] D. Chen, H. Jin, Z. Wang, L. Zhang, and F. Qi. “Unimolecular Decomposition of Ethyl Hydroperoxide: Ab Initio/Rice-Ramsperger-Kassel-Marcus Theoretical Prediction of Rate Constants”. *J. Phys. Chem. A* 115.5 (2011), pp. 602–611.

[246] J. P. Senosiain, S. J. Klippenstein, and J. A. Miller. “Reaction of Ethylene with Hydroxyl Radicals: A Theoretical Study”. *J. Phys. Chem. A* 110.21 (2006), pp. 6960–6970.

[247] S. S. Vasu, Z. Hong, D. F. Davidson, R. K. Hanson, and D. M. Golden. “Shock Tube/Laser Absorption Measurements of the Reaction Rates of OH with Ethylene and Propene”. *J. Phys. Chem. A* 114.43 (2010), pp. 11529–11537.

[248] C. F. Goldsmith, W. H. Green, and S. J. Klippenstein. “Role of O_2 + QOOH in Low-Temperature Ignition of Propane. 1. Temperature and Pressure Dependent Rate Coefficients”. *J. Phys. Chem. A* 116.13 (2012), pp. 3325–3346.

[249] J. A. Miller and S. J. Klippenstein. “The H + C_2H_2 (+M) = C_2H_3 (+M) and H + C_2H_2 (+M) = C_2H_5 (+M) reactions: Electronic structure, variational transition-state theory, and solutions to a two-dimensional master equation”. *Phys. Chem. Chem. Phys.* 6.6 (2004), pp. 1192–1202.

[250] L. Pan, Y. Zhang, J. Zhang, Z. Tian, and Z. Huang. “Shock tube and kinetic study of $C_2H_6/H_2/O_2$/Ar mixtures at elevated pressures”. *Int. J. Hydrog. Energy* 39.11 (2014), pp. 6024–6033.

[251] A. A. Konnov, I. V. Dyakov, and J. De Ruyck. “Measurement of adiabatic burning velocity in ethane-oxygen-nitrogen and in ethane-oxygen-argon mixtures”. *Exp. Therm. Fluid Sci.* 27.4 (2003), pp. 379–384.

[252] G. Jomaas, X. L. Zheng, D. L. Zhu, and C. K. Law. “Experimental determination of counterflow ignition temperatures and laminar flame speeds of C_2-C_3 hydrocarbons at atmospheric and elevated pressures”. *Proc. Combust. Inst.* 30.1 (2005), pp. 193–200.

[253] I. V. Dyakov, J. De Ruyck, and A. A. Konnov. "Probe sampling measurements and modeling of nitric oxide formation in ethane+air flames". *Fuel* 86.1-2 (2007), pp. 98–105.

[254] M. Goswami. "Laminar Burning Velocities at Elevated Pressures using the Heat Flux Method". PhD thesis. Technische Universiteit Eindhoven, 2014.

[255] F. N. Egolfopoulos, D. L. Zhu, and C. K. Law. "Experimental and numerical determination of laminar flame speeds: Mixtures of C2-hydrocarbons with oxygen and nitrogen". *Symp. (Int.) Combust., [Proc.]* 23.1 (1991), pp. 471–478.

[256] M. I. Hassan, K. T. Aung, O. C. Kwon, and G. M. Faeth. "Properties of laminar premixed hydrocarbon/air flames at various pressures". *J. Propul. Power* 14.4 (1998), pp. 479–488.

[257] K. Kumar, G. Mittal, C.-J. Sung, and C. K. Law. "An experimental investigation of ethylene/O_2/diluent mixtures: Laminar flame speeds with preheat and ignition delays at high pressures". *Combust. Flame* 153.3 (2008), pp. 343–354.

[258] M. Yao, Z. Zheng, and H. Liu. "Progress and recent trends in homogeneous charge compression ignition (HCCI) engines". *Prog. Energy Combust. Sci.* 35.5 (2009), pp. 398–437.

[259] N. M. Marinov. "A detailed chemical kinetic model for high temperature ethanol oxidation". *Int. J. Chem. Kinet.* 31.3 (1999), pp. 183–220.

[260] T. S. Norton and F. L. Dryer. "The flow reactor oxidation of C1-C4 alcohols and MTBE". *Symp. Combust.* 23.1 (1991), pp. 179–185.

[261] T. S. Norton and F. L. Dryer. "An experimental and modeling study of ethanol oxidation-kinetics in an atmospheric-pressure flow reactor". *Int. J. Chem. Kinet.* 24.4 (1992), pp. 319–344.

[262] A. Frassoldati, A. Cuoci, T. Faravelli, and E. Ranzi. "Kinetic Modeling of the Oxidation of Ethanol and Gasoline Surrogate Mixtures". *Combust. Sci. Technol.* 182.4-6 (2010), pp. 653–667.

[263] P. Saxena and F. A. Williams. "Numerical and experimental studies of ethanol flames". *Proc. Combust. Inst.* 31.1 (2007), pp. 1149–1156.

[264] N. Leplat, P. Dagaut, C. Togbé, and J. Vandooren. "Numerical and experimental study of ethanol combustion and oxidation in laminar premixed flames and in jet-stirred reactor". *Combust. Flame* 158.4 (2011), pp. 705–725.

[265] H. Hashemi, J. M. Christensen, and P. Glarborg. "Ignition and Oxidation Properties of Ethane at High Pressure". To be submitted, see Chapter 7. 2015.

[266] R. Sivaramakrishnan, M.-C. Su, J. V. Michael, S. J. Klippenstein, L. B. Harding, and B. Ruscic. "Rate constants for the thermal decomposition of ethanol and its bimolecular reactions with OH and D: Reflected shock tube and theoretical studies". *J. Phys. Chem. A* 114.35 (2010), pp. 9425–9439.

[267] J. Park, Z. F. Xu, and M. C. Lin. "Thermal decomposition of ethanol. II. A computational study of the kinetics and mechanism for the H + C_2H_5OH reaction". *J. Chem. Phys.* 118.22 (2003), pp. 9990–9996.

[268] C.-W. Wu, H. Matsui, N.-S. Wang, and M. C. Lin. "Shock Tube Study on the Thermal Decomposition of Ethanol". *J. Phys. Chem. A* 115.28 (2011), pp. 8086–8092.

[269] J. Kiecherer, C. Bänsch, T. Bentz, and M. Olzmann. "Pyrolysis of ethanol: A shock-tube/TOF-MS and modeling study". *Proc. Combust. Inst.* 35.1 (2015), pp. 465–472.

[270] R. Meana-Paneda and A. Fernandez-Ramos. "Accounting for conformational flexibility and torsional anharmonicity in the H + CH_3CH_2OH hydrogen abstraction reactions: A multi-path variational transition state theory study". *J. Chem. Phys.* 140.17 (2014), p. 174303.

[271] S. A. Carr, M. A. Blitz, and P. W. Seakins. "Site-Specific Rate Coefficients for Reaction of OH with Ethanol from 298 to 900 K". *J. Phys. Chem. A* 115.15 (2011), pp. 3335–3345.

[272] J. Zheng and D. G. Truhlar. "Multi-path variational transition state theory for chemical reaction rates of complex polyatomic species: Ethanol + OH reactions". *Faraday Discuss.* 157 (2012), pp. 59–88.

[273] I. Stranic, G. A. Pang, R. K. Hanson, D. M. Golden, and C. T. Bowmant. "Shock Tube Measurements of the Rate Constant for the Reaction Ethanol plus OH". *J. Phys. Chem. A* 118.5 (2014), pp. 822–828.

[274] Z. F. Xu, J. Park, and M. C. Lin. "Thermal decomposition of ethanol. III. A computational study of the kinetics and mechanism for the CH_3 + C_2H_5OH reaction". *J. Chem. Phys.* 120.14 (2004), pp. 6593–6599.

[275] E. E. Dames. "Master Equation Modeling of the Unimolecular Decompositions of alpha-Hydroxyethyl (CH_3CHOH) and Ethoxy (CH_3CH_2O) Radicals". *Int. J. Chem. Kinet.* 46.3 (2014), pp. 176–188.

[276] Z. F. Xu, K. Xu, and M. C. Lin. "Ab Initio Kinetics for Decomposition/Isomerization Reactions of C_2H_5O Radicals". *ChemPhysChem* 10.6 (2009), pp. 972–982.

[277] G. da Silva, J. W. Bozzelli, L. Liang, and J. T. Farrell. "Ethanol Oxidation: Kinetics of the alpha-Hydroxyethyl Radical + O_2 Reaction". *J. Phys. Chem. A* 113.31 (2009), pp. 8923–8933.

[278] J. Zador, R. X. Fernandes, Y. Georgievskii, G. Meloni, C. A. Taatjes, and J. A. Miller. "The reaction of hydroxyethyl radicals with O_2: A theoretical analysis and experimental product study". *Proc. Combust. Inst.* 32 (2009), pp. 271–277.

[279] T. Yamada, J. W. Bozzelli, and T. Lay. "Kinetic and Thermodynamic Analysis on OH Addition to Ethylene: Adduct Formation, Isomerization, and Isomer Dissociations". *J. Phys. Chem. A* 103.38 (1999), pp. 7646–7655.

[280] N. K. Srinivasan, M.-C. Su, and J. V. Michael. "Reflected shock tube studies of high-temperature rate constants for OH + C_2H_2 and OH + C_2H_4". *Phys. Chem. Chem. Phys.* 9.31 (2007), pp. 4155–4163.

[281] G. da Silva, J. W. Bozzelli, L. Liang, and J. T. Farrell. "Thermochemistry and kinetics of the alpha- and beta-hydroxyethyl radical+ O_2 reactions in ethanol combustion". In: *5th US Combust. Meet.* 2007, pp. 25–28.

[282] F. Caralp, P. Devolder, C. Fittschen, N. Gomez, H. Hippler, R. Mereau, M. T. Rayez, F. Striebel, and B. Viskolcz. "The thermal unimolecular decomposition rate constants of ethoxy radicals". *Phys. Chem. Chem. Phys.* 1.12 (1999), pp. 2935–2944.

[283] Z. F. Xu, K. Xu, and M. C. Lin. "Thermal Decomposition of Ethanol. 4. Ab Initio Chemical Kinetics for Reactions of H Atoms with CH_3CH_2O and CH_3CHOH Radicals". *J. Phys. Chem. A* 115.15 (2011), pp. 3509–3522.

[284] R. Sivaramakrishnan, J. V. Michael, and S. J. Klippenstein. "Direct Observation of Roaming Radicals in the Thermal Decomposition of Acetaldehyde". *J. Phys. Chem. A* 114.2 (2010), pp. 755–764.

[285] K. Yasunaga, S. Kubo, H. Hoshikawa, T. Kamesawa, and Y. Hidaka. "Shock-tube and modeling study of acetaldehyde pyrolysis and oxidation". *Int. J. Chem. Kinet.* 40.2 (2008), pp. 73–102.

[286] J.-X. Shao, C.-M. Gong, X.-Y. Li, and J. Li. "Unimolecular decomposition mechanism of vinyl alcohol by computational study". *Theor. Chem. Acc.* 128.3 (2011), pp. 341–348.

[287] P. H. Taylor, T. Yamada, and P. Marshall. "The reaction of OH with acetaldehyde and deuterated acetaldehyde: Further insight into the reaction mechanism at both low and elevated temperatures". *Int. J. Chem. Kinet.* 38.8 (2006), pp. 489–495.

[288] M. Cameron, V. Sivakumaran, T. J. Dillon, and J. N. Crowley. "Reaction between OH and CH_3CHO Part 1. Primary product yields of CH_3 (296 K), CH_3CO (296 K), and H (237-296 K)". *Phys. Chem. Chem. Phys.* 4.15 (2002), pp. 3628–3638.

[289] N. I. Butkovskaya, A. Kukui, and G. Le Bras. "Branching Fractions for H_2O Forming Channels of the Reaction of OH Radicals with Acetaldehyde". *J. Phys. Chem. A* 108.7 (2004), pp. 1160–1168.

[290] P. Morajkar, C. Schoemaecker, M. Okumura, and C. Fittschen. "Direct Measurement of the Equilibrium Constants of the Reaction of Formaldehyde and Acetaldehyde with HO_2 Radicals". *Int. J. Chem. Kinet.* 46.5 (2014), pp. 245–259.

[291] M. Altarawneh, A. H. Al-Muhtaseb, B. Z. Dlugogorski, E. M. Kennedy, and J. C. Mackie. "Rate constants for hydrogen abstraction reactions by the hydroperoxyl radical from methanol, ethenol, acetaldehyde, toluene, and phenol". *J. Comput. Chem.* 32.8 (2011), pp. 1725–1733.

[292] R. Sivaramakrishnan. "Personal Communication". 2014.

[293] K. T. Kuwata, T. S. Dibble, E. Sliz, and E. B. Petersen. "Computational studies of intramolecular hydrogen atom transfers in the beta-hydroxyethylperoxy and beta-hydroxyethoxy radicals". *J. Phys. Chem. A* 111.23 (2007), pp. 5032–5042.

[294] G. da Silva and J. W. Bozzelli. "Role of the alpha-hydroxyethylperoxy radical in the reactions of acetaldehyde and vinyl alcohol with HO_2". *Chem. Phys. Lett.* 483.1-3 (2009), pp. 25–29.

[295] F. Herrmann, B. Jochim, P. Oßwald, L. Cai, H. Pitsch, and K. Kohse-Höinghaus. "Experimental and numerical low-temperature oxidation study of ethanol and dimethyl ether". *Combust. Flame* 161.2 (2014), pp. 384–397.

[296] O. L. Gulder. "Laminar burning velocities of methanol, ethanol and isooctane-air mixtures". *Symp. (Int.) Combust., [Proc.]* 19.1 (1982), pp. 275–281.

[297] A. Konnov, R. Meuwissen, and L. De Goey. "The temperature dependence of the laminar burning velocity of ethanol flames". *Proc. Combust. Inst.* 33.1 (2011), pp. 1011–1019.

[298] D. Bradley, M. Lawes, and M. S. Mansour. "Explosion bomb measurements of ethanol-air laminar gaseous flame characteristics at pressures up to 1.4 MPa". *Combust. Flame* 156.7 (2009), pp. 1462–1470.

[299] J. P. J. van Lipzig, E. J. K. Nilsson, L. P. H. de Goey, and A. A. Konnov. "Laminar burning velocities of n-heptane, iso-octane, ethanol and their binary and tertiary mixtures". *Fuel* 90.8 (2011), pp. 2773–2781.

[300] F. N. Egolfopoulos, D. X. Du, and C. K. Law. "A study on ethanol oxidation kinetics in laminar premixed flames, flow reactors, and shock tubes". *Symp. Combust.* 24.1 (1992), pp. 833–841.

[301] K. Eisazadeh-Far, A. Moghaddas, J. Al-Mulki, and H. Metghalchi. "Laminar burning speeds of ethanol/air/diluent mixtures". *Proc. Combust. Inst.* 33.1 (2011), pp. 1021–1027.

[302] M. Christensen, M. T. Abebe, E. J. K. Nilsson, and A. A. Konnov. "Kinetics of premixed acetaldehyde + air flames". *Proc. Combust. Inst.* 35.1 (2015), pp. 499–506.

[303] A. Konnov. "Implementation of the NCN pathway of prompt-NO formation in the detailed reaction mechanism". *Combust. Flame* 156.11 (2009), pp. 2093–2105.

[304] S. S. Yoon, D. H. Anh, and S. H. Chung. "Synergistic effect of mixing dimethyl ether with methane, ethane, propane, and ethylene fuels on polycyclic aromatic hydrocarbon and soot formation". *Combust. Flame* 154.3 (2008), pp. 368–377.

[305] D. Liu, J. Santner, C. Togbé, D. Felsmann, J. Koppmann, A. Lackner, X. Yang, X. Shen, Y. Ju, and K. Kohse-Höinghaus. "Flame structure and kinetic studies of carbon dioxide-diluted dimethyl ether flames at reduced and elevated pressures". *Combust. Flame* 160.12 (2013), pp. 2654–2668.

[306] X. Qin and Y. G. Ju. "Measurements of burning velocities of dimethyl ether and air premixed flames at elevated pressures". *Proc. Combust. Inst.* 30.1 (2005), pp. 233–240.

[307] J. de Vries, W. B. Lowry, Z. Serinyel, H. J. Curran, and E. L. Petersen. "Laminar flame speed measurements of dimethyl ether in air at pressures up to 10 atm". *Fuel* 90.1 (2011), pp. 331–338.

[308] M. U. Alzueta, J. Muro, R. Bilbao, and P. Glarborg. "Oxidation of Dimethyl Ether and its Interaction with Nitrogen Oxides". *Isr. J. Chem.* 39.1 (1999), pp. 73–86.

[309] H. J. Curran, W. J. Pitz, C. K. Westbrook, P. Dagaut, J. C. Boettner, and M. Cathonnet. "A wide range modeling study of dimethyl ether oxidation". *Int. J. Chem. Kinet.* 30.3 (1998), pp. 229–241.

[310] H. Hashemi, J. M. Christensen, and P. Glarborg. "Experimental and Kinetic Modeling Study of Ethanol Combustion at High Pressures and Intermediate Temperatures". To be submitted, see Chapter 8. 2015.

[311] P. Marshall and P. Glarborg. "Ab initio and kinetic modeling studies of formic acid oxidation". *Proc. Combust. Inst.* 35.1 (2015), pp. 153–160.

[312] R. Sivaramakrishnan, J. V. Michael, A. F. Wagner, R. Dawes, A. W. Jasper, L. B. Harding, Y. Georgievskii, and S. J. Klippenstein. "Roaming radicals in the thermal decomposition of dimethyl ether: Experiment and theory". *Combust. Flame* 158.4 (2011), pp. 618–632.

[313] R. S. Tranter, P. T. Lynch, and X. Yang. "Dissociation of dimethyl ether at high temperatures". *Proc. Combust. Inst.* 34.1 (2013), pp. 591–598.

[314] S. A. Carr, T. J. Still, M. A. Blitz, A. J. Eskola, M. J. Pilling, P. W. Seakins, R. J. Shannon, B. Wang, and S. H. Robertson. "Experimental and Theoretical Study of the Kinetics and Mechanism of the Reaction of OH Radicals with Dimethyl Ether". *J. Phys. Chem. A* 117.44 (2013), pp. 11142–11154.

[315] J. Mendes, C.-W. Zhou, and H. J. Curran. "Rate Constant Calculations of H-Atom Abstraction Reactions from Ethers by HO_2 Radicals". *J. Phys. Chem. A* 118.8 (2014), pp. 1300–1308.

[316] R. S. Tranter, P. T. Lynch, and C. J. Annesley. "Shock Tube Investigation of CH_3 + CH_3OCH_3". *J. Phys. Chem. A* 116.27 (2012), pp. 7287–7292.

[317] S. Xu, R. Zhu, and M. Lin. "Ab initio study of the OH+ CH_2O reaction: The effect of the OH·· OCH_2 complex on the H-abstraction kinetics". *Int. J. Chem. Kinet.* 38.5 (2006), pp. 322–326.

[318] H. Guo, W. Sun, F. M. Haas, T. Farouk, F. L. Dryer, and Y. Ju. "Measurements of H_2O_2 in low temperature dimethyl ether oxidation". *Proc. Combust. Inst.* 34.1 (2013), pp. 573–581.

[319] E. Ranzi, A. Frassoldati, R. Grana, A. Cuoci, T. Faravelli, A. P. Kelley, and C. K. Law. "Hierarchical and comparative kinetic modeling of laminar flame speeds of hydrocarbon and oxygenated fuels". *Prog. Energy Combust. Sci.* 38.4 (2012), pp. 468–501.

[320] Z. Zhao, A. Kazakov, and F. L. Dryer. “Measurements of dimethyl ether/air mixture burning velocities by using particle image velocimetry”. *Combust. Flame* 139.1-2 (2004), pp. 52–60.